Monika Oftedal Voll

Deep processes in the Reinfjord Ultramafic Complex, Nord-Troms

A study of chromian Spinels and fractionation idicators in a layered ultramafic intrusion

Master's thesis in Bedrock and Resource Geology

Supervisor: Rune Berg-Edland Larsen

Co-supervisor: Bjørn Eske Sørensen

Trondheim, June 2019

Norwegian University of Science and Technology

Faculty of Engineering

Department of Geoscience and Petroleum

NTNU

Kunnskap for en bedre verden

Abstract

The Reinfjord Ultramafic Complex comprises one of several magmatic root systems in the Seiland Igneous Province, Northern Norway. Here, at a depth of 25-45 km, thousands of km^3 of ultramafic astenospheric melts passed through on the way towards more shallow levels.

The Reinfjord layered cumulate lithologies and replacive dunites contain several Cu-Ni-PGE reefs. By bulk rock chemistry from drill core RF1, RF2, RF3 and RF4, fractional magmatic evolution has been examined and suggested to explain many of the ore element reefs in the RUC.

To model fractional evolution, the well known Fe/(Fe+Mg) ratio has been used in addition to a newly proposed V/Cr ratio from bulk rock chemistry. The V/Cr ratio show potential for further use, especially when used together with Fe/(Fe+Mg). Three sequences of cumulates formed by fractional crystallization in a closed system, as well as an interval of cumulate assimilation and an interval of crystallization in an open conduit system has been identified. The two fractionation indicators proves especially useful for identifying intervals characterized by assimilation of wall rock.

A correlation between S and Cr in drill core RF4 noted by previous studies of the area has been examined. To this end, the chromian Spinels in the layered cumulates at the bottom of RF4 has been extensively studied. Chromite, Magnetite and Hercynite are present. Though assumed to be the last of the chromian Spinels to form, Hercynite is the most Mg-rich and Cr-poor of the Spinels. The Chromites and Hercynites of RUC show significant deviation from the linear Mg-Cr correlation in primitive Spinels observed elsewhere, indicating that for very deep magmatic systems, the crystallization of chromian Spinels are less affected by the melt's Mg content than previously assumed.

Indicators for fractional crystallization and the occurrence of elemental peaks in the drill cores has been used in a revision of previously interpreted profiles through RUC. The new additions to the model is that a fault located between RF1+RF3 and RF2+RF4 has been enlarged and proposed to account for ca 70m of vertical displacement between drill cores. In the proposed model, the Lower Layered cumulate Series is found below the replacive dunitic Central Series in the complex.

Sammendrag

Reinfjord Ultramafiske Kompleks er et av flere magmatiske rot-systemer i Seiland Magmatiske Provins i Nord Norge. Ved 25-45 km dybde passerte flere tusen km^3 med ultramafisk astenosfærisk magma gjennom rot-systemet på vei til overflaten.

Reinfjord består av lagdelte kumulater og replasive dunitter med flere Cu-Ni-PGE rev. Ved bruk av bulk rock-kjemi fra borekjærnene RF1, RF2, RF3 og RF4 blir fraksjonell magmatisk utvikling brukt for å forklare flere av revene fra Reinfjord.

For å indikere fraksjonell utvikling ble den velkjente Fe/(Fe+Mg)-indikatoren, i tillegg til en ny foreslått V/Cr-indikator brukt. V/Cr indikatoren har potensiale for videre bruk, spesielt når den brukes sammen med Fe/(Fe+Mg). Tre sekvenser med kumulater dannet av fraksjonell krystallisasjon i lukkede systemer, et intervall med kumulat-assimilering og et intervall med krystallisasjon i et åpent magmatisk pipe-system er identifisert i RF4. De to fraksjonerings-indikatorene er spesielt nyttige for å identifisere intervaller karakterisert av assimilering av sidebergarter.

En korrelasjon mellom S og Cr i RF4 har blitt observert i flere tidligere studier av området. For å undersøke det ble Cr-Spineller fra de lagdelte kumulatene i bunnen av RF4 studert. Kromitt, Magnetitt og Hercynitt er til stede. På tross av at Hercynitt er den Cr-Spinell fasen som er antatt at ble dannet sist, er det Hercynitt som har høyest Mg og lavest Cr blant Spinellene. Kromitt og Hercynitt i Reinfjord avviker betydelig fra den lineære Mg-Cr sammenhengen observert i primitive Spineller fra andre steder. Dette indikerer at i veldig dype systemer er krystallisasjonen av Cr-Spineller mindre påvirket av Mg-konsentrasjonen i magmaen enn tidligere antatt.

De fraksjonelle indikatorene og tilstedeværelsen av Cu-Ni-PGE rev er brukt til å revidere tidligere profiler gjennom Reinfjord Ultramafiske Kompleks. Tilleggene i modellen er at en forkastning mellom RF1+RF3 og RF2+RF4 har blitt forlenget og foreslås å forårsake ca 70m forskyvning mellom borekjærnene. I den foreslåtte modellen blir også den Nedre Lagdelte Serien funnet under de replasive Sentral-Serie dunittene i komplekset.

Acknowledgements

Thank you to my supervisors, Rune Berg-Edland Larsen and Bjørn Eske Sørensen for your guidance and assistance.

Thank you to Anna Pryadunenko and Trond Svånå Harstad for our discussions and your guidance when entering the realm of magmatic Spinels.

A warm thank you is sent to Alf Andrè Orvik for assisting with the igpet trigonal software and providing the 3D model of the Reinfjord plateau during fieldwork. The field camp would not have been the same without you. Thanks are also directed to Lars Tollefsrud, Frederik Reinhard, Jørgen Sakariassen and Donald Maute III for making the fieldwork a genuine pleasure.

Thank you, Kjetil Eriksen, for teaching me to use the SEM and assisting whenever I encountered difficulty. Thank you, Toril Sørløkk, for teaching me to properly crush rocks.

I wish to thank IGP and DIKU for funding the fieldwork and letting me travel to the Norwegian Geological Winter Meeting to present my work.

Thank you to my mother, Bente Oftedal, for your contributions on statistical methodology.

Virtual gratitude is sent to Lauren Tebay and her tutorial on how to use word properly, without which this thesis would have been infinitely more tedious.

Last but not least I wish to thank Simon Ross Stenger for providing the honorable Msc-goal *"My goal for this master thesis is to not become depressed".* You truly lowered the bar significantly and overall lessened my thesis-related stress. It has been greatly appreciated.

Table of contents

Table of contents

List of Tables

List of Figures

Abbreviations

Abbreviation	Meaning
ALS	ALS Scandinavia, lab
AVG	Average
BMS	Base Metal Sulfides
CIMP	Central Iapetus Magmatic Province
CS	Central Series
Chr	Chromite
ca	circa
Cpx	Clinopyroxene
xpol	Crossed Polarized Light
Dol	Dolomite
EPMA	Electron Probe Micro Analyser
EDS	Energy Dispersive Spectrometry
En	Enstatite
e.g.	example given
Fa	Fayalite
Fe-Ti	Fe and Ti-rich metamorphic magnetite
Fo	Forsterite
HREE	Heavy Rare Earth Elements
Hc	Hercynite
i.e.	in essence

IPGE	Iridium Platinum Group Elements
ARC	Island Arc
LIP	Large Igneous Province
La-ICP-MS	Laser ablation Inductively Coupled Plasma Mass Spectrometry
LREE	Light Rare Earth Elements
LLS	Lower Layered Series
Mt	Magnetite
MZ	Marginal Zone
max	Maximum
MORB	Mid Ocean Ridge Basalt
min	Minimum
NTNU	Norwegian University of Science and Technology
OIB	Ocean Island Basalt
Ol	Olivine
Opx	Orthopyroxene
fO_2	Oxygen faugacity
PPGE	Palladium Platinum Group Elements
Pn	Pentlandite
ppol	Plane Polarized Light
PGE	Platinum Group Elements
Po	Pyrrhotite
REE	Rare Earth Elements

RF1	Reinfjord drill core nr 1
RF2	Reinfjord drill core nr 2
RF3	Reinfjord drill core nr 3
RF4	Reinfjord drill core nr 4
RUC	Reinfjord Ultramafic Complex
SEM	Scanning Electron Microscopy
SIP	Seiland Igneous Province
STD	Standard Deviation
ULS	Upper Layered Series
WDS	Wavelength Dispersive Spectrometry

1 Introduction

1.1 What is the goal of this thesis – and why?

In this study, the nature of the Spinel and sulfide mineralization of the lower RF4 drill core in the Reinfjord Ultramafic Complex (RUC) in the Seiland Igneous Province (SIP) has been examined to resolve the following issues.

Which mechanisms facilitated the ore-forming events in RUC? Are the phases primary magmatic or have they experienced secondary remobilization during magmatic recharge and/or sub-solidus processes?

What can the fractionation indicators Fe/(Fe+Mg) and V/Cr tell us about the magmatic evolution of mafic-ultramafic systems?

How do the chromian Spinels formed in the RUC compare with Spinels formed in shallower locations?

What can the chromian Spinels tell about the magmatic evolution in the magma chamber?

What makes Reinfjord such a unique place, and why come to this remote place and study magmatic processes?

As phrased by Larsen et al (2018): *"Hopefully, this preliminary model of the SIP may contribute to a more profound appreciation of the deep-seated parts of giant magmatic systems and their importance for the lithospheric evolution of the Earth and, not least, may amplify more important areas of future research."*

1.2 Geological and geographical setting

The Reinfjord Ultramafic Complex (RUC) is located at 70 degrees North at the Øksfjord peninsula, Northern Troms Province, Norway. It is one of four ultramafic complexes in the Seiland Igneous Province (SIP), as seen in Figure 1.1. The SIP is a >5000 km^2 mafic and ultramafic (with minor alkaline, carbonatite and felsic rocks) complex that was emplaced at a depth of 25-35 km in the lower continental crust (Larsen et al., 2018). RUC is located in an alpine landscape, exposed at a mountain plateau at an altitude of 500-1000 meters above sea level. RUC covers 15 km^2 and consists of ultramafic cumulate rocks with a small degree of weathering (Grannes, 2016). The ultramafic cumulate lithologies are dunites, wehrlites, pyroxenites, websterites and Olivine clinopyroxenites.

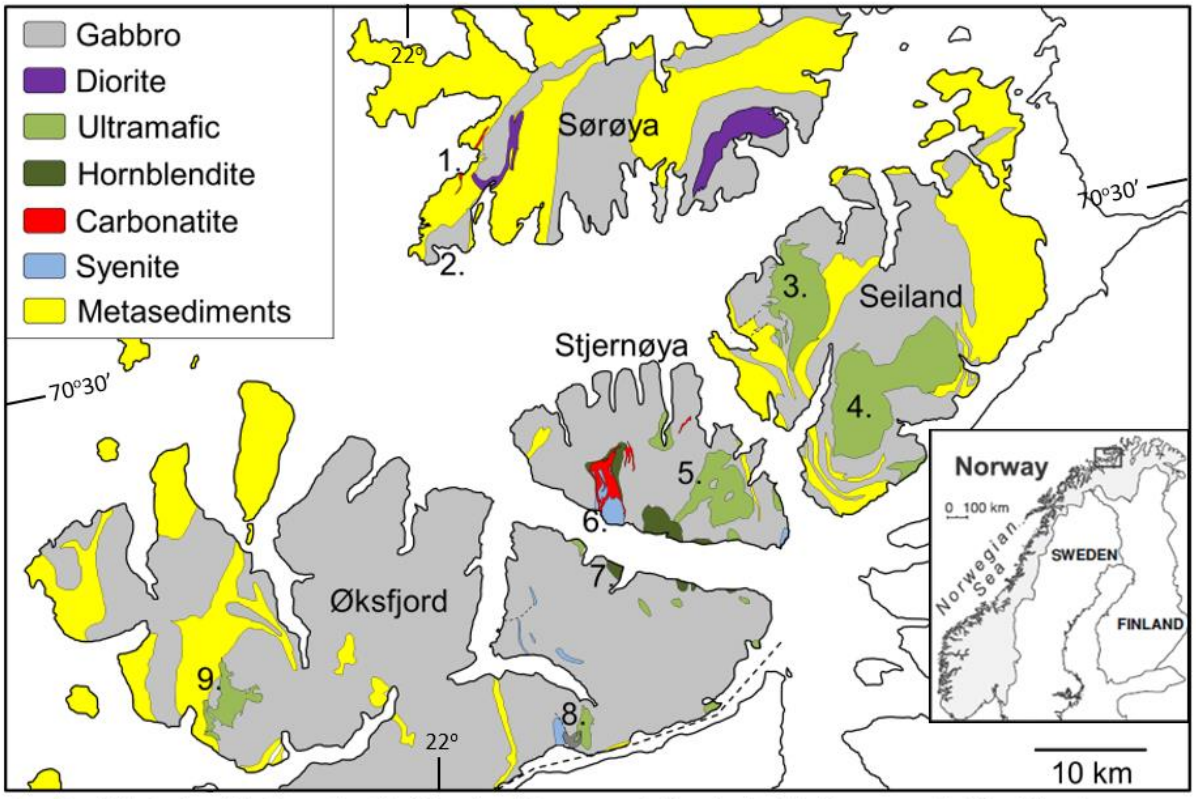

Figure 1.1

Regional geological map of the SIP with numbers marking localities (Bennett, 1986, Cadow, 1993, Elvenvold, 1993, Grant et al., 2016, Griffin, 2013, Larsen et al., 2018, Tegner, 1999). Reinfjord Ultramafic Complex is annotated as 9. Figure source: Larsen et al., (2018).

1.2.1 Global significance – the Central Iapetus Magmatic Province (CIPM)

The SIP is a result of the large juvenile igneous intrusive and extrusive Ediacaran event just prior to the opening of the Iapetus ocean (Ernst, 2010), the event co-incited with an event where the Earth's surface temperature increased by ca. 10 ºC., which ended the Cryogenian "Snowball Earth" époque (Scotese, 2002).

The magmatic event that formed the Large Igneous Provinces (LIPs) in Baltica, North America and Western Greenland mostly occurred 575-560 Ma ago (Higgins, 1998) is collectively named Central Iapetus Magmatic Province (CIMP) (Larsen et al., 2018). The CIMP is interpreted to have been formed by the initiation of continental rifting that caused the formation of the Iapetus ocean (Roberts et al., 2006, Roberts, 2010). Particularly in Labrador and Greenland, the CIMP is generally interpreted to have formed by partial melting of a carbonated fertile peridotite in the asthenosphere (Grant et al., 2016, Tappe, 2011) under the impingement of a mantle plume, e.g. Larsen et al. (2018).

In SIP we observe the only deep crustal exposure of the CIMP. We cannot be certain that the SIP deep seated conduit system (Larsen et al., 2018) connected with a LIP, but we can extrapolate that tens of thousands of km^3 of dense mafic and ultramafic magma (Larsen et al., 2018) must have passed through the deep passageways on their way towards the surface (Bennett, 1986, Grant et al., 2016, Griffin, 2013). SIP comprises one of a few localities where we can study the deep-seated evolution of a LIP forming system (Larsen et al., 2018).

1.2.2 Origin of the melts

There are two models for the origin of the magmatic melts. As presented by Griffin et al. (2013) and Sturt et al. (1980), there is the dunite melt model. It was made from observations of the Nordre Burmandsfjord Complex in the SIP (Sturt et al., 1980) (see Figure 1.1). It hypothesizes that the intrusive ultramafic rocks formed by large-scale contamination by the host gabbros of a dunitic parent magma. It is modeled that the magma had a MgO content of around 40 wt%, temperatures of 1650-1700 ºC, was 'dry' and had an extremely REE depleted composition. Opposing this hypothesis are Larsen et al. (2018), Bennett et al. (1986) and Grant et al. (2016). Larsen et al. (2018) state that a magma of the above modeled composition would have been among the warmest

and most magnesium rich melts ever reported, especially as late in the Earth's history as the Ediacaran. Griffin et al. suggested in their paper of 2013 that such a mantle composition could originate from melting of extremely depleted harzburgite residue within an upwelling mantle plume.

The model presented by Bennett et al. (1986) and supported by Grant et al. (2016) and Larsen et al. (2018) is called the picrite melt model. This was made from observations of the Reinfjord, Melkvann and Kvalfjord complexes in the SIP (see Figure 1.1). It proposes that the intrusions of the SIP consisted of melts mainly formed by fractional crystallization of picritic to komatiitic composition, with low to moderate amounts of contamination. This is supported by picritic to komatiitic early dykes found throughout the SIP, with chemical contents indicating that they underwent little fractional crystallization. They would have been in equilibrium with the more primitive Olivine and cpx compositions in the ultramafic complexes of SIP (Larsen et al., 2018). Larsen et al. (2018) argue that the high abundance of alkaline, carbonatite and other volatile enriched magmas, REE-enriched compositions of most of the SIP intrusions and the presence of Ni-Cu-PGE reefs from the RUC, it seems unlikely that the intrusive magmas were dry, as the dunite model proposes. The RUC is less affected by the contamination of the host rock gabbros than the other ultramafic complexes in the SIP (Grant et al., 2016).

Grant (in prep.) suggest that the RUC forming melts were two endmember magma compositions and melting temperatures (a carbonatitic metasomatized peridotite that melted at <1630^{o}C and a picrite melt formed by melting a peridotite with <10% pyroxenites at <1450^{o}C).

According to the 2018 paper by Larsen et al., four major ultramafic intrusive centers make up the *de facto* conduit systems which accommodated the flow of primitive asthenospheric melts to the continental lithosphere. These ultramafic conduits also facilitated the mixing of diverse types of melts in transient magma chambers such as for example RUC (Larsen et al., 2018).

1.2.3 Seiland Igneous Province (SIP)

The SIP consists of 5000 km^2 of mafic, ultramafic, alkaline and carbonatite rocks found in the islands of Seiland, Sørøya, Stjernøya and the Øksfjord peninsula (see Figure 1.1). The most recent

calculation of the proportions of different rock types by Larsen et al. (Larsen et al.), estimates 85% gabbros, 8-10% ultramafic rocks and 2-5% carbonatite, alkaline and other rock types in the SIP. The SIP is generally accepted to have formed from a mantle plume impingement into the lower crust (Grannes, 2016, Grant et al., 2016, Grant et al., in prep., Larsen, 2016, Larsen et al., 2018, Pastore et al., 2016, Sørensen et al., 2015, Tollefsrud, 2018)

Most of the SIP, RUC amongst them, is situated in a right way up position, dipping 0-20^{o} towards the NE (Larsen et al., 2018). The intrusions of SIP is part of the Upper Allochthon, in the lowest sequence of the Norwegian Kalak Nappe Complex that was upthrusted during the main Scandian phase (425-400 Ma) of the Caledonian orogeny (Corfu, 2007, Roberts et al., 2006). Late docking of the Kalak Nappe Complex during the Caledonian orogeny is an explanation for why the magmatic fabric of the SIP is so exceptionally well preserved (Larsen et al., 2018).

1.2.4 Igneous evolution

The general melt evolution observed by Larsen et al. (2018) is a reverse fractionation sequence. It evolves from alkaline to tholeiitic to komatiitic/picritic and back to tholeiitic and then alkaline. Although this general evolution is evident, it was also observed that the entire spectrum of melts were emplaced in the same conduit system simultaneously or in rapid succession. To add another layer of complexity; hydrous and carbonic rich assemblages are found in microscopic aggregates, in larger clots and in synmagmatic veinlets in the most primitive rocks. Here, they comprise 1-2% of the unaltered peridotitic cumulates (Larsen et al., 2018).

Dykes of ankaramite, picrite, lamprophyre, gabbro and wehrlite composition cross-cut most mafic and ultramafic parts of the SIP and are a late magmatic feature. Some dykes have chilled margins, and others hazy outlines, indicating that they were emplaced in both hot unconsolidated mushes and cooler solidified cumulates (Larsen et al., 2018). There are dyke swarms in all the ultramafic intrusions of the SIP, and >5 different generations may be identified (Reginiussen et al., 1995). Some very primitive picritic dykes were emplaced prior to or during the formation of the ultramafic intrusions and could be cogenetic with complexes such as RUC (Bennett, 1986, Grant et al., 2016). After studying the RUC dyke swarm, Orvik (2019) concluded that the dyke forming melts influxed through tributary and transport dykes during isobaric compositions, after minor cooling of the CS. The dyke-forming magma likely mixed in a deeper staging chamber from a heterogeneous

(variable degree of metasomatism) composition. The dykes from the dyke swarm have a significant volatile component. Orvik (2019) found it likely that the dykes formed contemporary with the carbonate clots, and found RUC formation conditions at 10-14 kbar, significantly higher than the previously assumed 8 kbar (Larsen et al., 2018).

The SIP generally has chondrite-normalized LREE enriched over HREE, but the entire spectrum is enriched (Roberts et al., 2006).

Sulfides with mantle S-isotope composition are important accessories found throughout the mafic as well as ultramafic rocks where they comprise 1-2 % of the cumulates. Clots of carbonate rich assemblages in unaltered peridotite rock and Amphibole and hornblende indicate that the primary ultramafic melts were unusually volatile rich (Larsen et al., 2018).

The O, C, Hf and Nd values in the SIP are the most juvenile of all the CIMP in the North Atlantic (Larsen et al., 2018, Roberts, 2010).

Chronologically, the ultramafic complexes began with emplacement of mafic melts, shortly followed by an ultramafic phase while the mafic cumulates were still hot and close to their solidus (Bennett, 1986, Griffin, 2013). In the RUC, there are numerous examples of Clinopyroxene rich cumulates that were replaced by irregular and discordant dunite and wehrlite bodies (Grannes, 2016). This occurred through melt-rock interaction with dissolution of Clinopyroxene and crystallization of Olivine (Grant et al., 2016), which reveals that the magma chamber was initially dominated by Clinopyroxene rich cumulates, and the magma evolved into more Olivine rich compositions (Larsen et al., 2018). The sequence of crystallization was from gabbroic cumulates, through Clinopyroxene rich cumulates and finally ending with Olivine rich cumulates i.e. a reverse fractional sequence. The hypothesis to explain this is presented by Grant et al. (2016).

In short, magmatic history is one of progressive thermo-chemical insulation. Prior to emplacement of the ultramafic complexes, basaltic melts were emplaced in to cold crustal sediments, resulting in predominantly gabbroic cumulates. Subsequently followed emplacement of ultramafic melts under the formation of the ultramafic cumulates. These formed the Olivine clinopyroxenite cumulates. Then ultramafic melts formed wehrlitic cumulates. Finally, dunites and replacive dunites were intruded and emplaced in a thermochemically insulated system (Grant et al., 2016).

Larsen et al. (2018) continued the work by Grant et al. (2016) and visualized the magmatic history in Figure 1.2.

The transition from mafic to ultramafic intrusions can therefore be explained by a continual influx of magma into the conduit systems, through repetitive emplacement of magmas partially replacing previously formed cumulates (Grant et al., 2016). The sequence evolved with numerous recharge events by progressively more primitive magmas into an open chamber system (Grant et al., 2016). This hypothesis neither agree with nor rule out the possible changes in mantle properties like depletion of the mantle plume due to continuous melt extraction (Griffin, 2013), changes in temperature from plume head to tail or an increase of melt production because of the removal of the lithospheric-asthenospheric lid.

Small volumes of alkali-carbonatite complexes appear to occur prior to and post large volumes of mafic and ultramafic magmatism in the SIP (Larsen et al., 2018), a feature also seen in other LIPs (Basu, 1993, Gibson, 2006). It is explained by plume melting models where carbonatites are formed either above or below the main plume head (Bell, 2004).

The dykes are cut by extensional shear zones, giving an extensional tectonic setting during emplacement of RUC intrusion (Sørensen et al., 2015)

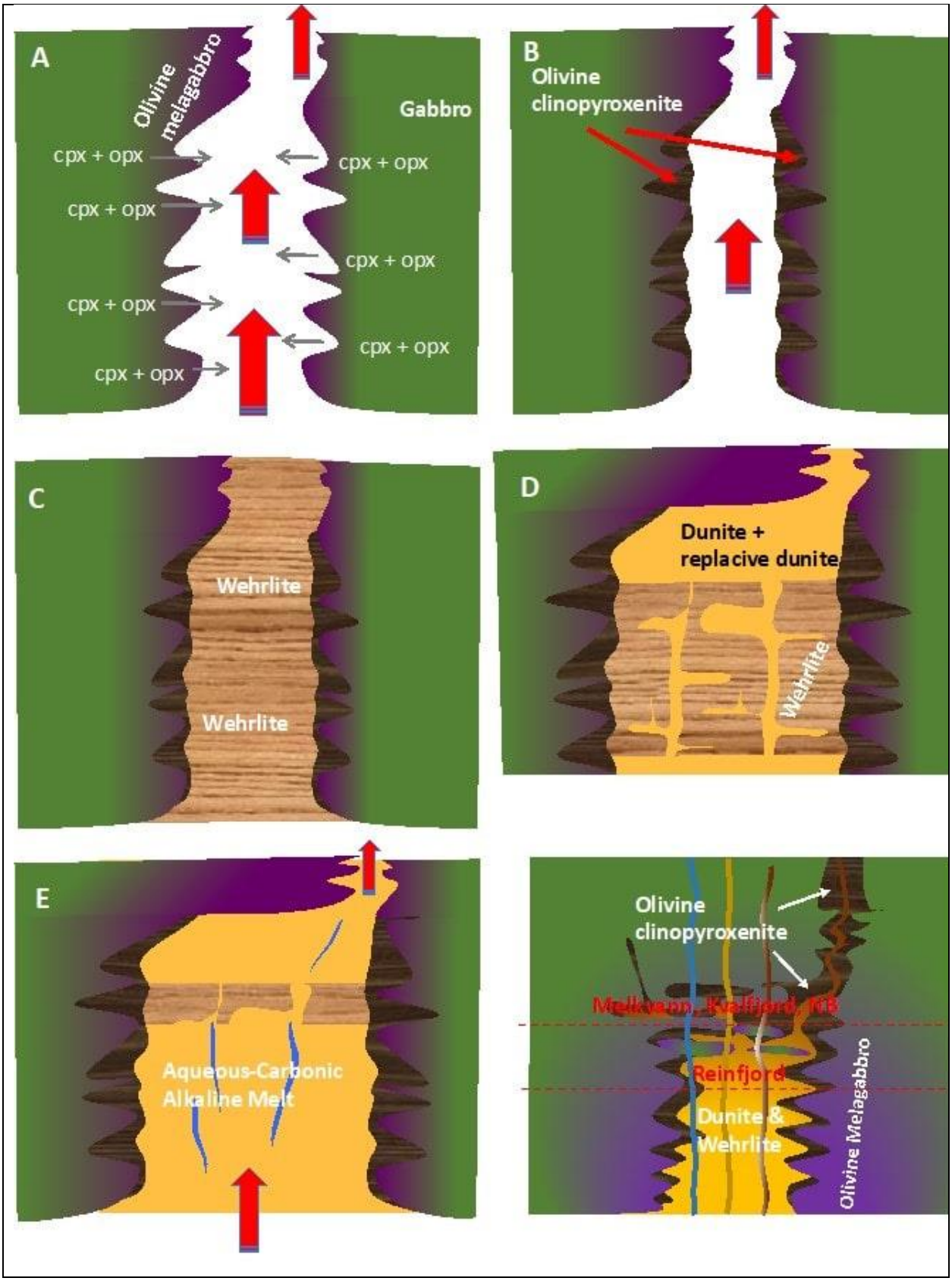
A
Olivine melagabbro
Gabbro
cpx + opx
cpx + opx
cpx + opx
cpx + opx
cpx + opx
cpx + opx
cpx + opx
B
Olivine clinopyroxenite
C
Wehrlite
Wehrlite
D
Dunite + replacive dunite
Wehrlite
E
Aqueous-Carbonic Alkaline Melt
Olivine clinopyroxenite
Melkvann, Kvalfjord, NB
Reinfjord
Dunite & Wehrlite
Olivine Melagabbro

Figure 1.2

Model by Larsen et al. (2018) of the evolution and formation of the SIP. White areas represent open unconsolidated magma conduits.
A) Assimilation by picritic-komatiitic melts (T=1400°C) intruding still hot gabbros. Partial meting and assimilation of cpx+opx in the gabbro.
B) Thermo-chemical insulation of the conduit system. Formation of the hybrid Marginal Zone. Formation of Olivine melagabbro to Olivine clinopyroxenite in the conduit walls.

C) Magma chamber growth and rise in T. Wehrlitic cumulates form during multiple recharge events.
D) Magma chamber growth and rise in T. Formation of replacive dunite and dunite cumulates through assimilation of wehrlitic cumulate pyroxene. Formation of Cu-Ni-PGE reefs. Homogenization of Olivine compositions (Grant et al., 2016).

E) Aqueous-carbonic alkaline melts infiltrate unconsolidated dunitic cumulates. Local remobilization of PGE-Au-reefs, particularly Au and Pd.
F) Emplacement of late dykes with compositions evolving from komatiitic/picritic to gabbroic and alkaline. Two red broken lines mark the relative depths of the four SIP ultramafic complexes (see Figure 1.1). RUC is deeper than the three others, and so displays less of the hybrid compositions found in Melkvann, Kvalfjord and Nordre Brumandsfjord.

Reinfjord is a deep (<25 km, 8 kbar (Larsen et al., 2018) and 30-45km, 10-14 kbar (Orvik, 2019)) crustal magma chamber in a conduit for giant magma volumes (Larsen et al., 2018). The dominant processes within the ultramafic conduit intrusions are fractional crystallization, crustal assimilation and melt-rock interactions between new batches of magma and previously formed cumulates (Grant et al., in prep.).

In 2016, Pastore et al. made a 3D model of the SIP using gravimetric data from TRIDENT Global (Fairhead, 2015), a gravity database of land and marine gravity measurements (Gellein, 2003), and magnetic data from surface samples analyzed by NGU (Olesen, 2010). The model can be seen in Figure 1.3 below. The geophysical model suggest that the RUC extend >9km below the current surface exposures (Pastore et al., 2016).

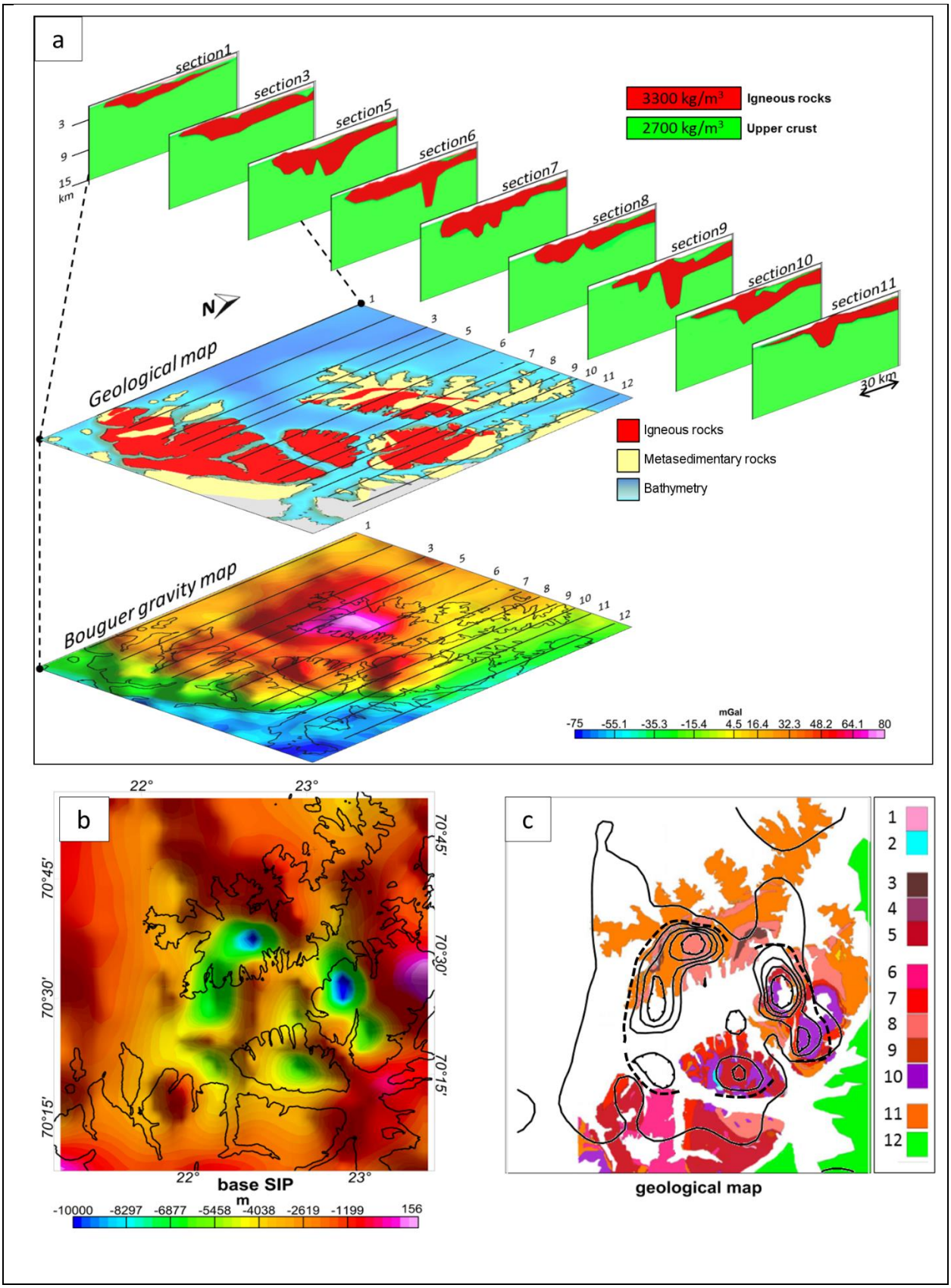
a
section1
section3
section5
section6
section7
section8
section9
section10
section11
3
9
15
km
3300 kg/m³
Igneous rocks
2700 kg/m³
Upper crust
N
Geological map
Igneous rocks
Metasedimentary rocks
Bathymetry
30 km
Bouguer gravity map
mGal
-75 -55.1 -35.3 -15.4 4.5 16.4 32.3 48.2 64.1 80
b
22°
23°
70°45'
70°30'
70°15'
base SIP
m
-10000 -8297 -6877 -5458 -4038 -2619 -1199 156
c
1
2
3
4
5
6
7
8
9
10
11
12
geological map

Figure 1.3

Models by Pastore et al. (2016) of the SIP based on gravity and geological data.
a) 3D model of the SIP from density modeling projected as parallel numbered sections. Below the sections and geological map is the gravity map the model based on (Fairhead, 2015, Gellein, 2003, Olesen, 2010).
b) Map of the base of the modelled mafic/ultramafic body of the SIP forming an annular pattern.
c) Depth contours of the base of the modelled mafic/ultramafic bodies in the SIP on the geological surface map (modified after (Roberts, 2007, Roberts, 2008))
Lithological legend in c):
1) Syenite
2) Carbonatite and nepheline syenite
3) Diorite
4) Olivine gabbro
5) Layered gabbro
6) Unspecified gabbro
7) Layered, foliated gabbro
8) Tholeiitic gabbro
9) Anorthosite
10) Peridotite
11) Metasediments interlayered with mafic intrusions
12) Metasediments

1.2.5 PT-conditions

Calculations of the P-T conditions that the RUC magmas experienced has been conducted by Orvik (2019) Gasser et al. (2015), Grant et al. (2016), Griffin et al. (2013) and Bennett et al. (1986) and most recently were revised by Sørensen et al. (2015) resulting in the chain of events presented in Figure 1.4.

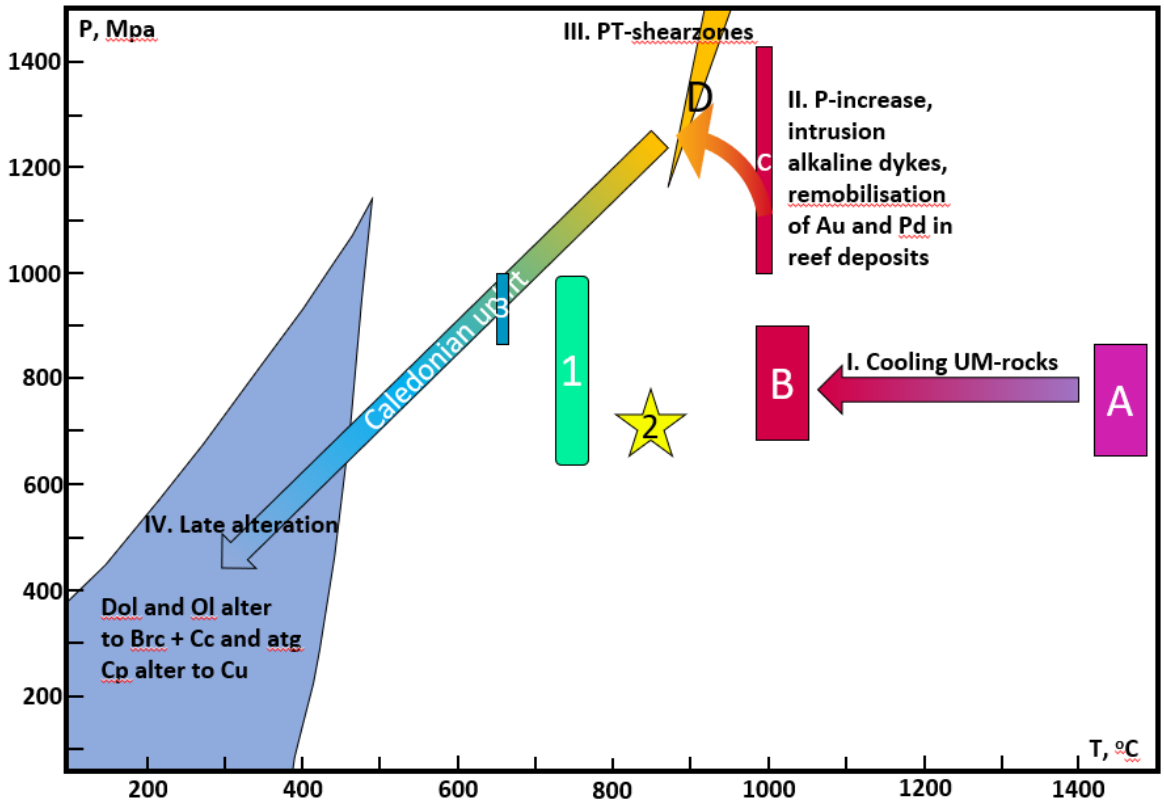

Figure 1.4

Diagram of the P-T evolution of RUC by Larsen et al. (2018) with Caledonian data from the Hasvik gabbro (see Figure 1.1).
1) Pre-intrusion temperature in the metasediment wall rock.
2) Conditions of contact metamorphism in the metasediment wall rock.
A) P-T of the picritic/komatiitic melts.
B) Cooling temperatures of the RUC from two-pyroxene thermometry.
C) Crystallization temperatures of lamproitic dykes.
D) P-T from pseudosections of extensional shear zones.
3) Caledonian uplift as experienced by the metasediment wall rock.

III) PT-condition of the Caledonian uplift from the Hasvik gabbro.
IV) Late alteration of Dolomite and Olivine forming brucite + calcite and chalcopyrite forming native copper.

To explain the substantial pressure increase in Figure 1.4 B) and C), it is hypothesized that there was emplacement of kilometers of flood basalts at the surface; similar to what we know from the Skaergaard intrusion in E Greenland (Larsen, 2006). An alternative hypothesis to explain the pressure increase is that the large volumes of dense ultramafic cumulates "pulled down" the entire continental lithosphere for the lithosphere to regain isostatic mass balance (Larsen et al., 2018).

Orvik (2019) found that the RUC dyke swarm formed at 10-14 kbar and similar temperatures as presented in Figure 1.4.

1.3 Reinfjord Ultramafic Complex (RUC)

The Reinfjord Ultramafic Complex (RUC) is a subhorizontal, steeply sided intrusion consisting of ultramafic cumulate rocks that intruded into the Langstrand Gabbronorites and, along the SW and NW, borders and metasediments (psammitic to politic garnet-bearing para-gneiss) with a contact aureole up to 2 km away from the contact (Bennett, 1974). The RUC have a well-developed layering with concentric development from pyroxene-rich rocks in the marginal sections and Olivine dominated cumulates towards and in the center (Larsen et al., 2018). There are modal variations of increasing Olivine and decreasing pyroxene and plagioclase from the gabbro contacts to the RUC center, as well as from early to late ultramafic rocks, with concentric zoning from Olivine melagabbro at the margins (Grannes, 2016) to pyroxenites, Olivine clinopyroxenites, wehrlites and dunites+wehrlites towards the dunitic core of the complex (Larsen et al., 2018). The most recent map of the RUC was made by Grannes (2016) and can be seen in Figure 1.6. The view of the RUC mountain plateau from Reinfjord village can be seen in Figure 1.5. Four drill cores has been drilled in the RUC. The RF1 (Iljina, 2013), RF2 (Schanche et al., 2012) were first drilled. Two more drill cores, the RF3 and RF4 were drilled in 2014 and were first described by Grant et al. (2016).

From Emblin (1985), the RUC consists of 3 parts:

The Lower Layered Series (LLS).

The Upper Layered Series (ULS).

The Central Series (CS).

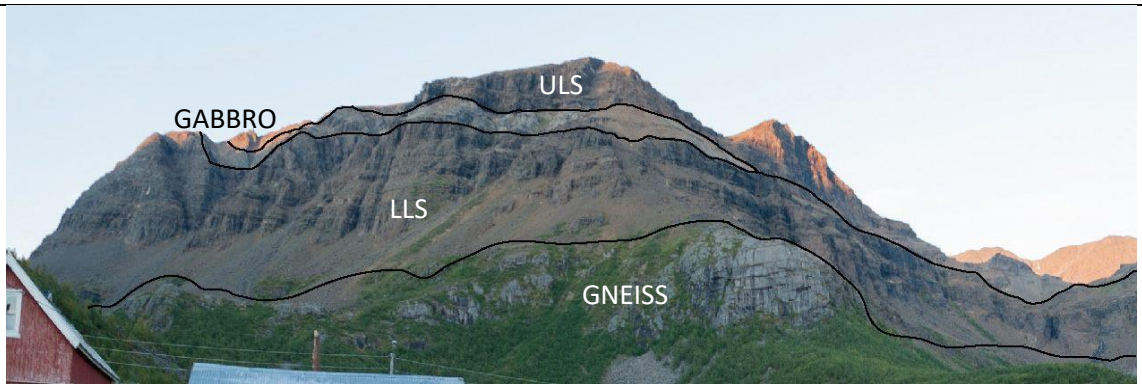

Figure 1.5

The RUC as seen from Reinfjord village (seen from SW). The lowest areas are a grey garnet gneiss. Above it is the LLS. The MZ between the two is covered by scree. A thin screen of gabbro separates LLS from ULS near the mountain top. (Photo by Lars Anker-Rasch, edited by Grannes, 2016).

The LLS and ULS vary from the rest of the ultramafic intrusions in the SIP as they have a well-developed layering (Larsen et al., 2018). They are separated by a 50 m thick gabbroic screen in the SW cliff wall (the only location we see the LLS clearly), yet it is uncertain whether the LLS and ULS formed at the same time (Larsen et al., 2018).

1.3.1 Marginal Zone (MZ)

The Marginal Zone (MZ) is a hybrid zone of mixing between the country rock gabbros + metasediments and the ultramafic intrusions. It comprise 25% of the RUC volume (Grannes, 2016). The MZ contain Olivine gabbro, pyroxene rich websterites, plagioclase rich ultramafic rocks and pyroxene pegmatites (Grannes, 2016).

1.3.2 Lower Layered Series (LLS)

The LLS is normally interpreted as the oldest of the ultramafic pulses (Grannes, 2016). It covers 7,5% of the RUC total volume (Grannes, 2016). It is rhythmically and modally layered and consists of 4 cyclic units of Olivine- and pyroxene- dominated cumulates (Bennett, 1986, Emblin, 1985). The LLS outcrops at the SW cliff face. The base layer of the unit is composed of Olivine rich lherzolitic cumulates with large oikocrystic Orthopyroxenes and cpx-poikilitic wehrlites. Above this are layers of more Clinopyroxene rich wehrlites and clinopyroxenites with oikocrystic Orthopyroxenes (Bennett, 1986). The Olivine composition is $Fo_{79,9\text{-}83}$ (Emblin, 1985). The contact between the LLS and country rocks is covered by scree (Grannes, 2016), as seen in **Error! Reference source not found.**.

1.3.3 Upper Layered Series (ULS)

The ULS is modally layered and consists of 7 cyclic cumulate units of Olivine- and Clinopyroxene-dominated cumulates (Emblin, 1985). It covers 22,5% of the RUC surface area (Grannes, 2016). It has an Olivine composition of $Fo_{81\text{-}83,5}$ (Emblin, 1985). The ULS outcrops along the W and E sides of the Reinfjord plateau, between 600 and 1000 m above sea level. The base of each unit mainly consists of wehrlite and dunite, with increasing levels of Clinopyroxenes in the upper layers, as Olivine clinopyroxenites become more dominant (Larsen et al., 2018). Layering varies from m to cm scale (Larsen et al., 2018), though a visual ca m scale layering is always observed in the field. The ULS show numerous examples of magmatic sedimentary structures, such as slumping, cross-bedding and load structures. The intrusive contacts with the wall rock is steep (Larsen et al., 2018).

1.3.4 Central Series (CS)

The CS is the youngest and most voluminous part of the complex, covering 45% of the RUC volume (Grannes, 2016). It occupies the central section of the plateau. The CS consists of cryptically layered dunites and wehrlites (Grannes, 2016). The cryptic layering is chemical variations in the mineral content (such as variations in Mg and Fe levels of Olivine) yet is chaotic and reversals of trends of Ol chemistry are common (Grant et al., 2016). The Olivine of the CS

has a composition of $Fo_{83\text{-}85,9}$. Dunitic dykes with 10 meters to cm scale thickness and common interstitial Olivine around primocryst pyroxene (Grannes, 2016). Irregular veins and structures, several places rooted in the CS, cut through the ULS (Larsen et al., 2018). The dunite dykes appear replacive, and Emblin (1985) and Grant et al. (2016) hypothesize that Olivine saturated melts have infiltrated semi-consolidated pyroxene rich cumulates and replaced the pyroxenes. By this cutting relationship, it is clear that the CS intruded after the emplacement of the ULS cumulates. If Emblin (1985) and Grant et al (2016) are correct in their hypothesis, the time period between the two intrusive events was short, as the ULS was a mush at the time of CS replacive dyke intrusion (Larsen et al., 2018). Within the cryptic layering of the CS, there are several reefs of sulfide hosted Ni, Cu, PGE deposits. Also common in the CS are cm to 10μm size carbonate rich clots (Larsen et al., 2018). A dyke swarm cuts through the CS in the central to northern part of the RUC.

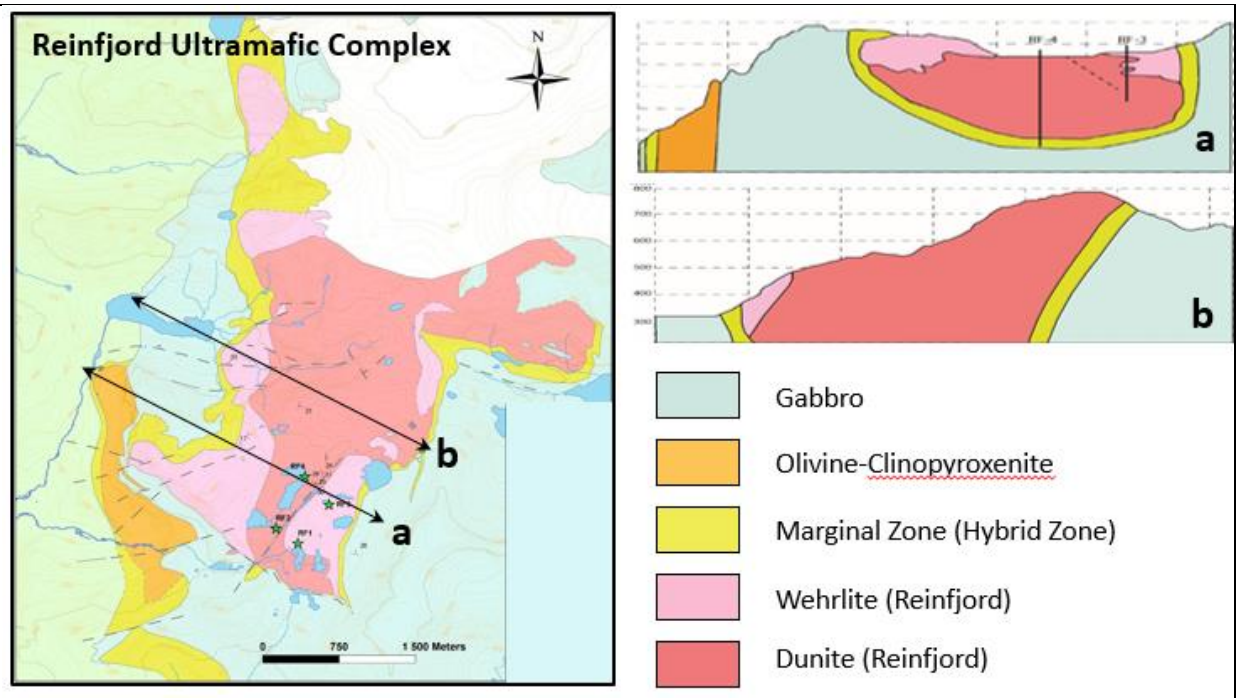

Figure 1.6

Reinterpretation of the RUC by Larsen et al. (2018), based on Grant et al. (2016) and Grannes (2016) The model is based on the RF1 through RF4 drill cores and geological surface mapping.

1.4 Previous work on ore forming Processes

Minor assemblages of magmatic carbonate and sulfide are common throughout the RUC, more so where the Cu, Ni and PGE reefs are located (Larsen, 2016, Larsen et al., 2018). The RUC contain both contact deposits (Søyland-Hansen, 1971) and reef deposits that are hosted in the dunitic CS cumulates (Larsen, 2016, Schanche et al., 2012).

The reef deposits of Reinfjord were located by an increased conductivity compared to the rest of the CS. They are modeled to sub-horizontal, saucer shaped at various depths, the strongest being at ca 100 meters depth below the surface, with 1,2% total sulfides (Larsen et al., 2018). The PGE reefs are decoupled from the Ni and Cu reefs by several meters. The Ni and Cu reefs are also mostly decoupled. Studies by Larsen et al. (2016) and Nikolaisen (2016) found that the ore mineral peaks are associated with dunitic cumulates of the CS. The PGE reefs of RF4 coincide with relatively S-poor dunitic rock. The PGM often occur in close association with sulfides, often pentlandite exsolutions in pyrrhotite tenors (Larsen, 2016, Nikolaisen, 2016, Tollefsrud, 2018). Gold-rich minerals occur in association with carbonate-sulfide assemblages (Larsen, 2016, Nikolaisen, 2016).

The Pt/Pd ratios of the anomalous PGE reefs are between 1:1 and 1:2, and the PGE-poor sections have a ratio of 2:1 (Tollefsrud, 2018).

Because of a distinct difference in sulfur isotope values between the dunites and the host rock gabbros and paragneisses found by Oen (2013) we know that the parental melts that formed the ultramafic cumulates gained its sulfur from a distinctly different source than the source regions of both paragneiss and gabbros; though both the dunites and gabbros have $\delta^{34}S$ within normal mantle range (Larsen et al., 2018). The mantle sulfur source became lighter as melt extraction evolved from producing basaltic melts that are now the gabbros, and evolved into a steadily more picritic/komatiitic melts that formed the ultramafic complexes (Larsen et al., 2018, Oen, 2013).

The SIP has been much less studied than similar formations other places despite it being the deepest exposed formation in the CIMP. The mafic and ultramafic rocks of Stjernøya were first documented by Oosterom (1963) and the western parts of Øksfjorden by Hooper (1971). The rocks of Reinfjord were first described by Bennett (Bennett, 1971, Bennett, 1973), and then reclassified by Emblin (1985). Emblin's classification is the one still in use with some modifications. Bennett

et al. (1986) published the first overview of the 4 ultramafic intrusions in the SIP, this has been supplemented by Larsen et al. (2018).

Robins and Gardner (1975) proposed a subduction setting for the formation of the SIP through subduction of oceanic crust under the Baltican continental plate. This was disproved by Krill and Zwaan (1987), when they found indications for formation during an extensional tectonic regime. This has been confirmed by Roberts et al. (2006) who conducted a dating of the intrusion and Sørensen et al. (2015) who researched the structural geology of the RUC. After Nordic Mining in collaboration with NTNU found a possible Cu-Ni-PGE deposit in 2013 (Iljina, 2013) 4 drill core holes were drilled, several publications have been made and several master theses and articles has been written on the deposit.

2 Theory

2.1 System for characterizing a magma – nomenclature

Ultramafic rocks contain at least 90% **mafic minerals**: **Olivine (Ol)**, **Clinopyroxene (Cpx)**, **Orthopyroxene (Opx)** and **Amphibole (Am)** and sometimes **biotite** (Siivola and Schmid, 2007, Streckheisen, 1973, Streckheisen et al., 2002).

There are several systems of characterization and nomenclature for composition of magmatic rocks and magmas (White, 2005), as they are mostly defined by three minerals in ternary compositional diagrams. The three minerals used in classification of ultramafic melts are the three most prominent minerals, i.e. Olivine (Ol), Clinopyroxene (Cpx) and Orthopyroxene (Opx). Mafic rocks have two of the latter and plagioclase.

In this thesis the QAPF modal mineralogy-based nomenclature will be used to characterize the cumulate rocks (see Figure 2.1).

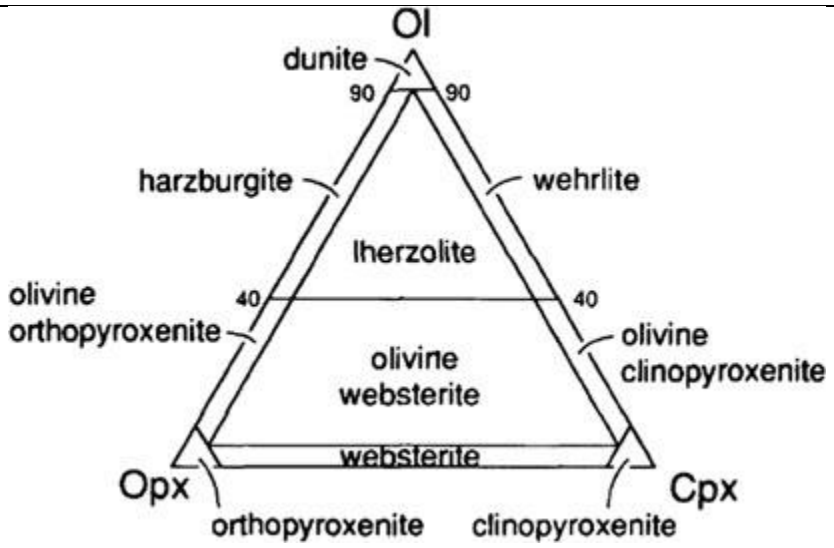

Figure 2.1

Classification of ultramafic rocks using the proportions of Olivine (Ol), Clinopyroxene (Cpx) and Orthopyroxene (Opx) (Streckheisen, 1973, Streckheisen et al., 2002).

2.2 Reefs

When potentially economically viable minerals are concentrated, they are termed **ore formations**. One such type of ore formation is a "**reef**". Reefs are continuous sub-planar sections of the rock enriched in economic metals. They are formed as density contrast or other physical properties that separates the ore minerals from the magma and either sink to the bottom of the magma chamber or rise to its roof.

This thesis deals with sulfide mineral occurrences in an ultramafic magma chamber.

There are two methods for concentrating sulfide to form ore deposits. One is through **sulfide immiscibility** and the other is through **partial melting** and/or **fractional crystallization** of the melt. The two can work simultaneously. These two will be presented below.

2.3 Magmatic processes

2.3.1 Bowens reaction series

Olivine is the first mineral to crystallize from a magma, forming at the highest temperatures as a magma begin to cool. The next mineral is pyroxene or sometimes plagioclase (Bowen, 1922).

2.3.2 Partial melting

Rocks gradually melt as T-P-fluid conditions allows it, this is called **partial melting**. When a rock melts, the magma can behave in two different ways. Either the magma remains in equilibrium with the melting rock, this is called **batch melting**, or it escapes immediately upon melting, this is called **fractional melting**. To form an **intrusion**, a rock in the Earth's lithosphere or asthenosphere must melt and the magma escape upwards. Buoyancy of the melt depends on density and **viscosity**. Viscosity is a measurement for a liquid's resistance to changing shape. When high, the melt is thick and not very mobile whereas low viscosity melts, such as mafic and ultramafic melts, migrate upwards. This ability is somewhat counteracted by the high density of mafic ultramafic melts compared to the lighter crustal rocks.

2.3.3 Fractional crystallization – cumulates

When crystalline phases form in a magma, they can either be transported with the magma; or they can be removed from the magma through gravity, either downwards (heavier) or upwards (lighter phases). The latter process is called **fractional crystallization** and occurs when the magma has a low viscosity and a mineral/melt density contrast. When fractional crystallization occurs, the crystals accumulate and form a **cumulate** (Robb, 2005). A cumulate rock does not have the same chemical composition as the melt from which it crystallized.

2.3.4 Magma density

The **density** of the magma will vary over the course of its crystallization as the melt will e.g. become less dense after the dense minerals pyroxene and Olivine has crystallized, incorporating heavy Fe ions. If the same melt predominantly crystallizes a light mineral such as plagioclase, the remaining melt would become denser. Generally, the minerals formed in an ultramafic magma are denser than the magma itself, so gravitational settling is the most common process to account for

mafic and ultramafic magmatic layering (Robb, 2005). Crystal settling, convective fluid flow and **diffusion**-related **chemical segregation** across density-stratified layers are the processes that form layered mafic and ultramafic intrusions (Grannes, 2016).

2.3.5 Recharge: pluming and fountaining

The process where a magma chamber is opened and intruded by a later magma is called "**recharge**" or **replenishment**. Depending on the densities of the two magmas, recharge can occur in two different ways. If the intruding magma is denser than the original magma, it will briefly rise due to emplacement pressure, and then sink through the original magma to stabilize at the bottom of the chamber. This is called "**fountaining**". If the intruding magma is less dense than the original magma, and the intrusive will rise through the magma chamber, mixing with the original magma as it travels. This is called "**pluming**. The two are illustrated in Figure 2.1.

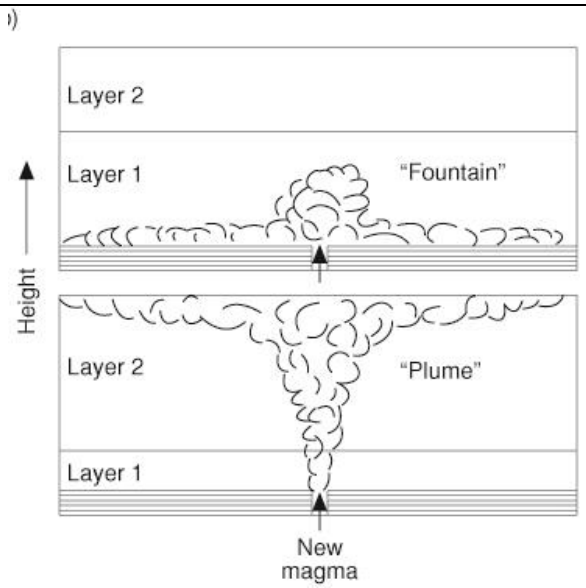

Figure 2.2

Upper image: "fountaining" - injection of dense magma in a magma chamber.

Lower image: "pluming" - injection of lighter magma in a magma chamber.

Figure made by Robb (2005).

A recharge event with either pluming or fountaining will lead to **turbulent** mixing of the two melts, but during a fountaining event the intruding magma will quickly settle at the bottom of the chamber, making the period of mixing shorter than in a fountaining event and mixing most efficient at the bottom of the magma chamber.

2.4 Geochemical processes

Most ores were formed from elements that were originally at trace element concentrations in the magma or rock and were subsequently enriched by processes discussed in this section. (Robb, 2005)

2.4.1 Compatible and incompatible elements

Compatibility is a measure of the probability of an element to partition into a crystal from the melt. **Incompatible elements** are thus elements that would remain in the melt because they do not fit into the atomic lattice of the ambient crystalline phases. **Compatible elements** will become depleted in the melt while incompatible elements are progressively enriched as the melt crystallizes (Robb, 2005). When a rock is partially melted, the initial melt will be highly enriched in incompatible elements and become progressively less so as a larger portion of the rock melts (Robb, 2005). When experiencing fractional crystallization and cumulate formation, compatible elements will readily substitute into the crystal lattice of the cumulus minerals, thus incompatible elements will become progressively enriched in the residual magma as a cumulate assemblage is formed (Robb, 2005).

How incompatible elements are concentrated in the melt during varying degrees of partial melting is shown in Figure 2.3 below. In the figure, **D** is the **bulk partition coefficient** of the residual and original solid (D_{res} and D_O respectively), **F** is **weight fraction of melt produced** (where F=1 means that all the solid has melted), **C_O** is **original concentration of the trace element in the parental solid** and **C_{liq}** is **the concentration in the liquid/melt** (Robb, 2005).

When F=1 and all the solid has been melted, the melt will have the same chemical composition as the solid did. If it was fractionally melted, as seen in Figure 2.3 b), elements with D<0.1 are mostly

removed at a smaller F than F=1, resulting in a higher relative concentration of the remaining elements than were in the original solid upon complete melting. A low degree of fractional melting is therefore optimal for creating an ore forming magma that is greatly enriched in incompatible elements. A high degree of fractional crystallization will have the same effect on the concentration of incompatible elements for ore forming purposes. Highly incompatible elements with very low D_{res} will have a maximum concentration of $1/D_{res}$ as F approach 0 (Robb, 2005).

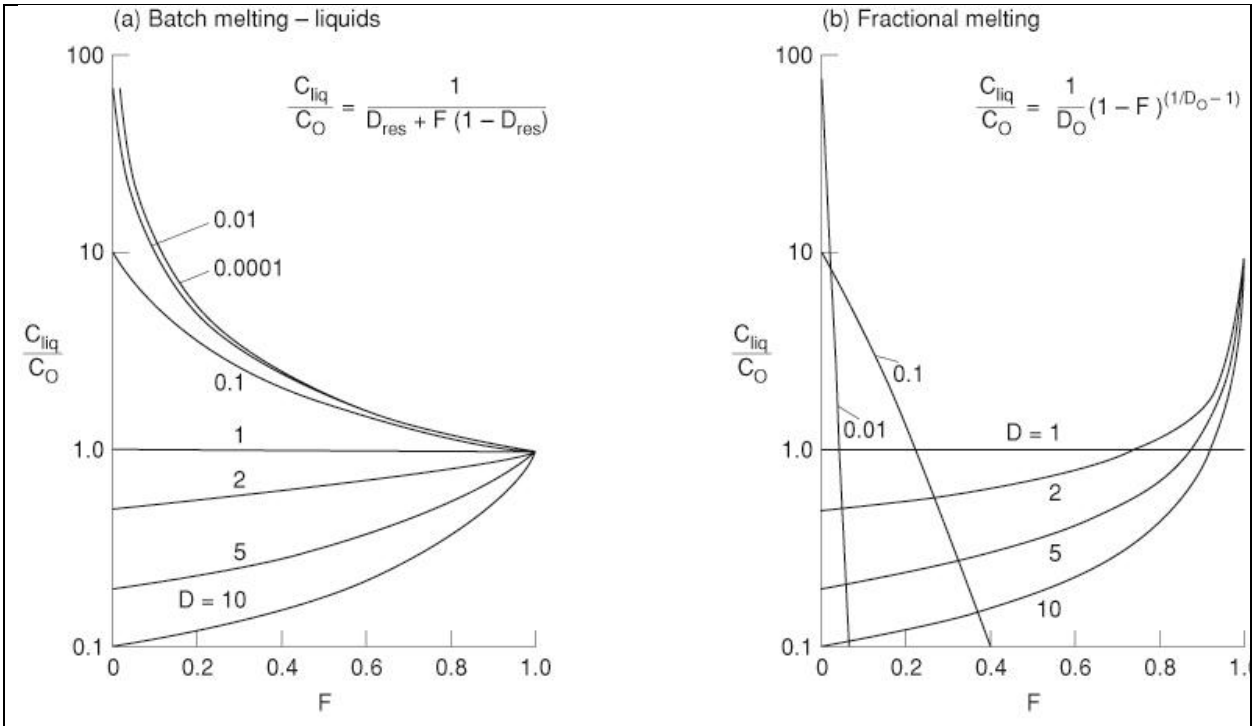

Figure 2.3

A) Batch melting where melt and residual solid are in equilibrium

B) Fractional melding without any reaction between melt and solid residue. Melt is immediately removed from the system.

Figure made by (Robb, 2005)

2.4.2 Sulfide immiscibility and solubility

As phrased by Laurence Robb (2005):

"Liquid immiscibility is the segregation of two coexisting liquid fractions from an originally homogeneous magma."

During liquid immiscibility, a liquid will split into chemically different factions, such as sulfide-silicate or oxide-silicate immiscibility or two silicate-rich melts with different compositions.

Chemically different immiscibility occurs when the solubility of an element is lower than its concentration in the melt. Sulfide-silicate immiscibility is one such type which is widely accepted as a commonly occurring feature in mafic and ultramafic magma crystallization (Robb, 2005). To reach sulfide immiscibility, the concentration of sulfur must be greater than the solubility curve at a given temperature and pressure gradient. The sulfide solubility curve can be seen in Figure 2.4 below:

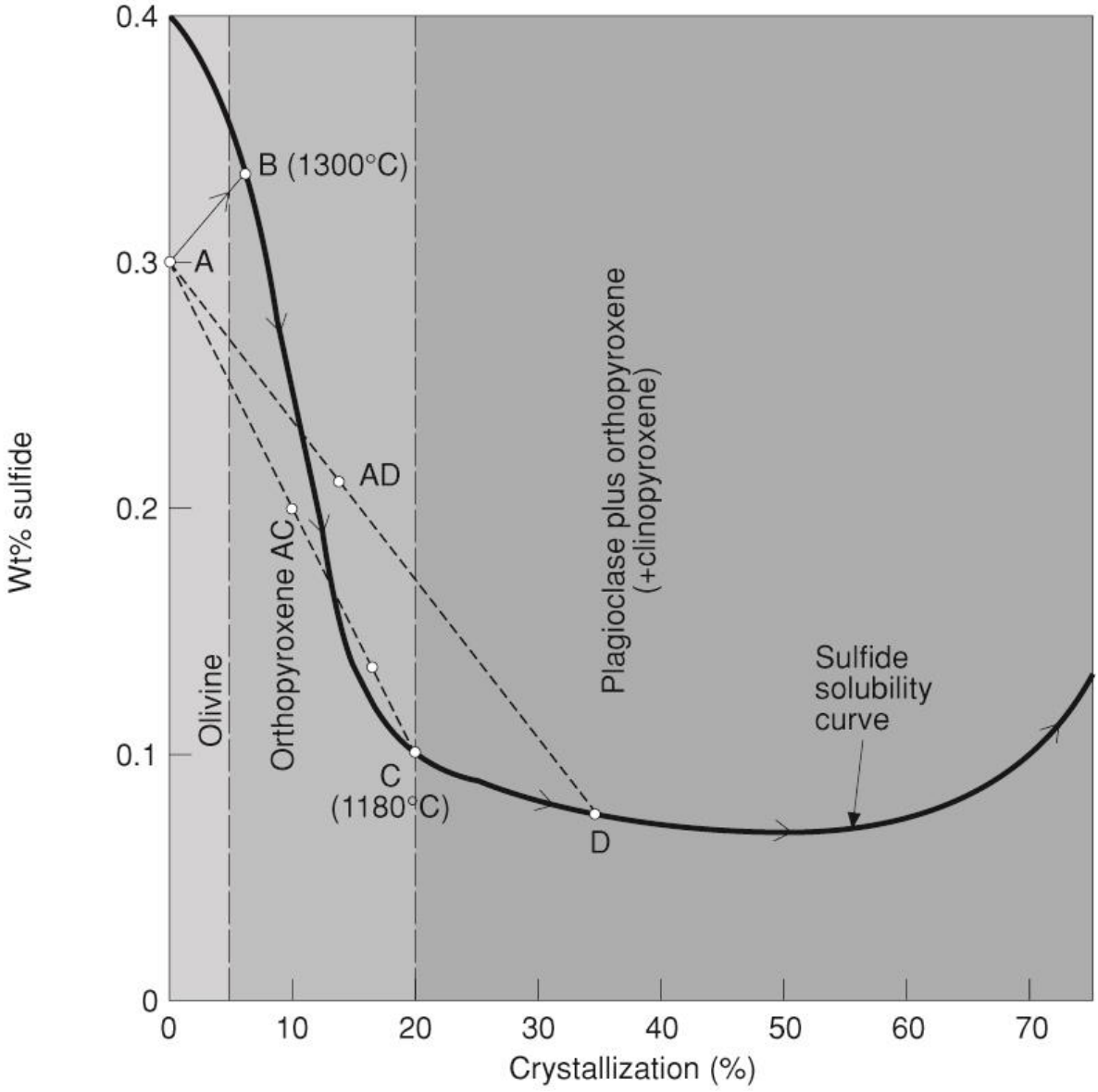

Figure 2.4

Sulfide solubility curve with variation in Wt% sulfide and % crystallization in a gabbroic melt. The cumulate assemblages are marked with different grey scale. A, B, C and D are melt compositions, AC and AD marking the mixing points between them (Robb, 2005)

To reach sulfide immiscibility, the S concentration in the melt must be above the solubility line in the diagram. Sulfide solubility decrease with decreasing temperature, increase with decreasing pressure and appear to decrease with increasing oxygen content in the magma (Maclean, 1969). Sulfide solubility increase with an increase in MgO, CaO and FeO, and decrease with an increase

in SiO_2 and Al_2O_3 (Naldrett, 2004). Because of the drastic pressure decrease when melt rise, the sulfide solubility will increase as the magma rise. To reach strong sulfide oversaturation, another process must intervene. One option is by increasing the total amount of sulfur in the melt through e.g assimilation of S-rich lithologies or recharge by a S-rich melt. Another option is by crystallizing part of the magma, so that the residual magma becomes oversaturated with sulfur.

When the sulfide saturation is greater than the solubility, sulfide droplets nucleate in the magma to form immiscible sulfide droplets, and some elements preferentially partition into the sulfide liquid.

2.4.3 Partitioning factor – chalcophile, siderophile and lithophile elements

Another important factor when describing an element's magmatic interaction is its partitioning coefficient between two phases. The partitioning coefficient describes which liquids the element has an affinity for and how strong this affinity is. The partitioning factor for various metals into a sulfide liquid from a silicate magma is displayed in Table 1.

Table 1: Estimates of sulfide-silicate partition coefficients for Ni, Cu, Co, Pt and Pd in ultramafic and mafic magmas. Table by (Robb, 2005), data from (Naldrett, 1989), (Barnes, 1995) and (Tredoux, 1995).

	Ni	Cu	Co	Pt	Pd
Komatiite					
27% MgO	100	250-3000	40	10^4-10^5	10^4-10^5
19% MgO	175	250-3000	60	10^4-10^5	10^4-10^5
Basalt	275	250-3000	80	10^4-10^5	10^4-10^5

Three features from the Goldschmidt classification (Goldschmidt, 1937) will be highlighted here: chalcophile, siderophile and lithophile element behavior. The periodic table separated into this system of characterization can be seen in Figure 2.5.

A **chalcophile** element will preferentially partition to form minerals with sulfide if sufficient sulfide is present. Examples of chalcophile elements are Cu, Pb, PGE, Zn, Ag, Cd etc. All metals

with chalcophile tendencies are likely to separate into an immiscible sulfide phase instead of remaining in the silicate magma (Robb, 2005).

A **siderophile** element will preferentially form alloys with iron if sufficient iron is present (Robb, 2005). The Goldschmidt definition of siderophile behavior is an element that will preferentially segregate into molten iron liquid – characterized by only neutral metallic bonds – if present. This is only the case in the Earth's molten outer core. Fe is the defining siderophile element. Sulfide liquids are mostly composed of Fe and S in near equal modal proportions. In the absence of liquid Fe metal, siderophile elements behave as chalcophile. Because of this, siderophile elements are concentrated in sulfide minerals along with chalcophile elements (White, 2005). Examples of siderophile elements are Ni, Co, Os and Ir.

A **lithophile** element will preferentially concentrate in silicate phases. Lithophile elements tend to form ionic bonds. Examples of lithophile elements are V, Th, Ta, Rb, Sr, Ba, Nb, U and the REE (White, 2005).

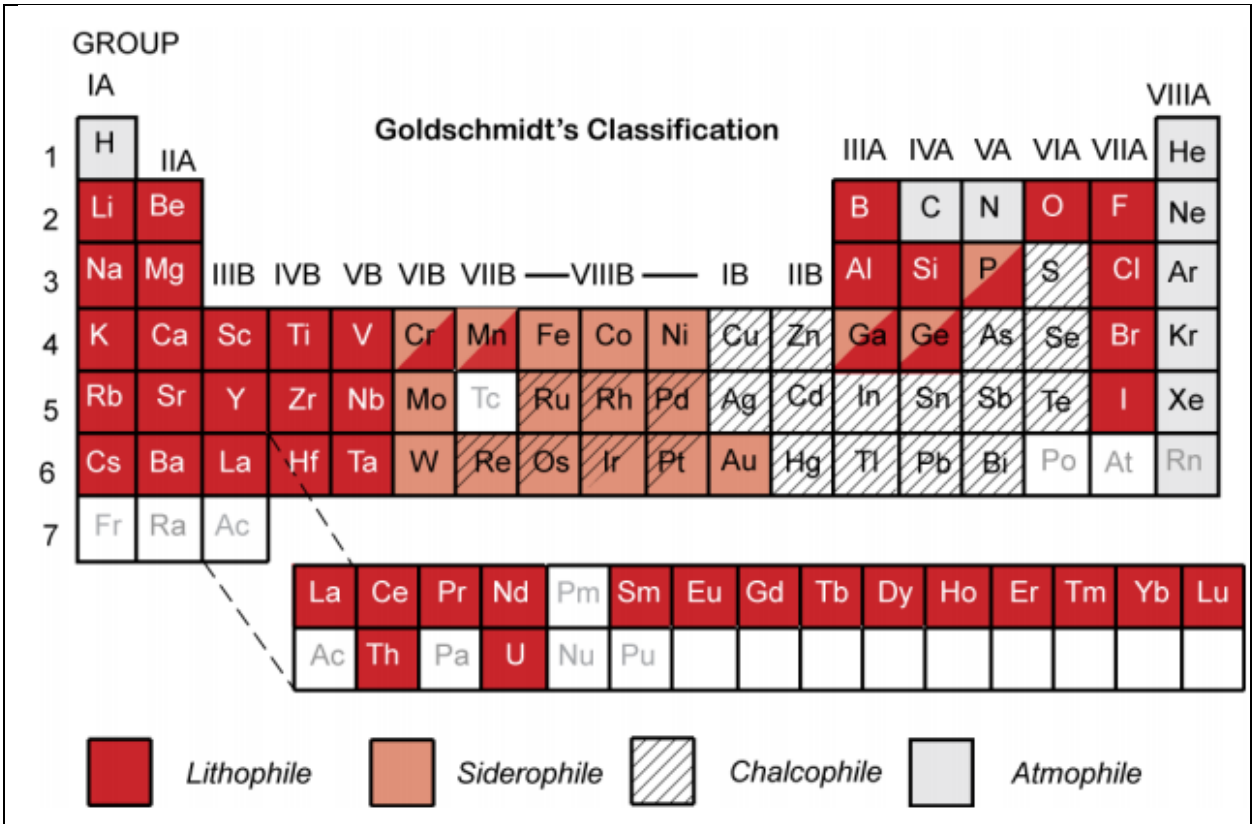

Figure 2.5

Goldschmidt's classification of elements and their properties (White, 2005).

The degree of compatibility of an element is important to understand its willingness to leave the magma to form a crystal, and the chalcophile and siderophile properties of the element are important to understand how the element will partition when in contact with both the magma and the immiscible sulfide droplets.

2.4.4 R-factor

The factor of the mass of silicate melt which has been into contact with sulfide liquid is called the "**R-factor**", as defined by Campbell and Naldrett (1979). An R-factor of 10 000 means that a droplet of sulfide liquid has been into contact with 10 000 times its own weight in silicate melt and scavenged elements all the while. When forming an ore deposit, it is preferential that the economic elements (Cu, PGE, Ni etc.) are concentrated as much as possible in sulfides, resulting in a highest possible grade for the ore. Ideally then, there will only be a small amount of sulfide droplets in the magma, and all economic elements will be partitioned into these. The globules will then be collected and strongly concentrated somewhere. To make an ideal ore deposit, then, we want the R-factor to be very high.

An equation to show the relation between the R-factor, the partitioning coefficient for the specific mineral between melt and sulfide, the concentration of a mineral in the magma and in the sulfide liquid is presented by Campbell and Naldrett (Campbell) in Equation 1:

Equation 1

$$C_{sulfides} = C_0 * D_{istribution\ coefficient}\ (R + 1) / (R + D_{istribution\ coefficient})$$

Where C_0 is the original concentration in the silicate melt, $C_{sulfides}$ is the concentration of the trace element in the sulfide liquid, $D_{istribution\ coefficient}$ is the partitioning coefficient for said element between the two immiscible phases and R is the R-factor.

If a sulfide droplet has been in contact with large quantities of magma and scavenged the strongly chalcophile elements from it, it will end up with a high $C_{sulfides}$, and subsequently, byEquation 1, it will have a large R-factor.

Figure 2.6 is a graph displaying how much Ni and Pt (y-axes) partitions into sulfide liquid depending on the R-factor (x-axis). Ni begins to partition heavily into the sulfide liquid immediately and reach its maximum partition at $R=10^{4.5}$. Pt on the other hand doesn't really begin to partition into the sulfide liquid before $R=10^{3}$, reaching its maximum at ca $R=10^{7}$. To form a PGE deposit, a very high R-factor is therefore required.

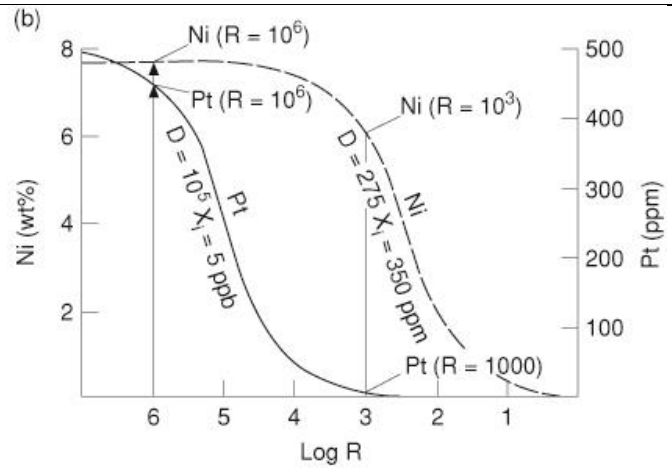

Figure 2.6

R-factor for Ni and Pt by (Robb, 2005).

For a greatest possible R-factor, turbulent pluming is preferential when new magma enters the chamber. This lets the sulfide droplets come in contact with large volumes of magma before the sulfide droplets' high density makes them sink to the bottom of the chamber, or outcropping segments, and settle there.

2.4.5 Element groups and abbreviations

Platinum Group Elements (PGE) include Pt, Pd, Ir, Os, Ru and Rh. The **Iridium Platinum Group Elements (IPGE)** include Ir, Os, Rh and Ru. The **Platinum Palladium Group Elements (PPGE)** include Pt, Pd and Au (Harris and Cabri, 1991).The **Rare Earth Elements (Higgins)** are the two lowest lines in the periodic table. They are separated into the **Heavy REE (HREE)** and the **Light REE (LREE)** based on the element's density. The LREE are to the left in the periodic table and the HREE are to the right.

Sulfide minerals: base metal sulfide minerals (BMS)

The sulfide minerals most commonly found in mafic and ultramafic rocks are Base Metal Sulfides (BMS). They are sulfide minerals with variations of the following cations:

Cu, Ni and Fe; and to a smaller degree Zn, Co, Cd, As, Se and Sn (Robb, 2005). The most common BMS are:

Chalcopyrite	$CuFeS_2$	
Cubanite	$CuFe_2S_3$	
Pentlandite	$(Fe, Ni)_9S_8$	
Pyrrhotite	$(Fe_{x-1})S$	where $0,2>x>0$

2.4.6 Crystallization of sulfide droplets

As an immiscible sulfide liquid forms, the base metals, chalcophile and siderophile elements partition into it forming a **BMS liquid**. The BMS liquid settles on the cumulate pile and forms a BMS and PGE rich layer (Barnes et al., 2008). As the sulfide liquid cools, it crystallizes into a **monosulfide solid solution** (**MSS**) and an **intermediate solid solution** (Thomson and Davisson). With falling temperature, pyrrhotite and pentlandite are exsolved from the MSS (Kullerud, 1969) and chalcopyrite and cubanite are exsolved from the ISS (Cabri, 1976).

Due to the high temperature, the first MSS to form from the sulfide liquid is Fe-rich, leaving the fractionated BMS liquid enriched in Cu, Ni, Co etc. (Barnes et al., 2008). As temperature decrease, Ni will partition into the MSS and crystallize along with the ISS as a Ni-rich MSS (Peregoedova, 1999).

As temperature falls below 600°C, pentlandite and pyrrhotite are exsolved from the MSS (Barnes et al., 2008).

From Barnes et al. (Barnes et al.) the following crystals will form in the MSS and ISS, and these elements will be concentrated in each:

Pyrrhotite (MSS) concentrates: Re and IPGE

Pentlandite (MSS) concentrates: Ni, Co, Re, IPGE, Rh and Pd

Chalcopyrite (Thomson and Davisson, 1937) concentrates: Cd, Ag, Zn

Neither BMS preferentially concentrate Au and Pt.

PGE, Au, Ni and Co in chalcopyrite do not seem to substitute for either Cu or Fe in tetrahedral sites in chalcopyrite. Ag, Zn and Cd might (especially Cu)

Co, Pd and maybe Rh substitute for Ni into pentlandite.

Re and IPGE may substitute for Fe in pentlandite and pyrrhotite.

2.5 Olivine and Mg-number

Olivine has the chemical formula Y_2SiO_4 where Y is a cation with a +2 charge. The two common types of Olivine are **Forsterite (Fo)** - Mg_2SiO_4; and **Fayalite (Fa)** - Fe_2SiO_4. Olivine has high interference colors (0.03-0.05 birefringence) and strong relief in optical microscopy. The mineral is orthorhombic and has mostly anhedral grains (Nesse, 2009).

There is generally a vast majority of Fo compared to Fa in the Olivine composition of a rock. In asthenosphere peridotites, the Fo percentage of all Olivine is ca 90%.

As the Mg-rich Forsterite is lighter than the Fe-rich Fayalite, Fo crystallize before Fa from a melt.

When an asthenospheric peridotite has partially melted (having a Fo-Fa ratio of ca 90-10) and crystallize fractionally, the deeper Ol crystals will have a higher Fo-proportion than the shallowly crystallized Ol. Studying the Fo-Fa ratios of magmatic intrusions is therefore a good way to find how much fractional crystallization happened prior to emplacement; which is important when discussing what other minerals and elements have been removed from the melt during intrusion. With progressive fractional crystallization the magma becomes less **primitive**. High MgO-melts are affected by varying degrees of recharge, eruption, assimilation and fractional crystallization

processes within deep crustal magma chambers (Jennings et al., 2017, Kamenetsky et al., 2002, Nielsen et al., 2006, Yaxley and Brey, 2004, Yu et al., 2015)

Magnesium number is a simple way to track increase and decrease in Mg vs. Fe atoms of a melt. It is calculated by Equation 2:

Equation 2

$$\text{Mg atoms}/(\text{Mg} + \text{Fe}^{2+}\ \text{atoms})$$

Iron number is an equally good indicator, calculated by Equation 3:

Equation 3

$$\text{Fe}^{2+}\ \text{atoms}/(\text{Fe}^{2+} + \text{Mg atoms}).$$

When the Fo ratio is known, the information of the extensiveness of fractional crystallization can be used when interpreting the concentrations of Ni and Cr (and other compatible elements) in the melt. Cr is strongly compatible and will crystallize from the melt at the earliest possible chance. Ni is an incompatible element that is compatible in Olivine. As Ol is omnipresent in the RUC cumulates, it will be referred to as compatible in this thesis. Ni easily substitutes into Olivine and will thus also be progressively depleted with fractional crystallization after emplacement.

2.6 Cr Spinels

The Spinel group consists of oxide minerals in a specific mineral structure. The three main Spinel minerals in ultramafic melts are:

Chromite	$FeCr_2O_4$
Magnetite	$FeFe_2O_4$
Hercynite	$FeAl_2O_4$

Spinels crystallize in a wide compositional range from mafic to ultramafic magmas and are (especially Chromite) among the first minerals to crystallize. These factors make Spinels good petrogenetic indicators for mafic and ultramafic magmas (Irvine, 1965, Irvine, 1967). Spinel composition is a complex function of melt (and source) composition, crystallization temperature, cooling rate and perhaps pressure (Kamenetsky et al., 2001). The wide range of solid solution exhibited by Spinels and their thermodynamics has been extensively studied (Chatterjee et al., 1982, Jacob, 1978, Sack and Ghiorso, 1991b).

The **Spinel prism** is a ternary diagram of Spinel composition with Al, Cr and Fe^{3+} as the end members (Stevens, 1944). Fe^{2+}, Mg, Al, Cr, Fe^{3+}, V and Ti are the main constituents for Spinels in this thesis.

The **Spinel gap** is a notable feature in the Spinel prism caused by two effects: The extensive solvus in the Spinel solid solution; and that Chromite crystallization cease due to reaction with Cr-bearing pyroxene where Spinels do not crystallize until the onset of Magnetite crystallization (Barnes and Roeder, 2001). This last explanation is important for layered ultramafic intrusions such as the Bushveld Complex (Roeder, 1994).

Kamenetsky et al. (2001) present comparable data on chromian Spinels and Olivines for a wide range of volcanic lithologies representative for the different magma types MORB, Back-arc spreading centres, ocean islands, continental rifts (Ernst, 2010) and island-arcs. These LIP data are however from rapidly cooled volcanic lava of LIP origin; and so not entirely comparable to the compositions found at depth in a LIP system. The Spinels Kamenetsky et al. (2001) studied were inclusions in primitive Olivine, not interstidial crystals as the Spinels in this thesis.

From Kamenetsky et al. (2001), Mg-number for Spinels are affected by several complex factors, namely:

1) The Mg-number of the parental melt

2) Partitioning of Al and Cr in the Spinel and Al concentration in the magma

3) Fe^{2+}/Fe^{3+} in the melt and fO_2

4) Post-crystallization re-equilibration with silicate minerals.

There is a positive correlation between TiO_2 and Al_2O_3 in Spinels and coexisting melt. The Ti and Al measured in Spinels are a good indication for the ratios that were present in the magma upon Spinel crystallization, as seen in Figure 2.7 a) and b). Increased Al activity in the system melt-Spinel reduces the partitioning of Ti into Spinel as seen in Figure 2.7 c) (Kamenetsky et al., 2001).

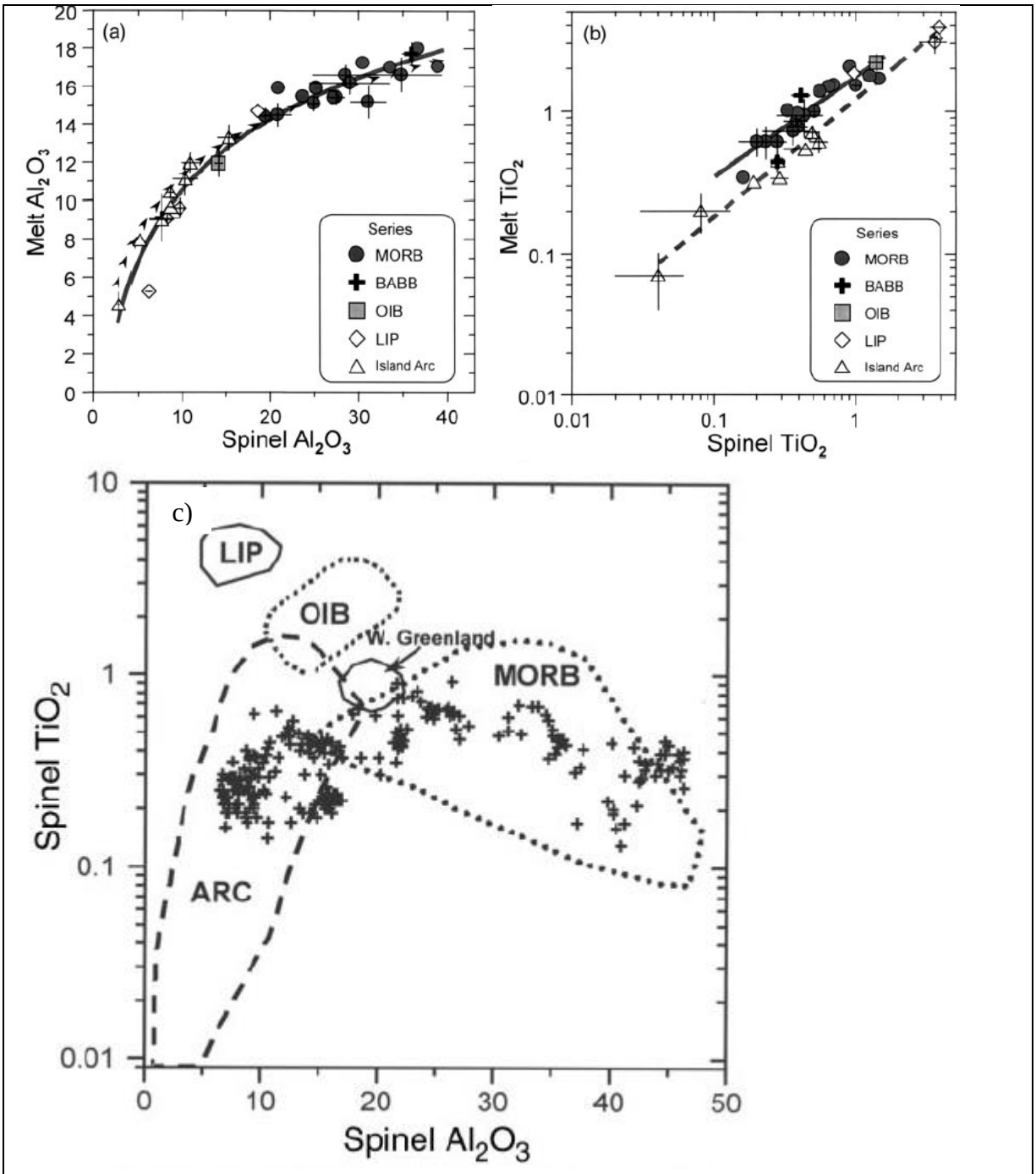

Figure 2.7

Al_2O_3 and TiO_2 wt% in Spinels and melt from Kamenetsky et al. (2001).

Al_2O_3 in melt and Spinel

TiO_2 in melt and Spinel

Al_2O_3 and TiO_2 in Spinel with marked where Spinels of different magmatic origin plot.

Barnes and Roeder (2001) studied the chemical compositions of 40 000 chromian Spinels formed in different magmatic settings. They found that Cr and Mg rich Spinels are characteristics of primitive mantle-derived magmas that have not been overprinted by crystal fractionation and crustal contamination. It is acknowledged that most Spinels are overprinted by chemical re-equilibration with surrounding phases. High Cr and Mg in chromian Spinels are the hallmarks of a primitive magmatic origin prior to re-equilibration (Barnes and Roeder, 2001).

2.6.1 Irvine model for Chromite formation

According to the ternary system diagram for Qz-Ol-Chr (see Figure 2.8), Olivine and 1-2% Chromite will form together for a brief period until Orthopyroxene replace Olivine in crystallization. To form a substantially more Chromite rich layer, some sort of disturbance must befall the magma to push its chemical composition into the Chromite stability field. Then only Chromite will be crystallized until again reaching the cotectic line and again crystallizing both Chromite and Olivine (then pyroxene). Such a chemical disturbance can come from mixing between two magmas or by assimilation of wall rock to alter the bulk chemical equilibrium (Robb, 2005). Such crystallization will cause the formation of a Chromite seam in the cumulates. If chemical disturbance does not take place, small quantities of Chromite will be evenly distributed in the cumulate rocks as long as the crystallization follows the cotectic line between Chr-Ol and then Chr-Opx, Chr-Cpx and Chr-Pl (Kamenetsky et al., 2001).

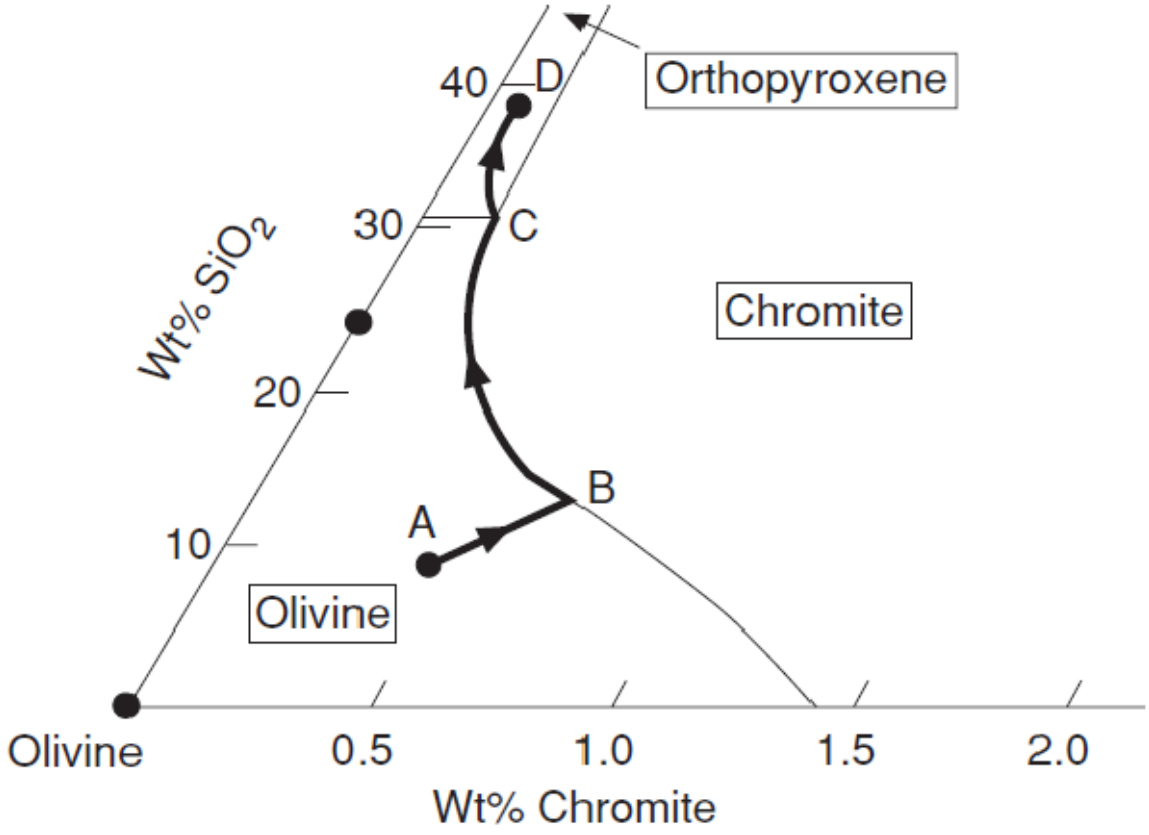

Figure 2.8

Phase diagram of the general crystallization trajectory for a mafic melt according to the Irvine model (Irvine, 1977).

2.6.2 Other mechanisms for crystallizing Chromite

Chromite crystallization can also be initiated by changes in Oxygen fugacity (fO_2) and change in total pressure of the magma. An increase in fO_2 will promote the stability of Chromite and possibly allow the mineral to be the only one crystallized for a time (Ulmer, 1969). One reaction that will increase the fO_2 is devolatilization: $4FeCO_3 \longleftrightarrow 2Fe_2O_3 + 4CO + O_2$ (Lipin, 1993). As CO_2 and CO are the dominant carbon species in mafic melts, it is likely that oxygen fugacity will be easily changed in mafic magma chambers.

Small changes in P have been shown to occur readily in basaltic magma chambers (Bottinga and Meurer, 1990, Lipin, 1993). Increasing total pressure will shift the phase boundary between Olivine and Chromite towards Olivine, leading to a push inside the Chromite stability field, and thus crystallizing only Chromite until bac on the cotectic line (Robb, 2005).

2.7 Clinopyroxene

Clinopyroxene is the term used for monoclinic minerals with the chemical formula $Y_2Si_2O_6$, where Y is a 2+ valence cation. Y_2 can be replaced by XZ, where X is a 1+ valence cation and Z is a 3+ cation. Some elements like Al can fill either the tetrahedron or the octahedron position in the Clinopyroxene crystal lattice (Nesse, 2009). The Clinopyroxene compositional diagram can be seen in Figure 2.9. Clinopyroxene can be separated from Orthopyroxene by the interference colors and that Orthopyroxene has parallel extinction.

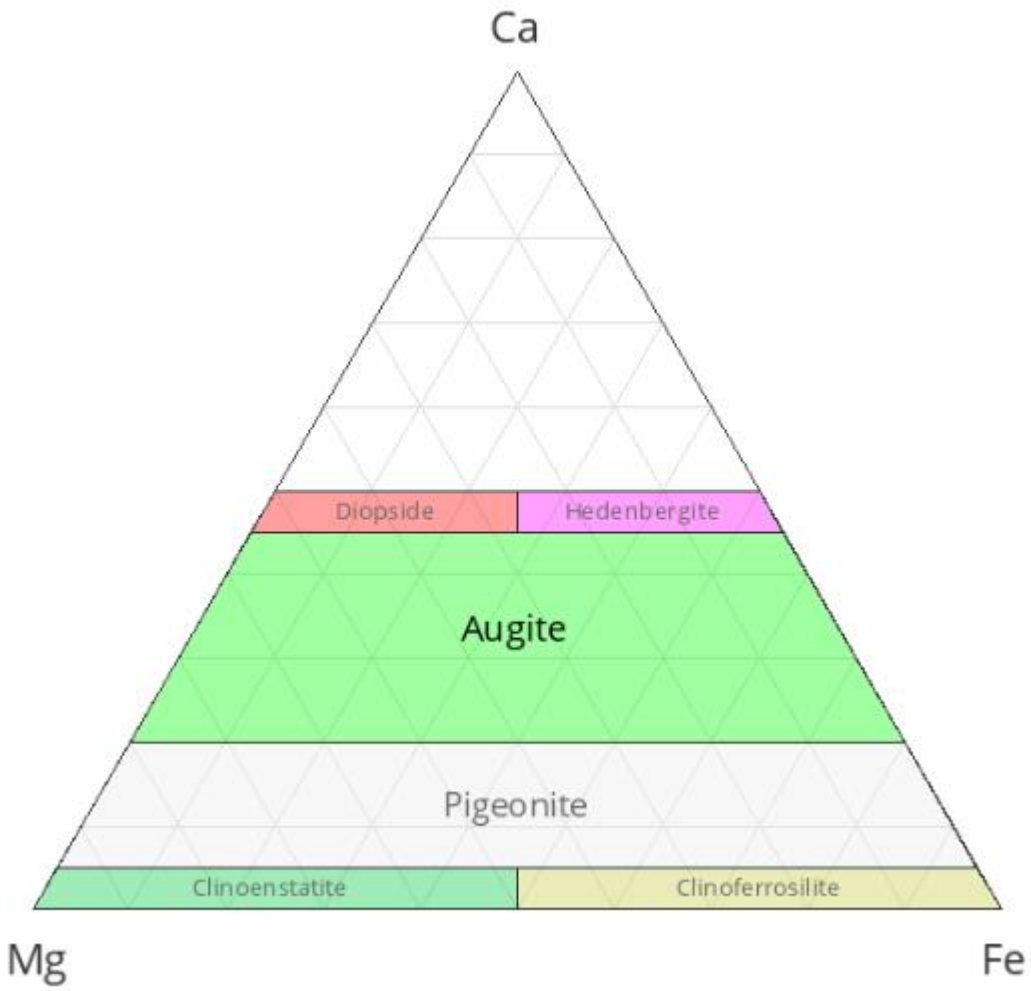

Figure 2.9

Clinopyroxene ternary diagram where Fe, Mg and Ca are 2+ valence cations in the Y position of its chemical formula. Figure source: (Mindat.Org)

2.8 Reverse fractional evolution

Reverse fractional evolution occurs when the crystallized rock becomes progressively more primitive towards the center of the intrusion, opposite to normal magma behavior. It can be explained by a continuous influx of magma and the previously crystallized cumulate rock providing a chemical and thermal insulation against the country rock, allowing the crystallization to happen at higher temperatures and with less outside contamination with each new reopening of the conduit.

2.9 Fe/(Fe+Mg) as a fractionation indicator

The elements Fe and Mg substitute for each other in many minerals, among them Olivine, pyroxene and Spinel. The first minerals crystallized in a melt will be substantially enriched in Mg relative to Fe, a process that depletes the Mg concentration in said melt. As crystallization progress, the crystals will be gradually more enriched in Fe. The ratio Fe/(Fe+Mg) is almost the same as the previously mentioned Mg-number (Mg/(Fe+Mg)). For crystals formed early in the melt, the ratio will be low as Mg is significantly larger than Fe. As fractional crystallization continues and the minerals become more enriched in Fe and depleted in Mg, the ratio will increase. A theoretical maximum value is reached when all Mg has been removed from the magma, and minerals only contain Fe. In that extreme case the Fe/(Fe+Mg) ratio is 1.

The Fe/(Fe+Mg) ratio is useful when working with lithologies where most of the lithology consists of minerals where Fe and Mg substitute freely. Dunite, Wehrlite and Pyroxenite all consist of mainly these two (or three) minerals: Olivine, Clinopyroxene (and Orthopyroxene).

2.10 V/Cr as a fractionation indicator

Both V and Cr are lithophile elements (see Figure 2.5), though Cr has some siderophile behavior (White, 2005). Lithophile elements will not be affected by i.e. sulfide immiscibility as both siderophile and chalcophile elements are. They are therefore more reliable elements for studying the progressive magma development than siderophile or chalcophile elements.

Cr is a highly compatible element. It will crystallize as soon as the chance presents itself. V on the other hand is highly incompatible in ultramafic melts, yet is compatible in Chromite (Mukherjee et al., 2015). This element will therefore almost exclusively be encased in Chromite and be progressively enriched in the melt by all other relevant crystallization processes. The ratio of division between an incompatible element and a compatible element will give a good indication of fractionation processes in the magma chamber. When fractional melting occurs, the incompatible/compatible element ratio in the melting rock will decrease as substantially more of the incompatible element relative to the compatible one will be part of the newly forming melt. When fractional crystallization occurs, the incompatible/compatible element ratio measured in the forming cumulates will likewise decrease, as the compatible element will be substantially more incorporated in the crystals of the cumulate than the incompatible element.

For these two reasons;

1) Both V and Cr are lithophile, and therefore remain unaffected by small scale chemical processes such as sulfide immiscibility during the magmatic evolution
2) Cr is a highly incompatible element and V is a highly compatible element in the magma, so the ratio between them will show how fractional crystallization progress

the V/Cr ratio is a good indicator for fractionation in magmatic rocks.

Because both elements will mainly be crystallized in Spinels, the method relies on that there is continuous Spinel crystallization.

2.11 Chondrites

2.11.1 Asthenosphere vs. chondrite

Consider the total chemistry of the Earth and ignore the partitioning of these elements into the metallic core, the Olivine rich mantle and silica rich lithosphere and crust. What you get will be similar to how the giant ball of magma Earth was prior to solidifying approximately 4,6-4 billion years ago. The total chemistry of the planetary body Earth equally distributed in its entire volume is called a **chondrite**. Celestial bodies such as meteorites, some moons and some small planets can be chondrites if they cooled without the time to segregate sections of their chemistry into separate sections of the body (Alexander, 2007). Based on meteorite chondrites we have an approximation

of what the total average chemical composition of the planet is, and this is often used when comparing rare elements in a rock formation to see how enriched it is relative to what the Earth is. In Figure 2.10 one can see the PGE concentrations in primitive and depleted mantle divided by the concentrations found in a chondrite.

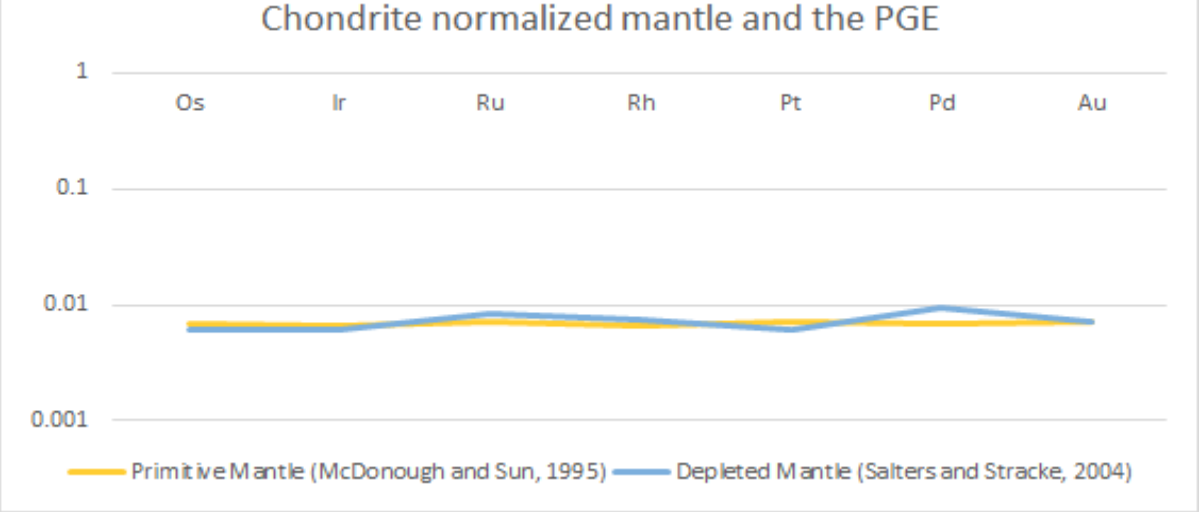

Figure 2.10

Chondrite normalized primitive and depleted mantle for the IPGE and PGE + Rh. (Mcdonough and Sun, 1995, Salters V.J.M. And Stracke, 2004)

2.12 Alteration processes and remobilization

There are many processes that will alter precipitated crystals at varying P-T conditions. Such alterations are mostly caused by the influx of fluids, such as H_2O, CO_2 and in smaller degrees NH_4, O_2 and S, as they and the ions dissolved in them react with the crystals and magma. Such fluids or immiscible magmas can also scavenge elements from a magma or precipitated crystals and remobilize them as they migrate through the magmatic body, precipitating them at another location than where the elements were originally. H_2O is the most important hydrothermal fluid as the high dipole moment lets it dissolve, transport and concentrate a wide variety of ions (Robb, 2005). In an equilibrium situation, trace elements must partition between melt, crystals and the hydrothermal fluid (Robb, 2005). As the infiltrating fluids are not in equilibrium with the surrounding rock/magma they will react to reach an equilibrium state. Because the fluid has such a low density it will subsequently continue its journey and repeat the process with the rocks that encounter it.

Chromian Spinels are known to readily re-equilibrate with the surrounding melt or crystals. Late metamorphic Magnetite is a common replacive for chromian Spinels.

2.13 Similar intrusions

Few other known deep crustal ultramafic conduit system intrusion exist (Chillas complex (Jagoutz et al., 2006, Jagoutz et al., 2007) and Sapat feeder pipes in Kohistan (Bouilhol et al., 2015) in Pakistan; Abulangdan and Emeishan LIP in China (Wang et al., 2014) and Kyondor (Burg et al., 2009) in Russia). They are commonly zoned with ultramafic centres (often dunite) and mafic rims (gabbro). They bear marks of multiple magma injections and reactions with pre-existing cumulates.

Two similar layered ultramafic-mafic intrusion from other LIPs will be presented in this section. The Zhubu ultramafic-mafic layered intrusion from the Emeishan LIP in China and the Bushveld layered mafic-ultramafic intrusion in South Africa. Both are more fractionated than the SIP and both were formed shallower in the crust than the RUC.

2.13.1 Zhubu, Emeishan LIP – China

The Zhubu Ni-Cu-PGE sulfide deposit is in a mafic-ultramafic intrusion that is part of the Emeishan LIP in southwestern China. The 260 Ma (Fan et al., 2008) flood basalts, together with associated Permian picrites and mafic-ultramafic intrusions, make up the Emeishan LIP. Crustal contamination caused sulfide saturation in the plumbing system of the LIP (Li et al., 2012, Wang et al., 2007). The Zhubu deposit was discovered in 1970 (Tgt-Ybgr, 1970) and illuminated by Tang et al. in 2013.

The Zhubu intrusion is 750m long, 400m wide and 580m deep subhorizontally modaly layered sequence wrapped by a 10-40m marginal zone (Tang et al., 2013). The layered intrusion has ultramafic lherzolite and Olivine websterite at the bottom, evolving to mafic gabbro and gabbrodiorite at the top. No chilled rocks separate the layered intrusion from the marginal zone. The marginal zone consists of lherzolite, Olivine websterite, websterite and contaminated gabbro with some small gneissic inclusions. A 0.5-1m hornfels zone border the marginal zone and Precambrian gneiss country rock. The sulfides (pyrrhotite, pentlandite and chalcopyrite) are mostly

found in the marginal zone with insignificant Ni, Cu, Pt and Pd grades in the layered complex. (Tang et al., 2013)

Generally, the Zhubu mafic-ultramafic intrusion is more evolved than the RUC. Plagioclase is a common phase in both mafic and ultramafic lithologies and the lithologies contain more pyroxene than Olivine. The Olivine in the ultramafic intrusive rocks are $Fo_{81-84\%}$. The Ni content in Olivine is between 1600 and 1800 ppm. The other Emeishan intrusives with similar Fo content have ca 500 ppm higher Ni in Olivine. (Tang et al., 2013)

The chromian Spinels of Zhubu has slightly lower Al and Cr contents than the Emeishan picrites. The Clinopyroxenes of Zhubu has slightly lower Mg#, TiO_2 and higher Cr_2O_3 than the Emeishan picrites. Small sulfide inclusions in Olivine indicate that sulfide saturation was reached prior to Olivine crystallization at "the conduit stage" in the Zhubu sulfide deposit (Tang et al., 2013).

2.13.2 Bushveld – South Africa

The Bushveld intrusion in South Africa is the world's largest layered intrusion covering an area of more than 60 000 km^2, with a volume of approximately 1 million km^3 (Harmer, 2000). The Bushveld layered mafic intrusion was emplaced 2.06 Ba (Kinnaird, 2005) over a duration of 3-5 Ma (Kinnaird, 2005).

The Rustenburg Layered suite is the main section of the Bushveld intrusion, containing 300-400km width and 9km depth of anorthosite, mafic and ultramafic rocks. From the base and up, the Rustenburg Layered suite contains a Marginal Zone (norite), Lower Zone (dunitic cumulate), Critical Zone (norite, Orthopyroxene and anorthosite layers), Main Zone (homogeneous gabbro-norite and norite) and an Upper Zone (gabbro, ferrodiorite and anorthosite) (Kinnaird, 2005). The Rustenberg Layered Suite contains the famous Merensky Reef (the world's main source of Pt), massive Chromite layers and massive Magnetite layers (Kinnaird, 2005).

The Bushveld intrusion has been thoroughly studied, yet there is no scientific agreement on the magmatic origin of the intrusion (Kinnaird, 2005). There are arguments pro and con (Kinnaird, 2005): origin from a meteor impact; back-arc subduction setting for magmatism; extensional strike-slip reactivation of Archean structures; that the origin magma was enriched in sea-water; that the origin magma was contaminated by crustal material thoroughly mixed with the magma; and finally, that the origin of the magma was a mantle plume.

3 Methods

3.1 Fieldwork

Two seasons of fieldwork were completed in August of 2017 and 2018. Field work was done either from helicopter assisted field camps at the Reinfjord plateau; or with the base of operations at the Reinfjord village and daily 3-4 hours 2-way hikes to the field localities.

In 2017 we aimed at identifying surface exposures of the reef deposits that theoretically should be present. To this end, the thesis author and Lars Tollefsrud (2018) explored the plateau with a handheld XRF to search for elevated concentrations of ore forming constituents. The southern part of the plateau was mapped using ipads equipped with the fieldmove digital mapping software. We spent a total of 2 weeks in the camp.

The field work in 2018 focused on the ore formation in the dykes (especially the dyke swarm). This field season was only a week due to logistical challenges but aimed at consolidating observations accrued during the 2017 field season.

3.2 Sampling the RF4 drill core

Sampling of the RF4 drill core was conducted October 5th 2017 at the Geological Survey of Norway (Ngu) Løkken drill core storage facility. Previous sampling was mostly recognizance sampling of 5 meter intervals whereas our focus was to increase the resolution to 1-2 meter scale at interesting sections of the drill core. Part of the RF4 drill core was re-sampled in 2017 by Lars Tollefsrud for his thesis of 2018. Tollefsrud sampled 1 meter intervals, between 39 and 68 meters depth, plus three samples above 39m. For this thesis, the re-sampling was done at 1 and 2 meter intervals at the following segments:

Table 2: Sampling intervals of the RF4 drill core

Depth [meters below surface]	Interval sample length [m]
281-310 meters depth	1 meter interval
310-338 meters depth	2 meters interval
338-357 meters depth	1 meter interval
357-391 meters depth	2 meters interval

The 1m interval area 281-310m was selected to coincide with peaks in Cr and the second largest PGE reef in the drill core. The 1m interval area 338-357m was selected to give high resolution data on the second largest Cu+S reef in the drill core and the areas just above and below.

During the RF4 drill core sampling, the lithologies were logged, with focus on the distribution of sulfide grains, mineral composition, grain size and dyke presence.

The drill cores were cut in "quarters". Quarters of the drill core were also sampled for thin sections. The thin section samples were selected to study mineralized intervals below, throughout and above the reefs.

3.3 Sample preparations

3.3.1 For La-ICP-MS

The samples that were sent for ICP chemical analysis were first crushed and split at the Department of Geology and Petroleum (IGP) at NTNU. A Retsch Jaw Crusher with tungsten carbide disks was employed three times for each rock sample, reducing the particle size to less than 0,5 cm. The samples were then split into 10 using a rotation splitter. The particle contents of the split material from one of the 10 split piles were placed in plastic zip lock bags of ca 100g and marked. Both jaw crusher and rotation splitter were thoroughly cleaned using first high-pressured air and then ethanol between samples to minimize contamination.

3.3.2 For microscopy

The samples for thin sections were cut by diamond saws at the Department of Geology and Petroleum (IGP), NTNU. They were made into 30 μm polished thin sections. 24 thin sections were made for this thesis.

3.4 Analytical equipment and procedures

3.4.1 Optical microscopy

Optical microscopy was the main tool used to identify minerals, modal mineralogy and mineral textures. Both opaque and translucent minerals were identified using optical microscopy during the work on this thesis. A Leica DM 2500P microscope was used, connected to a ProgRes CT3 USB mounted camera. Scans of thin sections in transmitted plane and cross-polarized light were made using an Epson Perfection V600 Photo Scanner with polarized filters.

Figure 3.1

Optical microscope with names of significant parts (Central, 2019).

3.4.1.1 Transmitted light microscopy

Transmitted light microscopy is a method used to identify translucent minerals. In Figure 3.1 an optical microscope with the names of its different parts can be seen. Below the sample stand, a light shines. The light travels through a polarizer, which restricts the light to only vibrate in one plane (usually the W-E plane), making it **plane polarized**. (Goeke, 2011)

As minerals' internal structures refract the light in different ways, different crystals can be identified by how the image caused by the light's passage through the crystal lattice looks to the human eye in the oculars above the sample. In optical microscopy, minerals are characterized by parameters such as color, cleavage, relief, grain shape, isotropy etc.

A second polarizer, polarizing perpendicular to the lower, can be inserted above the thin section. This polarizer makes the light vibrate only in the N-S plane. The transmitted light has become **cross-polarized light** (**xpl**). This is used to identify if a mineral is **isotropic** or **anisotropic**. Light travels at the same speed in all directions through an isotropic mineral, while in an anisotropic mineral the speed of light varies with direction.

In an isotropic mineral, then, the light will still be vibrating in the E-W orientation (resulting from the passage through the lower polarizer), and will not be let through the upper polarizer. This makes the isotropic mineral appear **extinct** when observing it through the oculars. When the upper polarizer is not inserted, however, the mineral is visible. (Goeke, 2011)

Anisotropic minerals' characteristic refraction of light into different speeds makes the light split into two components vibrating in perpendicular planes. **Refractive index** is defined as the velocity of light in vacuum divided by the velocity in a material. The two light components of different velocities will thus have different refractive indices. The difference in refractive index between the fast and slowly vibrating light directions is called **birefringence**. (Davidson and Abramowitz, 2008)

The two light velocities and directions will combine when observed in the oculars. As light can be viewed as a wave (Thomson and Davisson, 1937), the two light components will execute interference on one another. **Retardation** is a term used to quantify how much the waves are out of phase, defined thus:

Equation 4: Retardation of light

$$Retardation = Thickness\ of\ thin\ sectaion * Difference\ in\ Refractive\ index$$

The retardation gives each mineral interference colors, that can be used as part of their identifying parameters. (Davidson and Abramowitz, 2008)

3.4.1.2 Reflected light microscopy

When observing opaque minerals such as oxides and sulfides, reflected light microscopy is required. Opaque minerals reflect light - light cannot be refracted through them. For this reason, the light that is to be observed in the oculars comes from a light source above the sample stage through the objective lens via a prism. The light used in reflected light microscopy is usually polarized. As the light hits the sample, a portion will be reflected into the objective to the oculars and the person observing the mineral. (Rottenfusser et al.)

The three most common parameters for determining opaque minerals are reflectance, bi-reflectance and interference colors.

Reflectance is how large a proportion the mineral reflects into the ocular compared to what was sent from the light source. A high reflectance will appear as a bright mineral (such as sulfides) and a low reflectance will appear dark (such as Al-Cr Spinel, Magnetite or translucent minerals).

Bi-reflectance is the process with which a mineral absorbs certain wavelengths of light. As the light is polarized in one static orientation, and the sample stand is turned, this effect causes the mineral to subtly change color when turned. A similar process called pleochroism can be used in transmitted light microscopy. (Davidson and Abramowitz, 2008)

As in transmitted light microscopy, inserting the upper polarizer will cause some minerals to display interference colors. Anisotropic minerals will darken and brighten 4 times during a 360 degree stage rotation (Goeke, 2011). The interference colors observed in reflected light are more subtle than those seen in transmitted light microscopy.

3.4.2 Scanning Electron Microscope (SEM)

A Scanning Electron Microscope (SEM for short) transmits and detects electrons rather than light as in optical microscopy. As electrons interact with individual atoms through deflection, absorption and emission, SEM can be used to investigate the chemistry of the sample. SEMs can also be used to investigate distribution, textures, topography, morphology and crystallographic orientations (Vernon-Parry, 2000). In this thesis, SEM was mainly used to investigate mineral chemistry and take high resolution images.

An electron source (in this case, a field emission electron source) fires electrons down at the sample in the SEM chamber. The electron beam is focused by electromagnetic lenses and deflected in the X and Y direction by scanning coils that cause the beam to scan the surface of the sample (Vernon-Parry, 2000). The chamber with the sample is evacuated for air creating a vacuum to prevent chemical corrosion and disruptions for the electrons.

The SEM detects two types of electrons to create an image of the sample; **Secondary Electrons** (**SE**) and **Back-Scattered Electrons** (**BSE**).

SE are the electrons that have been absorbed and emitted by the atoms' K-orbitals and electrons that are knocked out of their atomic orbits by an incident electron from the electron beam (Vernon-Parry, 2000). Images generated using SE will show the topography of the sample and only in a small degree its chemistry (Vernon-Parry, 2000).

BSE are the electrons that are deflected from the surface of the sample by passing so close to the atomic nucleus that the electron's angle is deflected at a large angle. Elements with high atomic numbers and high density deflects incoming electrons more efficiently than elements with low atomic number and radius (Vernon-Parry, 2000). The image generated by BSE will show minerals with high atomic number (i.e. denser minerals) as brighter than the minerals consisting of lighter

elements. This is called grey-scale imaging (Tollefsrud, 2018) and was used in the SEM investigations in this thesis.

Energy Dispersive Spectrometry (**EDS**) is a method where the characteristic energy of x-rays absorbed and emitted from the atoms of the sample are used to identify and roughly quantify which elements are present in the sample. This was used in both SEM and EPMA analyses.

A Hitachi SU-6600 SEM with a field emission electron source was used in this thesis. The Hitachi SU-6600 has a resolution of 1.2 nm with an accelerating voltage of 30kV, and a resolution of 3 nm when the accelerating voltage is 1 kV. The magnification is between 10x and 600 000x (Hjelen, 2016b). The acceleration voltage used was 20 kV. A medium probe current (15) was used. The working height was set to 15 mm, the standard height for EDS analysis for the instrument. To prevent charging the samples, reduce thermal damage and enhance electron conductivity, the thin sections were coated with ≥20 nm of carbon. 0.05 and 0.1 cm in diameter permanent markers were used to navigate the thin sections in SEM and EPMA.

3.4.3 Electron Probe Micro Analyzer (EPMA)

An Electron Probe Micro Analyzer (EPMA) is an instrument very similar to the SEM used to quantify chemistry with much higher accuracy than a SEM. Like the SEM, EPMA uses an electron beam to generate an image of the specimen. An EMPA usually utilize both EDS (as described above) and **Wavelength Dispersive x-ray Spectrometry** (**WDS**). WDS has a lower detection limit for elements, higher spectral resolution and better peak to background ratio, which gives WDS analysis significantly higher quality. (Cameca, 2017)

A JEOL JXA-8500F EPMA was used for the studies in this thesis. The instrument has one EDS and five WDS detectors. These detectors can be used simultaneously, analyzing up to 5 elements with WDS and 16 elements with EDS (Hjelen, 2016a). For the pyroxene measurements, a 2 μm beam diameter, while for the Spinel measurements a spot beam (<1 μm) was used. The standards used in the analyses can be seen in Table 1 and Table 2.

The EPMA used was at the NTNU, Department of Geoscience and Petroleum (IGP) EM lab, with Morten Peder Raanes as operator after instructions from the author of this thesis. As the EPMA analyzes several µm into the sample, more than 1 analysis was always conducted of each mineral to give an accurate average chemical value. For the Spinels 2-3 measurements on different places in the grain were conducted. For the Clinopyroxenes, 5 measurements were made on each grain to give a reliable average chemical value. The standard deviations were calculated by variance of the average composition of each grain and can be seen in Table 3: Standard deviations for the oxides analyzed by EPMA for Spinels to Table 6: Standard deviations for the elements analyzed by EPMA for Clinopyroxenes after stoichiometry. Al is given for both tetrahedron and octahedron position in crystal lattice.

Table 3: Standard deviations for the oxides analyzed by EPMA for Spinels

	SiO2	MgO	TiO2	MnO	Al2O3	V2O3	FeO	Fe2O3	Cr2O3	NiO
σ	0,13	3,53	1,08	0,07	14,94	0,22	19,33	0,00	6,84	0,07

Table 4: Standard deviations for the elements analyzed by EPMA for Spinels after stoichiometry

	Si	Mg	Ti	Mn	Al	V3+	Fe2+	Fe3+	Cr	Ni
σ	0,00	0,08	0,05	0,00	0,61	0,01	0,21	0,43	0,19	0,00

Table 5: Standard deviations for the oxides analyzed by EPMA for Clinopyroxenes

	SiO2	TiO2	Al2O3	FeO	MnO	MgO	CaO	Na2O	K2O	Cr2O3
σ	0,94	0,16	0,93	0,43	0,01	0,92	1,93	0,26	0,00	0,21

Table 6: Standard deviations for the elements analyzed by EPMA for Clinopyroxenes after stoichiometry. Al is given for both tetrahedron and octahedron position in crystal lattice.

	Si	Ti	Al(tetr)	Al(oct)	Fe^{2+}	Mn	Mg	Ca	Na	K	Cr
σ	0,03	0,00	0,03	0,02	0,01	0,00	0,05	0,08	0,02	0,00	0,01

Suitable standards were chosen for EPMA analyses of Spinel (Table 8: Chromian Spinel standards used for the EPMA analyses) and Clinopyroxene (Table 7: Clinopyroxene standards used for the EPMA analyses).

Table 7: Clinopyroxene standards used for the EPMA analyses

Element	Standard used
SiO2	15.Diopsi.Ast21
Na2O	15.Jadei.Ast28
K2O	15.Sanidi.Ast41
MnO	15.Rhodo.Ast39
MgO	15.Diopsi.Ast21
CaO	15.Diopsi.Ast21
FeO	15.Olivi.Ast34
Al2O3	15.Jadei.Ast28
TiO2	15.Rutile.Ast40
NiO	15.NiSi.Ast52
Cr2O3	15.Cr2O3.Ast17
ZnO	15.Sphal.Ast42

Table 8: Chromian Spinel standards used for the EPMA analyses

Element	Standard used
SiO2	15.Olivi.Ast34
MgO	15.Chromite.T8
TiO2	15.Rutile.Ast40
MnO	15.Busta.Ast10
Al2O3	15.Chromite.T8
V2O3	15.V.AST9
FeO	15.Chromite.T8
Cr2O3	15.Chromite.T8
NiO	15.Olivi.Ast34

3.4.4 Inductively Coupled Plasma Mass Spectrometry (ICP-MS)

Bulk rock chemical analyses were conducted by ALS Scandinavia analytical lab in Luleå, Sweden using **Inductively Coupled Plasma Mass Spectrometry analysis** (**ICP-MS**). Crushed samples of the RF4 drill core were sent there in October 2018.

ICP-MS is an analytical method where argon plasma is heated to a temperature of 8000-10000°C. The temperature is maintained by a high frequency electromagnetic field. The sample material is pumped into the plasma, a process that leads to excitation of electrons in the atoms and emission of characteristic electromagnetic radiation as the electrons return to their low-energy state. The spectra registered from the process is used to identify and quantify different elements. (Ngu, 2015)

From ALS Scandinavia (Als, 2018), these three packages of analyses were conducted:

Table 9: Pt, Pd and Au with high resolution

PGM-MS25NS

PGM-MS25NS		
Element	Range (ppm)	Description
Pt	0.0005-1	Fire assay, ICP-MS finish
Pd	0.001-1	30g or 50g sample weight
Au	0.001-1	

Table 10: Full PGE suite (Pt, Pd, Ir, Os, Rh, Ru) and Au

PGM-MS23

PGM-MS23		
Element	Range (ppm)	Description
Au	0.005-10	Au, Pt, Pd, Ir, Os, Rh, Ru by nickel sulfide collection fire assay, ICP-MS finish
Full PGE suite	0.002-10	30g sample weight

Table 11: Major and minor elements

ME-MS61							
Element	Range (ppm)	Element	Range (ppm)	Element	Range (ppm)	Element	Range (ppm)
Ag	0.01-100	Cu	0.2-10 000	Na	0.01%-10%	Sr	0.2-10 000
Al	0.01%-50%	Fe	0.01%-50%	Nb	0.1-500	Ta	0.05-100
As	0.2-10 000	Ga	0.05-10 000	Ni	0.2-10 000	Te	0.05-500
Ba	10-10 000	Ge	0.05-500	P	10-10 000	Th	0.01-10 000
Be	0.05-1000	Hf	0.1-500	Pb	0.5-10 000	Ti	0.005%-10%
Bi	0.01-10 000	In	0.005-500	Rb	0.1-10 000	Tl	0.02-10 000
Ca	0.01%-50%	K	0.01%-10%	Re	0.002-50	U	0.1-10 000
Cd	0.02-1000	La	0.5-10 000	S	0.01%-10%	V	1-10 000
Ce	0.01-500	Li	0.2-10 000	Sb	0.05-10 000	W	0.1-10 000
Co	0.1-10 000	Mg	0.01%-50%	Sc	0.1-10 000	Y	0.1-500
Cr	1-10 000	Mn	5-100 000	Se	1-1000	Zn	2-10 000
Cs	0.05-500	Mo	0.05-10 000	Sn	0.2-500	Zr	0.5-500

Limit of detection (LOD) from ALS Scandinavia (Als, 2018) was set to $3*\sigma$. In the table below are the limits of detection and σ for the various analyzed elements.

Table 12: Standard deviation for the bulk rock chemical analyzed components

Element	Measure unit	σ	Element	Measure unit	σ
Ag	Ppm	0.167	Mn	Ppm	1.667
Al	%	0.003	Mo	Ppm	0.333
As	Ppm	1.667	Na	%	0.003
Ba	Ppm	3.333	Ni	Ppm	0.333
Be	Ppm	0.003	P	Ppm	3.333
Bi	Ppm	0.667	Pb	Ppm	0.667
Ca	%	0.003	S	%	0.003
Cd	Ppm	0.017	Sb	Ppm	1.667
Co	Ppm	0.333	Sc	Ppm	0.333
Cr	Ppm	0.333	Sr	Ppm	0.333
Cu	Ppm	0.333	Th	Ppm	0.333
Fe	%	0.003	Ti	%	0.003
Ga	Ppm	3.333	U	Ppm	3.333

3.5 Stoichiometry and calculations

For the bulk rock chemical analyses that were measured below the LOD, if less than 15% of the analyses were below LOD, ½ LOD was set as its value (Usepa, 2000).

The stoichiometric calculations based on the EPMA oxide chemical data were made as following:

Initially in the calculations, all Fe is assumed to be the 2+ valent ferrous version found in the oxide FeO. This is because the EPMA measured all Fe as FeO.

To begin the calculations, stoichiometric transition from oxide to moles were made using the following formula:

Equation 5: molar stoichiometry

$$mass\ oxide * Molar\ mass\ oxide = moles\ of\ the\ oxide$$

Then the number of cation and oxygens were calculated for each element oxide using the two following formulas:

Equation 6: number of cations and oxygens

$$moles\ of\ the\ oxide * number\ of\ cations\ in\ oxide = moles\ of\ cations$$

$$moles\ of\ the\ oxide * number\ of\ oxygens\ in\ oxide = moles\ of\ oxygen$$

The sums of both were calculated for each sample analysis. The charge was also calculated for each analyzed sample.

Then, as the total moles of cations were not 3 and the total moles of oxygens were not 4 as should be the case in Spinels according to the general Spinel formula: $A^{2+}B^{3+}{}_2O^{2-}{}_4$, a normalization of cations was conducted. The normalization divides the moles present of this particular cation by how many moles of all cations are present in the analysis. This gives the proportion of that particular cation. The proportion is then multiplied by 3, as the total number of cations in the formula should be 3. The equation is seen below:

Equation 7: normalization of cations

$$normalized\ number\ of\ cations = 3 * \frac{moles\ of\ cations}{sum\ (moles\ of\ cations)}$$

A normalization of oxygens was made using the normalized cations that were just calculated. The oxygen normalization uses the number of oxygens in the particular oxide formula and multiplies that with the ratio between the normalized cations and cations in the oxide formula. The equation is seen below:

Equation 8: normalization of oxygens

$$normlaized\ oxygens = normalized\ number\ of\ cations * \frac{oxygens\ in\ oxide\ formula}{cations\ in\ oxide\ formla}$$

Having done this, the number of cations and anions in the formula add up to 3 and 4, as the Spinel formula requires. The charge, however, does not balance. In this step of the calculations, the original assumption that all Fe is present as Fe^{2+} is discarded. The contribution from Fe^{3+} was calculated the following way:

Equation 9: Fe3+ calculated by charge imbalance

$$charge\ contributed\ by\ O - sum\ charge\ contributed\ by\ cations$$
$$= charge\ contributed\ by\ Fe3+$$

The charge contributed by oxygen in the mineral formula is 8-. For all analyses, the charge contributed by Fe^{3+} was a positive number. This charge is contributed by Fe^{3+} rather than Fe^{2+}. Fe^{3+} has 1 more positive charge than Fe^{2+}, and by the following formula:

Equation 10: charge excess equals number of moles

$$\frac{Charge\ contributed\ by\ X\ moles\ of\ Fe3+}{1\ extra\ charge} = X\ moles\ of\ Fe3+$$

The difference in charge found by completing Equation 9 is from Equation 10 the number of moles Fe^{3+} present in the formula. This number was subtracted from the total number of moles of Fe ions (previously presumed to be Fe^{2+}). The normalization of cations still holds, so does the normalization of oxygens and now the charge balances as well.

3.6 Sources of error

3.6.1 Sampling

When sampling the drill core it is possible that several thin sections were taken in areas that appeared interesting by rare features such as mylonitic sections, faults, dyke contacts etc. The two shallowest thin sections are from contacts with dykes i.e. reducing the number of samples representing the cumulates. Still, it is evaluated that the cumulate section is well represented by 18 of the 25 thin sections.

3.6.2 Sample preparations

During sample preparations (crushing, splitting, storage and extraction from storage) several sources of error are possible. It is possible that the cleaning of equipment between handling different samples were not thorough enough. Especially for the rotational splitter this source of error should be considered, as the glass containers that gathered the split material was not possible to clean with ethanol between samples, and so were only cleaned with compressed air.

As plastic zip lock bags were used to store the crushed and split samples, it is possible that some elements preferentially remained in the static electricity of the plastic bag more than others. These minerals would be the ones crushed into smallest pieces. Minerals that are very small (PGM for instance) could have suffered this source of error. This error would only affect the ICP-MS data.

As the samples were also handled at the ALS lab in Luleå, Sweden, contamination, technical or human error could also have occurred during their handling of the samples prior to analysis. This segment is found in the ALS manual for the main and minor elements that were executed for the samples:

"Four acid digestion quantitatively dissolves nearly all minerals in the majority of geological materials. However, barite, rare earth oxides, columbite-tantalite, and titanium, tin and tungsten minerals may not be fully digested. Despite the potentially incomplete digestion of REEs, the leachable portion of these elements may hold important exploration vectoring information and can be chosen as an add-on."

The analyses conducted at ALS only used 0,25g for minor and major element La-ICP-MS and 30g samples for the two PGE La-ICP-MS analyses. The lab must have split or otherwise separated the material to acquire only so small quantities for the analyses. This splitting process could have led to contaminations between samples. Additionally; if the samples were not split, i.e. that a spoonful of material was taken for analysis, sedimentary settling and segregation of grain sizes and densities could have led to inaccuracies in the analyses. However, in the end, blind analysis of selected samples and of standards with known composition supported that analytical and processing errors were minimal.

3.6.3 EPMA

The Chromite standard was measured 6 times over the course of the EPMA Spinel analyses, and can be seen in Figure 3.2. The totals vary between 99.1% and 101.7%. The samples that have totals below 98.9% and above 101.9% in Figure 3.3 have been removed from the dataset as they are considered outliers. If the EPMA experienced local drift and these poor totals are not caused by

buildup of charge, the decision to remove them would be faulty. As seen in Figure 3.3, the Spinel EPMA measurements do show some negative drift. As the standard sample analyses vary with 1.3% from a mean value at 100.4% (as seen in Figure 3.2), the EPMA measurements are not very accurate. When measuring the standard, the totals should be identical. As the measurements of the standard from Figure 3.2 do indeed have variation, the equipment causes a wide margin of error. Discarding sample measurements that are inside this equipment margin of error would therefore be wrong. Only one measurement of standard was made for the pyroxenes. This was the very first measurement, with a total of 99.2%. Because of this, the EPMA equipment error for the pyroxene measurements seen in Figure 3.4 is unknown. When removing outliers from the pyroxene data set, the risk of accidentally deleting data points that are within system error is therefore high. The risk of not removing outlier data points that are actually outside the equipment error zone is also high.

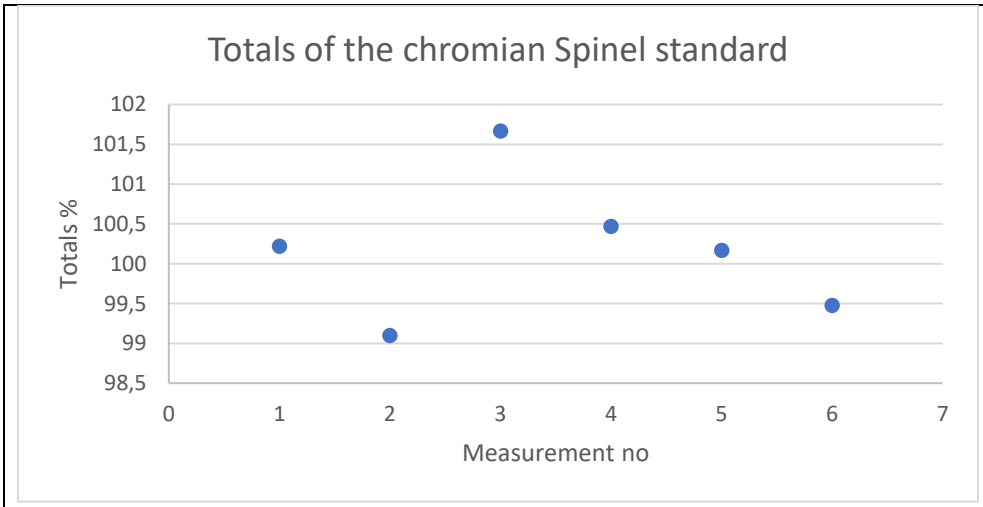

Figure 3.2

Totals from the Chromite Spinel standard measured during the EPMA analysis. Measurement no 2, 3, 4 and 5 were made in quick succession.

As can be seen in Figure 3.3, the EPMA results show a clear negative drift over time with 0.9% decrease in mean totals from the first to the last measurement. This also contributes to analytical error from the EPMA equipment.

The pyroxene totals are plotted in Figure 3.4 and show significantly more complex evolution in system accuracy than what the chromian Spinels do in Figure 3.3. Especially the measurements after number 150 have very high variance. The EPMA drift indicated by the trendline in Figure

3.4 has the same trend and variation from the beginning of the measurements (total mean=100.7%) to the end of the measurements (total mean=99.7%). A 1% negative drift is recorded.

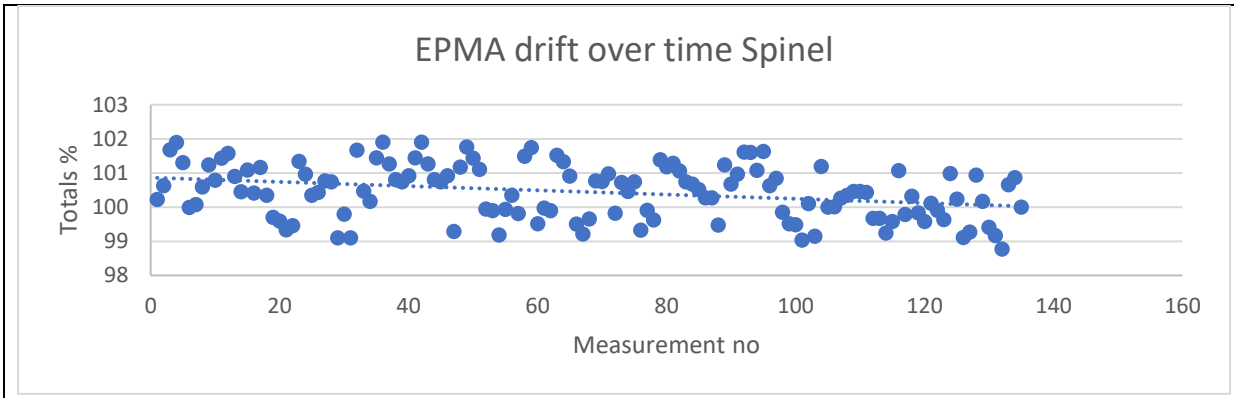

Figure 3.3

Spinel totals of all EPMA measurements not removed from the data set due to too low or high totals. The totals are plotted against measurement number and a trendline shows progressive negative drift during the analyses. To begin with, the mean total was 100.9%, while at the end the mean total was 100%.

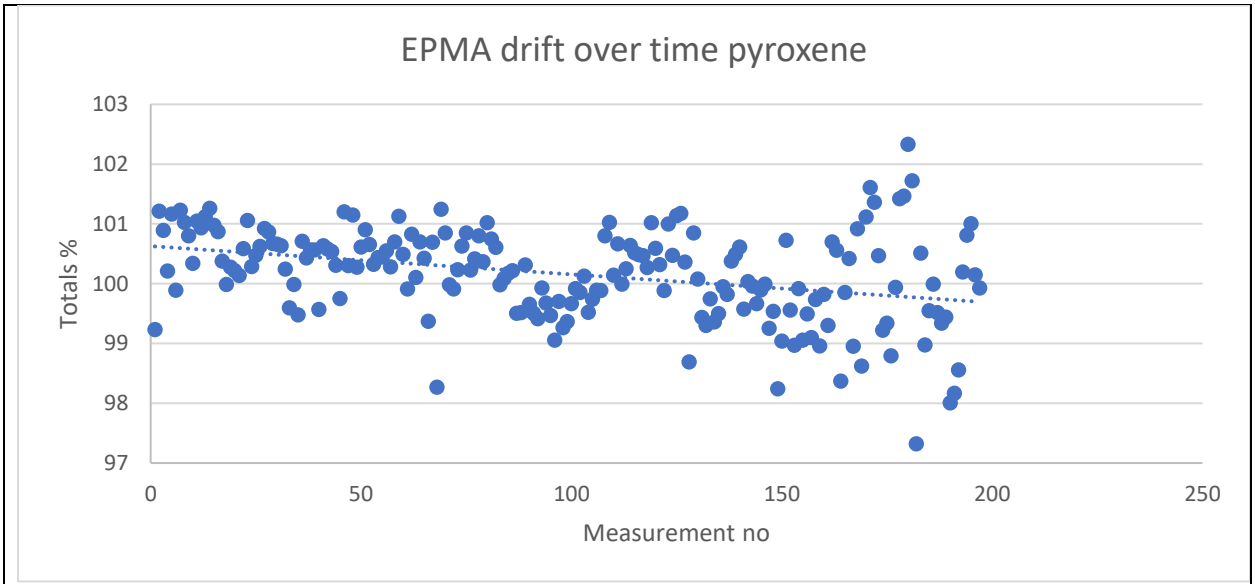

Figure 3.4

All EPMA measurement totals from the pyroxene measurements without removing outliers. The totals have a local dip between measurement no 83 and 113. After measurement no 150 the variance in totals increase exponenially. Unlike Figure 3.3 the drift is not systematic, though a decreasing trend (see trendline) shows that at the first measurements the mean total was 100.7 while at the last measurements the mean total was 99.7%.

Some analyses were made close to charged carbon particles and some too close to permanent marker. This has made these measurements less accurate but has not made the totals of the analyses remarkably high or low so they would be easy to remove from the data set.

The EPMA analyses from Clinopyroxene grains will with varying degree show higher concentrations of Fe, Cr, Ti and Orthopyroxene constituents due to lamellae and mineral exolutions because the beam thickness used for the Cpx analyses were too narrow to form an average chemical scan of the grains. For some of the measurements, the beam hit an exsolved phase. This error is higher for certain samples (325, 346, 348 and 364.5 in particular). The exolutions and lamellae were present in all Clinopyroxene grains, but in many of the samples they were so large that the EPMA beam could avoid them when measuring. For the listed thin sections however the lamellae and exolutions were so thin and small that they were impossible to avoid when making measurements. As the pyroxene beam width was 2 μm, some lamellae or exolutions could have been included in some of the samples in other Clinopyroxene grains as well. Working with average values for the grains can therefore be misleading as some of the measurements will include the impurities more than others.

Ideally the electron beam should have been wide enough to include the exsolutions in all the grains to give an accurate and comparable chemical description of each Clinopyroxene grain from before the grain exsolved.

However, as the measured Clinopyroxene chemistry is almost endmember diopside, error from exsolutions are minimal. As Orthopyroxene lamellae were avoided in EPMA analyses, the Ca will be slightly higher. The Mg/Fe ratio will be mostly unchanged. The Fe and Ti could be somewhat elevated in the samples where the exsolutions were very small compared to the grains with larger exsolved Fe-Ti oxides.

The element standards used in the EPMA analyses were chosen from a limited selection. For this reason, it is possible that some of the standards could have been more accurate for some elements.

The EPMA at Material Sciences that was used for analyses in this thesis have a history of delivering results of variable quality. The EPMA was corrected by a JEOL engineer less than a month prior to the analyses were made.

The EPMA measured all Fe as FeO. This is because the Fe ion peak when conducting EPMA analyses is very wide and the Fe^{2+} and Fe^{3+} peaks would be so close together that the two can not be separated: they both simply contribute to make the wide peak higher. However, as Fe^{2+} will be calculated to oxide wt% with only one cation and one anion, the Fe^{3+} should have been calculated to Fe_2O_3: two cations and three oxygen atoms. The correction that was implemented in the stoichiometry for this thesis do not implement Fe of different valence until very late in the calculations. For the calculations to be completely accurate, that segregation should have been done in the very first step of calculating from wt% to moles. The drawback in calculating Fe^{3+} is that errors in measured major elements propagate into much larger errors after the calculation of estimated Fe^{3+} (J. Wood and Virgo, 1989)

4 Results

4.1 Thin sections

Polished thin sections were made from the drill core RF4 at various depths. The names of the thin sections are the depth in the drill core where the rock was sampled. Scans of the thin sections were made using transmitted plane polarized light (ppl) and cross polarized light (xpl). The scans are displayed in Appendix A with brief descriptions of what is observed in the thin sections. Thin section 293.5-B and 320can be seen in Figure 4.1 and Figure 4.2 respectively.

4.1.1 Carbonaceous clots

In the center to lower right part of Figure 4.1 are two carbonaceous clots as described in the Geological and geographical setting. The feature is most apparent in the x-pol image of Figure 4.1 b) where the clots appear as very fine-grained grey areas with strong color variations. Such carbonaceous areas are smaller in the other studied thin sections.

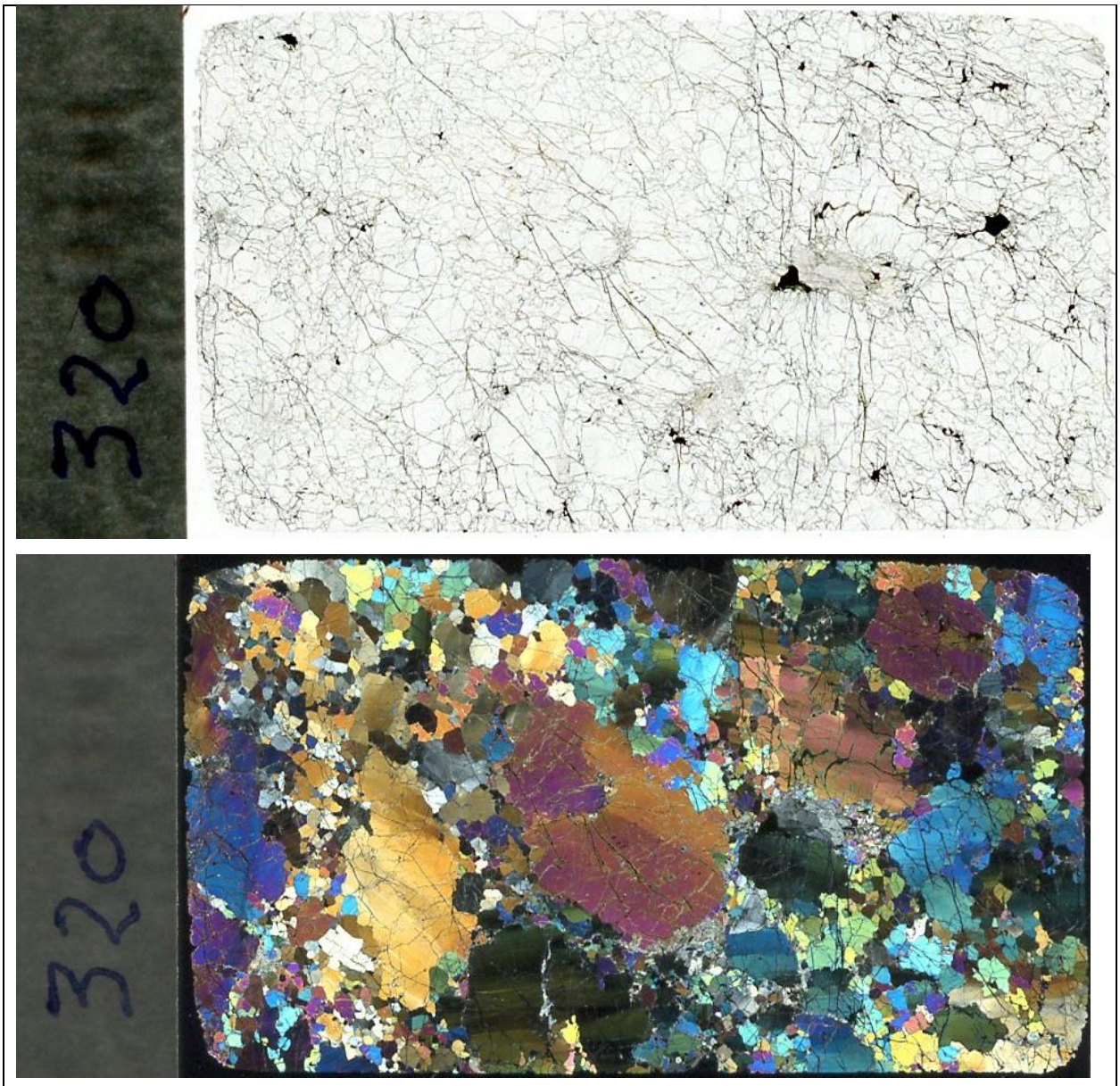

Figure 4.1

Thin section 320 scanned using transmitted plane polarized light (Figure 4.1 a) and crossed polarized light (Figure 4.1 b). Olivine of type 1 (large banded crystals) and 2 (small monochromatic crystals), as well as grey carbonate clots (grey fine-grained clots in the lower center-right) are present in the thin section.

4.1.2 Replacive dunites

In Figure 4.2, the process of replacive dunites described in the Geological and geographical setting can be observed in thin section scale. Thin section 293,5-B is a pyroxenitic cumulate. This is best observed in the ppol image in Figure 4.2 a). In the lower right corner of the thin section, a tail of

dunite infiltrates the pyroxenite cumulates, replacing them. The dunite infiltrates further than the large white tail in Figure 4.2, with small tendrils of fine-grained inter cumulus Olivine between the pyroxene crystals in the replacive dunite section's immediate vicinity. Some pyroxenes are not completely replaced by the dunite and remain as small fragments in a sea of Olivine.

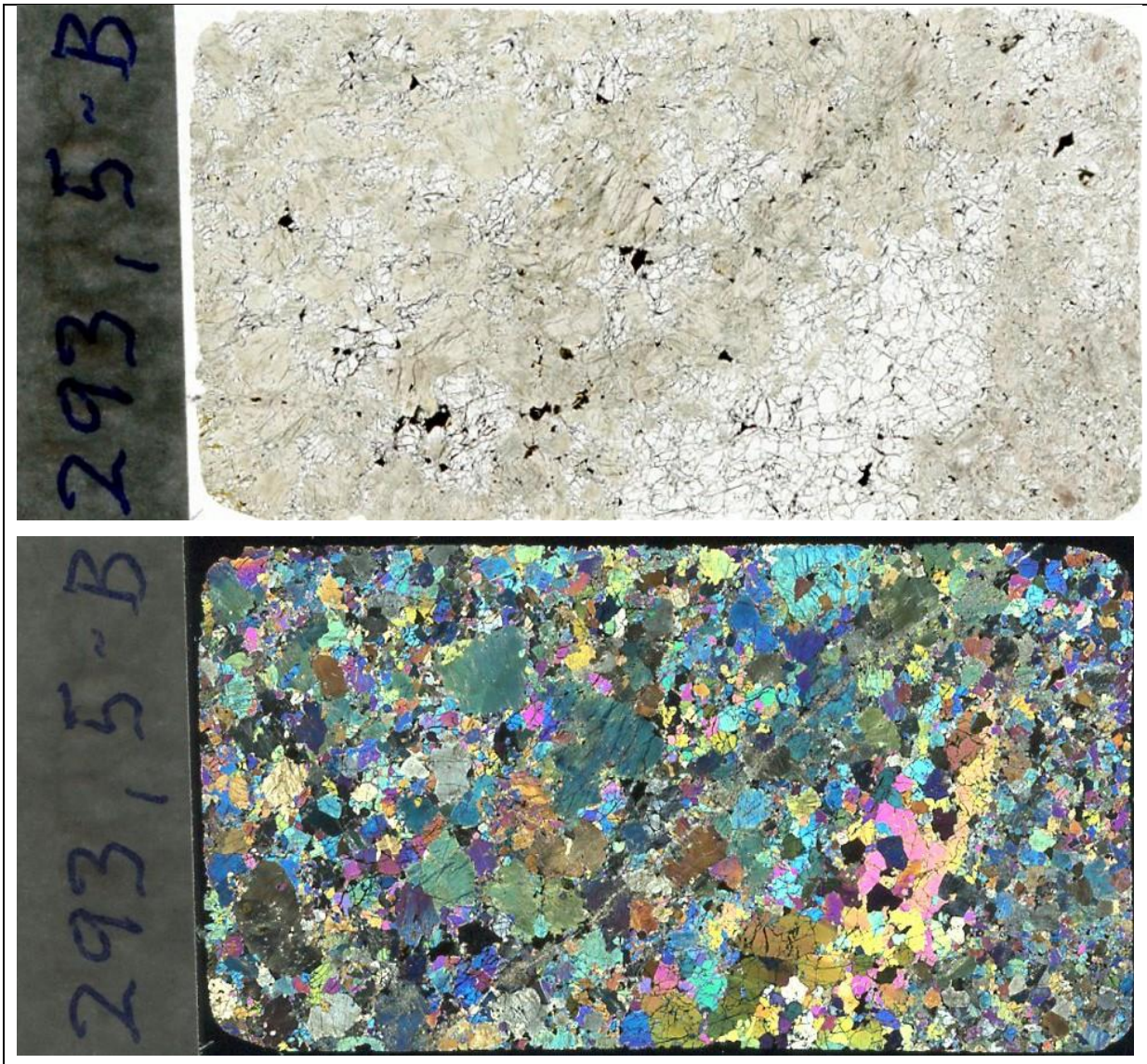

Figure 4.2

Thin section 293,5-B scanned in transmitted plane polarized light (Figure 4.2 a) and crossed polarized light (Figure 4.2 b). A replacive dunite tail (lower right) replace the Olivine clinopyroxenite with dunite.

4.2 Spinel

Chromian Spinels are present in most thin sections in this study. They are recognized by their lack of extinction or color fluctuation and their general grey color in plane polarized reflected light. In the few thin sections that do not have chromian Spinels, Fe-Ti oxides can easily be confused with Cr-Spinels as the oxides have only a slightly different reflectance and otherwise share characteristics with the Cr-Spinel grains. The different types of chromian Spinels are separated by their reflectance when working in optical microscopy and element density when working with SEM and EPMA.

4.2.1 Spinel nomenclature

The analyzed Spinel grains are separated into three groups based on their Ti and V concentrations and one Magnetite group based on their Fe^{3+} content (Figure 4.3). As seen in the chemical Spinel plots below (Figure 4.18-Figure 5.4**)**, these groups are also separated by other elements. The group "Magnetite" is separated by >80 wt% total Fe oxides and <10% Cr_2O_3. Another Magnetite phase is Al-poor and Ti-rich and is referred to as Fe-Ti oxides (Fe-Ti for short). No Fe-Ti oxides were analyzed by EPMA.

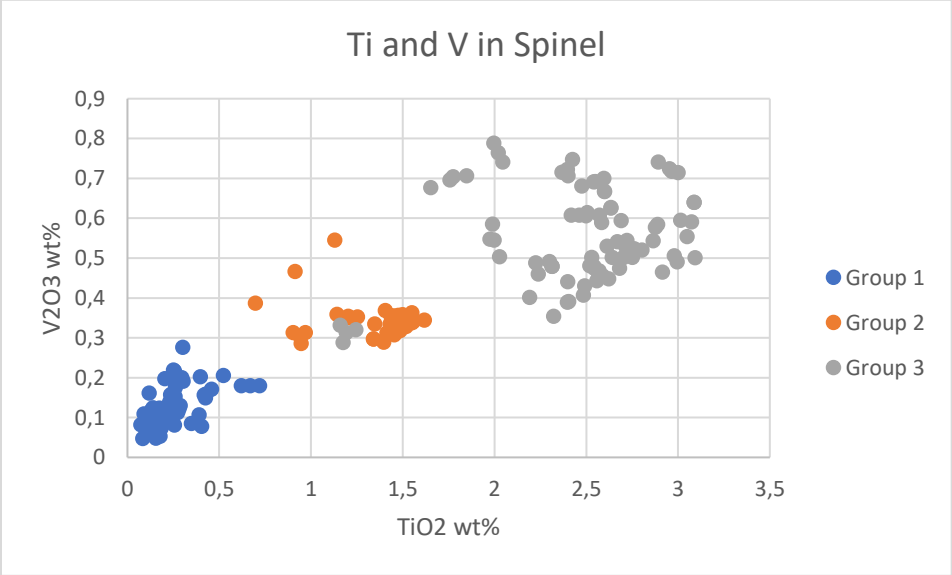

Figure 4.3

TiO_2 wt% plotted against V_2O_3 wt% for all Spinel EPMA measurements. Group 1, 2 and 3 are distinctly separated except for a group 3 grain in the group 2 cluster.

The chemistry of the groups is presented in the mineral formula diagrams Table 13 and Table 14. Elements that have less than 0.01 cation units in a chemical formula are not included in the two tables.

Table 13: Chemical formula for analyzed Spinels with min and max value of each element.

Group 1	$Fe^{2+}_{0.49\text{-}0.69}\ Mg^{2+}_{0.32\text{-}0.51}\ Al^{3+}_{0.96\text{-}1.62}\ Cr^{3+}_{0.26\text{-}0.69}\ O^{2-}_{4.01\text{-}4.05}$
Group 2	$Fe^{2+}_{0.72\text{-}0.87}\ Mg^{2+}_{0.16\text{-}0.29}\ Mn^{2+}_{0.01}\ Cr^{3+}_{0.7\text{-}0.89}\ Al^{3+}_{0.4\text{-}0.82}\ Fe^{3+}_{0.37\text{-}0.79}$
Group 3	$Fe^{2+}_{0.87\text{-}1}\ Mg^{2+}_{0.06\text{-}0.15}\ Mn^{2+}_{0.01}\ Fe^{3+}_{0.91\text{-}1.54}\ Cr^{3+}_{0.21\text{-}0.63}\ Al^{3+}_{0.10\text{-}0.37}$

The average mineral formula for each group:

Table 14: Chemical formula for analyzed Spinels with average chemistry for each Spinel group.

Group 1	$Fe^{2+}_{0.58}\ Mg^{2+}_{0.41}\ Al^{3+}_{1.28}\ Cr^{3+}_{0.49}\ Fe^{3+}_{0.2}\ O^{2-}_{4.03}$
Group 2	$Fe^{2+}_{0.79}\ Mg^{2+}_{0.23}\ Mn^{2+}_{0.01}\ Cr^{3+}_{0.81}\ Al^{3+}_{0.59}\ Fe^{3+}_{0.52}\ Ti^{4+}_{0.03}\ O^{2-}_{4.09}$
Group 3	$Fe^{2+}_{0.95}\ Mg^{2+}_{0.11}\ Mn^{2+}_{0.01}\ Fe^{3+}_{1.19}\ Cr^{3+}_{0.44}\ Al^{3+}_{0.22}\ V^{3+}_{0.02}\ Ti^{4+}_{0.07}\ O^{2-}_{4.2}$

The minerals of all groups have oxygen totals higher than the theoretical value of 4. All groups have calculated Fe^{3+} content. Since the stoichiometry used to calculate the other elements (including O) uses a standardized procedure, either equipment error or not perfect element composition in the minerals are the likely explanations for the elevated number of oxygen atoms in the mineral formula.

4.2.1.1 Spinel Group 1 – Hercynite (Picotite)

The Spinels in group 1 contain Fe as the main 2+ valence cation and Al as the main 3+ valence cation. Hence it is a Hercynite using the 2018 Spinel classification by Bosi et al. (2018). The Spinels in group 1 has an Fe^{2+}: Mg^{2+} ratio between 2:1 and 1:1. They have a Al^{3+}:Cr^{3+} ratio of between 2:1 and 3:1, with the average at 3:1. The Hercynite mineral this chemistry corresponds with is Picotite with a mineral formula of $(Fe,Mg)(Al,Cr)_2O_4$ (Mindat.Org). In figures and plots, these data are referred to as Hercynite (**Hc** for short) or as **group 1**.

4.2.1.2 Spinel Group 2 – Chromite (Alumoberezovite)

In the Spinels of group 2, Fe is the 2+ valence cation while Cr is the main 3+ valence cation. This is in the Spinel subgroup Chromite (Bosi et al., 2018). They have a Fe^{2+}: Mg^{2+} ratio of 7:1 and an Al^{3+}:Cr^{3+} ratio of ca 1:1.5. The mineral that best fits its chemical composition is Alumoberezovite

(Vakhromeev et al., 1936) with the composition $(Fe_{0.75}Mg_{0.25})(Cr_{0.75}Al_{0.25})_2O_4$ (Schorn, 1999-2019). The Fe:Mg ratio in the analyzed Spinels have higher Fe than the mineral formula from Schorn (1999-2019). The Cr and Al amounts are also slightly different from the Alumoberezovite formula (Mindat.Org), but not so much. No defined Chromite type has as high Fe:Mg ratios as the Spinels in this group, and so Alumoberezovite is approximated. The group 2 Spinels have almost as high concentration of Fe^{3+} as Al^{3+}. In figures and plots, these data are referred to as Chromite (**Chr** for short) or as **group 2**.

4.2.1.3 Spinel Group 3 – Magnetite

The Spinels of group 3 has Fe^{2+} and Fe^{3+} as the dominant cations. It is a Magnetite type Spinel (Bosi et al., 2018). Group 3 is difficult to characterize a concise composition because they contain both Fe^{3+}, Cr^{3+} and Al^{3+}, but almost only the 2+ valence cation Fe^{2+}. NiChromite has the chemical formula (Ni, Co, Mg, Mn, Fe) $(Cr, Fe, Al, Ti)_2O_4$ (Bates and Jackson, 1987), and so include the elements in the measured chemical formula (except for V). However, NiChromite is named after the element Nickel, as this is a substantial part of the mineral. There is almost no Ni present in the Spinels from Reinfjord. Also, NiChromite has more Cr than Fe^{3+}, which is not observed in group 3. Using this mineral name will therefore be misleading. Group 3 is the only group with significant Vanadium in the mineral formula. In Table 13 and Table 14 V is V^{3+} although it could as well be V^{4+} valence (Canil, 1999). In figures and plots they are marked Magnetite (**Mt** for short) or **group 3**.

4.2.2 Spinel BSE images

SEM and EPMA images were recoded of the most complex Spinel grains (Figure 4.4 to Figure 4.13 as well as Figure 4.6 and Figure 4.16). The imaged grains show important and varying contact relations, chemical gradients, textures and surrounding silicate minerals. Figure 4.14 and Figure 4.15 are EDS maps of two particularly interesting Spinel grains with gradual chemical variations within a single grain.

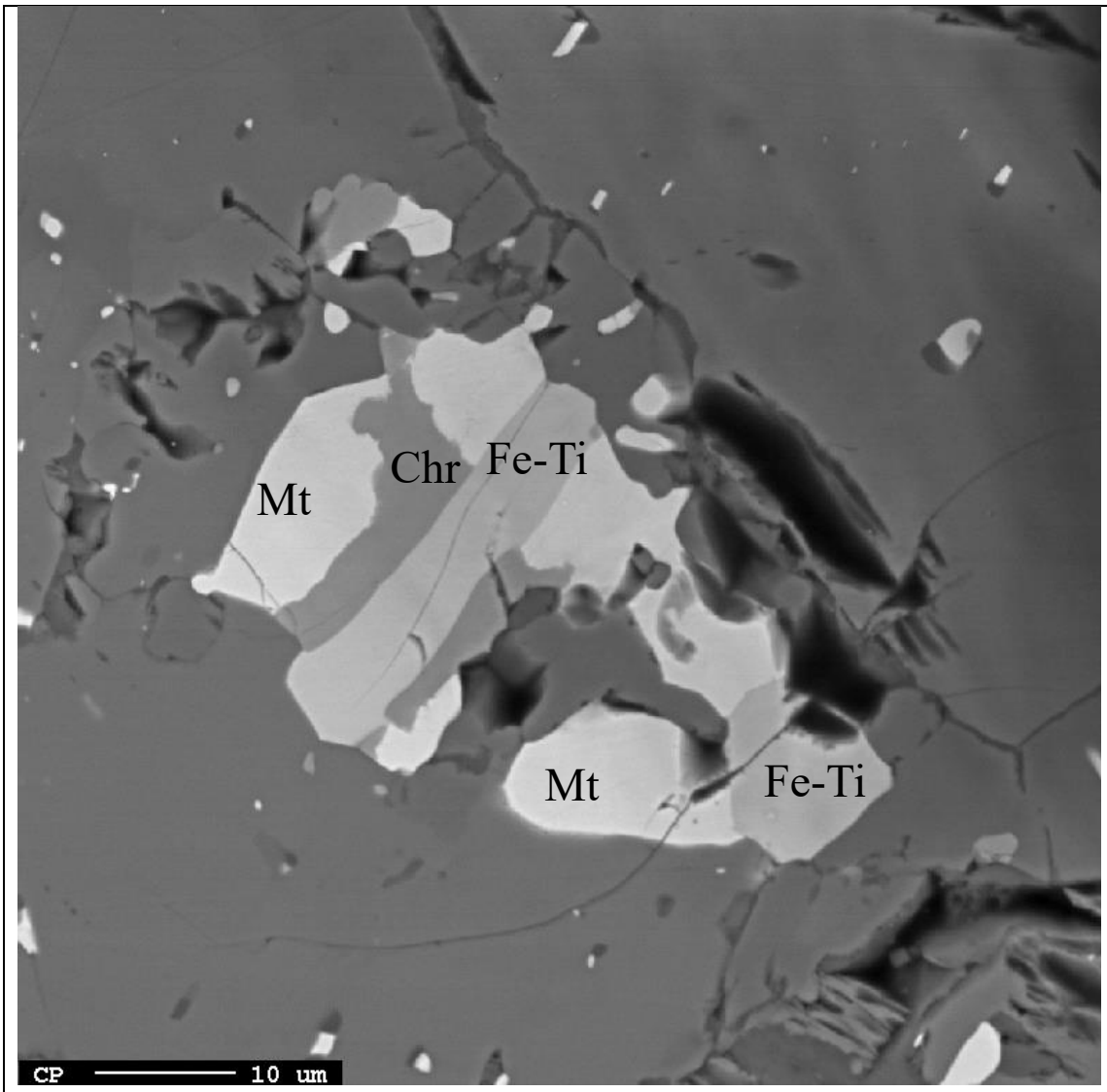

Figure 4.4

A BSE image of Cr-Spinel grain from thin section 364,5 with Magnetite, Chromite and Fe-Ti oxide. Both primary Spinel phases are cut by an Fe-Ti oxide. The Chromite in this figure has an outlier total and plots at the border between Spinel group 1 and group 2 in Figure 5.3.

The Spinel grain in Figure 4.4 and the Spinel grain in Figure 4.12 are the only Spinels in the RF4 drill core (between 280 and 390m depth) where Spinel of group 2 and group 3 are in contact in the same grain. In Figure 4.4 that contact is sharp, while in Figure 4.12 the contact defines a chemical gradient.

The entire Spinel grain in Figure 4.4 is cut by a Fe-Ti oxide. This phase overgrows a Magnetite of group 3 in the lower right corner in Figure 4.4. The Fe-Ti is a later formed phase than both group 2 and group 3 Spinels.

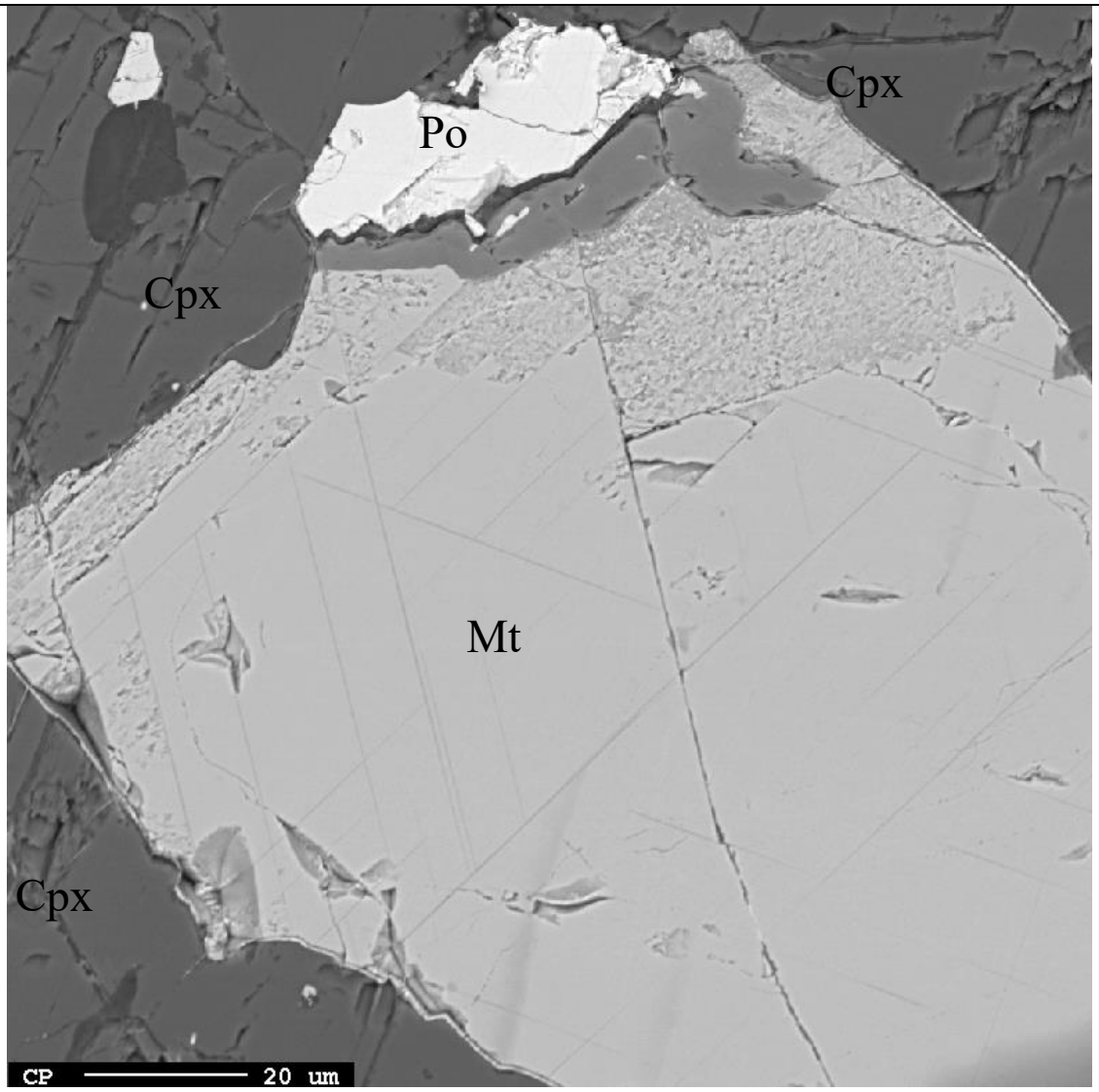

Figure 4.5

BSE image of an interstitial euhedral Magnetite grain found in thin section 320. A Pyrrhotite grain is in contact with the Spinel in the upper corner. Between the two are a small contact aureole of dark grey and a larger gnarled looking contact zone. The EPMA totals from analyses on this grain are outliers.

The bright Pyrrhotite sulfide grain at the top of Figure 4.5 is in contact with one of the mineral's euhedral crystal borders. Diffusion of a heavy element from Spinel to Po, results in a darker border between the two.

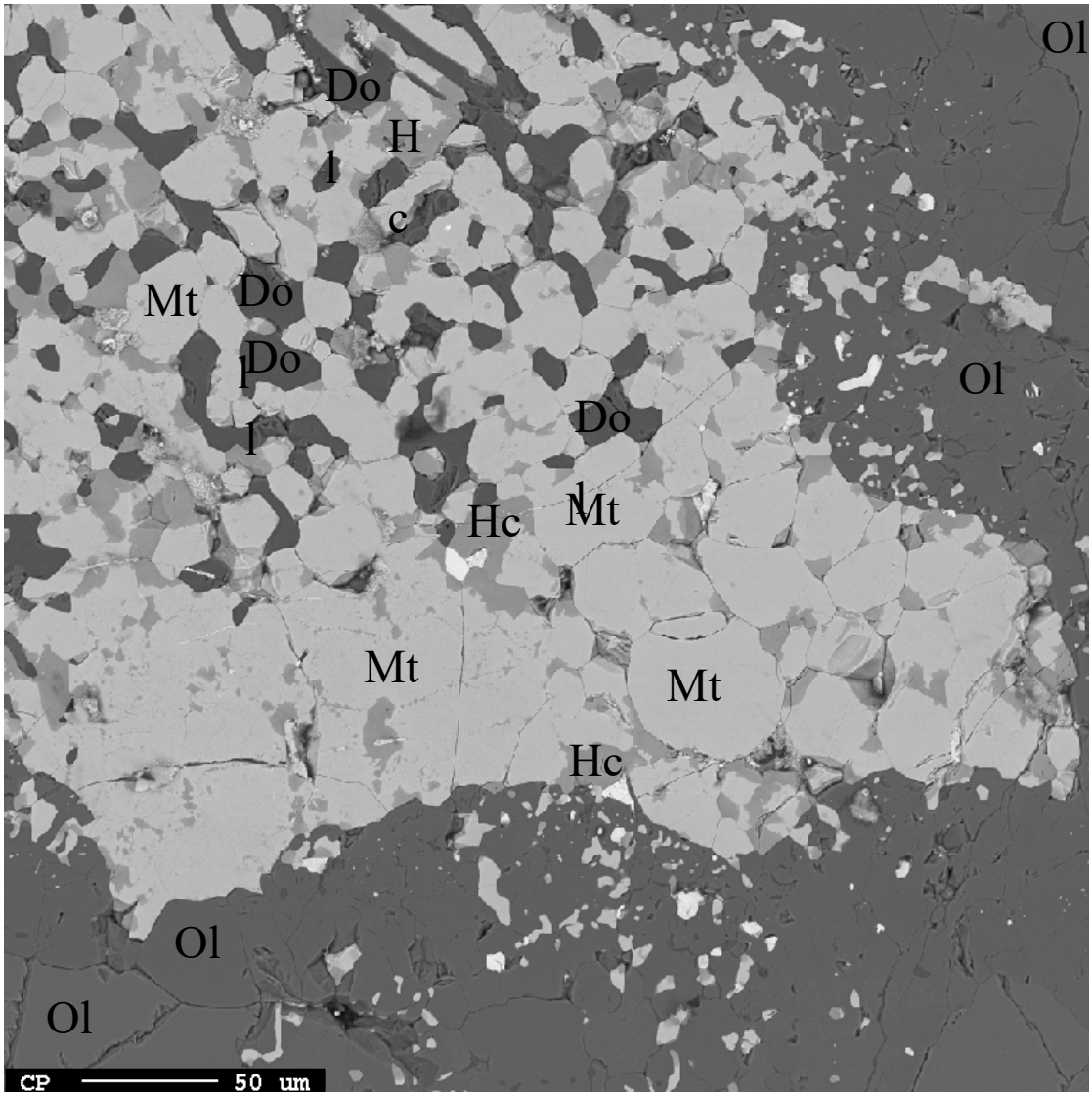

Figure 4.6

BSE image of several small, interstitial Chromite grains that have grown together to form a large patchwork aggregate of chromian Spinels in thin section 320. The grains contain two Spinel phases, the dark Hercynite is found close to the grain boundaries and the bright Magnetite is found everywhere the grain. The Spinel phases have sharp boundaries. Between the aggregate of Spinels are Dolomite grains. The aggregate is surrounded by a slightly darker Olivine than the cumulate Olivine at the upper right and lower left corners of the image.

Magnetite of Spinel group 3 and Hercynite of Spinel group 1 appear in Figure 4.7, Figure 4.8, Figure 4.9, Figure 4.10, Figure 4.11, Figure 4.13 and Figure 4.6.

In Figure 4.7, Figure 4.8, Figure 4.10 and Figure 4.6 Hercynite is a later crystallizing phase, found only along the outer edges of the mineral or along fractures in the Magnetite.

In Figure 4.9, Figure 4.11 and Figure 4.13 the two minerals appear to have crystallized/solidified simultaneously. The border between the two Spinel phases is smooth and often rounded in Figure 4.9. In Figure 4.11 the border between the Spinel phases is angular and polygonal, yet forming roundish inclusions.

Figure 4.10, Figure 4.11, Figure 4.12 and Figure 4.6 have late interstitial minerals in close contact. In Figure 4.7, Figure 4.10, Figure 4.12 and Figure 4.6 there are two types of Olivine in the image; the cumulate type is brighter (denser) while the type found in contact with the chromian Spinels is darker (less dense) and consists of small intergrown crystals. In Figure 4.10 and Figure 4.6, Dolomite is also present. In Figure 4.10 it is in contact with part of the Spinel crystal, as well as both types of Olivine. In Figure 4.6 it is only in contact with the Spinel. In Figure 4.12, the Spinel grains are in contact with Amphibole.

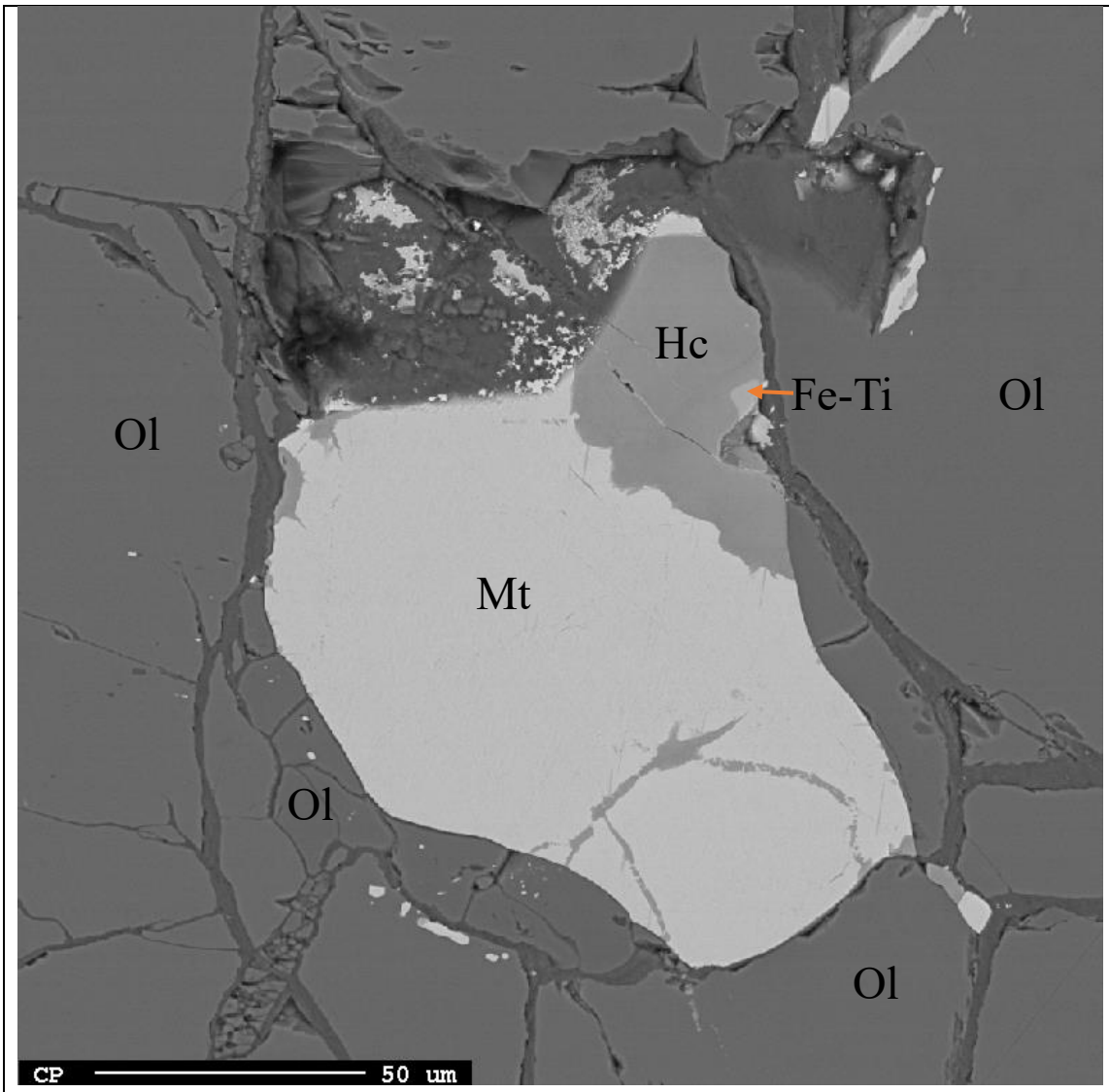

Figure 4.7

BSE image of a Cr Spinel grain in thin section 378-A. The grain contains a Magnetite and a Hercynite Spinel phase. The Hercynite phase fills a fracture in the Magnetite grain. A small Magnetite grain is in contact with Hercynite and Serpentine. A darker Ol phase is in contact with the Spinel in the lower left part of the image.

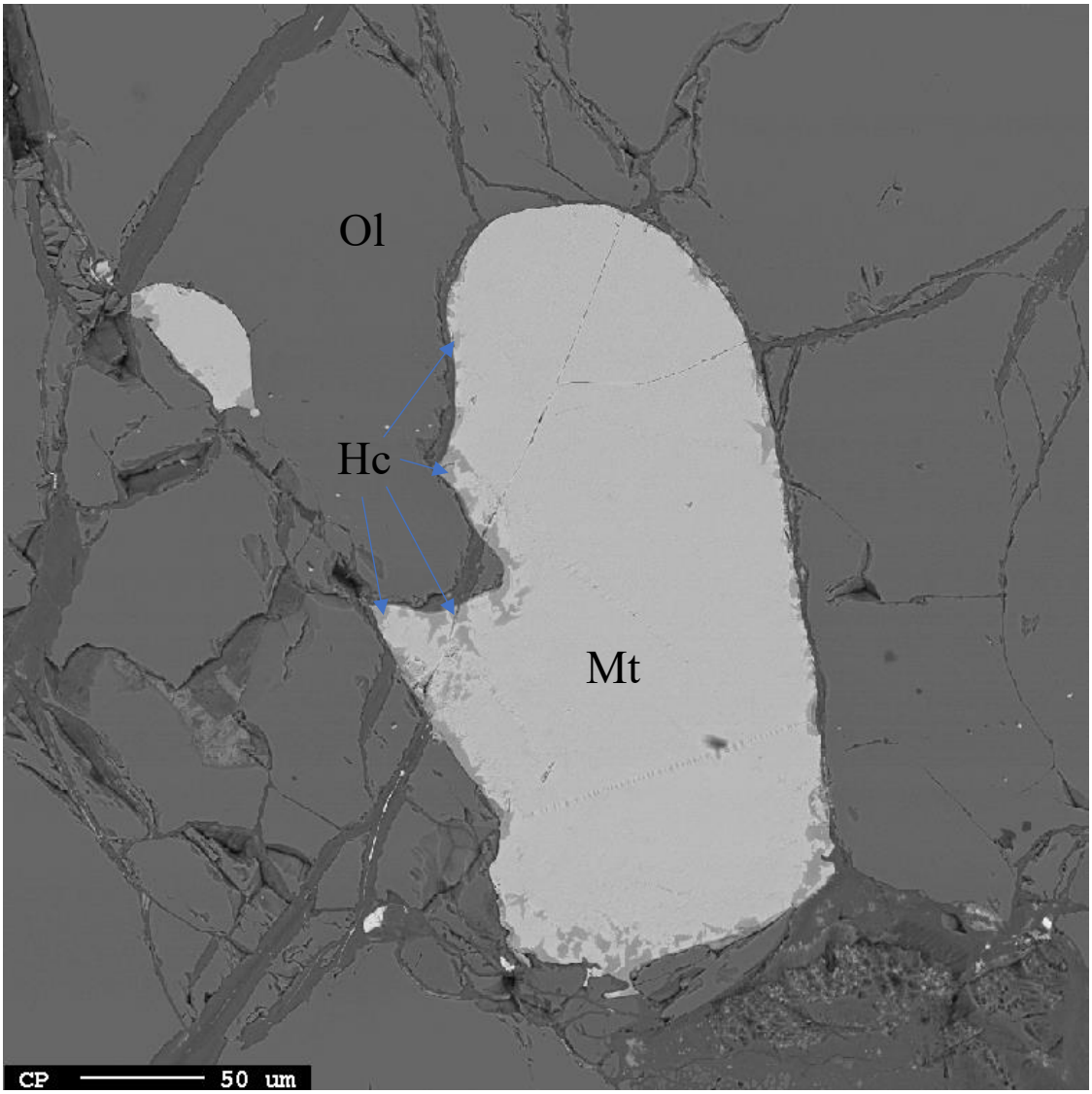

Figure 4.8

BSE image of a large Cr Spinel grain from thin section 315-A with two Spinel phases. The main phase, Magnetite, is in the center of the grain. Along the outer edges are areas are areas of Hercynite.

Figure 4.7 and Figure 4.8 have Hercynite occurring along the grain boundaries of a larger Magnetite grain. In Figure 4.7 only a small portion of the Hercynite occurs this way, whereas in Figure 4.8 all the Hercynite occur this way. The Hercynite is mostly found in contact with serpentinized Olivine whereas this textural pattern is not so common in Figure 4.8.

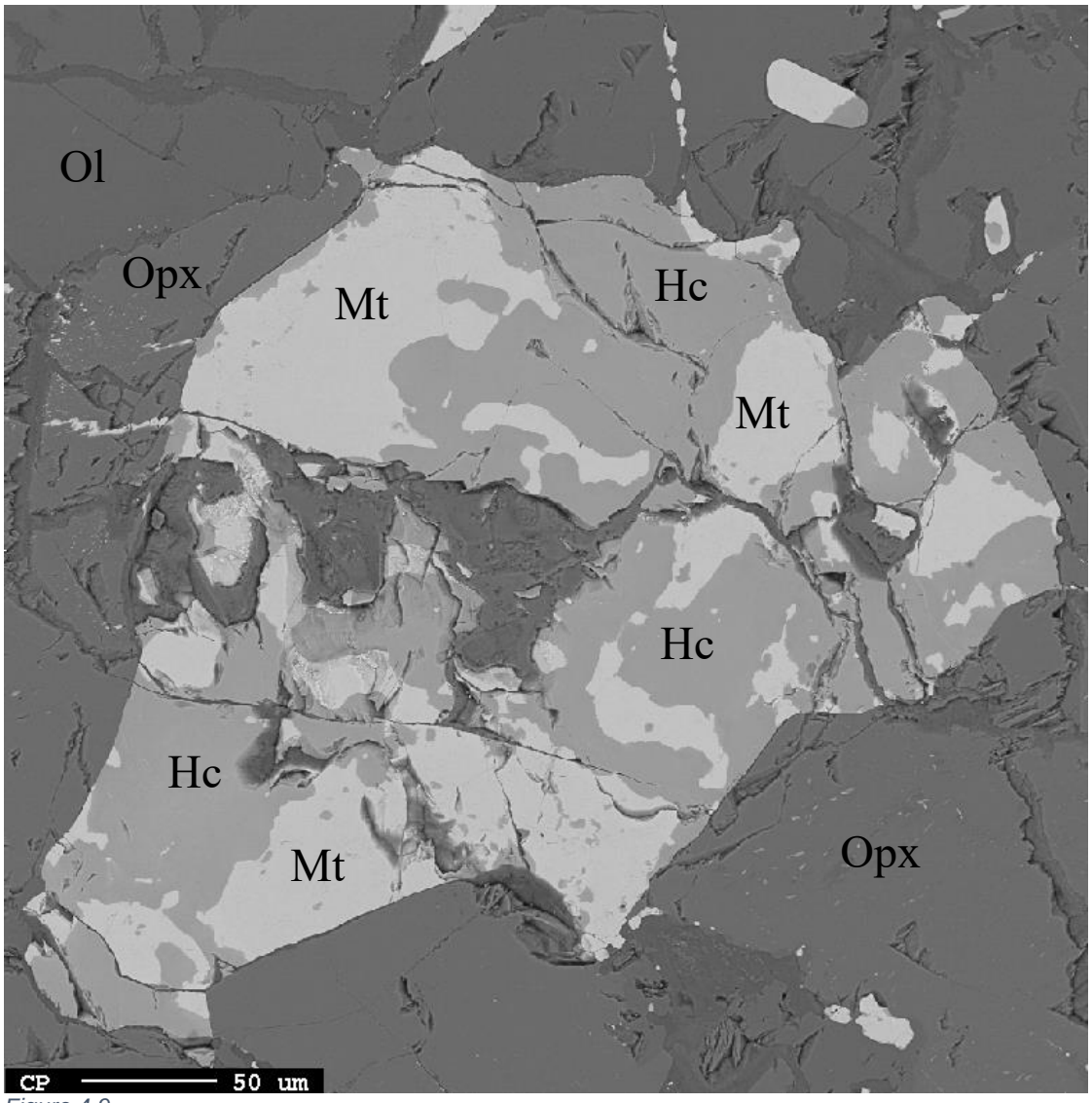

Figure 4.9

BSE image of a complex Cr Spinel grain from thin section 346, containing the Spinel phases Hercynite and Magnetite. The Spinel grain only border Orthopyroxene and Olivine.

In Figure 4.9 and Figure 4.11 Hercynite and Magnetite have distinct chemical boundaries and occur both as Hc blobs in patches of Mt and Mt blobs in patches of Hc. The grain in Figure 4.9 is in contact with fresh Ol whereas in Figure 4.11 Dolomite and a dark (primitive) Ol phase is common.

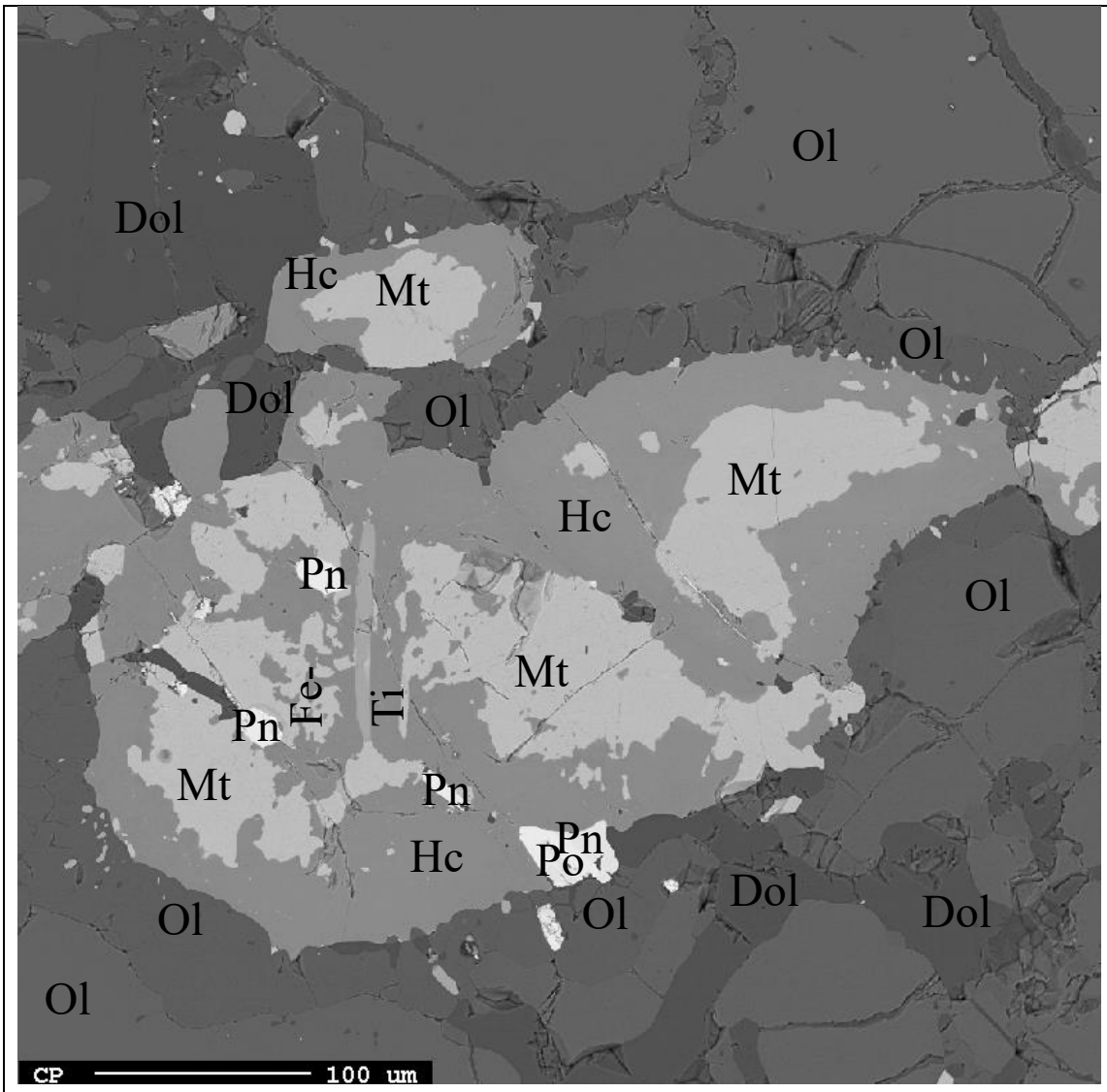

Figure 4.10

BSE image of chromian Spinel grains with two Spinel phases from thin section 325. The dark Hercynite phase constitutes ca 60% of the grain and grows outside the grey Magnetite phase. There is an inclusion of Fe-Ti oxide in the left center of the image, and several inclusions of bright sulfides (mainly Pentlandite, one occurrence of Pyrrhotite). A less dense Olivine phase and Dolomite surround the Spinel grain. Outside the altered contact zone are cumulate Olivine crystals.

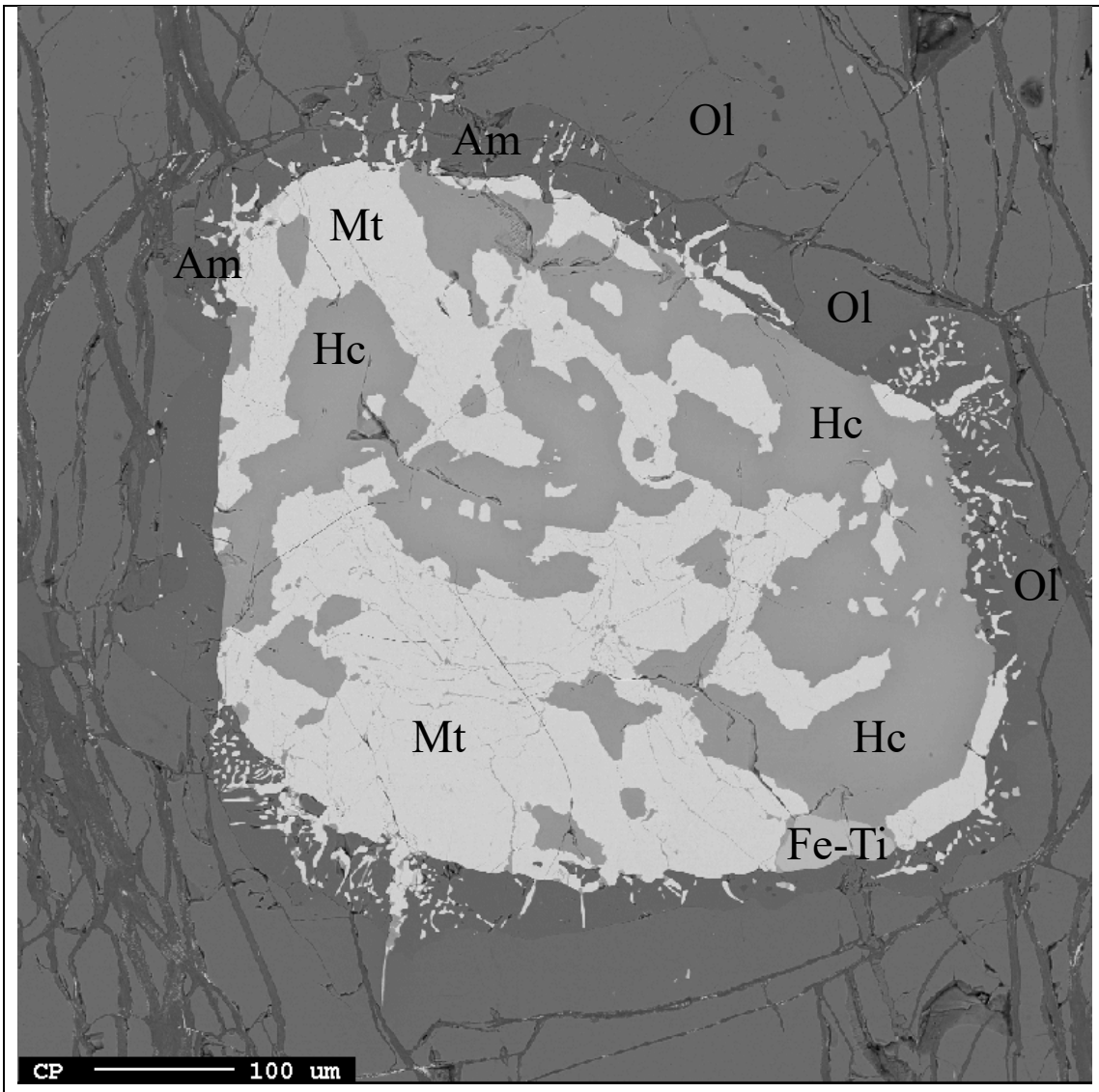

Figure 4.11

BSE image of a large Cr Spinel grain from thin section 348, containing the two Spinel phases Hercynite and Magnetite and small outshooting grains of both phases. A small Fe-Ti oxide cuts Hercynite in the lower right corner. The grain is surrounded by outshooting grains that cuts into Amphibole and Olivine. The Amphibole is only found in contact with the Spinel grain.

In Figure 4.11 and Figure 4.12 the Spinel do not occur as a single grain, but rather as a large grain with small grains shooting into the surrounding minerals. Parts of the grain is surrounded by Olivine and Dolomite in Figure 4.11 and Amphibole in Figure 4.12. Most of the outshoots are in the halo, but some cut through to cumulate Olivine in both figures. In Figure 4.11 the large grain consists of Hercynite and Magnetite (group 1 and 3). The outshoots of this mineral are mostly Hercynite, but in the longest outshoot at the bottom of the figure, both Spinel phases are present.

In Figure 4.12 the large Spinel grain gradually change compositions between Spinel group 2 and 3. The outshoots in Figure 4.12 vary in greyscale just like the large Spinel grain.

The large Spinel in both Figure 4.11 and Figure 4.12 are fractured (more so in Figure 4.12). Some of the fractures in both grains continue into the surrounding cumulate Olivine and Clinopyroxene grains. It is unclear whether the fractures cut the outshoot Spinels due to their small sizes.

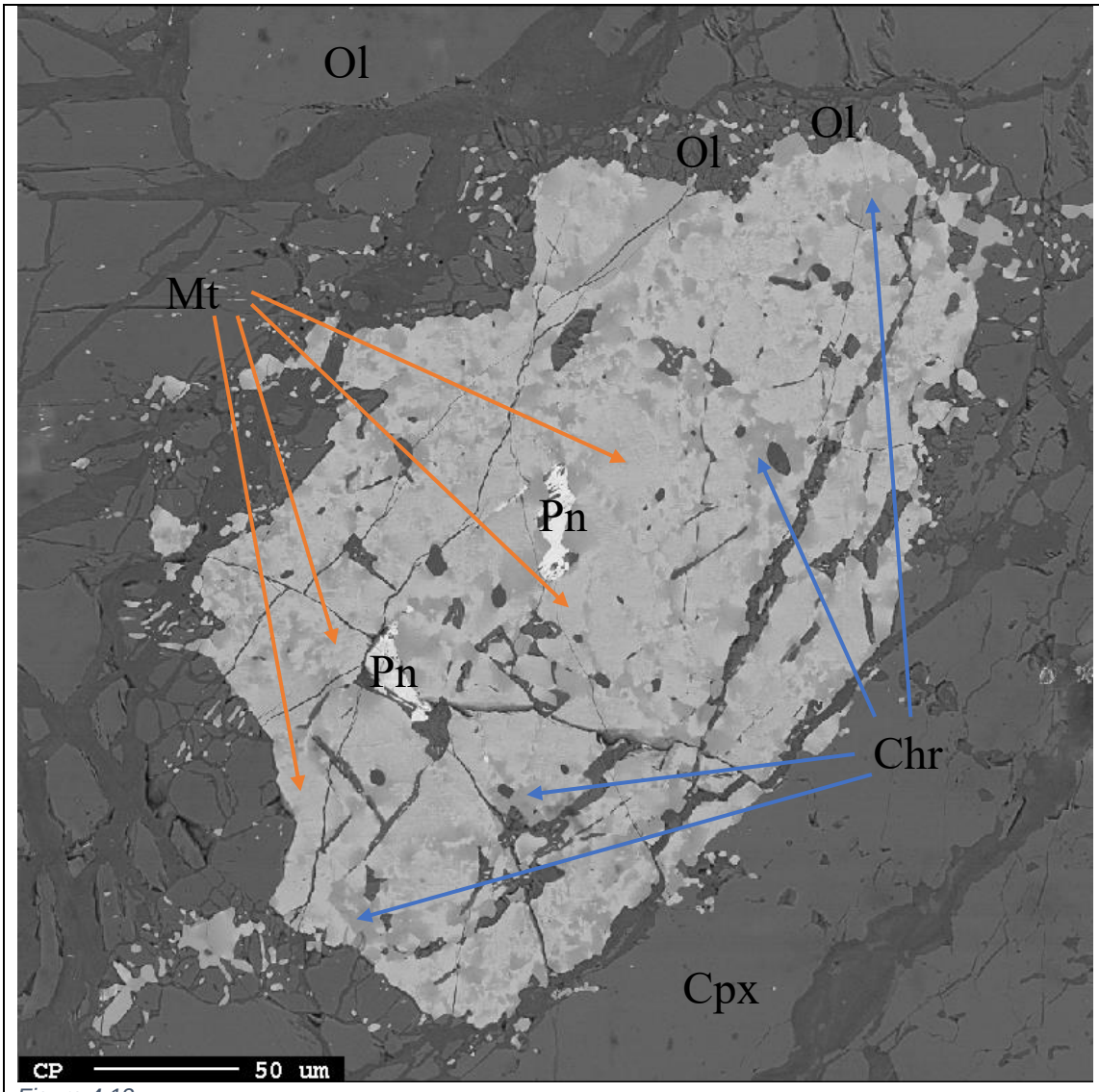

Figure 4.12

BSE image of a large, complex Cr Spinel grain from thin section 369,5-B with chemical gradual variations between two phases of Spinel: Magnetite and Chromite. The grain has two inclusions of Pentlandite. The grain has numerous offshoots of both Spinel types.

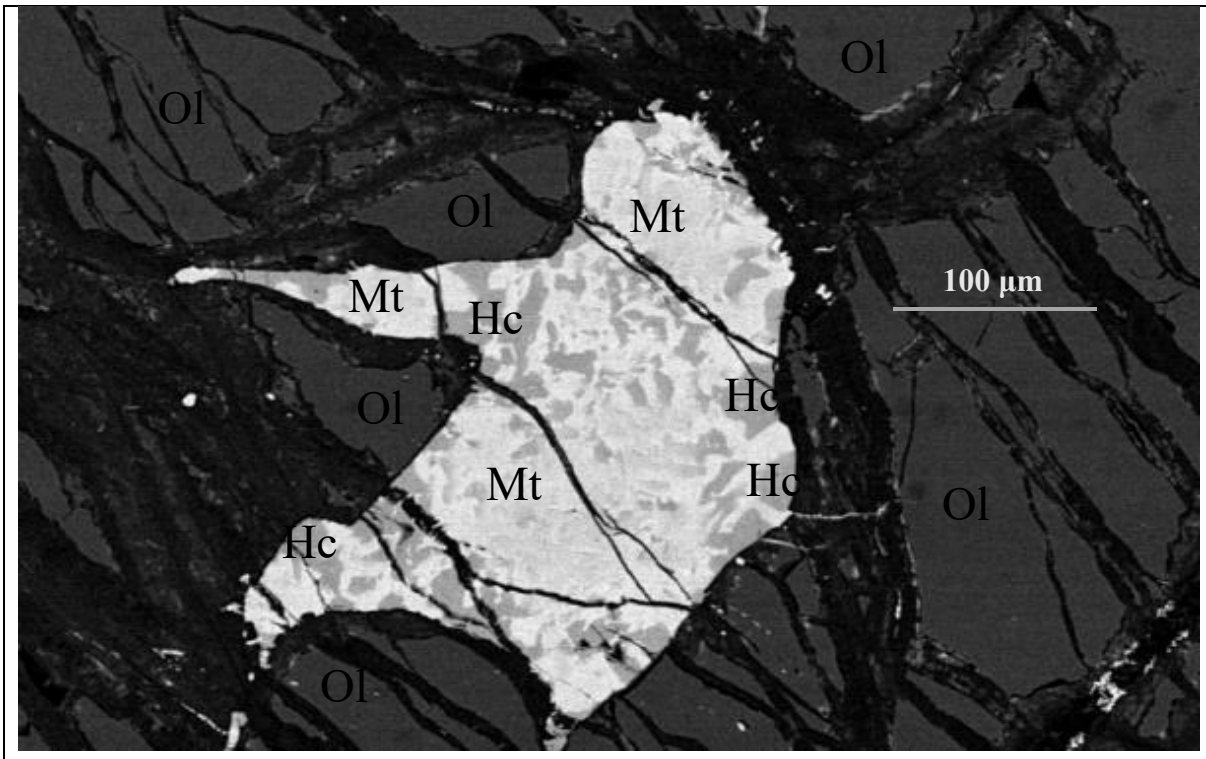

Figure 4.13

BSE image of a complex Cr Spinel grain from thin section 369,5-B. The Spinel varies between the endmember compositions Magnetite (Mt) and Hercynite (Hc). The Spinel grain is interstitial and surrounded by Olivine. Fractures that cut the Spinel continue into the Olivine.

In Figure 4.12 and Figure 4.13 the large Spinel grain has a gradual chemical transition between its two endmember minerals. The chemical gradients look optically like they appear in Figure 4.12 and Figure 4.13. EDS chemical mapping has been conducted on both, and the results can be seen in Figure 4.14 and Figure 4.15.

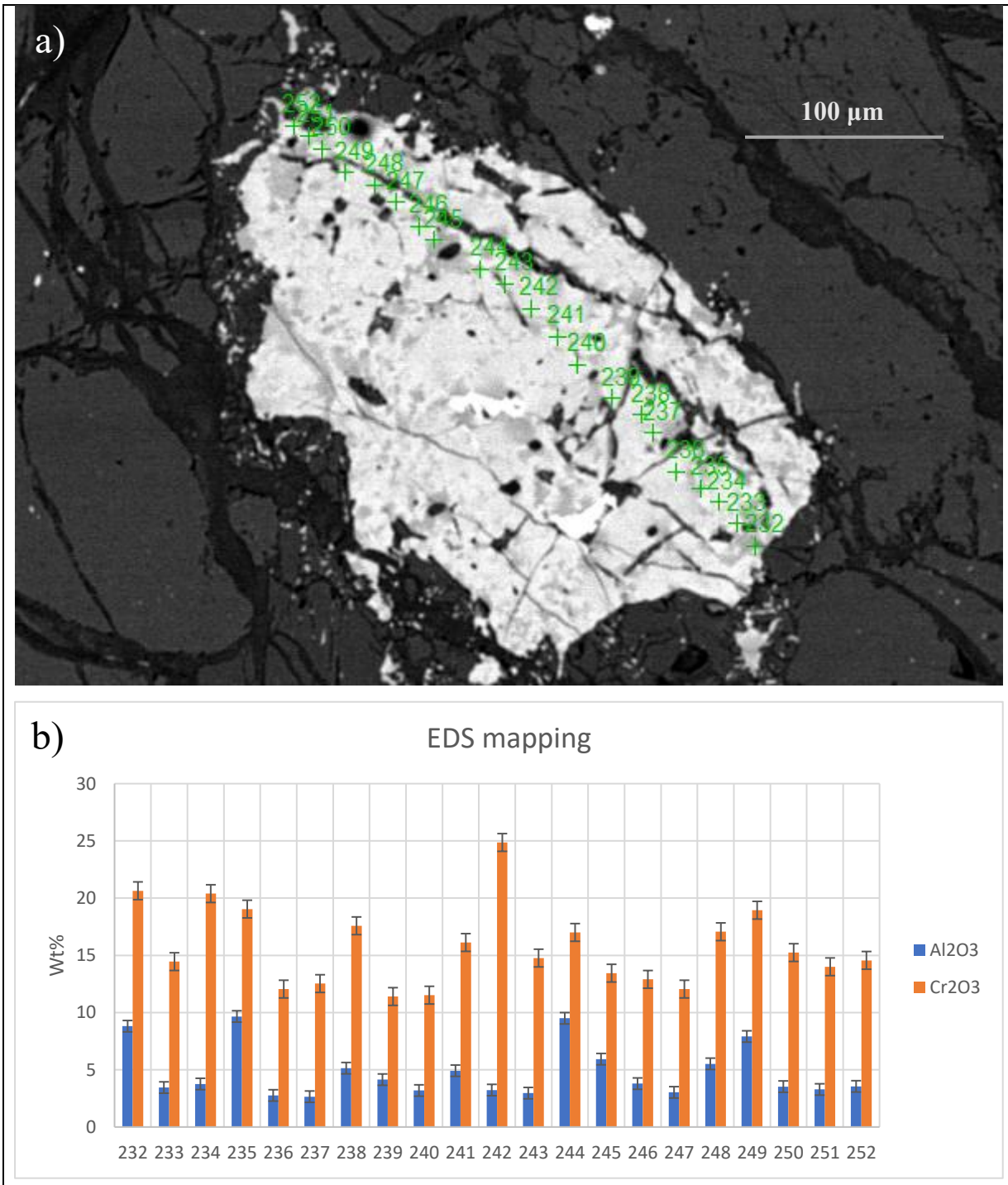

Figure 4.14

EDS mapping of the Spinel grain in Figure 4.12 using a SEM.

a) BSE image of the Spinel grain with marked where the EDS beam analyzed.

b) Measured Al and Cr as wt% plotted with error bars.

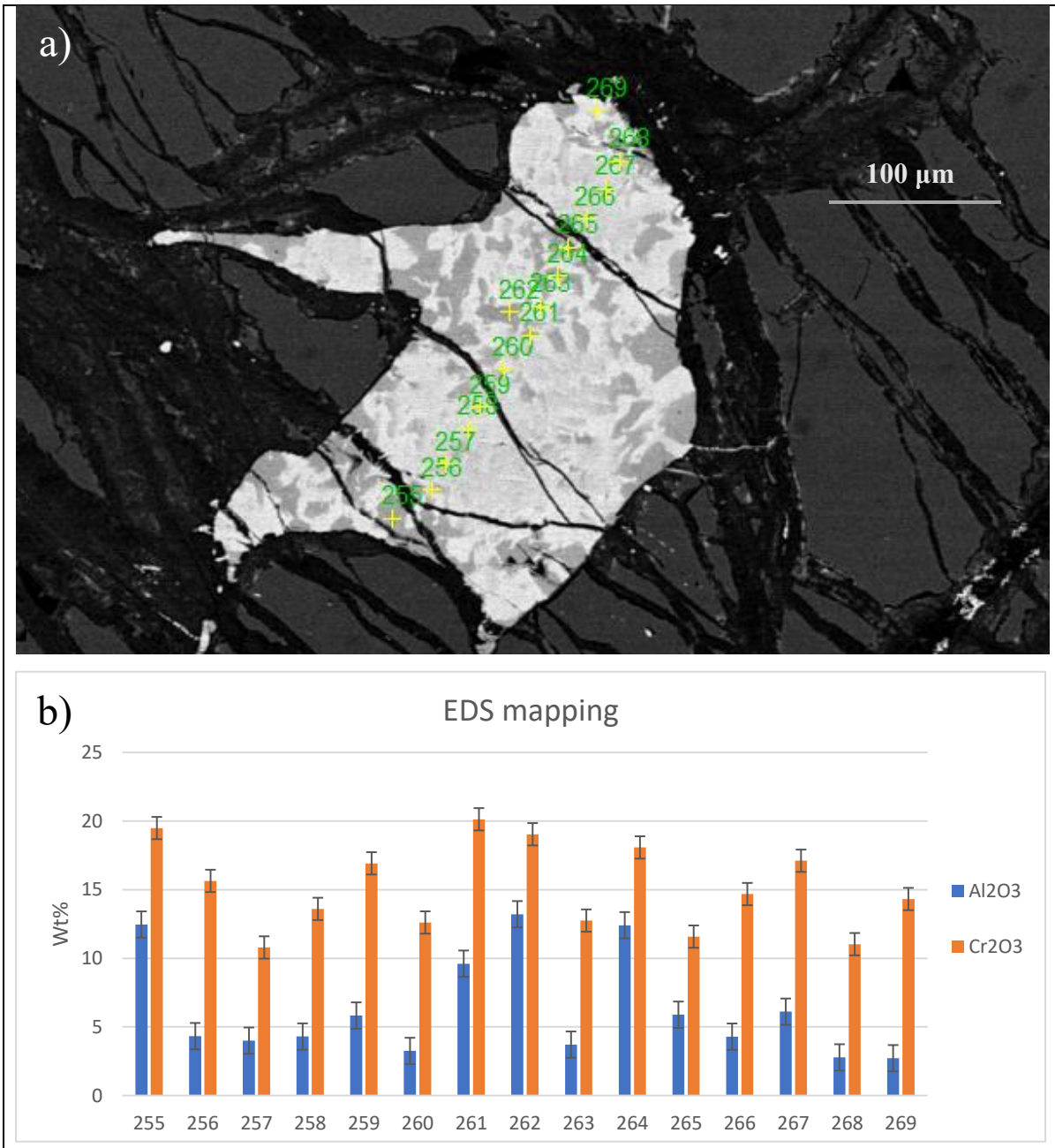

Figure 4.15

EDS mapping of the Spinel grain from Figure 4.13 using a SEM.

a) BSE image of the Spinel grain with marked where the EDS analyzed.

b) Measured Al_2O_3 and Cr_2O_3 as wt% plotted with error bars.

The full chemical data from the EDS mapping in Figure 4.14 and Figure 4.15 can be found in Appendix B.

The chemical mapping of Al and Cr (Figure 4.14 b) and Figure 4.15 b)) are mostly consistent. In Figure 4.14 b) there are several measurements at ca 3 wt% Al_2O_3, with gradual increase to 9 wt% Al_2O_3. There are several measurements of 12-13 wt% Cr_2O_3, with the maximum value at 25 wt% and several measurements at ca 20 wt% Cr_2O_3. In Figure 4.15 b) there are several Al_2O_3 measurements at 3 wt%, the highest reaching ca 12 wt% Al_2O_3. There are several Cr_2O_3 measurements at 12 wt%, the highest measurements being at ca 20 wt% Cr_2O_3. If the one 25 wt% Cr_2O_3 measurement is excluded, their chemical maps vary between the same endmembers. From Figure 5.3 and the chemical Spinel data in Appendix B, the chemical endmembers in Figure 4.14 are group 2 and group 3 while in Figure 4.15 they are group 1 and group 3.

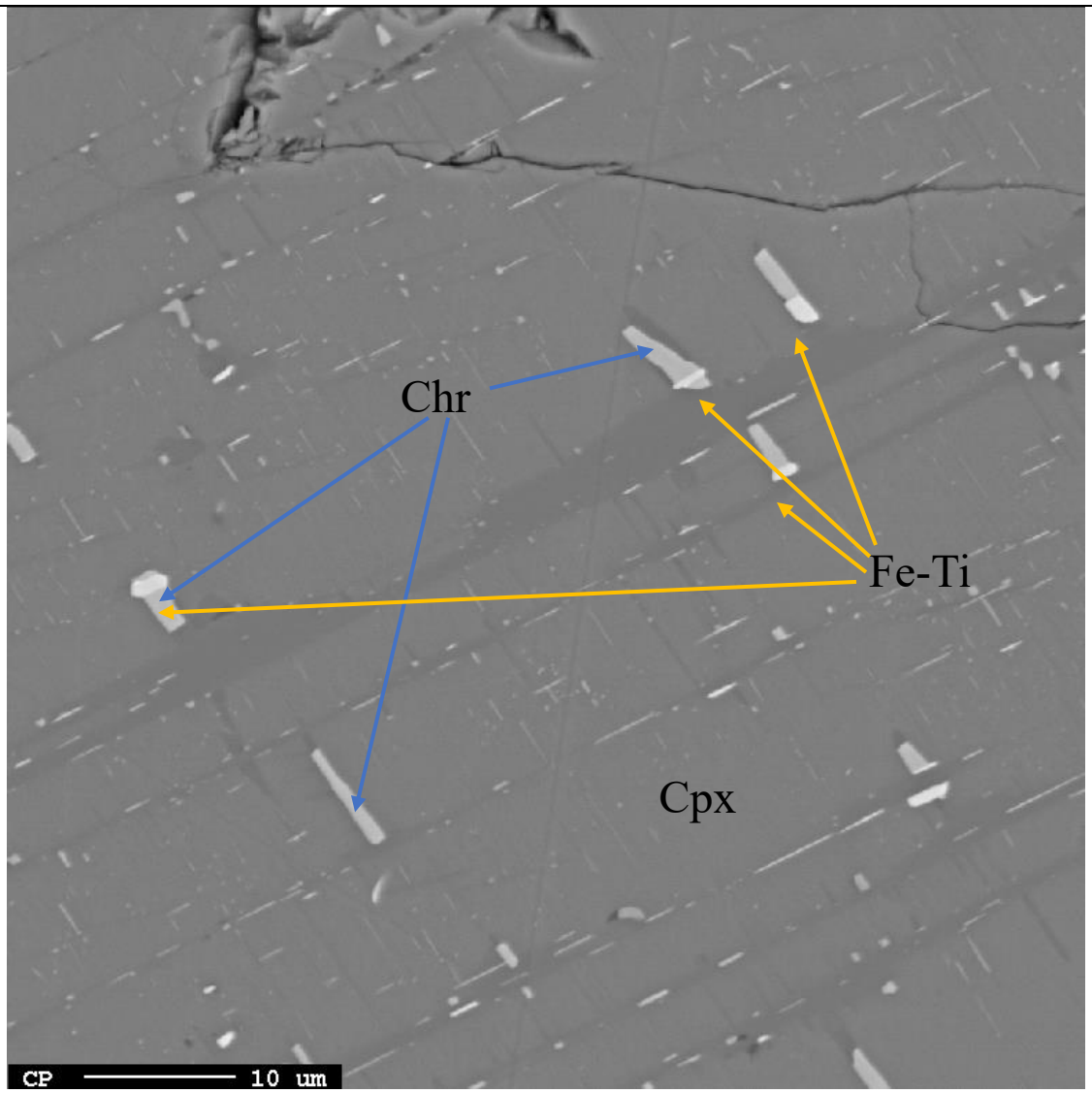

Figure 4.16

BSE image of Fe-Ti oxide inclusions (bright) and Chromite inclusions (darker grey) along the cleavage planes of a Clinopyroxene in thin section 348.

One Clinopyroxene grain analyzed by EPMA (see Figure 4.16) had both Fe-Ti oxides and Chromite inclusions along cleavage planes. The two has clearly defined grain boundaries and are often found in contact with one another as inclusions.

4.2.3 Spinel Chemistry

There are both interstitial chromian Spinels and Spinel grains found as inclusions in silicate minerals. Most of the EPMA analyzed grains were found as individual cumulate or interstitial crystals (Appendix B).

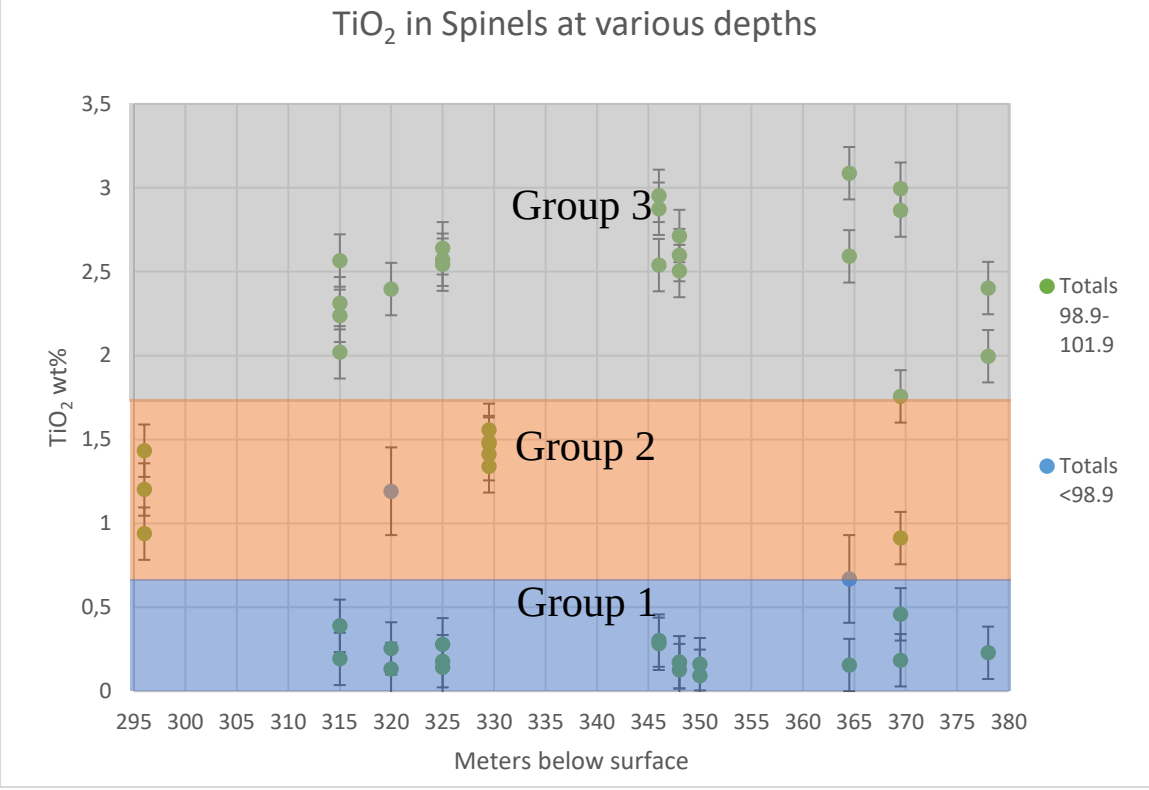

Figure 4.17

The average measured TiO_2 content in each analyzed Spinel mineral plotted with σ uncertainty bars. Two grains with outlier totals have been included as they are potentially important to understand the Spinel crystallization. The blue point in group 2 from 320m is part of the Magnetite group based on Fe content.

Excepting one mineral in thin section 369,5 (which plots at the border between group 2 and 3) and one mineral in thin section 364.35 (which plots at the border between group 1 and 2), all measurements are strictly within a single group. Thin section 296 and 329,5 have only Spinels from group 2. All other thin sections have Spinels from both group 1 and 3. Thin section 369,5B has Spinels with compositions of all three groups. Thin section 364.35 might have Spinels in all

three groups. Thin section 315, 320, 325, 346, 348, 350, 378 and possibly 364,35 only have Spinels from group 1 and 3.

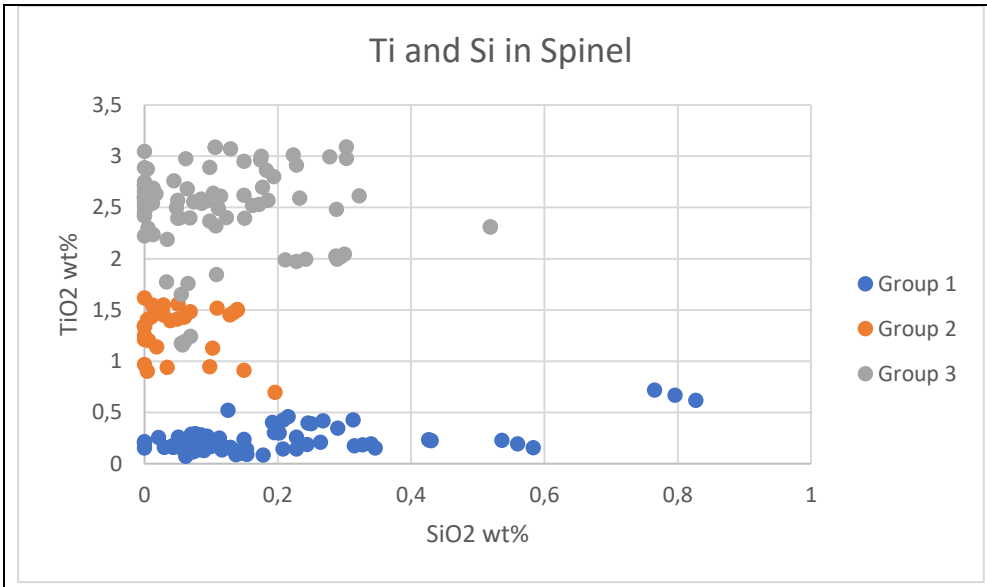

Figure 4.18

SiO_2 vs. TiO_2 from all Spinel measurements.

There appear to be no correlation between the two 4+ valence cations (Ti^{4+} and Si^{4+}) in the analyzed Spinels. Except for outliers in Group 3, the groups are separated by their TiO_2 concentration. The SiO_2 varies most in Group 1 and least in Group 2. However, as Group 1 has the greatest number of analyses and Group 2 has the fewest, this could be a statistical bias.

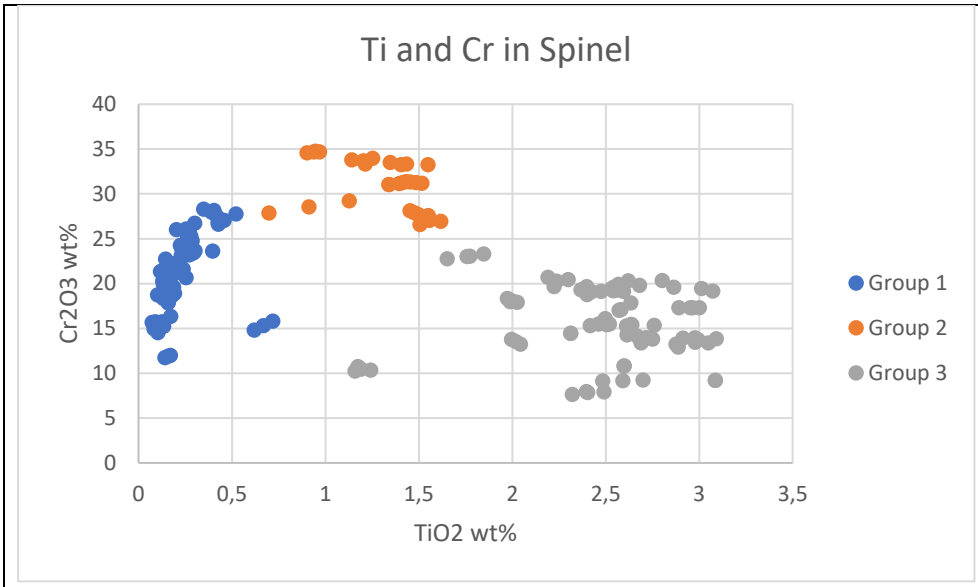

Figure 4.19

TiO_2 and Cr_2O_3 plotted in wt% from all Spinel measurements.

In Figure 4.19, the Cr and Ti content of the Spinel groups can be seen. Group 1 has steeply increasing Cr content while the three other categories have more or less constant Cr values for the group's range in TiO_2. Group 2 has the highest Cr concentrations. Group 3 has higher TiO_2 but lower Cr_2O_3. The group 1 outlier is the Chr/Hc from Figure 4.4 and the group 3 outlier is the Mt from Figure 4.4.

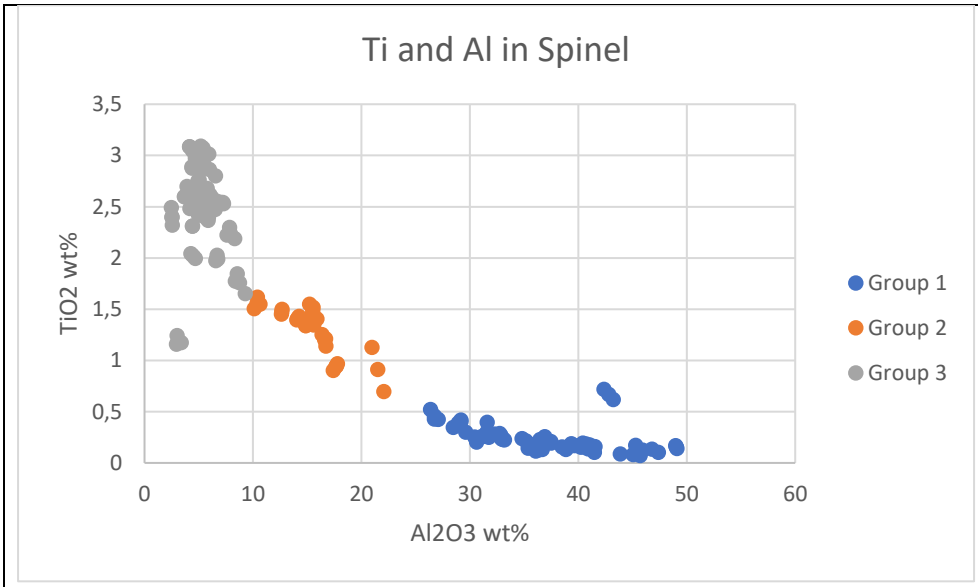

Figure 4.20

TiO_2 and Al_2O_3 plotted as wt% from all Spinel measurements.

In Figure 4.20 the Al and Ti correlation can be seen for all analyzed Spinels. There is a negative correlation between the two elements, where Group 3 plots the most Ti rich and Al poor; and group 1 plots the most Ti poor and Al rich. The negative correlation is exponential. The outlier group 3 analyses are from the Spinel in Figure 4.14 and the group 1 outlier is the Chr/Hc from Figure 4.4.

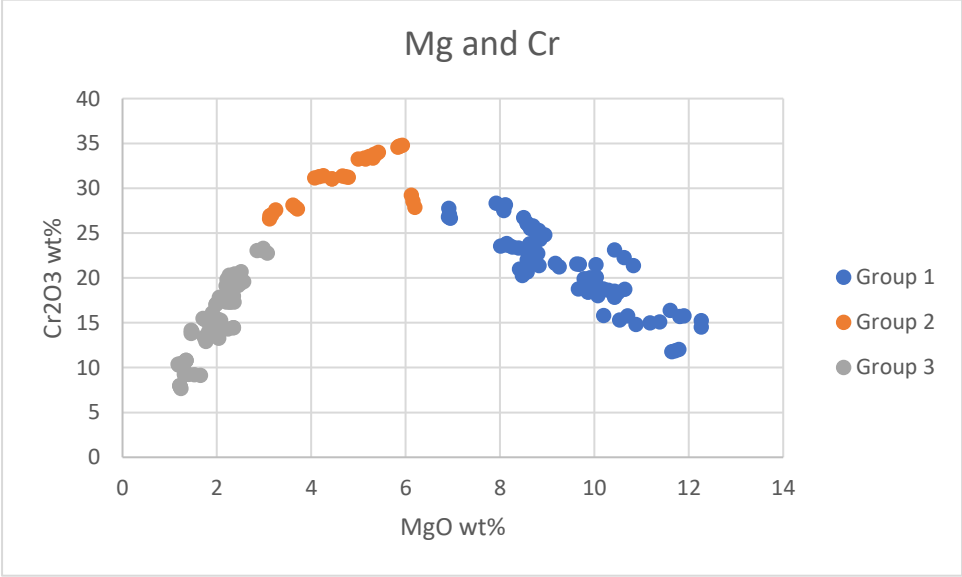

Figure 4.21

Mg and Cr plotted as wt% oxides from all Spinel measurements.

In Figure 4.21 the two primitive Spinel inticators – Mg and Cr – are plotted. The Chromite and Magnetite Spinels have a positive correlation between the elements, where Chr is more enriched in both. Three outlier Chr measurements and the Hercynite Spinels do not follow this trend. They have a negative correlation between Mg and Cr. The most Mg rich Spinels are in the Hc group. These are significantly Cr depleted.

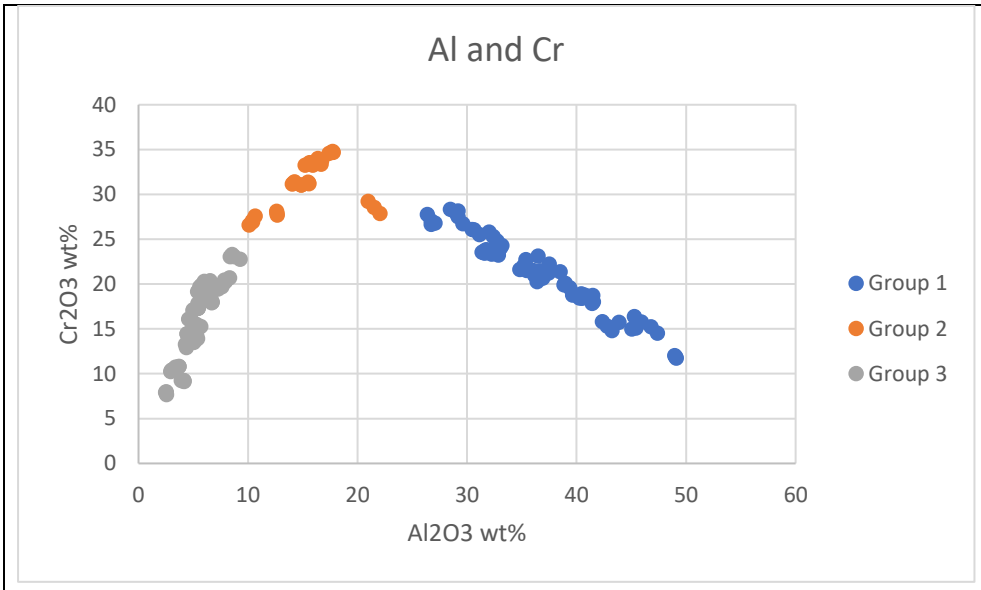

Figure 4.22

Al_2O_3 and Cr_2O_3 plotted as wt% from all Spinel measurements.

There are two distinct trends in the diagram of Figure 4.22. Group 3 and group 2 (except for a few outliers) are on positively correlating trend. Group 1 has a negative correlation between the two elements.

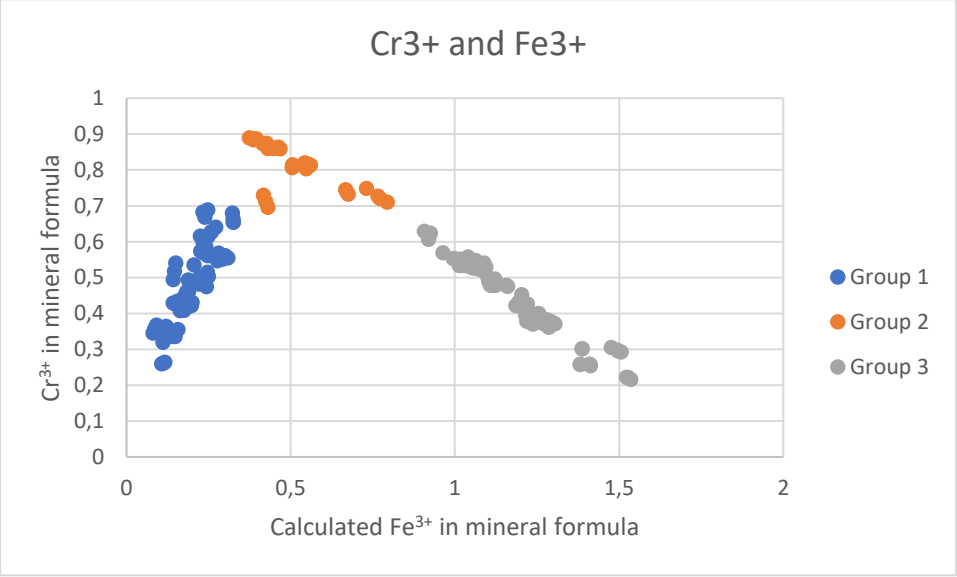

Figure 4.23

Calculated Fe^{3+} in mineral formula plotted against Cr^{3+} in mineral formula from all Spinel measurements.

In Figure 4.23 the opposite trend from Figure 4.22 can be seen. Group 1 has a strong positive correlation between the two elements, whereas group 2 and 3 has a strong, distinct negative correlation between the elements. The same outlier observed in Figure 4.22 is observed in Figure 4.23. The group 1 correlation has a wider scatter than the group 2 and 3 correlation.

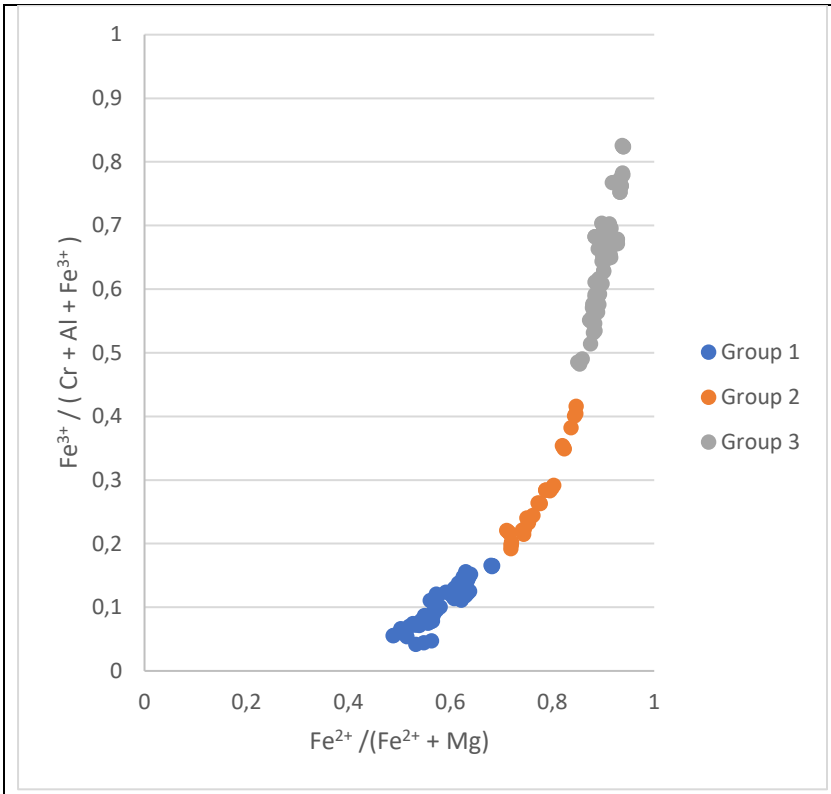

Figure 4.24

Fe^{2+}-number plotted against Fe^{3+}-number from all Spinel measurements.

The diagram in Figure 4.24 shows all analyzed Spinels plotting in the Fe^{2+}# vs Fe^{3+}# as proposed by Barnes & Roeder (2001). Group 1, 2 and 3 plot in a semicontinous exponential curve with medium to very high Fe^{2+}# and very low to high Fe^{3+}#.

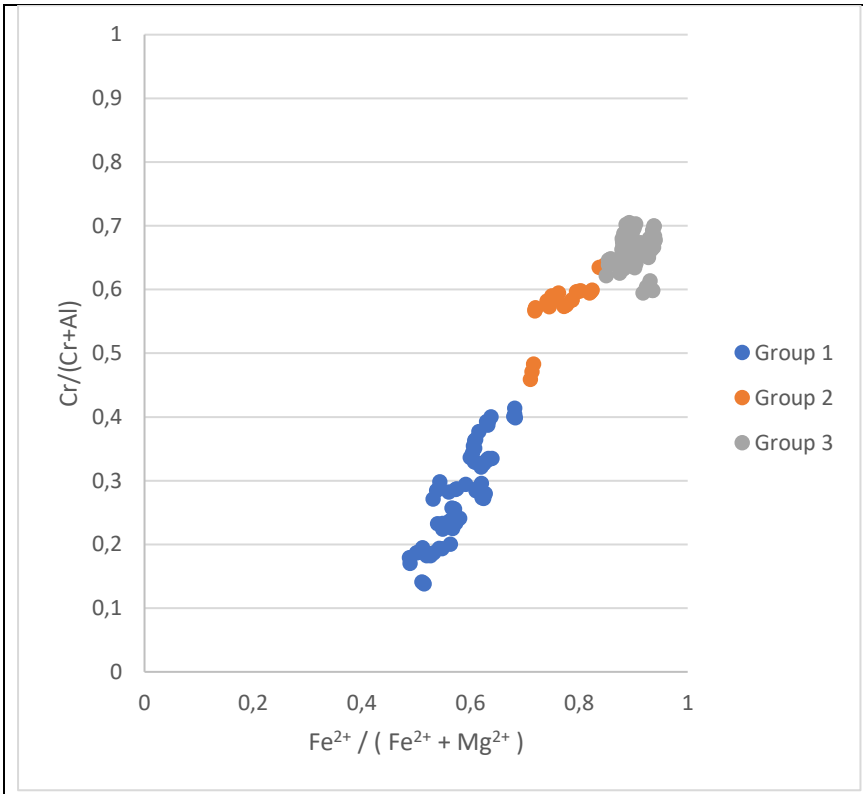

Figure 4.25

Cr-number plotted against Fe^{2+}-number from all Spinel measurements.

All Spinel groups plot in a continuous trend between medium to very high Fe^{2+} number and very low to moderate Cr number in Figure 4.25. The diagram was proposed by Barnes & Roeder (2001).

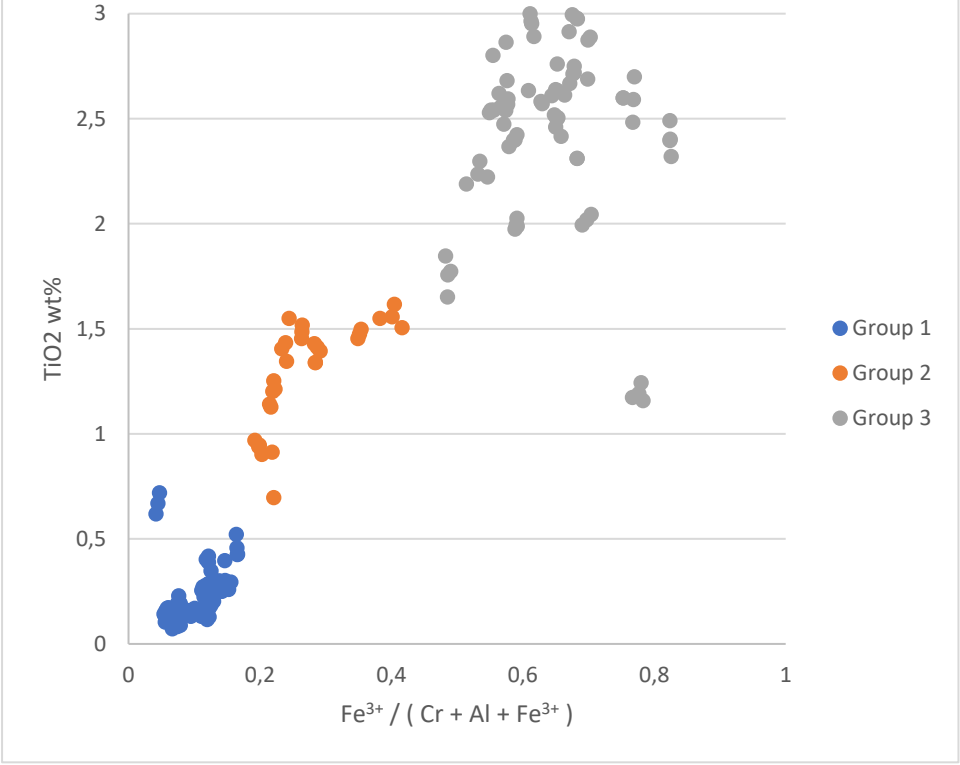

Figure 4.26

TiO_2 measured in wt% plotted against Fe^{3+} -number for all Spinel measurements.

The TiO_2 vs. Fe^{3+} number diagram (see Figure 4.26) was proposed by Barnes and Roeder (2001). This diagram goes to 3 wt% TiO_2. Group 1 plots very low on both axes. Group 2 plots intermediate, with a very steep increase in TiO_2 before the trend flattens out at a Fe^{3+}# of 0.25. Group 3 plots high in both variables and has a wide scatter. The outlier group 3 measurement is the mineral from Figure 4.12 and the group 1 outlier is from Figure 4.4.

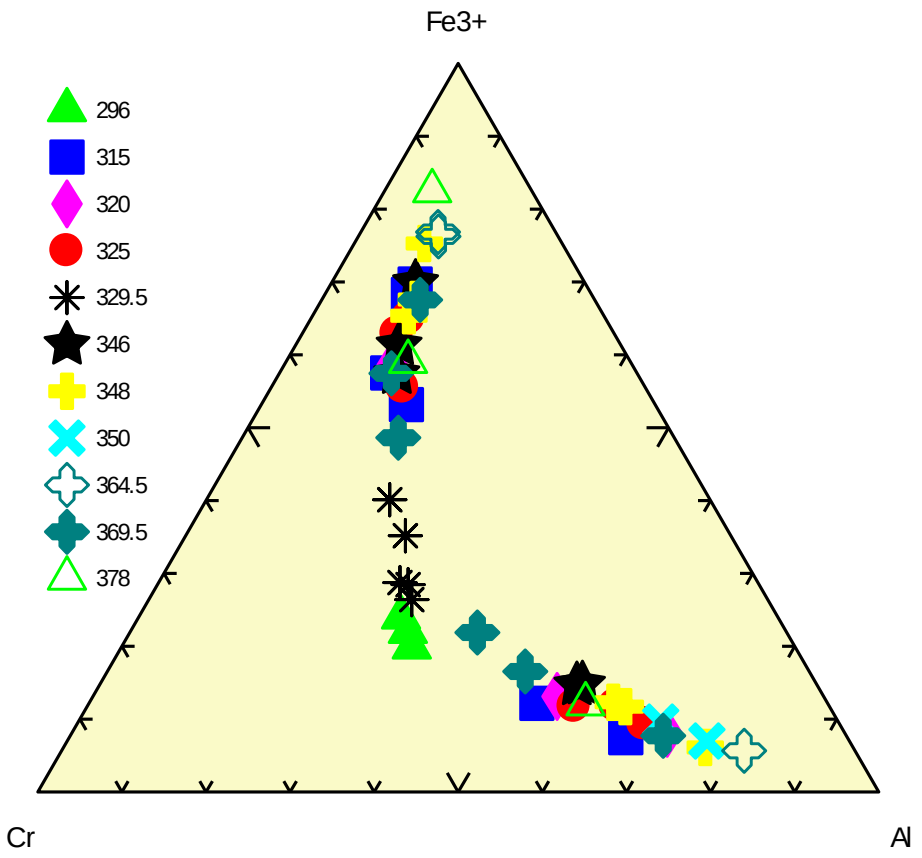

Figure 4.27

Ternary Spinel prism diagram with proportion of Cr^{3+}, Al^{3+} and Fe^{3+} in the mineral formula as the input parameters. The average measured values for each Spinel grain are plotted, sorted by sample depth. "296" in the legend signifies "thin section is from 296 m depth in RF4".

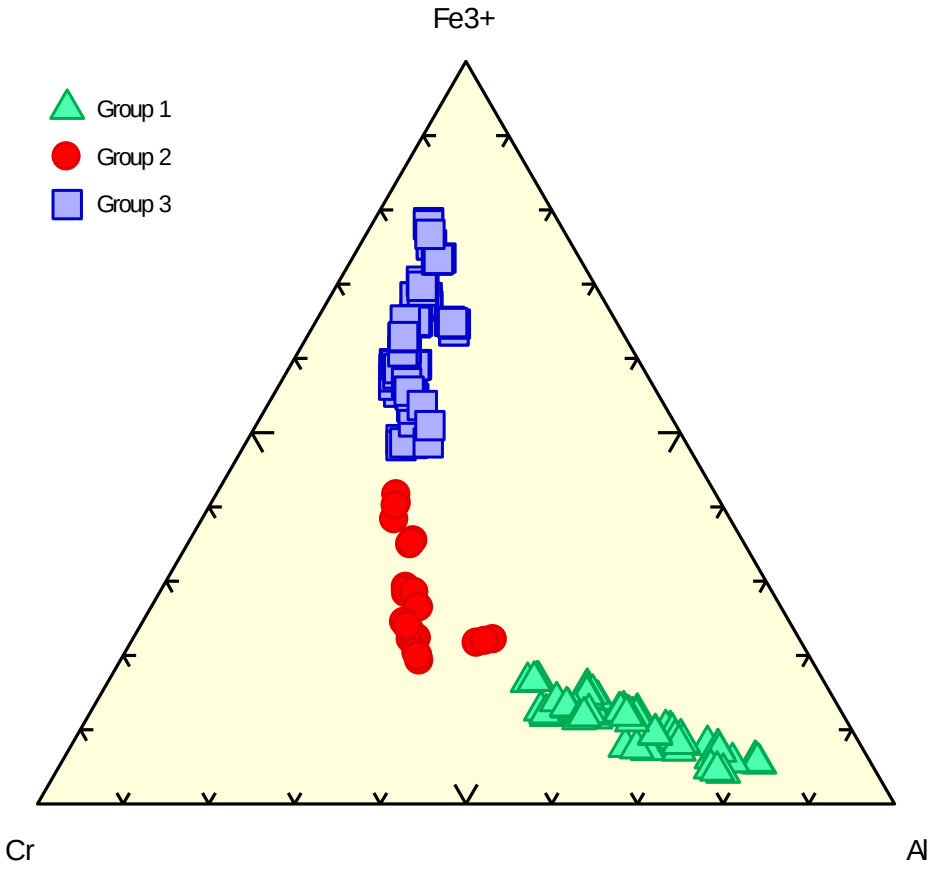

Figure 4.28

Ternary Spinel prism with proportion of Cr^{3+}, Al^{3+} and Fe^{3+} in the mineral formula as the input parameters. All EPMA analyses with reasonable oxide totals are plotted in this diagram, sorted by mineral group.

The ternary Spinel prisms in Figure 4.28 and Figure 5.4 plot where the analyzed Spinels from the different groups (Figure 5.4) and the average Spinel compositions measured in each analyzed Spinel grain (Figure 4.27) according to the ternary diagram proposed by Stevens (1944). Most of the trends seen in Figure 5.3 is also seen in Figure 4.28. The group 2 composition is a separate intermediate phase between the endmembers of group 1 and group 3. Group 2 consists of all the analyzed Spinels from thin section 296 and 329,5 and possibly one measurement from thin section 369,5. Most thin sections have chemistries plotting in both group 1 and group 3, except for thin section 350 which only contains Spinels of group 1. Of the thin sections with analyses in both group 1 and 3, thin section 364,5 is noteworthy by having the Spinels of the most Al rich composition and the second and third most Fe^{3+} rich compositions.

From Figure 5.4 it is clear that group 3 and group 2 Spinels have a constant Al:Cr ratio but varying concentrations of Fe^{3+}. This is visualized by those Spinel types plotting on a vertical line in the Spinel prism. Group 1 Spinels have a constant Cr:Fe^{3+} ratio and varying concentrations of Al. These Spinels plot in a gently right-dipping line towards the Al endmember.

4.3 Clinopyroxene

Most of the thin sections contain Clinopyroxene. Some also contain Orthopyroxene and Amphiboles. Clinopyroxene occurs as cumulate grains (Figure 4.2) complex interstitial grains (Figure 9.7) or larger oikocrysts (Grant et al., 2016). Clinopyroxenes were analyzed by EPMA and EDS in 12 samples. Averages of the chemical EPMA results are plotted in Table 15 and in Figure 4.29. The complete EPMA results are found in Appendix B.

Table 15: Chemical average and σ values for the analyzed Clinopyroxene grains. Calculation of σ was made by total variance of each grain's variance. :

	SiO2	TiO2	Al2O3	Cr2O3	FeO	MgO	CaO	Na2O
AVG	50.510	0.849	4.719	0.648	3.894	15.764	23.134	0.560
STDEV	0.27	0.02	0.214	0.01	0.23	0.27	0.85	0.01

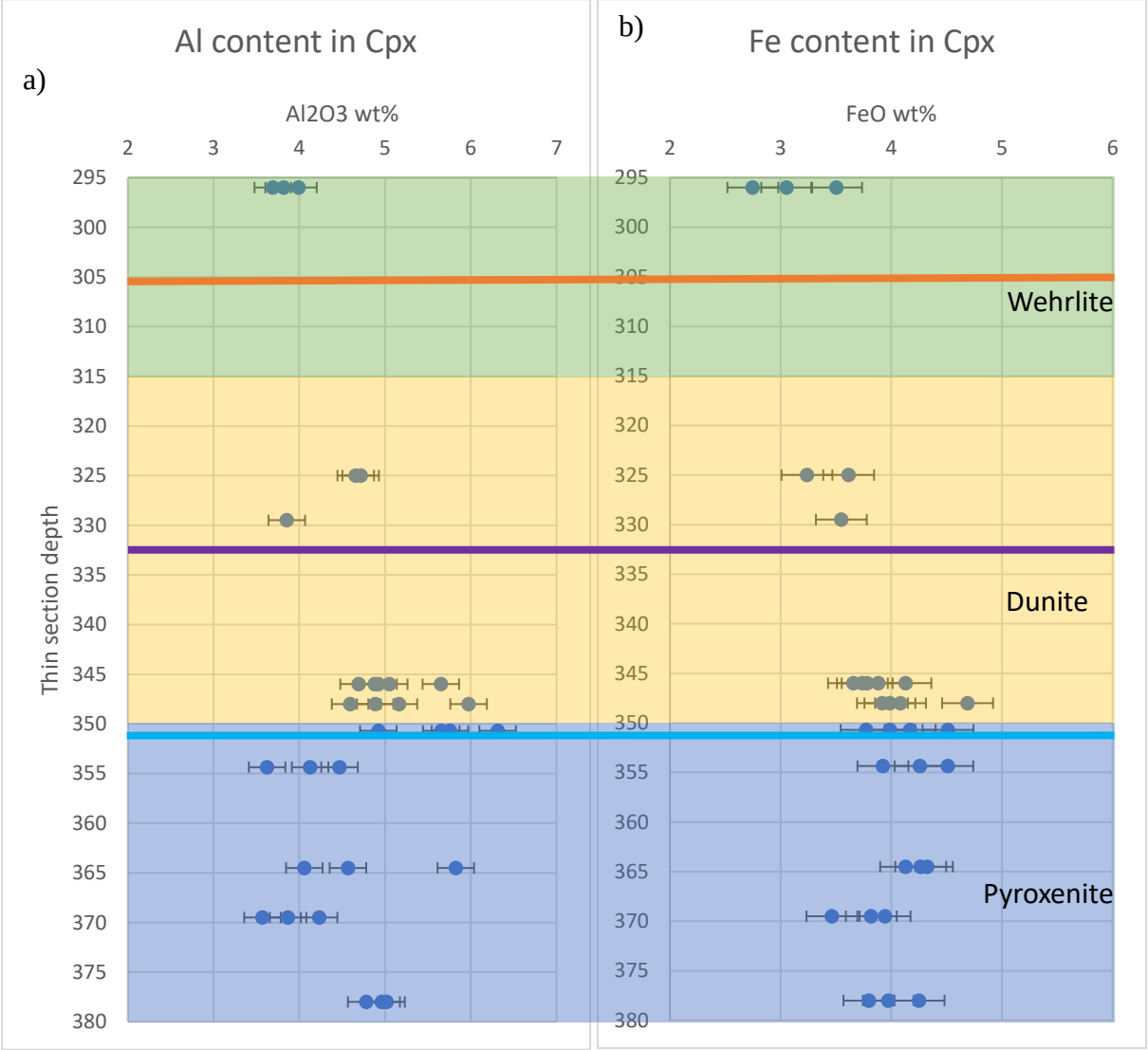

Figure 4.29

Diagrams of the Al_2O_3 (a) and FeO (b) wt% content in the analyzed Cpx grains. The average chemical value based on 5 analyses is plotted in the diagram. Error bars show 1 σ (calculated by total variance of each grain's variance). The diagrams are color coded by lithology (yellow: dunite, green: wehrlite, blue: pyroxenite), and the fractionation lines from Figure 4.37 are marked.

From Table 15, there is generally little chemical variation in the analyzed Spinel grains. From Table 22 to Table 24 in Appendix B and the ratio between σ and average chemistry in Table 15, Ca, Mg, Si, Cr and Na have only minor variation. Al and Fe (plotted in Figure 4.29), as well as Ti show larger variations.

In Figure 4.29 Fe and Al content have a generally positive correlation. Deviating from this correlation is seen in the Clinopyroxenes from 354.35m depth and the Clinopyroxene grain from

329.5m depth. At 354.35m among the most Al poor, and yet also very Fe rich Cpx crystals are found. This is 4 meters below the blue fractionation line from Figure 4.37. At 329.5m the Cpx is slightly Fe enriched and very Al poor. The discrepancy in this thin section is most notable when comparing with the Cpx analyses 4.5m above. 329.5m is only 3m above the purple fractionation line from Figure 4.37.

The Cpx analyses just above the blue line are the most Al and Fe rich in the assembly. These analyses are both in the highest strata of pyroxenite and the deepest part of the dunite body. There is no discernible change in chemistry between the lithological boundary. The dunite Cpx grains appear to have overall decreasing Al and Fe content with decreasing depth. The wehrlite Cpx appear to have similar chemical composition to the shallow dunite Clinopyroxenes. There are seemingly random variations in Cpx chemistry in the pyroxene unit.

4.4 Olivine - Three types

Olivine is the dominant silicate in most of the RF4 drill core. As noted by Tollefsrud (2018), there are three types of Olivine.

The first type of Olivine is very coarse-grained and anhedral. These are cumulate crystals that have highly irregular grain boundaries, make up large aggregates and usually have polychromatic grains with wide, parallel deformation bands. Type 1 has inclusion trails of Chromite or Dolomite+Magnetite+enstatite±CO_2 formed at 750-850°C (Grant et al., 2016, Larsen et al., 2018, Sørensen et al., 2015)

The second type is interstitial, fine grained, monochromatic in x-polarized light and have subhedral to euhedral grain shape. Crystals of this Olivine type is mostly interstitial grains with occasional triple junctions. Olivine of type 2 has low degree of internal deformation. This Olivine type may have formed from Olivine saturated interstitial melt (Grant et al., 2016).

The third type is very fine-grained and is associated with zones of deformation and late magmatic intrusions of dykes.

All three Olivine types can be seen in Figure 4.30. From the thin sections of this study, type 1 can be seen in Figure 4.1 together with type 2; as well as in Figure 9.11 as a prime example. Type 2 Olivine can be seen in Figure 4.1, and Figure 9.7, together with type 3 and in Figure 4.2. Type 3 can be seen between pyroxene crystals in the lower part of Figure 9.18.

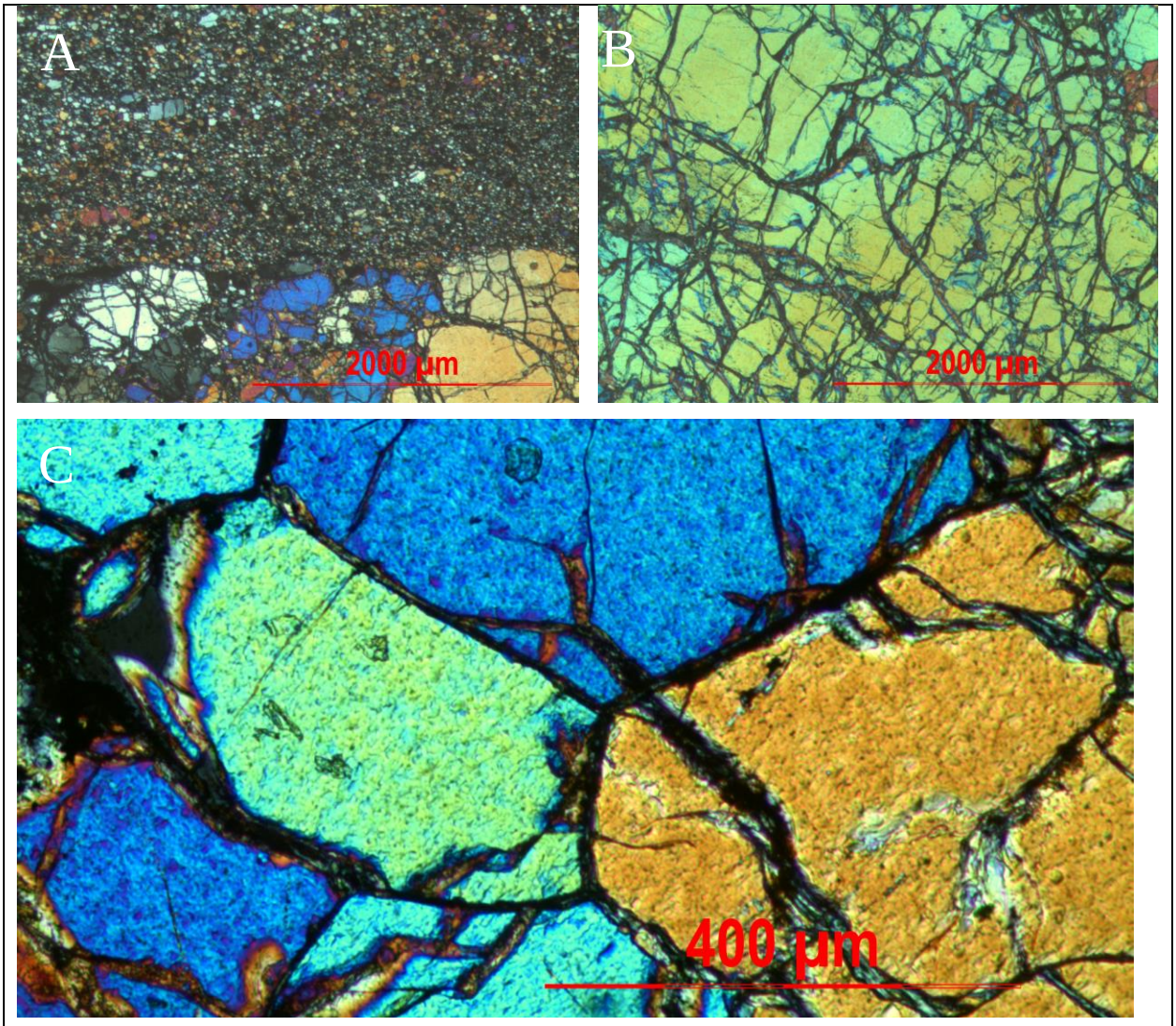

Figure 4.30

Images from Tollefsrud (2018) of the Olivine types from x-polarized transmitted light microscopy

a) Type 3 (small crystals, upper part of image) and type 1 (large crystals in lower part of the picture)

b) Type 1

c) Type 2

4.5 Chemical graphs and diagrams

Chemical bulk rock diagrams of drill core RF3 and RF4 will be presented and compared in this section. In the cases where the chemistry is plotted against drill core depth, the graphs will be described from the bottom and up to accommodate for right-way up gravitational magmatic stratigraphic cumulate deposition.

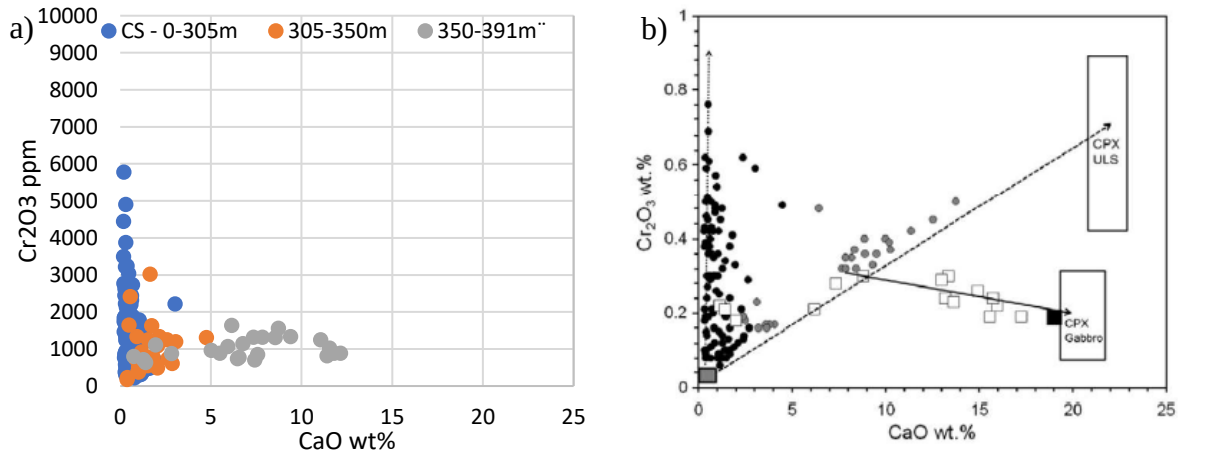

Figure 4.31

Plots of the CaO and Cr_2O_3 in bulk rock concentrations from the data of 2019 (a) and 2016 in the figure by Grant et al. (2016) (b).

Legend for figure b):
Black circles: drill core samples from CS dunite-wehrlite

Grey circles: drill core samples with ULS characteristic

White squares: Drill core samples with MZ characteristic

Black filled square: contaminant composition from Griffin et al. (Griffin, 2013)

Grey square: Olivine compositions.

The Cr vs Ca diagrams in Figure 4.31 show how the MZ pyroxenites (350-391m), CS Dunites and Wehrlites (305-350m) and CS upper dunites and part of the wehrlites (0-305m) plot chemically compared to previous work by Grannes et al. (2016). The 350-391m lithologies plot closer to the CPX Gabbro-line from Grannes' figure than any other trend. The 305-350m interval plot at the bottom of the CS trend from Figure 4.31 b) and the 0-305m interval plots along the complete CS interval in Figure 4.31 b).

4.5.1 Correlating the RF4 and RF3 drill cores

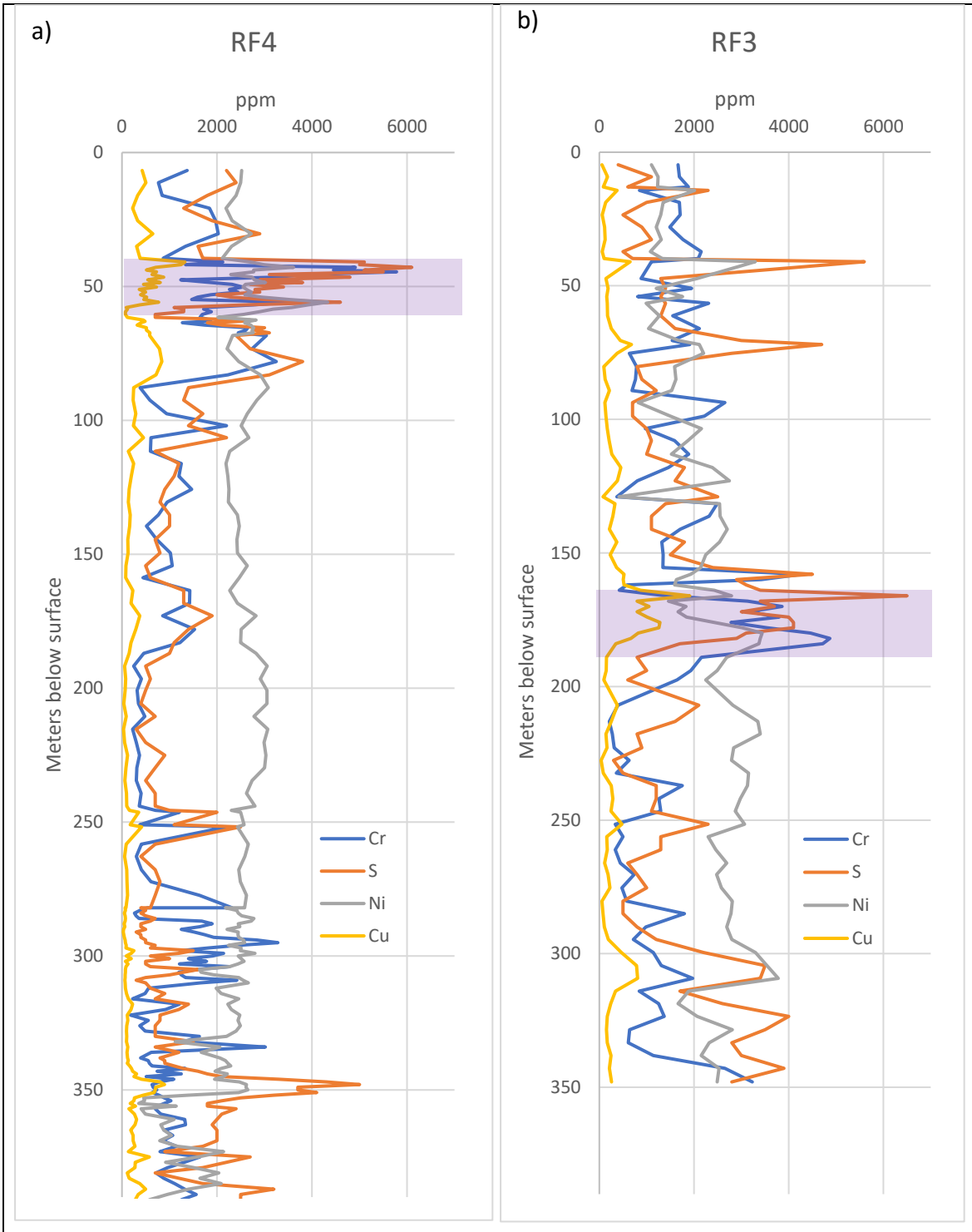

Figure 4.32

Diagrams of the elements Cr, S, Ni and Cu from the drill core RF4 (a) and RF3 (b). In both diagrams a correlating area has been marked with purple.

In the two graphs of Figure 4.32 (a and b) the elements Cr, S, Ni and Cu has been used to correlate the two drill cores RF4 and RF3 (350m further South East). The area marked in purple in both figures stands out in both drill cores, and show the same trends for the various elements. From the top of the purple area, down, there are two narrow main S peaks followed by a wider high S and Cr area. Between the two narrow S peaks, a Cr minimum occurs. Below the deepest narrow S peak, the Ni content stabilize. ca 25 meters below the lower end of the purple area is a wide S peak. The Cu graph has a major peak, followed by a ca 10m area of steadily high Cu levels and a second, smaller peak to mark the edge of the purple area.

The RF3 drill core is displaced by ca 125 meters compared to RF4. Subsequently, deeper areas are only present at depth in the RF4 drill core and shallower rocks are only present in the RF3 drill core.

Figure 4.33 is an edited version of Figure 4.32, where the green area of correspondence and a blue/red area of discrepant chemical signature has been added for RF3 and RF4. The red and blue areas in Figure 4.33 should have corresponding chemical signatures when assuming a gently NE dipping large continuous replaced and cumulate lithology cut by both drill cores. The blue area in Figure 4.33a is characterized by a steady, ca 3000 ppm concentration of Ni, ca equal concentrations of S and Cr between 1000 and 2000 ppm, and a low wide peak in Cu. The red area in Figure 4.33b is characterized by a sudden drop in Ni, a sudden increase in S so the concentration of S is higher than Ni, continuation of the 1000-2000 ppm concentration of Cr and a 800ppm wide peak in Cu. The correlation between Cu and S is very good in RF4 in the blue area and poor in RF3 in the red area. Especially the Ni, S and Cu concentrations are radically different in the blue and red marked areas.

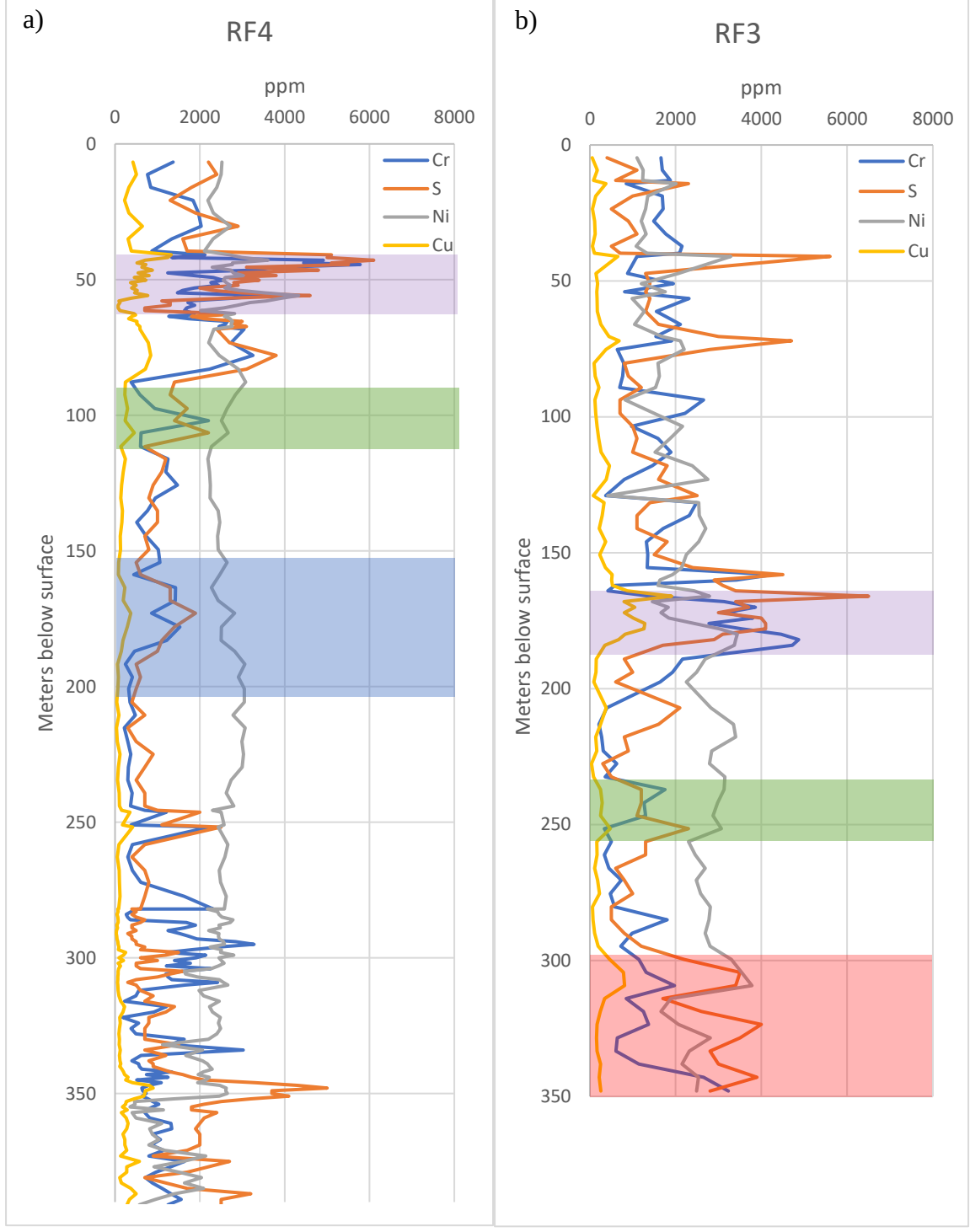

Figure 4.33

Diagrams of the elements Cr, S, Ni and Cu from the drill core RF4 (Figure 4.33 a) and RF3 (Figure 4.33 b). In both diagrams two chemically correlating areas has been marked with purple and green. At depth that should correlate, two not correlating areas have been marked with blue (in Figure 4.33a) and red (in Figure 4.33b).

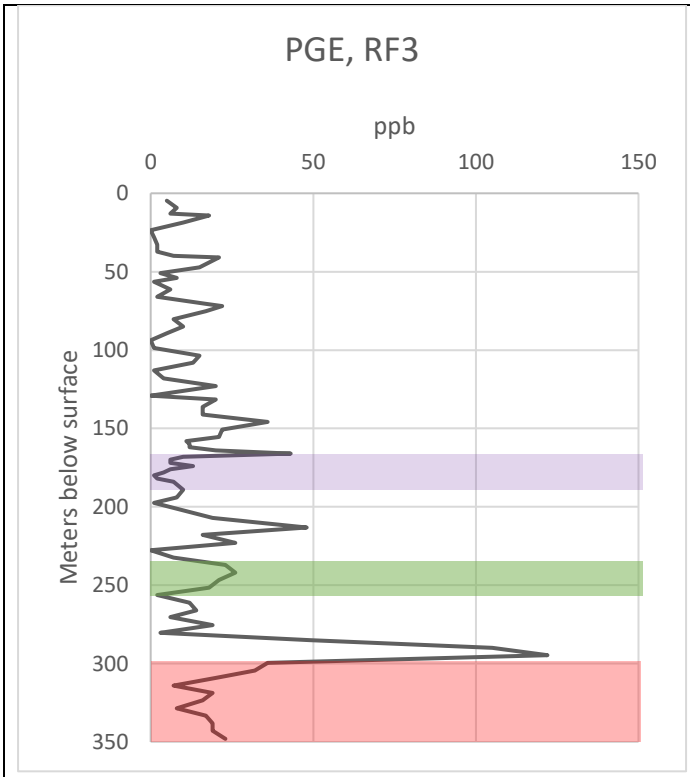

Figure 4.34

The Pt+Pd+Au for the RF3 drill core. The correlating purple and green areas from Figure 4.33 and the non-correlating red area from Figure 4.33 b) have been added.

In the PGE-graph in Figure 4.34 the purple, green and red areas from Figure 4.33 b) are added. The largest PGE anomaly in RF3, 122 ppb, is found just above the red area.

4.5.2 The RF4 drill core – S, Cr, ore forming elements and Ca

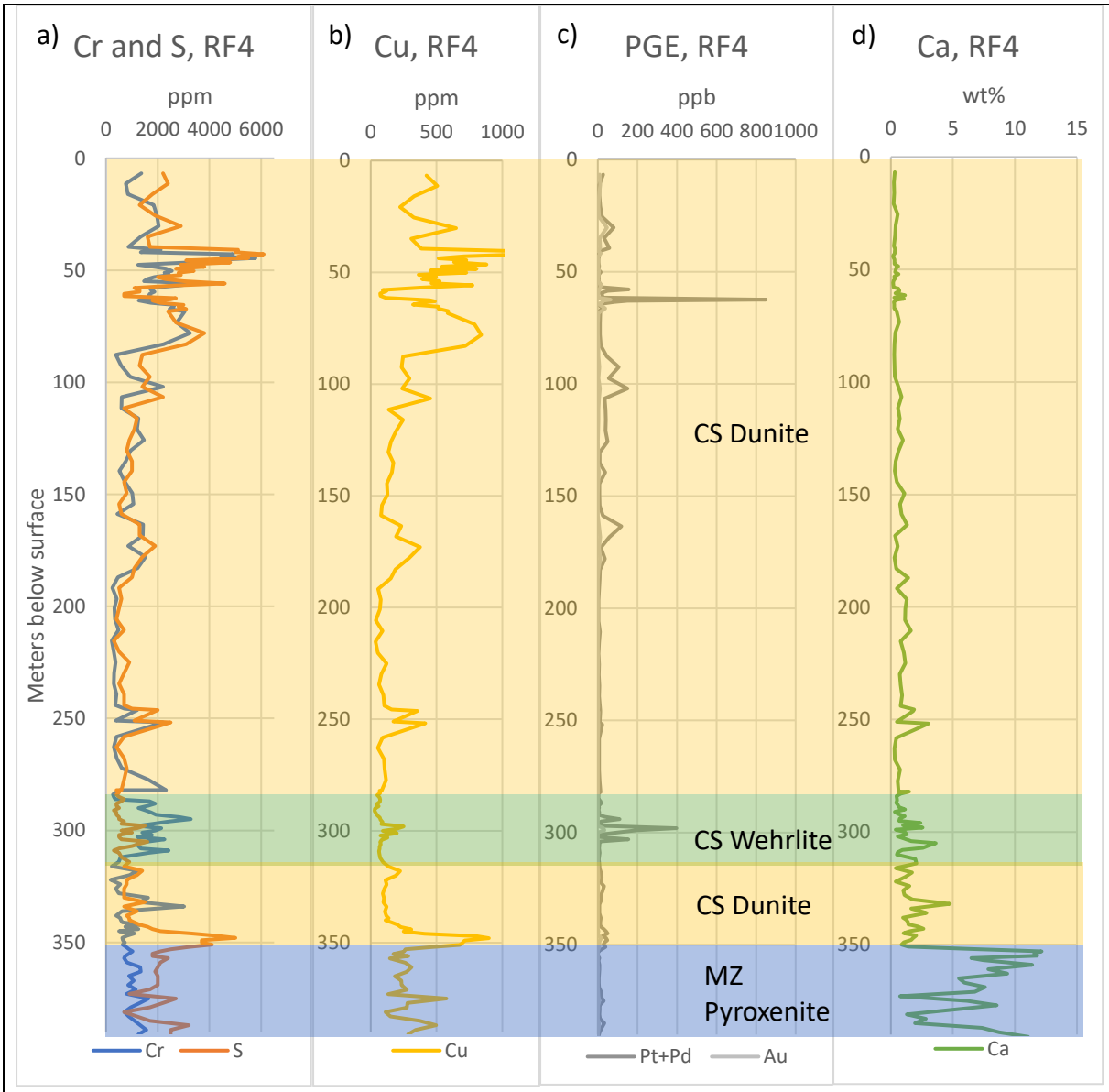

Figure 4.35

Chemical bulk rock diagrams plotted against RF4 drill core depth below surface. The drill core lithologies are color coded where yellow: Central Series Dunite, green: Central Series Wehrlite and blue: Pyroxenite in either the Lower Layered Series or the Marginal Zone. The division by series is from Grannes (Grannes, 2016)

a) Diagrams of the Cr and S concentrations in the RF4 drill core

b) Diagram of the Cu concentration in the RF4 drill core

c) Diagrams of the Pt+Pd and Au concentrations in the RF4 drill core

d) Diagram of the Ca concentration in the RF4 drill core

Figure 4.35 a) shows the peculiar connection between Cr and S in the drill core. Not only do the two graphs correlate almost 1:1, they also have the same concentration of the elements from 0-270m depth in the upper dunite body. Below this, the lithology changes to wehrlite and the correlation between the elements become poorer. In the wehrlite the Cr concentration is higher than S, and the possible correlation around 300m is poor. When the lithology again changes to dunite, the correlation between the elements returns to a good correlation with similar concentrations. Prior to the change into pyroxenite, the S concentration increase drastically while the Cr concentration remain constant and low. S peaks in the transition between dunite and pyroxenite, and then decrease with depths until at ca 365m the S and Cr correlation is again prominent, though with a higher S than Cr concentration. As the depth increase in the pyroxenite, so do the Cr concentration.

The Cu graph in *Figure 4.35* b) has an almost perfect correlation with the S graph.

The Pt+Pd and Au graphs in *Figure 4.35* c) show the same general trends. The concentration of Pt+Pd is systematically higher than the concentration of Au, less so at the top of the drill core. The PGE main peaks are displaced relative to the Cu and S peaks. The main S+Cu peak in the core is at 40 m depth, while the main PGE-reef is located at 60-70 meters depth. The next PGE peaks are at 90 and 100 meters, ca 10 meters above any similar S+Cu peak. Around 300 m there are several closely spaced PGE-reefs. These seem to correlate with small variations in S and Cr, but not well. The second main Cu and S-peak - at the border between the deepest dunite body and pyroxenite at 350 meters - mark a sudden drop in the PGE 5 meters into the pyroxenites. This drop corresponds to the prominent drop observed in both S and Cu. In the pyroxenites, there appear to be a decent correlation between the PGE and the S+Cu graphs.

From *Figure 4.35* d) it can be observed that the Ca content is almost nonexistent throughout the upper dunite body. The same trend is seen in the wehrlite body, though with small variations and a general increase towards the bottom of the unit. In the deepest dunite unit the Ca content is higher and varies with small maximums and minimums. Immediately after entering the pyroxenites the Ca value soars and then fluctuate wildly. The large variations in Ca content in the pyroxenite unit do not appear to correlate with either of the other elements discussed here.

4.5.3 The RF3 drill core – S, Cr, ore forming elements and Ca

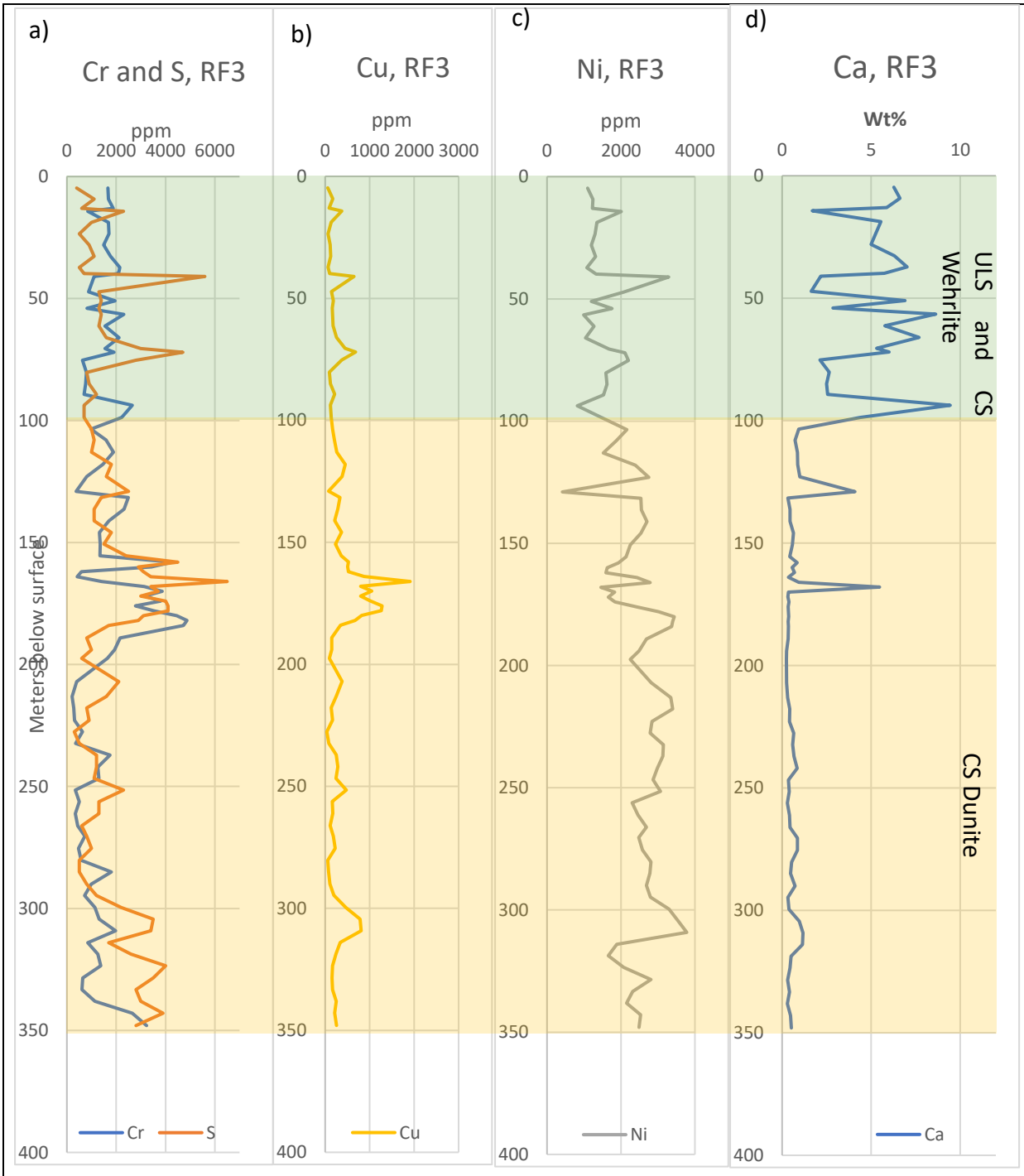

Figure 4.36

Chemical bulk rock diagrams plotting against RF3 drill core depth below surface. The lithologies are color coded. Yellow: Central Series Dunite; and green: Upper Layered Series and Central Series Wehrlite.

a) Graphs depicting the concentration of Cr and S in the RF3 drill core

b) Graph displaying the concentration of Cu in the RF3 drill core

c) Graph depicting the concentration of Ni in the RF3 drill core

d) Graph displaying the concentration of Ca in the RF3 drill core.

The RF3 drill core consists of 100 meters of Upper Layered Series Wehrlite that has probably been eroded from RF4. Below that the same Central Series Dunite body as seen in RF4 makes up the rest of the drill core.

The graph in Figure 4.36 a) shows the degree of correlation between Cr and S in RF3. In the wehrlite the two elements seem to have an opposite correlation: Cr minimums correspond with S maximums. It looks like S is displaced 5-10m relative to Cr.

In the dunite the correlation between the elements also appear poor. The main S peaks at 160m and 170m depth corresponds with first a Cr peak and then a Cr minimum. The S maximum ends with a wider peak at 180m that is followed by an apparently corresponding Cr maximum at 190m. The Cr seems to be partly displaced by ca 10m in this lithology too. From 300m and below the two elements correspond better. The S has a significantly higher concentration in this interval, but the peaks of the two elements coincide.

The graphs of Figure 4.36 a), b) and c) display various ore forming elements (Cu, Ni and S).

In the wehrlite, the ore forming elements Cu, Ni and S all have a good correlation in terms of where the peaks are. The correlation between the elements continue into the dunitic part, though Ni becomes more varied. At 130 m there is a Ni and Cu minimum and S maximum. The main ore peak in RF3 occurs at 160-180m depth. There are 3 S peaks in this area, only 1 Ni peak (Ni actually has minimums corresponding with the two other S peaks), and there are 2 Cu peaks. The correlation here is thus not very accurate, but the general trend that there are significant peaks in the area is prominent among all. After the reef, Ni rise and remain relatively stable until 310 m. In the same section, Cu and S follow the same trends. At 300 meters, the second Cu peak initiates a steep rise in S and a period of three cyclic peaks of both S and Ni with steadily decreasing Ni compared to S. Cu is constant after its peak at 300, and thus has no correlation with the two other ore forming elements.

Moving on to Ca and Figure 4.36 d). In the wehrlittic part of the drill core, ore forming element peaks coincide with Ca minimums. Periods of low ore forming element concentration coincide with periods of high Ca concentration. In the dunite part of the drill core, there are only two Ca peaks; elsewhere the Ca concentration is steadily very low. The first Ca peak in dunite perfectly coincide with the anomalous high S of Figure 4.36 a), low Cu (see Figure 4.36 b) and Ni (Figure 4.36 c) point at 130 m depth. The second Ca peak perfectly coincide with the largest S and Cu peak in the core, the only place in the 160-180 m reef where Ni has a peak. After these two instances, a small bulge in Ca perfectly corresponds with the Cu, Ni and S peak at 310 m.

4.5.4 Fractional crystallization indicators for RF4

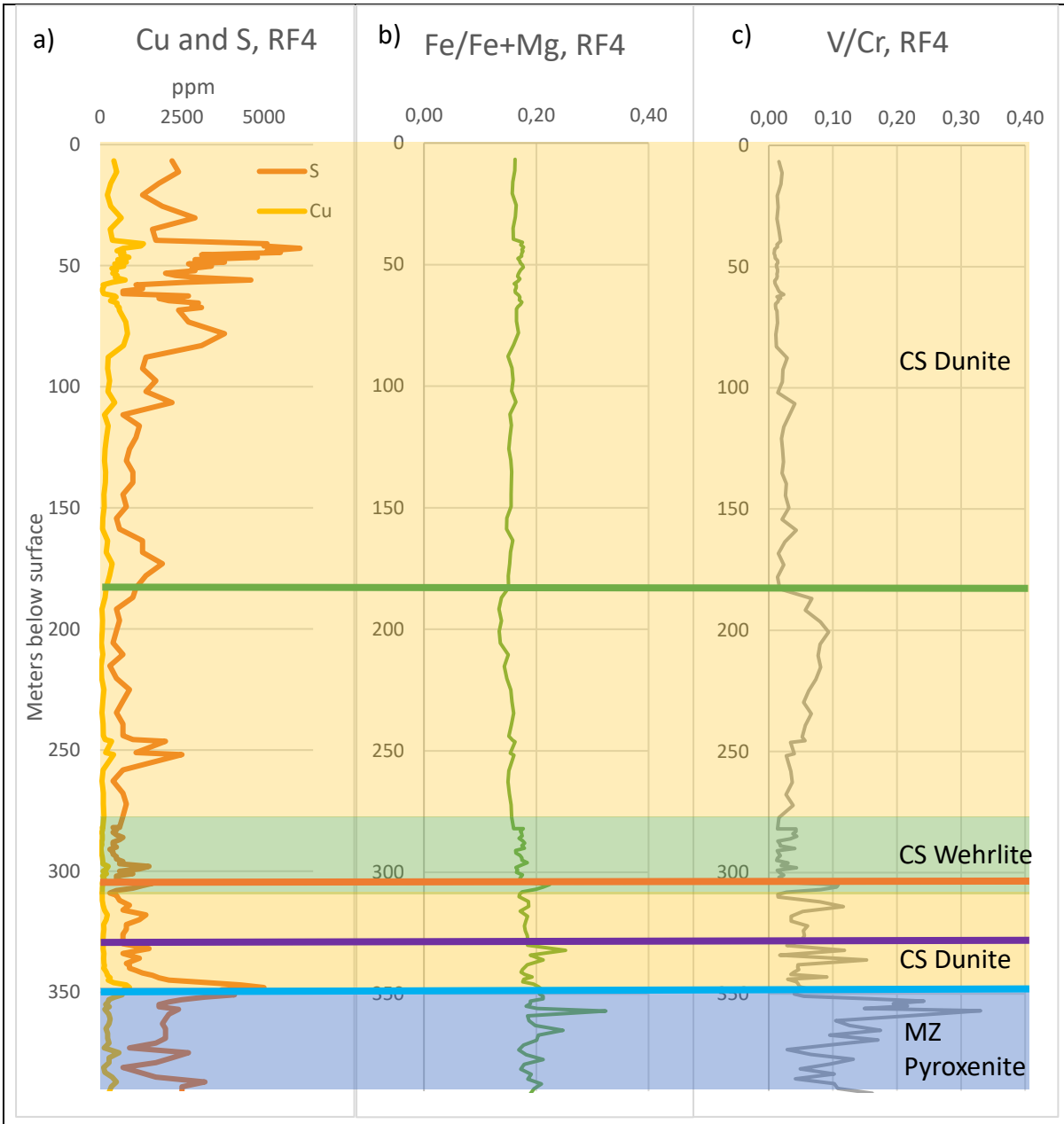

Figure 4.37

Fractionation graphs of RF4. The blue, purple, orange and green fractionation lines indicate significant change in at least one fractionation indicator. The drill core lithologies are color coded where yellow: Central Series Dunite, green: Central Series Wehrlite and blue: Pyroxenite in either the Lower Layered Series or the Marginal Zone. The division by series is from Grannes (Grannes, 2016).

a) Graphs showing the concentrations of Cu and S measured in ppm, of drill core RF4.

b) The graph shows the Fe/(Fe+Mg) ratio of the bulk chemistry in RF4.

c) The graph shows the V/Cr ratio of the bulk chemistry in RF4.

The diagrams in Figure 4.37 display the Cu and S graphs in a logarithmic scale (Figure 4.37 a) and how they correlate with two graphs indicating fractionation (Fe/(Fe+Mg) and V/Cr).The instances of major drops in V/Cr is marked with a blue, purple, orange and green line.

The Fe/(Fe+Mg) graph in Figure 4.37 b) is not a dramatic graph. It has variations around 0,2, most so in the pyroxenite section, less so in the deepest dunite and the wehrlite sections of the drill core. The upper dunite part of the drill core is almost perfectly constant at 0.16 with no significant variations. The major drops in Fe/(Fe+Mg) do in the case of the purple and orange lines correlate perfectly with the drops observed in the V/Cr graph. The purple line is placed mostly based on the Fe/(Fe+Mg) ratio. In the pyroxenite this correlation is more dubious. From 390m to 360m there is a trend of increasing Fe/(Fe+Mg) with large local variations. The large drop in Fe/(Fe+Mg) occurs at 360m, 5-10m before it follows the V/Cr ratio. There is a distinct and dramatic drop of the V/Cr graph at the same depth as the large Fe/(Fe+Mg) drop, but the V/Cr ratio increase above it while the Fe/(Fe+Mg) ratio remain low.

The Fe/(Fe+Mg) graph shows no noteworthy change at the green line.

The V/Cr graph in Figure 4.37 c) has large variations both between lithologies and inside a single, seemingly continuous lithological unit. Beginning at the bottom, the V/Cr ratio begins low and then increase (although with local maximums and minimums) to its maximum 10 meters prior to the lithological change into dunite, after which it plummets to 0,05. In the lowermost dunite unit there are large local variations in the V/Cr ratio, but no obvious increasing or decreasing trends. The highest of the frequent V/Cr variations observed is 5 meters into the wehrlite segment, marked by the orange line. In the rest of the wehrlite segment, the V/Cr ratio is lower than the lowest recorded in both dunite and pyroxenite. Small variations occur. The trend is however stable around 0,025. As the lithologies change to the upper dunite body, the V/Cr ratio slowly increase until it reaches a wide peak at 200 meters depth. The ratio then gradually declines over 20 meters until it reaches 0.02. From 180 m depth to the surface, the V/Cr ratio is constant at 0.02.

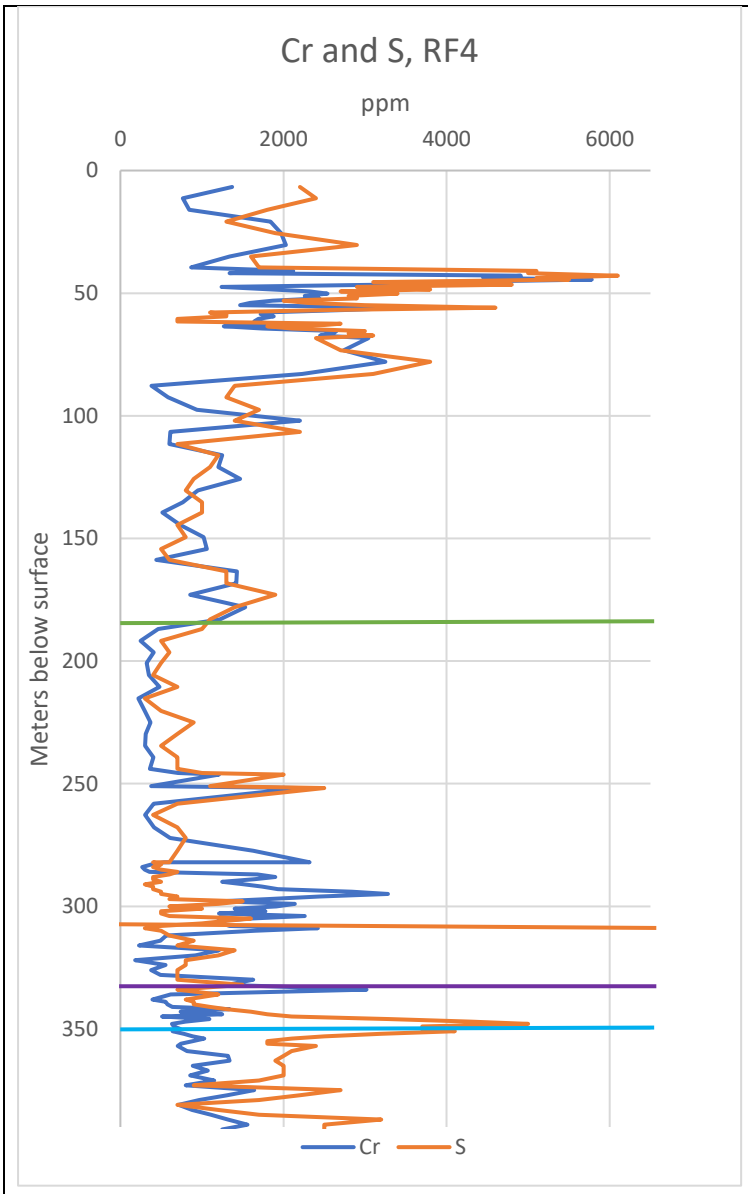

Figure 4.38

The green, orange, purple and blue fractionation lines marked in Figure 4.37 overprinted onto a diagram of Cr and S in the RF4 drill core.

The blue, green, orange and purple lines from Figure 4.37 are marked in the Cr and S diagram as seen in Figure 4.38. How the lines correspond with changes in the chemistry will be described from the lowermost parts and upward.

The blue line - marking the minimum point after the largest peak in the drill core - perfectly matches the S-peak in the transition between LLS or MZ pyroxenite and CS dunite. From 391 to

350m, the Cr concentration gradually decline. This is also seen in the increasing V/Cr ratio for the same interval in Figure 4.37 c).

Before the purple line, S and Cr were both present but at relatively low and equal concentrations. After the purple line – in the middle of the deepest CS dunite unit – there is a significant Cr peak without a characteristic corresponding S peak.

The orange line does not appear to correlate with any significant change in either Cr or S in Figure 4.38.

The green line, which marks return to a V/Cr ratio at a constant 0.02 (very low) after a steady increase and wide peak from Figure 4.37, do not appear to coincide with a change in either S or Cr in the cumulate rocks in Figure 4.38.

4.5.4.1 Ni and fractionation in RF4

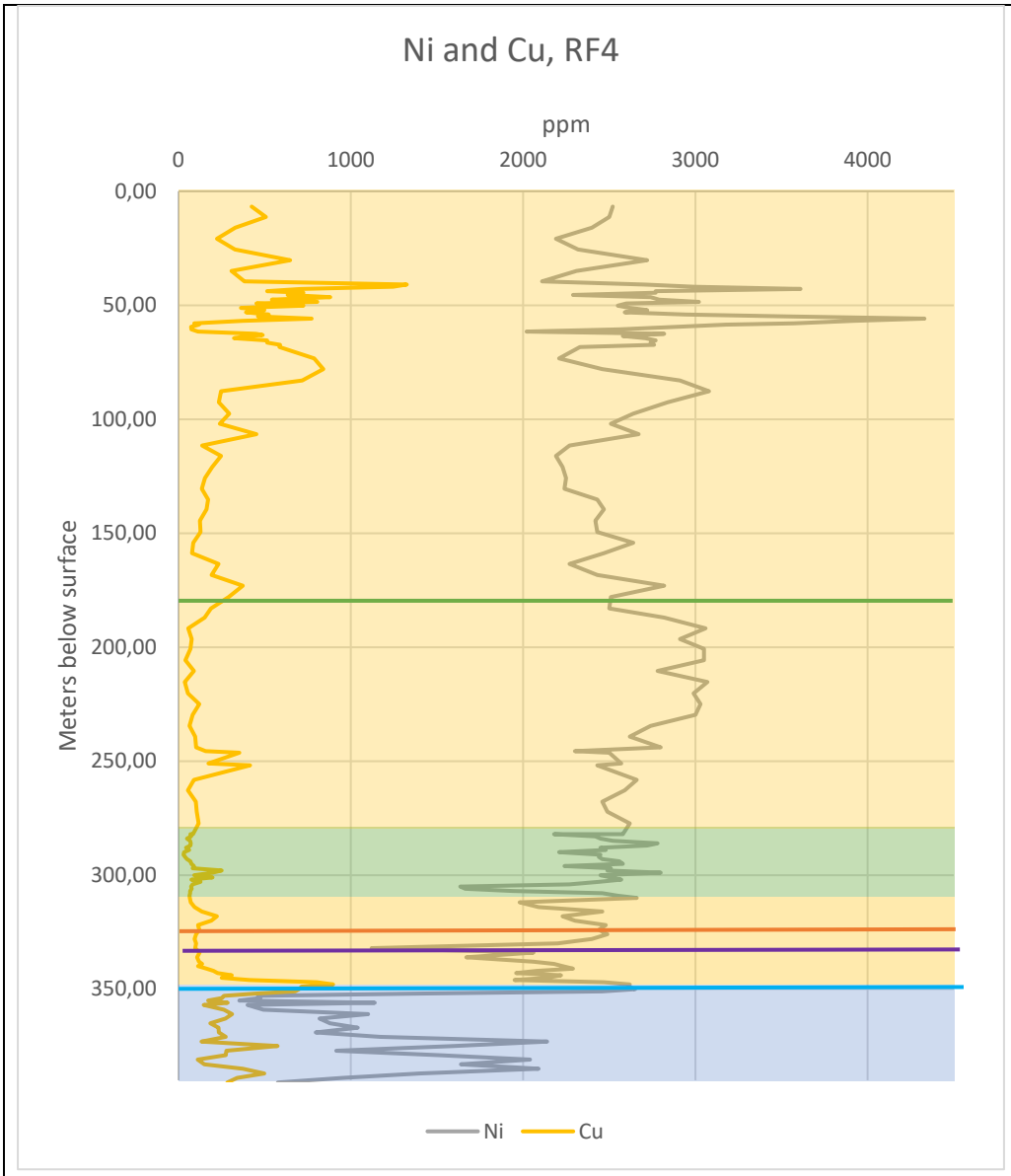

Figure 4.39

Diagram depicting how the Ni and Cu concentrations of the RF4 drill core correlate with the green, orange, purple and blue fractionation lines from Figure 4.37.

Figure 5.8 shows how Ni and Cu behave relative to the colored markers noting significant changes in V/Cr. It will be presented from deepest and upwards.

The Ni concentration sinks from 391m to 360m where it reaches its minimum. After the minimum value there is a dramatic increase in Ni culminating in a local maximum corresponding with the blue line and a Cu peak.

From the blue line into the deepest dunite unit, the Ni again gradually decrease until it reaches a local minimum at 330m. Then comes another abrupt increase in Ni concentration without any increase in Cu. This Ni minimum followed by a sudden increase in concentration perfectly correlate with the purple line. In the upper part of the deepest dunite unit, two phenomena are observed. The first being a gradual decrease in Ni. The second being that this gradual decrease occur in wobbles, and that the peaks of these wobbles are constantly at Ni = 2500 ppm. The bottoms of the wobbles make a perfect linear decrease until the orange fractionation line is reached. Then the wobbling ceases, and a varying, yet more or less constant Ni and Cu level is reached. The Ni remain relatively constant and have a 50m wide peak between 240-190m. The peak ends at the green line. Below the green line, there has is a poor correlation of Ni and Cu peaks. From 130m there is a better correlation, but not good.

4.5.5 Fractional crystallization indicators for RF3

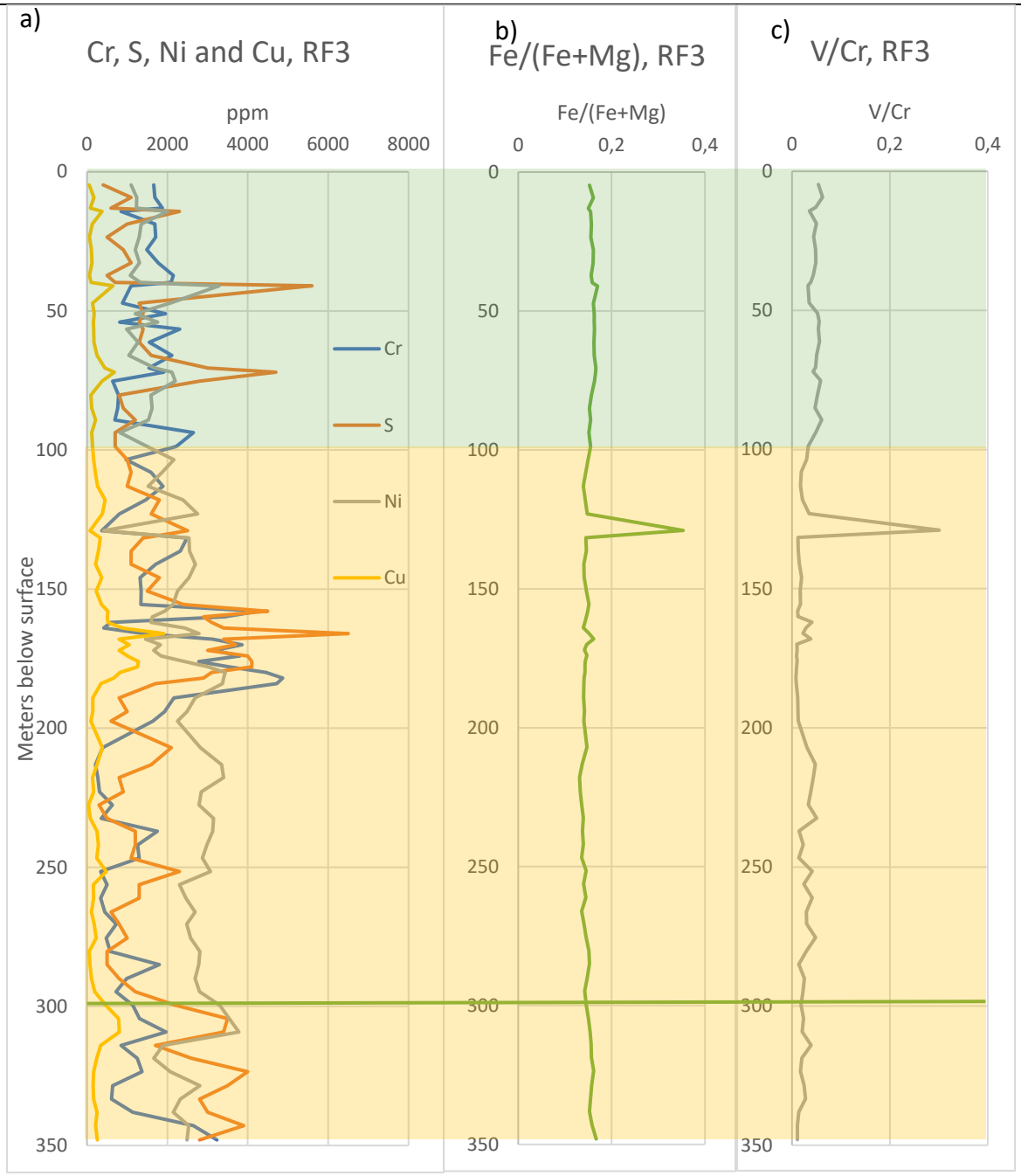

Figure 4.40

Chemical and fractionation indicator diagrams are marked with the green fractionation line from Figure 4.37, using the indicator of displacement from Figure 4.32, and color coded lithologies.

a) Graphs of the concentrations of Cr, S, Ni and Cu in the RF3 drill core

b) Graph of the Fe/(Fe+Mg) ratio in the RF3 drill core, where Fe and Mg are molar proportions

c) Graph of the V/Cr ratio in the RF3 drill core

The graphs in Figure 4.40 display how the RF3 drill core and its ore elements behave using the same V/Cr and Fe/(Fe+Mg) ratios as is used to indicate fractionation in RF4. The V/Cr plot is generally quite stable around 0,02-0,04 in the dunite segment of the core except for a very large peak at 130 meters depth followed by a sharp drop. The Fe/(Fe+Mg) ratio in Figure 4.40 b) shows the same pattern.

The ore forming elements in Figure 4.40 a) show a decrease in Cr, Ni and Cu yet an increase in S occurs at 135m. Above the peak the V/Cr and Fe/(Fe+Mg) return to their former normal values.

Only the green line from RF4 is visible in the RF3 depth interval (Figure 4.40). Above the green line, there is a large segment where the Ni concentration is substantially higher than the concentration of S in the cumulates. The green line mark where the S-graph increase to not only catch up with the Ni concentration, but surpass it as Ni decrease at 315 m. Cr and S has a good correlation below the green line. Above the green line, the concentrations of S and Cr is comparable. Below the green line, the concentration of S is around double of the concentration of Cr. Cu is not correlated with S below the green line.

4.5.6 Fractional crystallization in RF1 and RF2

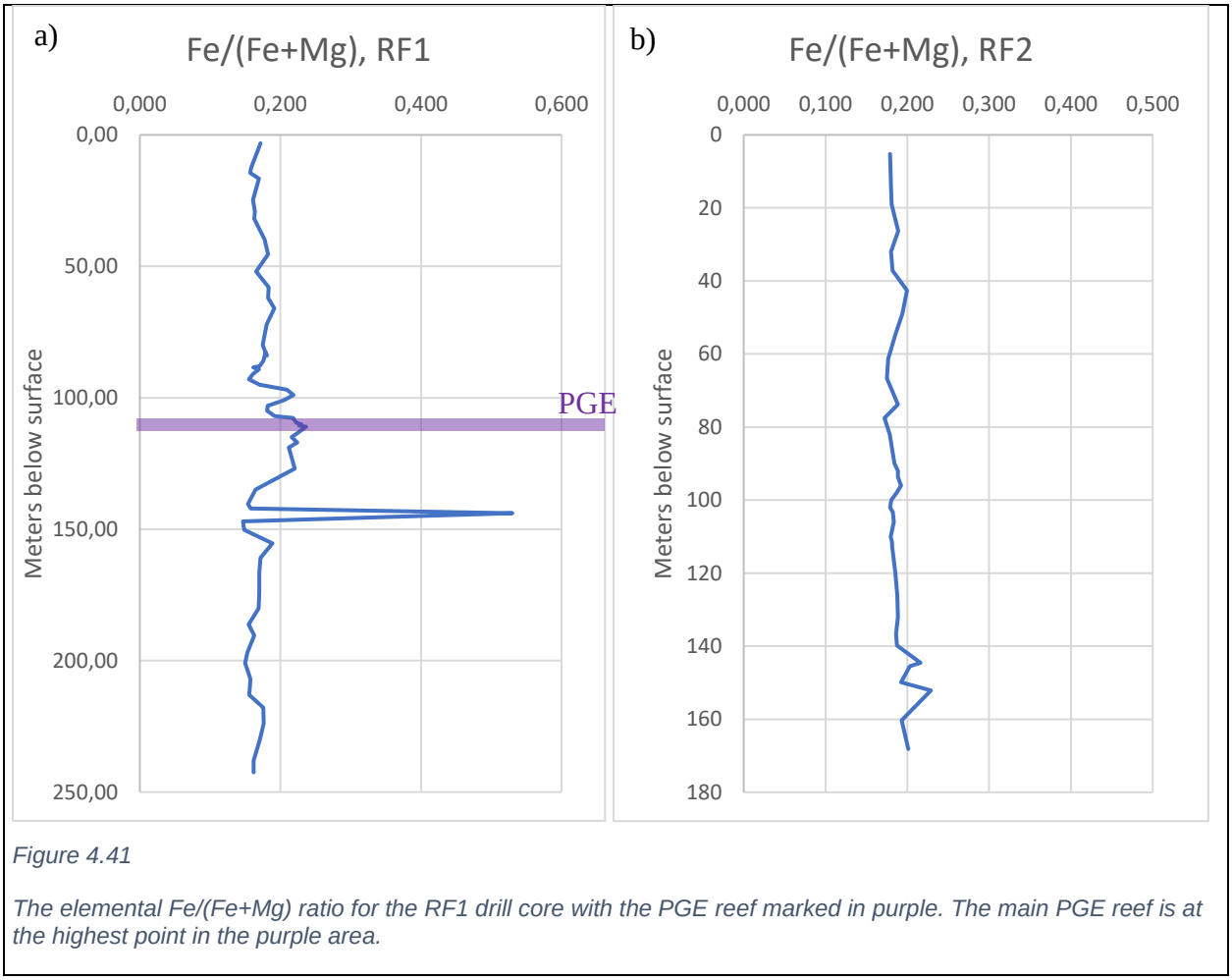

Figure 4.41

The elemental Fe/(Fe+Mg) ratio for the RF1 drill core with the PGE reef marked in purple. The main PGE reef is at the highest point in the purple area.

The Fe/(Fe+Mg) ratio for RF1 and RF2 can be seen in Figure 4.41. RF2 has very low degree of fractional crystallization according to the Fe-number in Figure 4.41 b). The ratio is ca 0.2 in the 168-140m interval. The ratio stabilize at a constant 0.18 above 140m. RF1 has larger variations in the fractionation indicator in Figure 4.41 a). The fractionation indicator wobbles up to 150m depth. At 150m there is a local minimum followed by a leap in fractionation ratio that returns to a low value in the next measurement. Above the highly evolved peak, a gradual increase in Fe/(Fe+Mg) continues until the PGE reef marked in purple. Above the PGE reef is a local minimum followed by a small peak and return to the wobbling low fractionation values from the bottom of the drill core.

4.5.7 Fractionation vs. elements in RF4

In the following section, various diagrams will be presented on how different elements plot compared to the fractionation indicator V/Cr in the RF4 drill core.

4.5.7.1 Mn vs. V/Cr

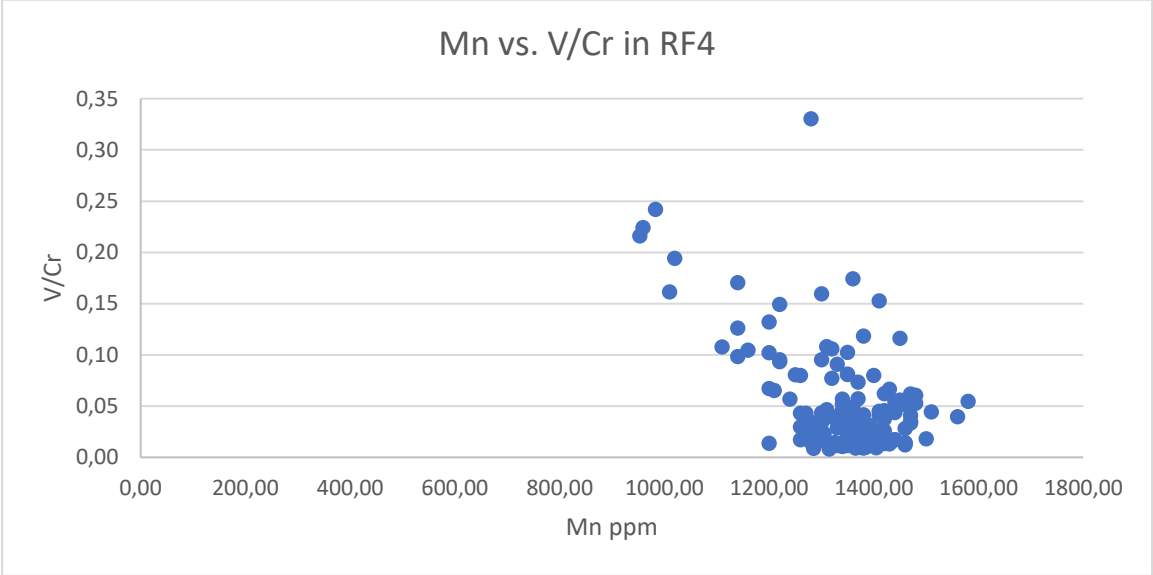

Figure 4.42

Scatterplot of the Mn concentration and V/Cr ratio of samples at varying depths in the RF4 drill core.

The scatterplot in Figure 4.42 show Mn plots compared to the V/Cr fractionation ratio. With increased degree of fractionation (increased V/Cr), the Mn concentration decrease in the cumulates, however this is not a strong correlation since most of the data points clusters at one end of the pattern. Most of the cumulates have a low fractionation ratio and Mn concentration of ca 1400 ppm.

4.5.7.2 Ni vs. V/Cr

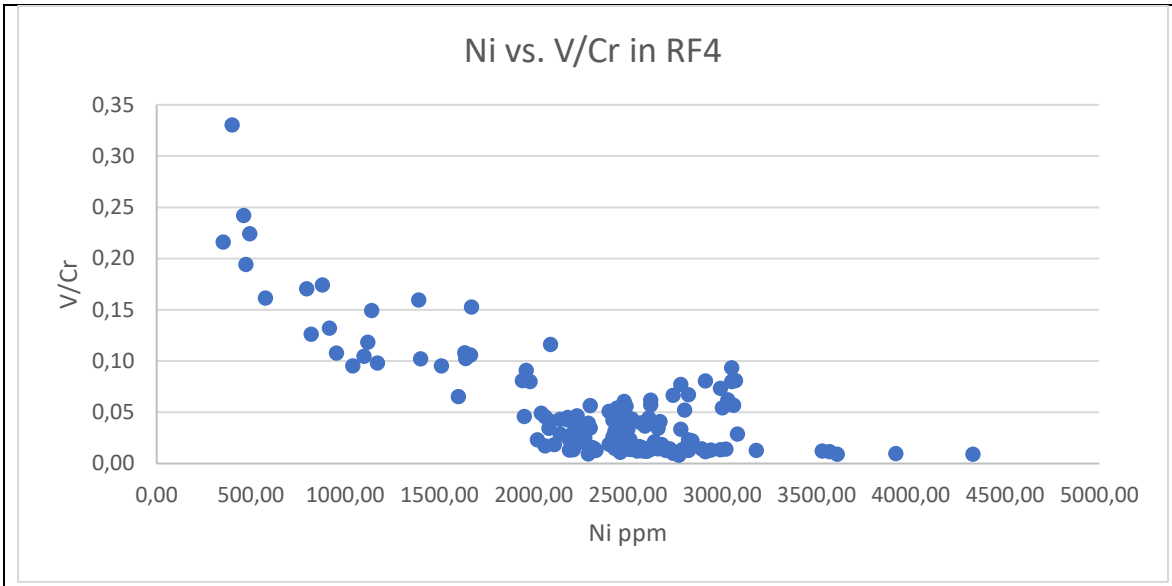

Figure 4.43

Scatterplot of the Ni concentration and V/Cr ratio for samples at varying depths in the RF4 drill core.

The concentration of Ni in the cumulates decrease with increasing fractionation (see Figure 4.43). Most of the cumulate samples have between 2000 and 3000 ppm Ni. In the 2000-3000 ppm Ni and 0.025-0.1 V/Cr ratio interval there is a distinct opposite trend where Ni increase with increasing V/Cr. This is probably caused by the samples of the 280-180m interval, ending with the green line in Figure 4.37 and Figure 4.39. As seen in both chemical plots, both Ni and V/Cr have a very wide and low peak in that interval.

4.5.8 Al, Na+K and Ca

Al and the alkali elements Na and K are found mainly in pyroxene, particularly Clinopyroxene, and Amphibole in the cumulates (Tollefsrud, 2018), while Ca is mainly found in Clinopyroxene. Al also has a significant concentration in the type 1 Spinels. Plagioclase, a mineral that would contain significant amounts of Al, Na, K and Ca, is almost never found in the RF4 drill core (Grannes, 2016, Nikolaisen, 2016, Tollefsrud, 2018). There are occasional Amphibole crystals in RF4 (Tollefsrud, 2018, Nikolaisen, 2016).

RF3 has not been as extensively studied in thin sections as RF4, so it is assumed that these observations are also true for RF3.

4.5.8.1 Al, Na+K and Ca in RF4

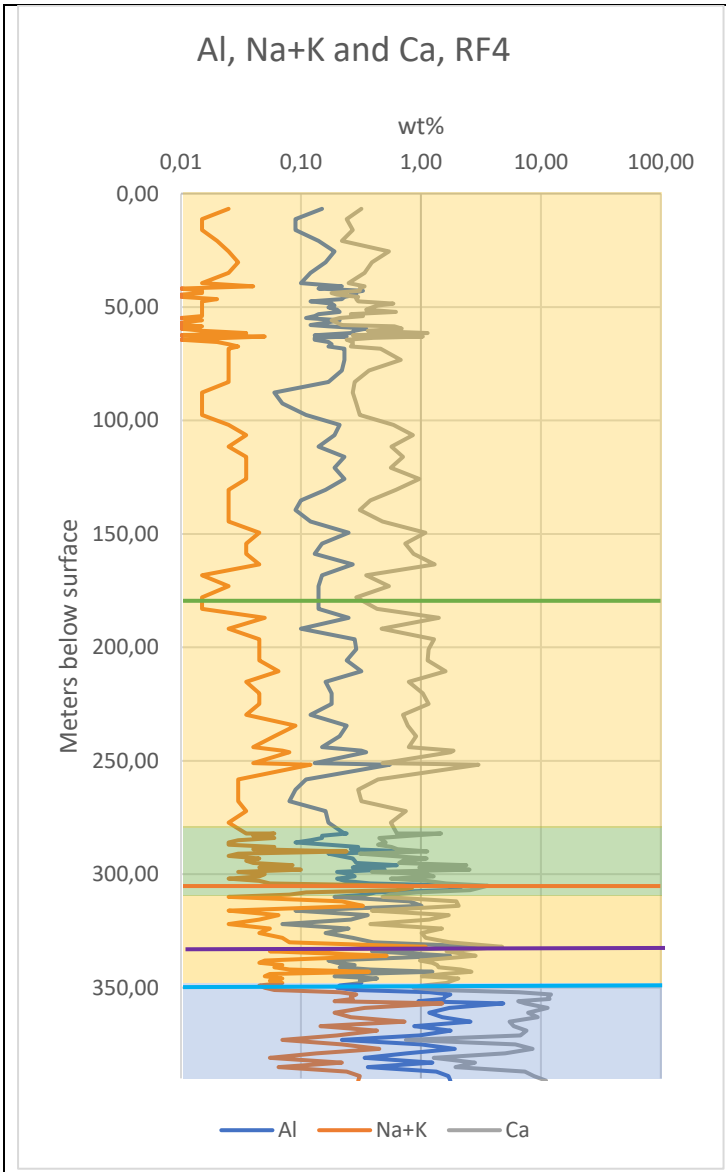

Figure 4.44

Bulk rock concentration of Al, Na+K and Ca in the RF4 drill core, plotted with a logarithmic scale. Fractionation lines are added and lithologies are color coded.

Figure 4.44 visualizes how Al, Na+K and Ca vary in the RF4 drill core with a logarithmic scale

The three elements have a very good correlation throughout the drill core. The relative proportions of each elements vary somewhat; there is for example less Al between 200 and 250 m, while Na+K

has a higher relative concentration in this segment than in the rest. In the segment 300-360 it is difficult to compare the relative quantities as they vary greatly with local minimums and maximums in the section. The peaks, however, follow each other with great accuracy for all three elements. When one element has a local minimum, so do the two other graphs.

4.5.8.2 Al, Na+K and Ca in RF3

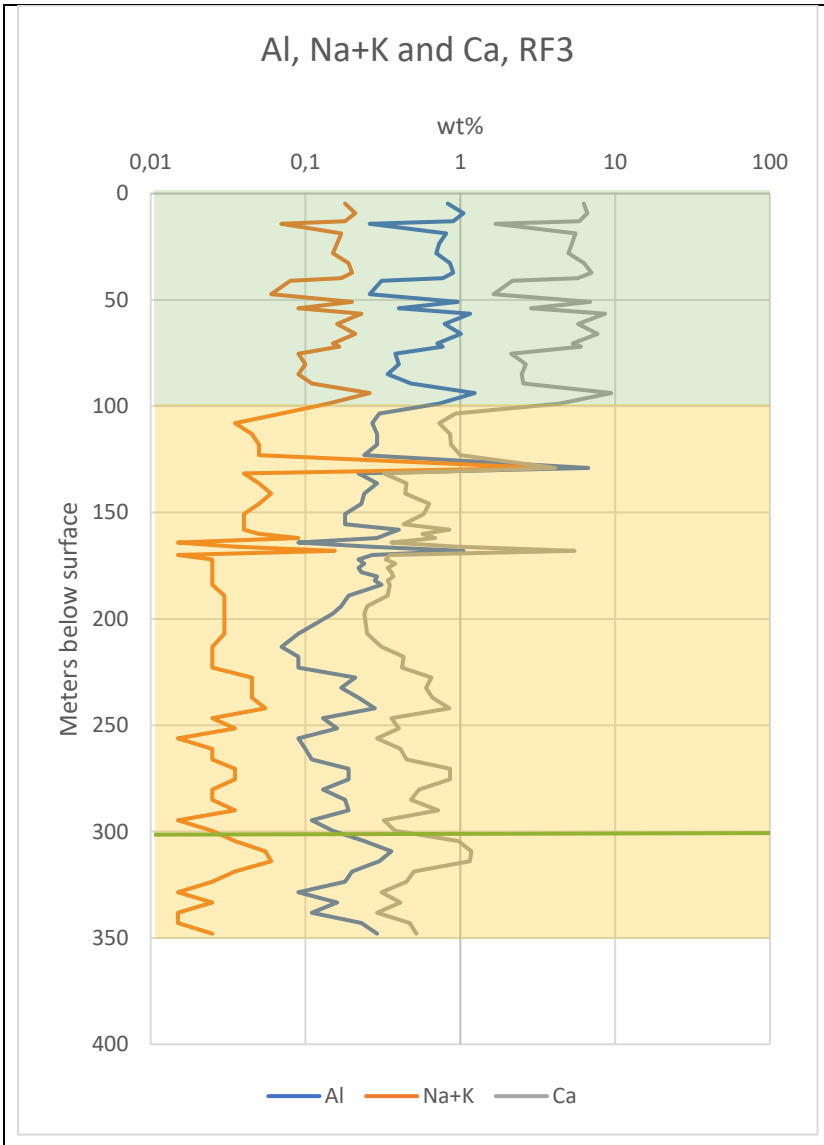

Figure 4.45

Bulk rock concentration of Al, Na+K and Ca in the RF3 drill core plotted with logarithmic scale.

The weight percent of Al, the alkali elements Na and K and Ca are plotted against depth with a logarithmic scale in Figure 4.45. The three graphs generally follow each other so that the peaks occur at the same depths. Between 130 and 230 m the Ca content is lower relative to Al and Na+K than in the rest of the drill core. In this same section the elements have a lower correlation than in the rest of RF3. Na+K has a peak equaling the concentration of Ca at 130 m and more abrupt changes than what is observed in Al and Ca for the rest of the period. Al has an area of decreasing concentration between 190 and 230 m while both the other graphs are constant in that interval.

4.5.9 Sulfide ore elements – Ni trend

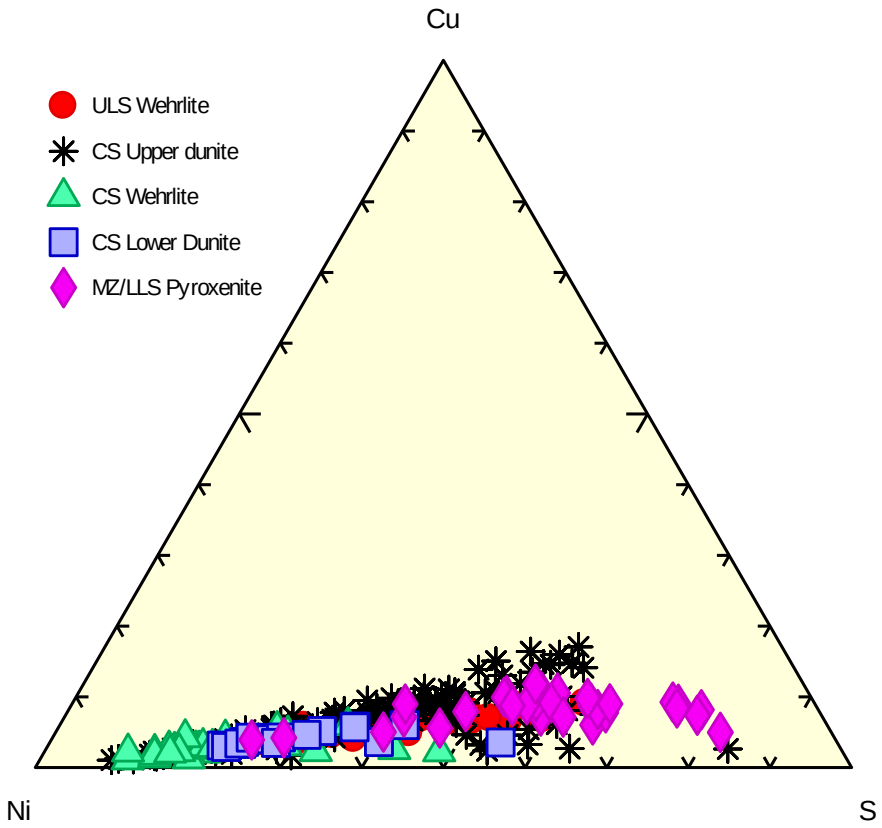

Figure 4.46

Ternary diagram of the bulk concentrations of Ni, S and Cu, all measured in ppm, in the RF4 and RF3 drill core. The lithologies as described in section 4.5.2 and 4.5.3.

Figure 4.46 shows how the RF4 and RF3 rocks plot with regards to Ni, Cu and S content, all measured in ppm, in a ternary diagram. This is the only system where there is a clear trend in the bulk Ni concentrations compared to the other main bulk sulfide elements. The cumulates with a high Ni content has a very low S and Cu content. As the Ni content decrease, the S and Cu content increase. This continues until a critical point is reached and decrease in Ni gives a decrease in Cu and increase in S. Only few rocks from the Pyroxene and one lithology from the upper dunite body have rocks with this anomalous bulk rock composition. All rocks from RF3 plot along the main trend. The CS Wehrlites are on average the most Ni rich and Cu poor lithology. CS Upper Dunite (present in both RF3 and RF4) has the most Ni rich sample but a wide spread with average values in the middle between the S and Ni endmembers. CS Lower Dunite has a Ni rich, S poor composition. ULS Wehrlite has almost the same average composition as CS Upper Dunite, though the Wehrlite contains less Cu than the dunite. The MZ Pyroxenite has a greatly varied composition with similar Cu as CS Upper Dunite.

4.5.10 PGE

4.5.10.1 PGE in the reefs of Reinfjord

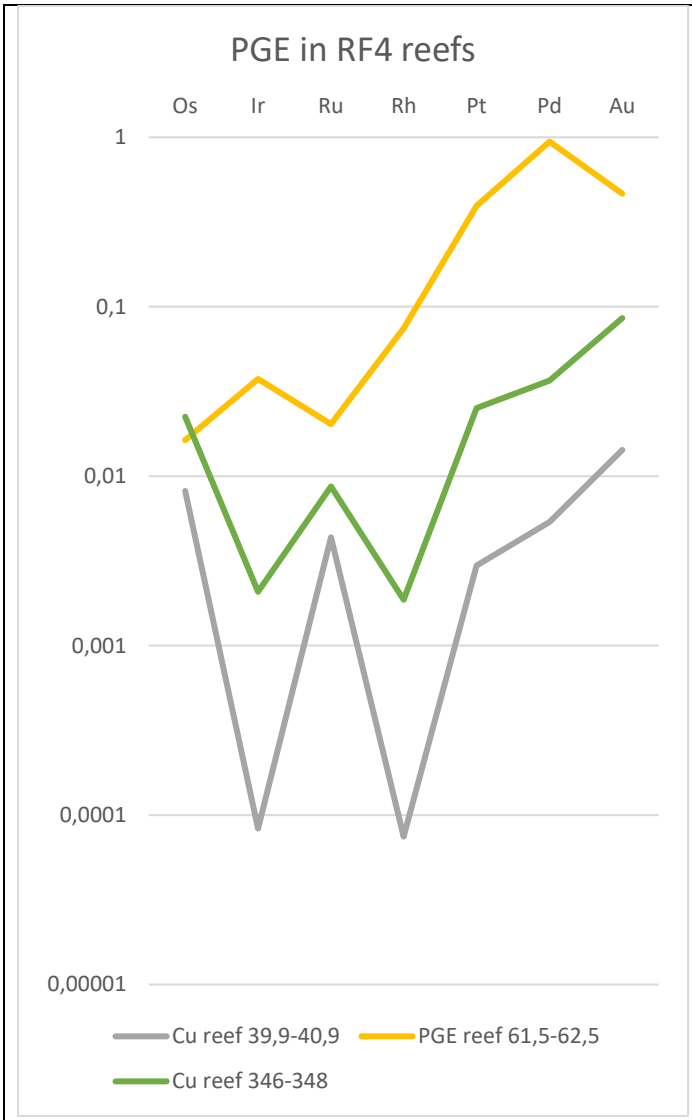

Figure 4.47

Chondrite normalized PGE + Au signature for the two major Cu-reefs and the main PGE-reef in RF4.

The two Cu-reefs in Figure 4.47 share the same PGE trend, but the Cu-reef at 39,9-40,9m has significantly lower PGE concentrations than the Cu-reef at 346-348m. The difference is greatest for Ir, Rh, Pt, Pd and Au and smallest for Os and Ru. The PGE-reef in Figure 4.47 has similar Os concentration as the two Cu-reefs, slightly higher Ru concentration than the Cu-reefs and otherwise significantly higher concentrations of all PGE+Au. Excepting Ru and Au, the PGE-reef

graph shows an increasing trend. The Cu reefs are more depleted in Ir and Rh than the primitive and depleted mantle in Figure 2.10. They have similar concentrations of Os and Ru, and are enriched in Pt, Pd and Au. The PGE reef in RF4 is enriched in all PGE+Au compared to primitive or depleted mantle.

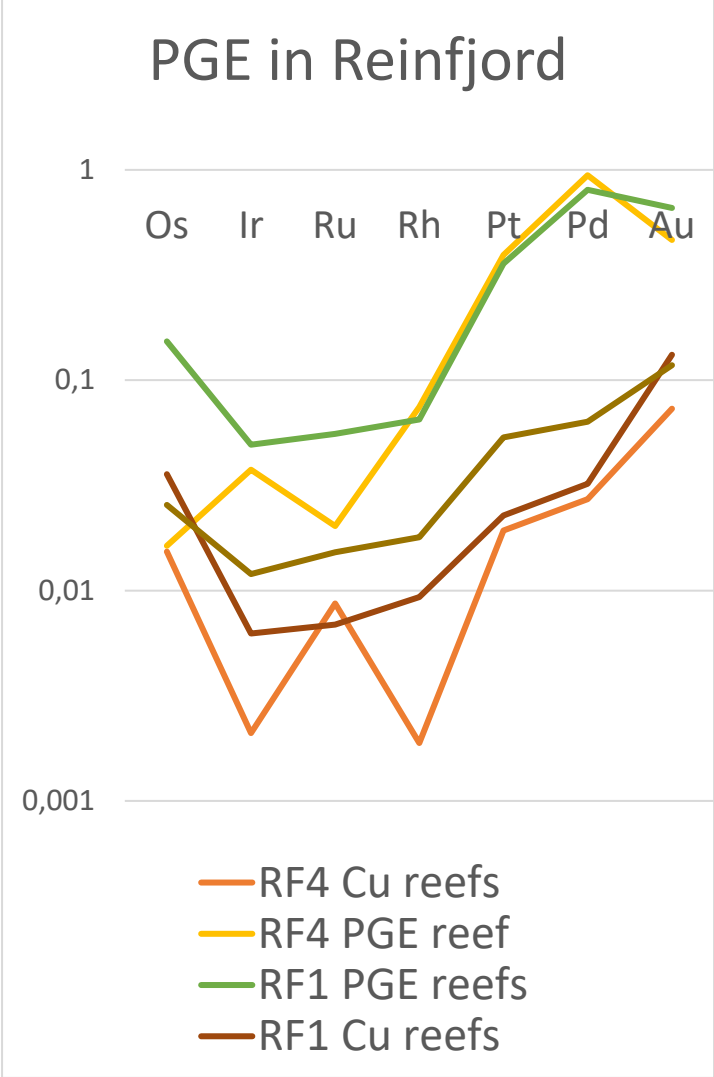

Figure 4.48

The average chondrite normalized PGE + Au signatures of the bulk rock chemistries for PGE and Cu-reefs of the RF4, RF2 and RF1 drill cores.

Figure 4.48 features the various PGE + Au distribution in the Reinfjord PGE and Cu-reefs. All the elements were normalized to chondrite concentrations.

The Cu-reefs from RF1 and RF2 are very similar, having a negative Ir, Ru and Rh anomalies and positive Os, Pt, Pd and Au anomalies. All PGE are more enriched in the RF1 and RF2 reefs than in primitive or depleted mantle from Figure 2.10. The average Cu-reef from RF4 (see Figure 4.47 for individual PGE for the Cu-reefs) follows much the same trend as RF1.

Ru do not follow the trend. Ru is higher in the RF4 Cu-reef than the RF1 Cu-reefs and lower than the RF2 Cu-reefs. The RF4 Cu-reefs has a slightly lower Pt, Pd and Au concentration than the reefs from RF1 and RF2.

The PGE-reef from RF4 is significantly different from the PGE-reefs of RF1 for the elements Os and Ru - and to a lesser degree - Ir; The IPGE. The PGE-reefs of RF1 has the same general graph shape as the Cu-reefs of RF1 and RF2 (except for Au), only with systematically higher concentrations. The PGE-reef of RF4 do not share this shape for the IPGE. The Os concentration of the PGE-reef in RF4 is actually the same as in the Cu-reefs. The Ir concentration is marginally smaller than in the PGE-reefs of RF1. The Ru concentration is significantly lower than in the RF1 PGE-reefs. It looks like some of the Ru are found in the Cu-reefs rather than in the PGE-reefs in RF4. This feature is prominent in both the graphs of RF4 and not the other drill cores. The Rh, Pt and Pd concentrations are all very similar to those of the PGE-reefs of RF1. The Au in RF4 has a more significant drop compared to that measured in the RF1 PGE-reefs.

Most of the Cu-reef concentrations are between 0.7-6% of chondrite PGE concentration in the RUC. The PGE-reefs of the RUC lie between 2-15% of chondrite IPGE concentrations and between 65-94% PPGE of chondrite concentrations. The Au concentration in the Reinfjord Cu-reefs are between 7-13% of chondrite value. The Au concentration in the Reinfjord PGE-reefs are between 46-66% of chondrite concentration.

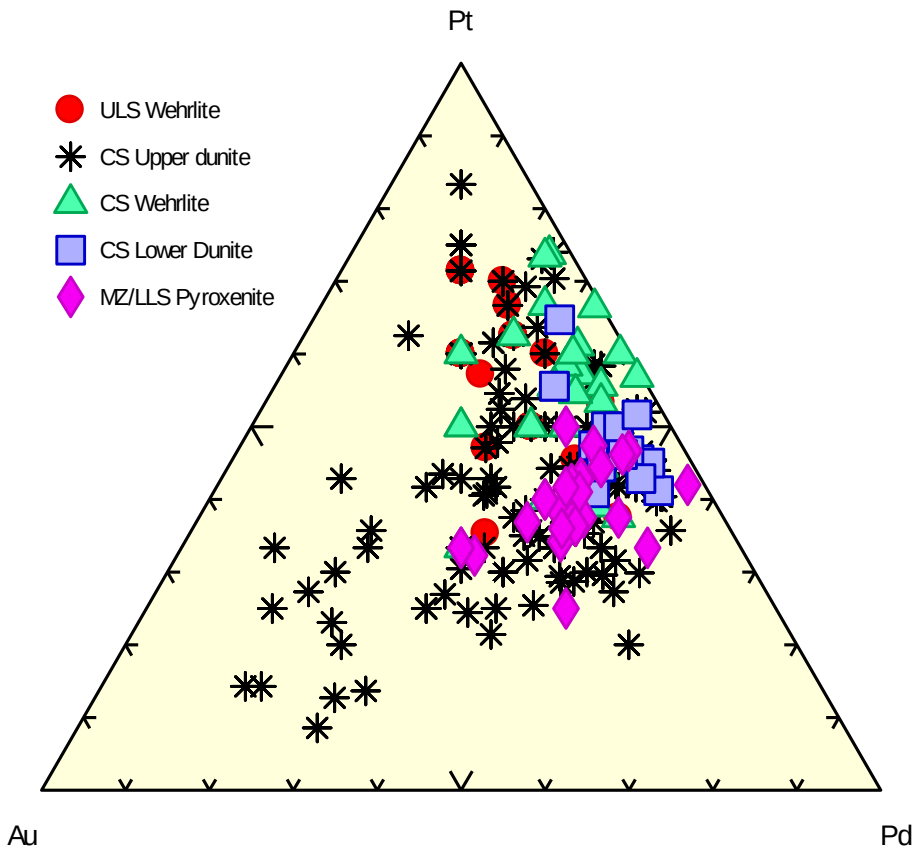

Figure 4.49

Trigonal diagram of the PGE Au, Pt and Pd from the bulk rock data of RF3 and RF4. Lithologies are as described in section 4.5.2 and 4.5.3.

The ternary Pt-Pd-Au diagram in Figure 4.49 roughly shows the bulk rock PGE signatures for the entire RF3 and RF4 drill cores. The ULS Wehrlite, CS Wehrlite and CS Lower Dunite have similar PGE compositions; with low Au and slightly more Pt than Pd. The CS Lower Dunite has a higher Pd content than the two others. The MZ/LLS Pyroxenite has a higher Pd than Pt content with low to moderate levels of Au. The CS Upper Dunite has a great variation in PGE compositions. The most Pd rich composition, the most Au rich composition and the most Pt rich composition all are within this lithology. Most of the CS Upper Dunite plots in the same area as the other 4 lithologies, but a significant fraction plot with the same Pt:Pd ratio but higher Au contents.

4.5.10.2 Pt and Pd in RF4

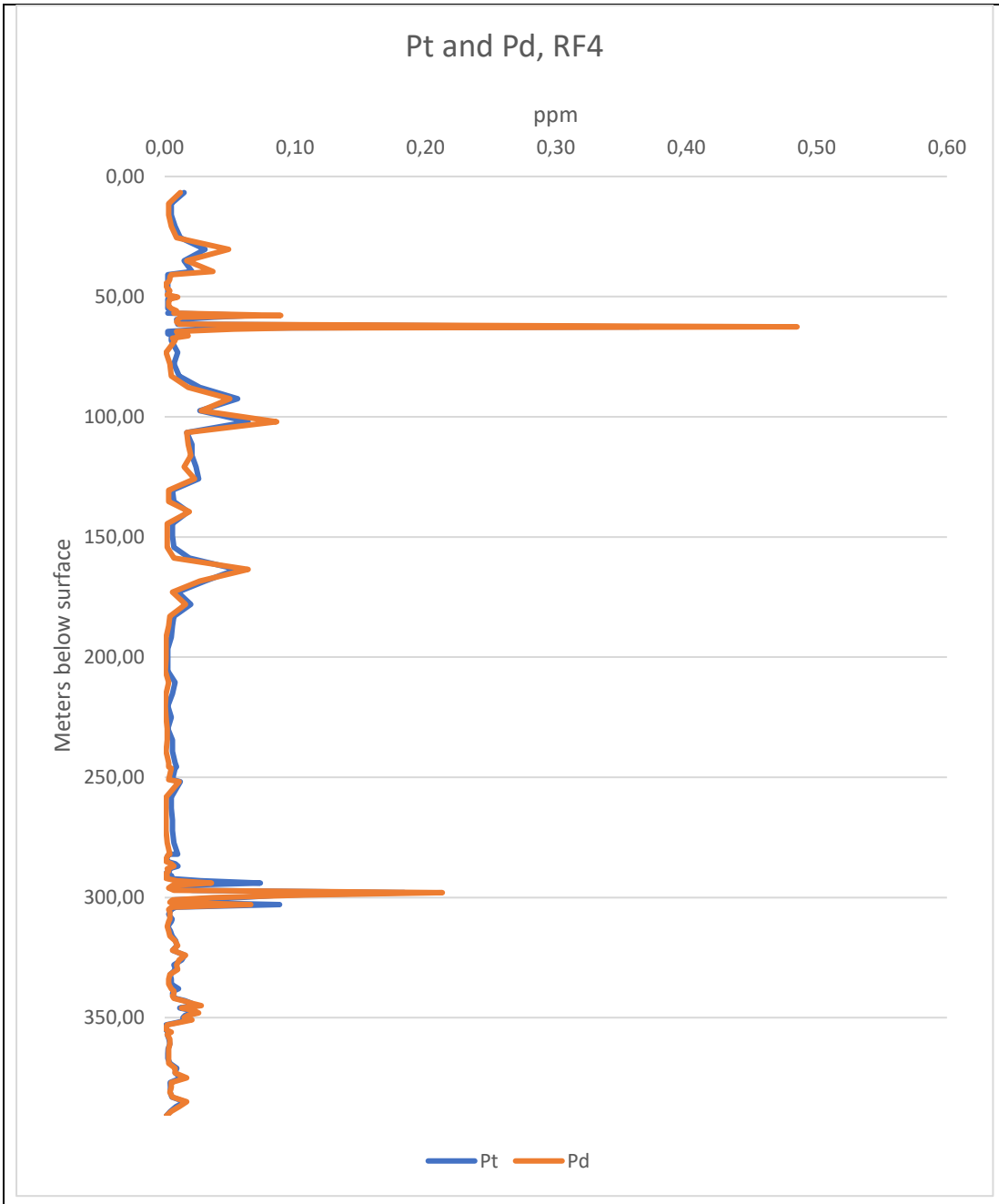

Figure 4.50

Diagram of Pt and Pd bulk rock concentration from the RF4 drill core.

The graphs in Figure 4.50 show an exceptionally good correlation between the concentration in Pt and Pd in the RF4 drill core.

4.5.11 Fractionation and ore peaks

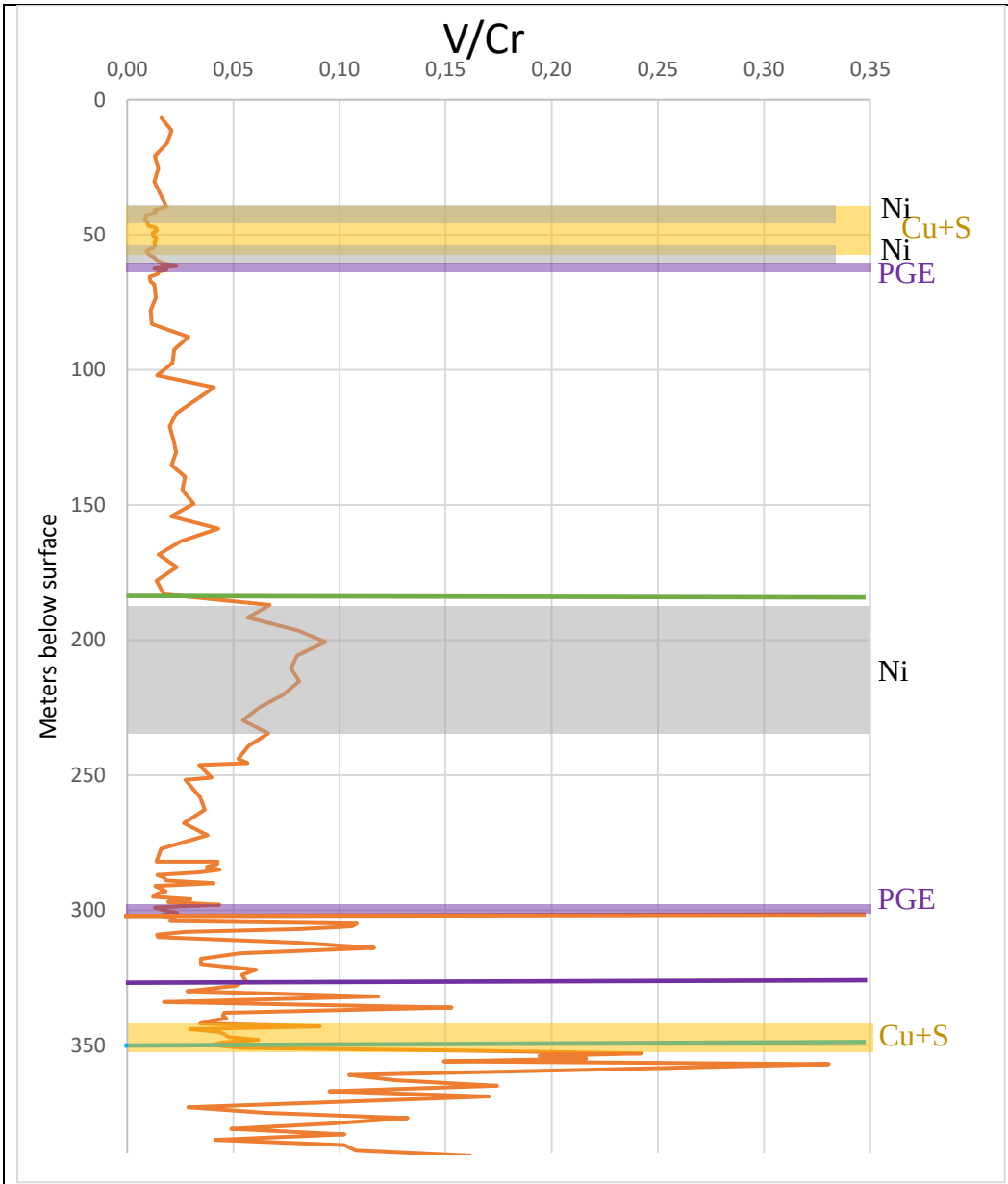

Figure 4.51

The V/Cr ratio of the RF4 drill core is plotted against depth along the vertical axis. The prominent ore element reefs and peaks of the ore forming elements are marked using semitransparent color coded boxes. Yellow: Cu and S-peak. Grey: Ni peak. Purple: PGE-reef. The blue, purple, orange and green fractionation lines from Figure 4.37 are marked.

In Figure 4.51 all prominent ore reefs and peaks of Ni, Cu, S and PGE are marked in a diagram of the V/Cr ratio with the colored lines marking abrupt changes in fractionation indication. From the top of the drill core, down:

The main Cu and S-peak is 19m wide and located at the same place as two narrow Ni-reefs with 8 meters between them. The lower Ni-reef continues 3 meters below the end of the S and Cu-reef. Immediately below the second small Ni-reef is the 1m thick major PGE-reef. The PGE-reef is even narrower than the Ni-reefs, though this could be caused by a difference in sampling interval. All these four reefs are found in an area of more or less constant V/Cr ratio.

10m below the green fractionation line is a 45m thick Ni peak that is likely hosted in Olivine. The Ni peak coincides with the V/Cr equally wide V/Cr peak.

Immediately above the orange fractionation line is the second largest PGE-reef in the RF4 drill core. This PGE-reef is 3m thick; not as narrow as the main PGE-reef 230m above.

The second largest Cu and S-peak is 20m wide and ends 2m below the blue fractionation line.

Details of the reef concentrations and depths for the reefs in Figure 4.51 can be seen in Table 16.

Table 16: Element reefs and peaks in the RF4 drill core with depth and concentration.

Reef type	Start depth (m)	End depth (m)	Average grade	Maximum grade
Cu	39,5	58,5	608 ppm	1325 ppm
S	39,5	58,5	3505 ppm	6100 ppm
Ni	39,5	45,5	2855 ppm	3610 ppm
Ni	53,08	61,5	3216 ppm	4330 ppm
PGE	61,5	62,5	849 ppb	849 ppb
Ni peak	187	234,5	2968 ppm	3070 ppm
PGE	297	300	230 ppb	397 ppb
Cu	345	352	664 ppm	898 ppm
S	345	352	3900 ppm	5000 ppm

4.5.12 RF1 and RF2 key data

Table 17: Chemical XRF data from the RF1 and RF2 drill cores first presented by Nikolaisen (2016).

	Surface [masl]	PGE [masl]	PGE avg [ppb]	PGE max [ppb]	Cu depth [masl]	Cu avg [ppm]	Cu max [ppm]	LLS [masl]
RF1	651	544-538	617	1362	565-546	852	1732	431
RF2	600*	---------	---------	---------	---------	---------	---------	460
RF3	655*	---------	---------	---------	491-477	1160	1910	---------
RF4	636	574	849	849	596-586	778	1325	331

*Surface altitude is approximated from the most recent RUC geological map (Grannes, 2016) and the contour lines from Norgeibilder.no .

The RF1, RF3 and RF4 have prominent Cu-reefs with 11-21m thickness and comparable ore grade in Table 17. RF4 has a narrower reef and both lower average and maximum Cu concentration than RF1. The 14m thick Cu-reef in RF3 has the highest both average and maximum Cu concentration. 2-8m below the Cu-reef in RF1 and 9m below the Cu-reef in RF4 are PGE-reefs where the RF1 reef is substantially thicker and more PGE enriched than the PGE-reef in RF4. There is no PGE-reef below the RF3 Cu-reef.

The centers of the Cu-reefs were used to compare Cu-reef altitude in the drill cores and calculate the altitude the Cu-reef should be found in RF2 in Table 18. The Cu-reef in RF1 is 71,5m above the Cu-reef in RF3. The Cu-reef in RF2 is calculated to be 78,65m above the Cu-reef in RF4. In RF2 the reef should be found at 669,65masl. Since the RF2 was drilled at ca 600masl surface level the expected Cu-reef has likely been eroded so it is not possible to compare the expected location with the actual one.

Table 18: Measured distance between the centers of the Cu-reefs in RF1, RF3 and RF4 and calculated vertical displacement between RF2 and RF4

	Horizontal distance [m]	Vertical displacement [m]
RF1-RF3	500	71,5
RF2-RF4	550	78,65*

*Calculated assuming the same reef inclination on the NW side of the fault as observed between RF1 and RF3 on the SE side of the fault.

5 Discussion

Chemical graphs presented with depth will consistently be presented from the bottom up to more accurately depict the magmatic deposition. It is however important to remember that the deepest cumulates were not necessarily formed first as late intrusions can cut previously formed cumulate rocks.

5.1 Recharge events

5.1.1 Reliability of recharge indicators

5.1.1.1.1 V/Cr

The V/Cr ratio uses the bulk rock concentrations of the compatible, lithophile to siderophile (White, 2005) element Chromium and the incompatible, lithophile (White, 2005) element Vanadium to say something about fractionation. Both elements are mainly found in chromian Spinels where they are both compatible, but Cr mostly so. During crystallization, Cr is more rapidly removed from the melt than V. The Spinels will capture the relative proportions of the two elements in the melt at the moment of crystallization.

Following the Irvine (1967) model for crystallization in mafic melts (see Figure 2.8) Chromite will crystallize simultaneously as Olivine and then pyroxene. After an interlude without chromian Spinel crystallization due to Cpx formation, primary Magnetite will crystallize and incorporate both elements. Under ordinary circumstances, there should be chromian Spinels in the cumulate assemblage.

Vanadium has a wide range of oxidation states (+2, +3, +4 and +5)(Clark, 2019) and can therefore be found in trace amounts in most minerals in the cumulates. Using the bulk rock concentration of V is therefore a good indicator as it does not prefer a single type of mineral whose crystallization will vary.

As long as the concentrations of V and Cr are above the margin of error, and there is in-situ chromian Spinel that crystallized from the main magma in the mineral assemblage, these two elements make a good basis for interpreting fractional evolution. As Cr only equilibrate to a small

degree, and V seems to not partake in equilibration, the ratio should be reliable. As seen in Appendix D, both are significantly above the detection limit.

5.1.1.1.2 Fe/(Fe+Mg)

Fe/(Fe+Mg) is an indicator that is intended to be used for minerals where Fe and Mg can substitute for each other. As Mg is lighter than Fe it will be incorporated into said crystals prior to Fe. In this thesis, the bulk rock Fe and Mg concentrations are used, not only the concentrations from the Fe and/or Mg bearing minerals. Fe and Mg substitution is however true for Olivine, Clinopyroxene and Orthopyroxene; the three minerals constituting around 98-100% of the cumulate rocks. Using the bulk rock values is therefore not a large problem.

Fe is a siderophile element with chalcophile tendencies. Because of this, some Fe will be removed from the melt whenever sulfide immiscibility occurs in the magma. From Grant et al. (2016) it is suggested that sulfide immiscibility is a common occurrence in the ultramafic magmas that formed the cumulates. It is very possible that sulfide immiscibility had occurred prior to intrusion (Nikolaisen, 2016), and so some of the Fe could have been removed by other means than the process the Fe/(Fe+Mg) ratio is meant to indicate. Grannes (2016) found that up to ca 15-20% fractionation had likely occurred in the melt prior to cumulate formation in the RUC magma chamber. If sulfide immiscibility occurred in the process of fractional evolution, loss of Fe could faultily cause the Fe/(Fe+Mg) ratio to drop without significant fractional crystallization as Fe could be scavenged by the sulfide droplets faster than Mg is depleted by silicate crystallization.

Because of these two reasons, the Fe/(Fe+Mg) ratio is less accurate and more prone to error than the V/Cr ratio. The Fe/(Fe+Mg) ratio is however a common fractionation indicator, V/Cr is a novel indicator that has not been tested by the scientific community.

5.1.2 Interpretation of indicators

5.1.2.1 RF4

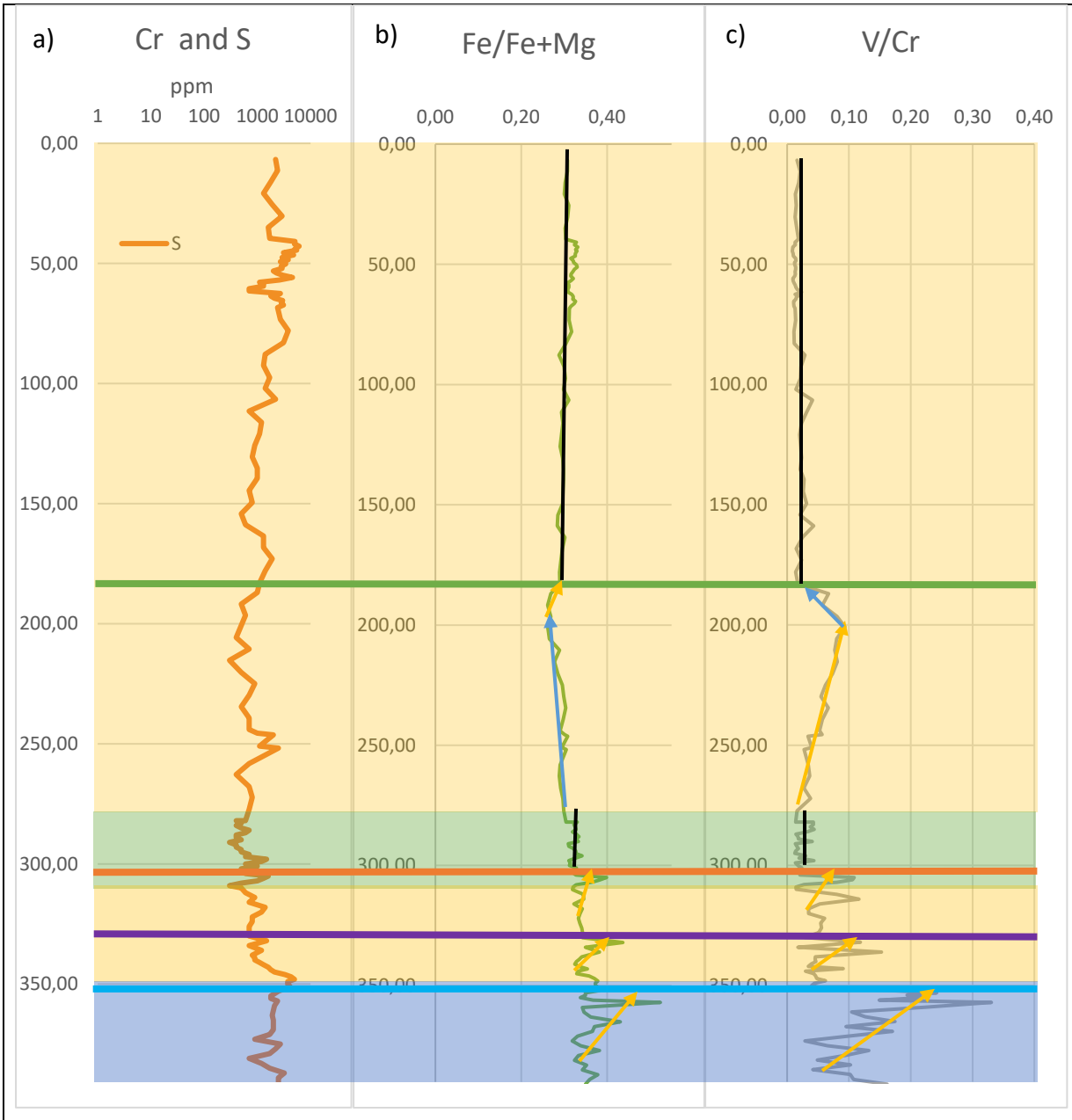

Figure 5.1

Edited Figure 4.37 from Results with added trends. Yellow arrow is a positive fractional trend, blue arrow is a negative fractional trend and black line is an interval of constant fractionation values.

a) Graphs showing the concentrations of Cu and S in a logarithmic scale, measured in ppm, of drill core RF4.

b) The graph shows the Fe/(Fe+Mg) ratio of the bulk chemistry in RF4.

c) The graph shows the V/Cr ratio of the bulk chemistry in RF4.

Fe/(Fe+Mg) and V/Cr are the two chemical indicators used to identify fractionation in this thesis. Both indicate fractionation when they increase, recharge when they decrease and steady influx of similar magma when constant. The two indicators can be seen in Figure 5.1 above. Both indicators show the same trends between 390-280m and 180-0m depths. However, between 280m and 180m the V/Cr graph and the Fe/(Fe+Mg) graphs show opposite trends. The V/Cr graph begin at 280m depth with a slow buildup of incompatible elements compared to the compatible ones. Then, at 200m the ratio gradually decreases over a 20m interval. In the Fe/(Fe+Mg) graph a very gentle decrease begins as the lithology change at 280m depth. This trend continues until 198m where a more sudden, yet still small, increase in the ratio brings the graph up.

5.1.2.1.1 Discrepancy at 280-180m depth

One way to explain the slow decrease observed in the V/Cr graph in Figure 5.1 c) between 200-180m is by small influxes of magma that mix as thoroughly with the magma already in the chamber. Such a process would increase the proportion of the compatible elements relative to the incompatible elements in the fractionated magma. As the geochemistry is measured with 5m intervals, any sudden changes in cumulate composition immediately following such a small recharge becomes invisible due to the large sampling interval. The graph use 20m to reach its minimum, yet always decrease with the same shallow slope. If this hypothesis is correct, several small recharge events must have taken place over a long period of time to account for the observed V/Cr trend.

The Fe/(Fe+Mg) ratio shows the opposite trend for this interval. As a melt that has a higher V/Cr ratio would also have a higher Fe/(Fe+Mg) ratio, this undermines the hypothesis presented in the previous paragraph. However, the Fe/(Fe+Mg) indicator assumes that Fe and Mg is only incorporated into crystals where they can substitute for each other. These minerals are Olivine, pyroxene and Spinel. Sulfides incorporate Fe due to its chalcophile tendencies, but not Mg. One way to explain a decrease in the Fe/(Fe+Mg) ratio that is not due to primitive recharge is by the scavenging of Fe during sulfide immiscibility. This seems unlikely to be the cause of the gentle Fe/(Fe+Mg)-decrease seen in Figure 5.1 b) between 280 and 198m. To account for the discrepancy, sulfide immiscibility must have been active during the formation of 80 meters of cumulates. As seen in Figure 5.1 a) there is only one S peak in the interval, and S is otherwise anomalously low.

Another way to form the observed ratios is by intrusion of magma that has a different chemical composition than the one in the magma chamber. This new magma must have a substantially lower concentration of Cr relative to V than the magma originally in the chamber (more evolved). The new magma must also have a different Fe/(Fe+Mg) ratio than the original magma (more primitive). A large recharge event would cause a sudden change in both fractionation ratios, not the gradual transition observed in Figure 5.1 b) and c). By many small recharge events of the new magma, and the subsequent mixing of the two magmas, the chemistry of the formed cumulates could be like what is observed in the graphs. This hypothesis would explain the discordance at 280-200m depth, but to explain the final part of the discrepancy at 200-180m depth recharge of yet another magma enriched in Cr and depleted in Mg must intrude at ca 200m depth. Immediately above the strange interval 200-180m, both fractionation indicators flatten, indicating deposition in an open conduit system with continuous flow of a chemically unchanging magma. The final 20 meters below this could be caused by the influence of this large intrusive event. If so, the conduit at 180-0m was emplaced after the cumulates below it. This explanation is unlikely because the intruding melt would need to evolve into a more primitive Fe/(Fe+Mg) ratio while changing to a more evolved V/Cr ratio.

A third way to explain the discrepancy between the two indicators at 280-180m is to imagine an open magma conduit system where the composition of the intruding magma changes over the course of cumulate formation. The incoming magma must change to either a lower concentration of Fe or higher concentration of Mg, as well as becoming more depleted in Cr relative to V to account for the cumulate evolution seen in Figure 5.1 b) and c). If the intruding magma originates from fractional melting of deeper rock, the V would be significantly enriched relative to Cr as incompatible elements are enriched in low degrees of partial melting, and becomes less so with more extensive partial melting. This would cause the opposite V/Cr trend compared to what is observed here. If the intruding magma melted and assimilated a large Cr-poor or V rich, Mg rich or Fe poor lithology deeper in its intrusion, that could cause the observed chemical evolution. Grannes (2016) suggested that areas where reverse fractional evolution is observed in the cumulates are caused by the melt's interaction with previously emplaced cumulates. If this is the case here, those previously formed cumulates must have been depleted in Cr or enriched in V compared to the magma that deposited the cumulates at 280m depth.

Another explanation could be that substantial parts of the cumulates from this area are crystals that were relocated by the magma and deposited here. This seems unlikely, as the 100m interval of the chemical discrepancy is substantial. Also, the magma would have no obvious reason to suddenly release the crystals it carried to be deposited here.

Another possibility is that the discrepancy is a random feature. The V/Cr ratio is given great credit in this thesis, as it logically should be a very good indicator for fractionation. It is however a ratio rarely used in science, and may not be as accurate as it appears for the rest of the drill core. Because the V/Cr ratio corresponds so well with the Fe/(Fe+Mg) ratio for the other drill core intervals, its significance could be overrated. The discrepancy, then, could be a random fluctuation that should not be given too much notice. The Fe/(Fe+Mg) ratio in the 280-200m interval show a very weak negative trend, very unlike what is observed for the rest of the drill core. As the trend is so gentle, it could be statistically insignificant. This explanation is possible but deemed unlikely as the trends of both Fe/(Fe+Mg) and V/Cr have the same slope for 80 meters. If randomness dictated the graphs in this interval, a larger variation in the slope would be expected.

The best way to explain the discrepancy is to envoke partial assimilation of primitive cumulate wall rock. The assimilation of primitive wall rock would cause the Fe/(Fe+Mg) ratio to gradually decrease. Fractional crystallization would occur, so the V/Cr ratio would increase, but due to assimilation of wall rock, their V and Cr would have been added to the concentrations in the crystallizing melt, causing the V/Cr ratio to increase with a significantly lower inclination than observed in the lower parts of the drill core. This explanation assumes that the V/Cr ratio for the assimilated cumulates must have been close to constant to affect the total V and Cr concentrations in the magma in the proposed manner. The melted material must therefore have been deposited in an open conduit system. At 200m depth the assimilation is modeled to either stop (by e.g. temperature decrease) or for the chemistry of the assimilated wall rock to change. Another possibility is for the large open-conduit intrusive above the 180-280m interval to chemically affect the underlying lithology in a sort of internal CS marginal zone. If the last explanation is true, then the CS was deposited in at least two major intrusive events.

As seen in the large 255-180m Ni-peak in Figure 5.8, the compatible element Ni agree with the Fe/(Fe+Mg) graph in Figure 5.1 b), not the V/Cr increase in Figure 5.1 c). Ni, like Cr, is gradually depleted during closed fractional crystallization. That Ni increases between 280m and 200m

discredit the V/Cr ratio in this interval. The Ni evolution could however be explained by the proposed assimilation of wall rock, where more wall rock chemistry has been equilibrated at shallower levels. That would cause the total Ni content to be continuously refilled by the wall rock, and a total positive trend as observed.

5.1.2.1.2 Closed chamber

Fractionation ratios increasing upward indicate that the cumulate formed by a limited volume of magma undergoing fractional crystallization. This is mostly observed when a magma chamber is closed. Initially the ratio incompatible/compatible is low. As crystals form, more of the compatible elements will be encased in crystals relative to the incompatible elements. As crystallization continue, less of the compatible elements are available in the melt to form crystals, and so the ratios increase. When a fractionation ratio suddenly decrease it indicates a sudden recharge of new magma that has undergone significantly lower degrees of fractional crystallization or by other means have a different chemistry. The two fractional crystallization indicators in Figure 5.1 agree that there are three instances of fractional crystallization in a closed magma chamber in the following intervals:

- 391-350m
- 350-335m
- 335-305m

The deepest interval, 391-350m, has the largest buildup before a sudden and dramatic drop in both ratios. The V/Cr graph shows the increasing trend more clearly than the Fe/(Fe+Mg) graph, which is characterized by local peaks. There are two "drops" visible in the two ratios; the first drop at 355m is visible in both the Fe/(Fe+Mg) and V/Cr graph. Above this the Fe/(Fe+Mg) graph has a slight increase while the V/Cr graph has a large increase before decreasing from a V/Cr ratio of 0.24 to 0.05 over a 2m interval. 2m above the V/Cr graph reaching its minimum at 350m, the lithology changes from pyroxenite to dunite**.** Excepting the tumultuous end, this is what fractional crystallization in a closed magma chamber interrupted by a recharge event of a more primitive magma looks like. Both graphs have a minimum at 355m and increase to a peak at 352m. Above this, the Fe/(Fe+Mg) graph is constant while the V/Cr graph plummets. This phenomenon could be explained by two recharges, the first with a low Cr concentration. This recharge event would

“reset” the Fe/(Fe+Mg) graph, but as the Cr concentration in the mixed magmas is low, the V/Cr ratio would not fall as far. The small increase in both ratios is explained by a short period of fractional crystallization until a second recharge event, this time by a melt with the same Fe and Mg concentrations as the first but a higher Cr concentration. That would make the Fe/(Fe+Mg) ratio remain constant while the V/Cr ratio plummets.

The middle interval, 350-335m, do not have the same magnitude as the deepest, but the slope in this interval is as steep as in 391-350m. This is the graph that shows an increasing trend in the Fe/(Fe+Mg) ratio most clearly. The V/Cr ratio has large variations. As with the deepest recharge event, the Fe/(Fe+Mg) ratio have one peak followed by a drop while the V/Cr graph has two peaks and a drop. In this case the Fe/(Fe+Mg) peak and the final V/Cr peak coincide at the same depth. This is also explained by fractional crystallization in a closed magma chamber ended by a recharge event at 335m. Because the Fe/(Fe+Mg) ratio has such a clear trend, the variations in the V/Cr ratio are assumed to be statistically random variations.

The shallowest interval, 335-305m, has the least obvious buildup for both Fe/(Fe+Mg) and V/Cr graphs. Though the trend is visible in both graphs, it is disputable whether this is in fact several very local buildups interrupted by non-recharge related events such as change from dunitic cumulates to wehrlitic cumulates or sills. The trend could be stipulated because it looks very similar to the middle interval. The interpreted recharge event occurs 3 meters into the wehrlite lithology. The main argument against this being a fractional crystallization buildup, as seen in the two intervals below, is that there is a sudden minimum in both indicators exactly where the lithology changes at 310m. The values here are very uncertain as they correspond to the place the where the pyroxene proportion in the cumulates increase from <10% to 10-40%. The chemistry just above and just below 310m should be representative for cumulate formation, but the point of drastic change is a poor place to gather important information. The main argument for this being a fractional crystallization buildup, as seen in the two intervals below it, is the large peak 3m into the wehrlite section followed by a sudden drop in both indicators, neither of which increase again afterwards. Because this is 3m into the new lithology, it is more reliable than the chemistry at the point where the lithologies change. As discussed in section “PGE at 300m – orange fractionation line”, a PGE reef immediately above the orange fractionation line support the fractionation-and-recharge interpretation for this interval.

The large fluctuations in the fractionation ratios in the closed chamber intervals could alternatively be caused by chemical disturbance by e.g. sills or dykes, as these are plentiful in the northern part of the RUC. For several of the local minimums and maximums in 391-305m interval of Figure 5.1, the fractionation graphs agree. This indicate that at least some of the fluctuations can be attributed to chemical magmatic differences. Sills/dykes are the most likely candidates. For the 391-350m LLS Olivine clinopyroxenite interval, Langstad-gabbro xenoliths could also account for some of the differences.

5.1.2.1.3 Open chamber

Constant fractionation indicators suggest that the cumulates/replaced minerals were formed a continuous influx of large volumes of magma in an open magma chamber/conduit. This is because the cumulates do not change in composition as the fractional crystallization occurs, as they would if a finite volume of melt experienced fractional crystallization. As the magma forming the cumulates has constant chemical signature, most of the magma volume escaped upward rather than being deposited here (Grant et al., 2016).

Two places in Figure 5.1 the fractionation indicator ratios are constant: 305-280m and 180-0m. This indicate that the cumulates formed came from a continuous influx of magma of constant chemical composition.

The deepest constant interval is at 305-280m depth. This interval has relatively large fluctuations, and the average ratio from both V/Cr and Fe/(Fe+Mg) is higher than the other interval. Because both fractionation indicators are higher on average for this interval it seems reasonable to assume that the magma passing through the chamber here is more evolved than the magmas that formed the 180-0m cumulates.

The shallowest constant interval is 180-0m. This interval has some fluctuations but is mostly constant. Most of the fluctuations are between 85-40m. The fluctuations are higher than the mean in the Fe/(Fe+Mg) graph and below the mean in the V/Cr graph. This is the same type of discrepancy as observed in the interval 280-200m, but at a much smaller scale. The scale is so small here that it is most likely a random variance. It is however possible that a small degree of wall rock assimilation took place in this interval to explain the discrepancy.

5.1.2.1.4 RF3

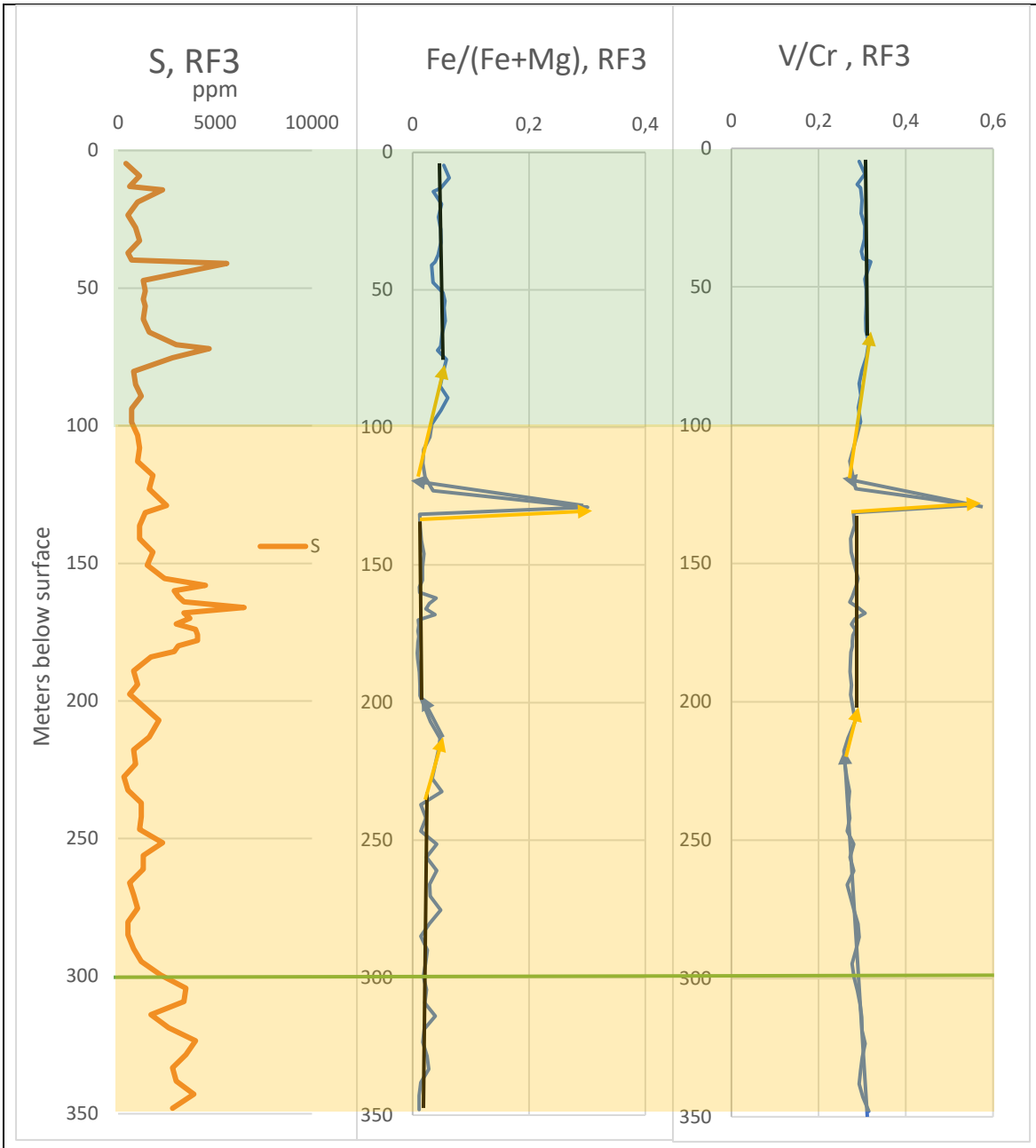

Figure 5.2

Edited Figure 4.40 from Results with added trends. Yellow arrow is a positive fractional trend, blue arrow is a negative fractional trend and black line is an interval of constant fractionation values.

a) *Sulfur concentration in the RF3 drill core, measured in ppm.*

b) *Fe/(Fe+Mg) ratio to indicate fractionation in the RF3 drill core.*

c) *V/Cr ratio to indicate fractionation in the RF3 drill core.*

The fractionation graphs for the RF3 drill core (Figure 5.2) are generally more unclear and more disagreeing than those seen in RF4. In the interval 349-240m the Fe/(Fe+Mg) ratio show a gentle decline, indicating evolution to a less fractionated magma, while the V/Cr ratio is more or less constant with local variations. The trend changes at 240m according to the V/Cr ratio, but at 223m according to the Fe/(Fe+Mg) ratio. Between ca 230m and ca 200m the V/Cr ratio has a gentle decline while the Fe/(Fe+Mg) ratio has a gentle incline. From ca 200m depth upward the two fractionation indicators agree. They are constant in the interval from ca 200m to 130m. This coincides with a S reef. A small, local peak in both fractionation indicators coincide with the largest S peak in the drill core. Then both graphs show a sudden increase, indicating recharge of a much more evolved magma. Then, between 127 and 120m the ratios drop to their "normal" values. A gentle incline characterize 120 to ca 75m. In the upper part of this incline the S peaks. Then, at 80m according to the V/Cr graph and 70m according to the Fe/(Fe+Mg) graph, the ratios return to constant values with little variance. A small peak at 42m coincide with the second largest S peak in the core.

The green line from Figure 5.2 and Figure 4.40 is placed based on the observed displacement between the RF3 and RF4 drill cores. Nothing appear to change in either fractionation indicator above or below the line, but the S concentration in the cumulates change.

5.1.2.1.5 Discrepancies

Three places in Figure 5.2 the Fe/(Fe+Mg) graph and V/Cr graph disagree on when a change in trend occurs: 349-240m, 240m-215m and 215-200m. The entire RF3 drill core is however analyzed at 5 meter intervals and is therefore more vulnerable to i.e. dykes setting off the larger trends than RF4. In the RF4 drill core such small anomalies were easy to ignore when interpreting the large scale chemical trends. In the RF3 drill core, a 10m discrepancy is only 2 chemical data points that are for various reasons off pitch. All discrepancies are between very gently dipping trends. Pinpointing exactly where they change is therefore difficult. Because the trends have so gentle slopes, peaks and bottoms in one trend that are features from random fluctuations can appear to belong to either of the trends. However, as a local maximum so well corresponds with where a peak in the next trend would be at that depth, it is interpreted as part of that large trend. This phenomenon probably explains the disagreeing change between a positively inclined trend and a constant one at 70 or 80m depth in Figure 5.2 b) and c) respectively.

The three disagreeing fractional trends at 349-240m, 240m-215m and 215-200m all have very gentle slopes. Either the discrepancies are interpreted to be caused by random fluctuations in one of the graphs that is faultily interpreted as a large trend – or they are caused by assimilation of wall rock in the same way as the discrepancy in RF4 was explained. It is hard to decide which is more likely from the diagrams in Figure 5.2.

5.1.2.1.6 Closed chamber

Between 120-80 or 70m depending on the fractionation indicator, both indicators agree on a gently increasing trend. This could be a case of a closed chamber situation with very large volumes of magma, so that a fractional evolution causes small changes in the chemistry. It could also be an open system where the chemical composition of the intruding magma changes over time. Or it could be caused by an open system where a more evolved wall rock is gradually assimilated in the cumulate forming melts. The only certainty is that the incline for the fractionation indicators are much less drastic than the three deep fractional events recorded in RF4 between 391m and 305m.

A large anomaly in both fractionation indicators is found at 130-120m depth. Both fractionation indicators show a substantially more evolved lithology than is found elsewhere in RF3 and RF4. This is believed to be a late sill, partly because it is found in RF3 and RF1, but not in the corresponding place in RF4 and RF2. The phenomenon is further discussed in section “RF3 and RF1 evolved sill”.

5.1.2.1.7 Open chamber

RF3 has an open chamber system between 80m and 0, and possibly between 349-130m. This is clear by the agreeing constant fractionation indicators at 80-0m and the almost constant fractionation indicators between 349-130m.

The 80-0m interval consists of intermittent CS wehrlite/dunite and ULS pyroxenite/wehrlite. The ULS areas are most easily observed in the Ca-diagram in Figure 4.36 d). Despite the lithology changing from CS to ULS, the fractionation indicators remain constant. That suggests that at least some of the ULS cumulates were formed in an open conduit system. This is contrasted by the 391-305m periodically fractional closed system cumulate formation believed to be the LLS. Up until now it has been unclear whether the LLS and ULS were formed as one large unit that was later

separated by the CS replacing dunites. If the open system fractionation trends continue for the rest of the ULS, this will be a significant difference between the layered cumulate series.

The potential 349-130m interval is part of the CS dunites. In RF4 this unit is characterized by unchanging fractionation indicators. That suggests that the negligible variations in fractionation indicators in this interval in RF3 are random fluctuations rather than important trends.

5.2 Elements affected by recharge events

5.2.1.1 S at 350m – blue fractionation line

There is a significant S peak in the transition between the MZ pyroxenite and the LLS dunite (see section LLS or CS) at 350m. The peak begins prior to the lithological change marked by the blue fractionation line, but the vast majority of the S reef is deposited above the fractionation line. Settling sulfide liquid would be much heavier than the underlying mushy cumulates, and so it is possible that the weak anomaly below the fractionation line is caused by sulfides that have sunk up to 3m into the cumulate mush. As magma mixing during a recharge event is one of the main methods for crossing the sulfide immiscibility curve, the recharge indicated by the blue fractionation line is believed to cause the large S anomaly in RF4.

5.2.1.2 Cr at 335m – purple fractionation line

There is a Cr peak at the same depth as the purple fractionation line. This is believed to be caused by influx of a magma more SiO_2 rich than the one forming the dunitic cumulates, causing the mixed magmas to enter the Chr stability field and only crystallizing Chromite for a brief period, as suggested by Irvine (1965) to explain Chromite seam formation. The Chr seam reaches 3020 ppm Cr over a 2m interval. 4m above the Chr seam have an average of 1460 ppm Cr. It is believed that this is caused by increased Chr crystallization also after the cotectic Chr-Ol line was reached, or possibly by Chr crystals held in suspension by magmatic turbulence during cumulate formation along the cotectic Chr-Ol line after the formation of the Chr seam.

5.2.1.3 PGE at 300m – orange fractionation line

The second largest PGE anomaly in the RF4 drill core is found just below the third fractionation line. This is discussed in detail in section Lower PGE reef: RF4 (339-336 m.a.s.l. = 297-300m).

The three lowest fractionation lines are followed by increased bulk rock concentrations of the compatible elements Cr and Ni. This further supports the hypothesis that the fractionation lines indicate actual recharge events instead of e.g. assimilation of primitive wall rock as that would lead to further depletion of the compatible elements while the Fe/(Fe+Mg) ratio increased.

5.3 S and Cr correlation

In RF4 there appear to be a good correlation between S – an element that needs to reach oversaturation to form crystals – and the compatible element Cr – found almost exclusively in chromian Spinels (Chr). An ordinary uninterrupted and uncontaminated fractional crystallization sequence would lead to the opposite effect: Chr would crystallize early and S would form from the late residual melt. The following processes affect the solubility of S and the stability of Chr crystallization so that the correlation is possible.

With recharge of magma rich in both SiO_2 and S, the mixed magma in the chamber will be pushed into the Chr crystallization field (Irvine, 1965) while the total S could reach oversaturation and form S droplets. This process would be clearly visible in the fractionation graphs where fractionation occurs. It does not happen in the lower part of the drill core (the MZ and LLS part), but it could be a significant contributor to the correlating largest S and Cr peaks in the CS. The CS is characterized by large volumes of hot primitive magma passing through the RUC magmatic conduit. Fractionation is not observed, likely due to the continuous influx of magma. Nikolaisen (2016), Tollefsrud (2018) and Grant et al (in prep.) has distinguished several different magma intrusions in the CS lithological unit. For recharge events with varying magmatic composition to occur is therefore not farfetched.

Remelting/resorbtion of previously formed Chr in a late stage of crystallization where S has been enriched to reach oversaturation would cause both elements to crystallize from the magma. This

is an unlikely scenario as remelting/resorbtion of significant rock volumes to substantially increase Cr-concentration would also likely cause the S concentration to drop below oversaturation.

Small changes in pressure or fO_2 are known to affect both the crystallization of Chr-Ol and the S solubility in a melt. Pressure change is often observed in basaltic magma chambers (Bottinga and Meurer, 1990, Lipin, 1993). Increasing pressure would lead the stability field into the only Chr field, while the S solubility curve would be slightly lowered. If the S concentration was very close to saturation such a pressure fluctuation would cause oversaturation and the formation of both sulfide and Chromite minerals. This process is also a plausible candidate to explain the good correlation between Cr and S peaks in the CS dunites.

Crystallization of Chr can cause locally lowered fO_2. MacLean (1969) noted that sulfide solubility appears to decrease with increased fO_2. If his observation is correct and generalized, sulfide solubility should increase when Chr crystallization causes decreased fO_2, and can therefore not cause the observed correlation.

The RF3 do not have the same correlation between Cr and S as RF4. The characteristic Ni+S+Cu – S+Ni – PGE reef sequence observed in RF1, RF3 and RF4 is the only place where Cr and S correlate in RF3. As that is the largest S peak in the RF3 drill core it is likely that the first explanation has caused the anomaly. The fact that the rest of the RF3 CS do not have Cr-S correlation indicate that whichever process formed the rest of the correlations in the RF4 either functioned locally or were originally also present in the RF3 but have been metasomatically relocated e.g. through sulfide remobilization in late metasomatic fluids. Since the cumulates were formed in a round magma chamber, it is possible that either RF3 or RF4, which are separated by 350m, is in the bowl's edge rather than its center. Such a displacement could also lead to a displacement of 5-15m between the Cr and S peaks from cumulate settling.

In thin sections interstitial chromian Spinel crystals are often found in contact with sulfides. Either as sulfide inclusions in chromian Spinels (such as in Figure 4.10 and Figure 4.12) or as sulfide in contact with Spinels along grain boundaries (such as in Figure 4.5). The sulfide in Figure 4.5 interacted chemically with the Magnetite crystal during cooling, causing a symplectite texture.

This is the only observation of a chromian Spinel becoming unstable (forming a symplectite texture) due to contact with a sulfide.

5.4 Spinel crystallization

Grant et al. (2016) noted that chromian Spinels are found as inclusions in Olivine of type 1, rarely in type 2 and never in type 3. The Spinels also occur interstitially, at times in contact with pentlandite, chalcopyrite and pyrrhotite. Chr and Dol+Mt+En±CO2 are found as inclusion trails in type 1 cumulate Olivine (Grant et al., 2016, Larsen et al., 2018, Sørensen et al., 2015). From this it is clear that the permeating calcareous late magma that formed the carbonate clots was in in the Chr-Ol or Dol-Mt-Opx stability field during intrusion. These inclusion trail Chr and Mt have not been analyzed, and it would be interesting to do so to see if there are chemical differences between the interstitial/cumulate Chr and Mt and the phases that were definitely formed by the pervasive calcareous melt.

5.4.1 Primary and secondary Spinels

In the analyzed MZ and LLS Spinels (see section "Marginal Zone, Lower Layered Series or Central Series"), most of the Spinels are either Mt or (assumed) late Hc. The presence of Chr is rare, as seen by the scarcity of group 2 Spinels in the Spinel diagrams (Figure 4.17 to Figure 4.28). This is likely explained by few of the melts reaching the cotectic Ol-Chr line in Figure 2.8. There might be a bias from analyzed grains as the interstitial chromian Spinels were the focus of these chemical analyses. Chr formed by crystallization along the Ol-Chr cotectic would likely often form as inclusions in Ol, which were rarely analyzed in this study. As Mt is abundant, it seems that most of the cumulate forming melts crystallized along the Cpx-Mt and Opx-Mt cotectics. The lithologies sampled in this study are generally pyroxene rich compared to the dunitic CS previously studied (Grannes, 2016, Grant et al., 2016, Tollefsrud, 2018), which likely explain the abundance of Mt compared to Chr.

The group 3 Magnetite is believed to be a primary magmatic cumulate mineral. The basis for this is mainly that the group do not follow the metamorphic Magnetite trends of Barnes and Roeder (2001). Also, group 2 and 3 appear to often follow the same gradual chemical evolution in the

Spinel chemical diagrams (Figure 4.19-Figure 4.28), indicating that they formed from the same melt at different times of crystallization.

Group 1 Hercynite often follow another chemical transition than the one seen in Mg-Chr (see Figure 4.19-Figure 4.28). This insinuate that Hc formation was caused by a secondary influence, either replacing or late crystallization from a different source than the cumulate Chr and Mt.

There is some metamorphic Magnetite in the analyzed samples. It is termed "Fe-Ti" due to its extreme Ti-enrichement compared to the other chromian Spinels. No Fe-Ti crystals were analyzed by EPMA, but several were tested by WDS during EPMA preparations.

5.4.2 Crystal formation and texture

5.4.2.1.1 Rounded grains

The Spinel grains in Figure 4.6, Figure 4.7, Figure 4.4 and the smaller grains in Figure 4.9 as well as the main Spinel crystal in Figure 4.11 are rounded. The grains in question all consist of both group 1 (Hc) and group 3 (Mt) Spinels. The grains could have either crystallized into a round shape or been rounded by movement.

Chromian Spinels have strong crystallinity. For so many grains to crystallize into a round shape is unlikely. If the grains crystallized in the magma chamber and then sank through the magma before settling in the cumulates, the hot and abrasive magma and cumulate mush could have caused the rounding effect on originally more well-formed grains. Since Hercynite and Magnetite are denser than mafic to ultramafic magma, Spinel grains would begin to sink as the crystals nucleated, faster as the crystal grew. In this hypothesized crystallization, crystallization would therefore occur as the grain moved through magma. If the melt had a high viscosity, the abrasion caused by movement through magma would probably be enough to cause the rounding observed on the above-mentioned Spinel grains.

There are two other ways that magma movement could cause the observed rounded texture: melt intruding through the cumulates; and the Spinel crystals being moved by the magma post crystallization yet prior to intrusion into the magma chamber and subsequent cumulate formation. As noted by Tollefsrud (2018) and observed in optical microscopy, there are in several places sign of calc-alkaline magmatic pervasive intrusion through the cumulates (see Figure 9.18 and Figure

9.19). This manifests as small spots of calcareous minerals where globules of melt have passed through. As this is a rare phenomenon, though observed in several thin sections, it seems unlikely that this post cumulate intrusion could cause the rounding texture observed in the Spinels. However, the rounded grains in Figure 4.6 have carbonates between the Spinel grains. Also, if a pervasive magma post cumulate formation caused rounding of the Spinel grains, all Spinels should be rounded – not only some as is the case here – and the calcareous spots should be found in contact with the rounded grains. This is not the case for all the rounded grains, and so this hypothesis is rejected.

It is difficult to say whether the second explanation, "crystals being transported with the magma prior to intrusion into the magma chamber" is plausible. If the rounded Spinels had a significantly different chemical composition compared to the Spinels that are not rounded, the hypothesis would be strengthened. That is not the case from the chemical graphs in Figure 4.27, Figure 5.4, Figure 5.5 and Figure 5.6, so the hypothesis cannot be rejected based on chemistry. Excepting the mineral in Figure 4.12, which is from 348m depth, very close to the recharge event at 350m, and the Spinel in Figure 4.6 (320m depth), all the rounded Spinels are in the 390-350m pyroxenite lithology that is characterized by fractional crystallization. For all the rounded grains to be transported into a fractionating magma chamber and yet to be deposited 10 meters apart in the cumulate column is highly unlikely. The hypothesis cannot be completely rejected, but it can be rejected that it explains the texture of all the rounded grains.

The chromian Spinels have a strong crystallinity, and so it is likely that a rounded texture was caused by post crystallization deformation and/or recrystallization.

5.4.2.1.2 Euhedral grain

Contrasting the rounded grains discussed above, the Magnetite grain of group 3 seen in Figure 4.5 is euhedral. It is the only euhedral interstitial or cumulate chromian Spinel observed in the thin sections. That a euhedral grain exists indicate that at least some of the Magnetite crystallized unhindered from the magma in stable conditions and was not rounded by passage through magma. That could indicate that the Magnetites of group 3 crystallized under different conditions where Magnetite crystallized freely compared to Hercynite and Chromite. As most of the group 3 Mt Spinels are anhedral, it is likely that the crystal simply crystallized in-situ whereas most other

grains sank to the bottom of the magma chamber and were to varying degrees rounded. The Magnetite in Figure 4.5 has a symplectite texture around the sulfide contact halo, but also other places along its border. This indicate that an actively scavenging sulfide phase made parts of the Mt crystal unstable by scavenging its chemical components. As the sulfide-symplectite texture is not observed in other Spinels, it seems that most of the sulfides formed after the Spinel crystals were too solidified to be scavenged from.

5.4.2.1.3 Replacement texture

In Figure 4.10, Figure 4.6, and Figure 4.7 the Magnetite Spinels clearly crystallized prior to Hercynite. In Figure 4.10 and Figure 4.6 the Hercynite is only found along the border of the Spinel grains. In Figure 4.7 the Hercynite is found less auspiciously along the Spinel grain boundary but it is also found filling in a previously formed fracture that cuts the Magnetite grain. From these grains it is evident that the Al rich Hercynite formed after or possibly replacing the previously formed Magnetite.

It has been suggested that substantially Al enriched (>40 wt% Al_2O_3) chromian Spinels formed due to very high pressure (Irvine, 1967). Dick and Bullen (1984) suggests that the melt/Spinel partitioning coefficient for Cr decrease with strongly increased pressure. However, Allan et al. (1988) showed that such Al rich chromian Spinels can crystallize under very low-pressure conditions (MORB), and suggest that Al-rich chromian Spinels may be caused by a low pressure re-equilibration, magma mixing or wall rock assimilation into the melt.

Magnetite and Chromite are the Spinel compositions commonly found as inclusions. This indicate that the Spinels of group 3 and 2 co-crystallized with Olivine and that the Spinels of group 1 either formed during a later crystallization step or are a replacive feature. Thus, Hercynite is a later formed Spinel phase than Chr and Mt. Three late processes could account for its formation:

1) Crystallization from residual magma
2) Crystallization from pervasive melt
3) Chemical re-equilibration

As Magnetite-Hercynite contact has large contact-relation variation, 3D features not observed in the 2D thin sections is likely to distort some of the presented grains.

Hypothesis 1) *Crystallization from residual magma*, is supported by the low Cr:Al ratio in the Hercynites. As plagioclase is rarely present in thin sections, Al would mainly concentrate in the residual melt. This is observed by Grant et al. (2016). However, a residual magma would have significantly lower Mg:Fe than previously formed Spinels from the same magma. Hc is the most Mg-rich of Spinel group, so (assuming that the melt-Spinel Mg:Fe correlation supported by Barnes and Roeder (2001), Kamenetsky et al. (2001), Roeder (1994), Irvine (Irvine, 1965, Irvine, 1967) among others is valid at RUC P-T conditions), this can't be it.

Explanation 2) *Crystallization from pervasive melt*, is supported in that such a pervasive melt is likely to be more primitive than the fractionated melt in the magma chamber, and that both Dolomite and the late, primitive Olivine rim are in contact with both Hercynite and Magnetite in some of the replacive Spinels, implying that both phases grew while in contact with the magma forming these abnormal minerals. However, such minerals are not found in contact with all the Hercynite. Only some of the altered Spinels contact carbonates, indicating that e.g. the CS forming melts could have formed some of the abnormal minerals. If all Hercynite Spinel were formed from contact with or crystallization from a pervasive melt, the distinct lack of chemical change around most of the monocrystalline interstitial Hercynite must be explained by unfortunate 2D cut of 3D textures. Also, the pervasive melt must have had a significantly different Cr:Al ratio than the cumulate-forming melt.

Hypothesis 3) *Re-equilibration*, is a known and expected process that alters most chromian Spinels post crystallization and prior to geologists studying them. If Hercynite were formed by re-equilibration with surrounding silicate minerals, substantial Al must have been present in those silicates, and they must have absorbed substantial Cr. This is not observed in the cumulate Ol that surround most of the Hercynite Spinels. So either significant 2D cut of 3D features must be assumed, or Hc did not form by chemical re-equilibration. Since most Hc is found as monomineralic crystals, re-equilibration with Mt can not account for the majority of Hc in the thin sections. It is possible that re-equilibration between Spinel and surrounding Ol, where Fe went to Spinels and Mg went to Ol could explain the primitive Ol around some Spinels. However that gives no further clues as to the formation cause of the replacive Hercynite.

A final possibility is that Hercynite formed as a post-Mt crystal from the cumulate-forming melt, and that in the Reinfjord P-T conditions, the crystal is only stable with a substantial Mg-enrichement. This assumes that the melt-Spinel Mg:Fe correlation (Barnes and Roeder, 2001, Irvine, 1965, Irvine, 1967, Kamenetsky et al., 2001, Roeder, 1994) is not valid for the formation of the Hercynite.

Of the presented hypotheses, Hc formation from crystallization from or interaction with a pervasive melt (either the CS-forming melt or the carbonatite metasomatized melt that formed the carbonate clots is implied) seems the most likely. Whether the primitive Ol in contact with some of the Mt-Hc Spinels is formed by chemical re-equilibration with the Spinel or was crystallized form the pervasive melt is uncertain.

5.4.2.1.4 "Unmixing" texture

The minerals of Figure 4.9, Figure 4.12, Figure 4.11 and Figure 4.13 show two chromian Spinel phases crystallizing seemingly randomly in one large Spinel grain. In Figure 4.9, Figure 4.11 and Figure 4.13, the two Spinel phases are Hercynite and Magnetite. In Figure 4.12 the two endmember Spinel phases are Chromite and Magnetite. Each grain will be discussed separately. For each mineral with a possible liquid immiscibility texture, there liquidus could be either primary or caused by a re-melting of the mineral and subsequent re-solidification.

The Spinel grain in Figure 4.9 consists of several patches of Spinel Hercynite and Magnetite with small globules of both. Neither phase is more prominently found along grain boundaries. Both phases have even, curving borders between each other. Small globules of Hercynite is found in large patches of Magnetite and vice versa. Neither phase appear to fill in fractures. The borders between the two Spinel phases are sharp. All these are arguments imply that the grain formed by segregation of a once homogenous liquidus phase into two of different chemical composition. However, as only one plane of the grain is observed it cannot be excluded that the observed textures could be caused by the mineral's 3D shape and an unfortunate cut. The Spinel grain does not

appear to contact crystals formed by a late residual or pervasive magma, but it cannot be ruled out due to 3D crystal shape.

The Spinel in Figure 4.12 has a gradual transition between Chromite and Magnetite. It has been suggested that there is a compositional gap between Chromite and Magnetite caused by an immiscibility gap which rapidly widens below 600 °C (Sack and Ghiorso, 1991b). Barnes and Roeder (2001) found that there are Spinels with chemistries between those two "immiscible phases", suggesting a miscible gap in natural compositions between those endmembers. This Spinel shows that there is a miscible area between the endmember chemical compositions of Chromite and Magnetite. During equilibration within the grain either through re-equilibration with outside phases (as there is a rim of Olivine of a slightly less dense composition in contact with the grain, this seems likely) or re-melting, the grain was stable when solidifying with all chemical gradients as seen in Figure 4.14.

The other Spinel with a chemical compositional gradient can be seen in Figure 4.13 and Figure 4.15. It consists of Hercynite and Magnetite endmember compositions with gradual chemical transitions between the two. The transition is shaper than the Spinel in Figure 4.12, but it must be taken into account that the two endmembers have a larger chemical gap than those from Figure 4.12. The grain in Figure 4.13 do not have a reactive contact. It is surrounded by fractured, interstitial Olivine crystals. As pointed out by Barnes and Roeder (2001), this does not mean that the grain has not undergone chemical re-equilibration as that process can occur between solid grains as well as between grain and melt. It does however lessen the likelihood of re-melting causing the chemical gradient as the only magma the grain has been in contact with seems to be the one it crystallized from as Olivine was co-crystallizing. Between the Magnetite and Hercynite endmembers is the Spinel gap. Barnes and Roeder (2001) noted that Spinels can have compositions inside the Spinel gap, but it is rare and occurs under abnormal circumstances. The chemically graded Spinel in Figure 4.13 have an average chemical composition inside the Spinel gap, and a continuous chemical gradient between the two endmembers. This is believed to be easily overprinted as Barnes and Roeder (2001) found this composition very rarely in their 40 000 Spinel

database. That makes this grain highly unusual. As with the Spinel in Figure 4.12, it is likely that the stability field where there is a miscible gap between Spinel group 1 and 3 is narrow: this is the only Spinel crystal where this duality is observed, in all others the two phases have fully segregated when solidifying. Because the grain do not appear to have undergone late magmatic modification, this stability field is likely to be under the cumulate formation P-T conditions of 10-14 kbar (Orvik, 2019) and 1000-1450°C (Larsen et al., 2018). It is possible that Spinels with this chemical composition and gradient are so rare because it is a feature only formed at great depths and easily overprinted by later processes. It is also possible that though the endmember compositions of the grain are on either side of the Spinel gap, the chemical gradient follows the stable area outside the Spinel gap. The quality of the EDS mapping in Figure 4.15 is poor, but the chemical diagrams from analyses between the endmember compositions are remarkably similar to the mapping conducted on the Chr-Mt grain in Figure 4.14. The complete chemical data can be seen in Appendix C.

The Spinel grain in Figure 4.11 is similar to the grain in Figure 4.9, but without the smooth curved contacts. The grain consists of Hercynite and Magnetite. Neither Spinel phase seems to be more often found along the grain boundaries. There are globules of Magnetite in patches of Hercynite and vice versa. Neither phase has crystallized in previously formed fractures. The borders between the two Spinel types are however polygonal rather than curved. This indicate that where the Spinel grain in Figure 4.9 probably segregated and solidified during a liquid-like state, the Spinel grain in Figure 4.11 had time for the phases to develop solid subhedral outer borders. The borders between the two Spinel phases are sharp. As there are fragments of both phases in one another it is proposed that the grain began as one homogeneous solution which segregated. The polygonal mineral borders indicate that this was not a liquid-like solution state, rather one in which at least one of the phases was solid during segregation. It cannot be ruled out that some of the mineral texture is caused by a 3D phenomenon and that the 2D cut gives an unrealistic presentation of the grain. As the Spinel in Figure 4.11 has a chemically different Olivine and Amphibole along some of its grain boundaries, it seems plausible for chemical re-equilibration or re-melting by a late phase to have caused the chemical random zoning.. Oxide liquid immiscibility, solid solution for only a period, chemical re-equilibration or re-melting followed by one of the previously mentioned

mechanisms could have caused the phases to segregate. If so, the crystal in Figure 4.11 had more time to form crystals during solidification than that in Figure 4.9.

If chemical re-equilibration caused the observed textures, the re-equilibration must have occurred with equal intensity in the entire Spinel grain, and the Spinel must have solidified in a state of chemical variation rather than diffusing into a mixed composition. This seems unlikely as diffusion generally works to reach a single stable state, not several with large chemical variations.

The alternative is for the textures to be formed by a heating event. Because the Mt-Hc (and Mt-Chr) texture is not only a core-rim texture (as discussed in section "Replacement texture"), but a chemical gradient-texture as well as a seeming immiscibility-texture, the Hc forming process must have occurred at significant T to have caused the likely Spinel re-melting that formed the two latter textures. Alternatively, the formation of the Hc phase must have occurred prior to a reheating event that caused Mt-Hc re-melting and complex unmixing-textures. The two Spinel grains with chemical gradients and the curved immiscibility-grain (Figure 4.9) are all from thin section 369,5-B. This is >22m from the contact with the Langstad-gabbronorite in the center of the MZ Olivine clinopyroxenites. It is possible that the proposed re-heating of these grains during or after the formation of Hercynite could be the intrusion and mixing with the Langstad-gabbronorite that formed the MZ. The grain from Figure 4.11 is from thin section 348, 2m above the transition from MZ Olivine clinopyroxenite to LLS dunite (see section "Marginal Zone, Lower Layered Series or Central Series"), 4m above a suggested recharge event horizon. It is entirely possible that the proposed re-heating of this Spinel was done by the recharging magma. Why two of the re-melted chromian Spinels from thin section 369,5-B solidified with chemical gradients and one with sharp Hc-Mt boundaries is not understood.

5.4.2.1.5 Outshoots

Figure 4.12, Figure 4.11 and possibly Figure 4.6 have small outshoots from the main Spinel grain. All three grains are surrounded by Olivine of a slightly less dense composition than the interstitial Olivine grains in the same figures. In Figure 4.11 the Spinel also contacts an Amphibole grain. However, the outshoots in both Figure 4.12 and Figure 4.11 penetrate outside the anomalous contact minerals and into the cumulate Olivine (Figure 4.11) and Clinopyroxene (Figure 4.12).

Another interesting feature from all three outshooting Spinels is that both the Spinel phases present in each Spinel grain is also present in the outshoots, and with the same transition sharpness between Spinel phases as the larger grain has. The fact that small chemically identical fragments of a larger Spinel grain is observed in three instances, at 320m, 348m and 369,5m depths indicate a process that affected the entire cumulate column – or at the very least a significant portion of it. To explain the outshoots, it is proposed that the Spinel volume expanded after the surrounding interstitial and cumulate minerals were crystallized, causing them to fracture. This would explain that the outshoots are found in both the contact minerals and the farther interstitial silicate grains. Since the outshoots are not fragmented but appear continuous, some recrystallization must have occurred post the volume expanding event, or the Spinel was in a liquidus phase when it happened and "squished" to fill the opened fractures. From (Levy and Artioli, 1998), experimental data on Chromite expansion from Bushveld and Xerolivado Chromite crystals, Chromites of composition similar to that of Group 2 expand between ca 800°C and ca 1400°C. This indicate that the cumulates experienced reheating after some of the chromian Spinels had been completely encapsulated by other minerals, but only some Spinel crystals fractured during this process. The study by Levy and Artioli (1998) was conducted in vacuum, and so do not account for the effect pressure would have on the heated Chromite crystals.

A heating event like the one needed to cause the thermal Chromite expansion proposed by Levy and Artioli (1998) took place after cumulate deposition of the LLS in the RUC. This heating event was the intrusion of what became the CS replacive dunites. If the CS-heating of chromian Spinels formed the outshoots, it is likely that the proposed chemical gradient and complex Hc-Mt textures discussed in the previous section occurred at different P-T-fO_2-chemical conditions.

As ever it is also possible that the outshoots might be a 3D texture that is misleadingly cut.

5.4.2.1.5.1 Volume change

In Figure 4.7 Hercynite fills in a previously formed fracture in primary Magnetite. Both phases are later fractured. Small fractures cut both Hercynite and Magnetite in the replacive grains in Figure 4.10 and Figure 4.6. Numerous fractures cut the outshooting Spinel grains in Figure 4.12 and Figure 4.11. None of these fractures propagate into the surrounding silicate minerals. The cause of the fractures that is proposed here is volume subtraction of solid grains. Like when water saturated

mud dries up, loses its volume and cracks. If the Chromite volume-increase with temperature observed by Levy and Artioli (1998) occurs at high pressures, the cooling from such high temperatures will consequently cause a volume decrease in the same Chromites. If this is the case (and volume expansion is the only hypothesis to explain the observed Spinel outshoots in Figure 4.6, Figure 4.12 and Figure 4.11), all the Chromites must have expanded during a reheating event where only some grains ended up fracturing the surrounding silicates while others filled existing porosity. This explains why only 3 chromian Spinel grains with outshoots are observed. All grains were then cooled, and their volume decreased. For some grains the strain must have been accommodated, as fractures is not observed in all chromian Spinels. In others, especially the large grains in the figures mentioned above, the strain caused randomly oriented fractures in the Spinel grains. Because the fractures in all the above mentioned grains cut both Hercynite and Magnetite both these phases must have been formed prior to the fracturing event.

It is also possible that the fracturing observed is a very late structure formed either during the Caledonian orogeny, the isostatic re-equilibration related to the ice ages, the drilling process or the thin section cutting process. Some Spinels (e.g. Figure 4.13) are cut by fractures that continue into the surrounding cumulate silicates. These fractures have a distinct orientation. The fractures discussed in this section are randomly oriented, indicating that Caledonian orogeny and ice age (de)glaciations are unlikely to have formed them.

5.4.3 Recrystallization

According to several papers (Barnes and Roeder, 2001, Kamenetsky et al., 2001, Roeder, 1994) it is common to find ferrian Chromite rims on igneous Chromite grains. The ferrian Chromites, or metamorphic Magnetite, is in this thesis found as patches along the outside Spinel border (e.g. in the lower right corner of Figure 4.11) or cutting the Spinel through what is assumed to be previously formed weakness zones (e.g Figure 4.4).

There is a common system of grain-rim interaction in some of the Spinels as previously mentioned, but that is Magnetite grains with Hercynite (very Fe^{3+} poor) rims. As discussed in the Replacement texture section this is only observed in some grains. As discussed in the Volume change section, Spinel type 1 and 3 must have both formed prior to the extensive mixing and fracturing observed in some grains. Some of the chromian Spinel grains that have Spinel type 1 and 3 in contact are

found in contact with abnormal silicates and carbonates: Figure 4.11 is in contact with Amphibole and a more Mg rich Olivine than the cumulate Olivines. Figure 4.7 and Figure 4.12 are in contact with a more Mg rich Olivine than the cumulate Olivine. Figure 4.10 and Figure 4.6 are in contact with both Mg rich Olivine and carbonate minerals. The Mg-rich Olivine is more primitive than the cumulate Olivine and represents either re-equilibration with chromian Spinels where the Olivines were enriched with Spinel Mg or a pervasive primitive magma that assumedly re-equilibrated with the Spinel as well as crystallizing Olivine. The CS-forming Ol-saturated intrusive magma is a likely candidate, so is the pervasive carbonaceous melt that formed the calc-alkaline clots. Grant et al. (2016) noted that the CS forming melt formed interstitial Olivines in Olivine clinopyroxenites. They claim that channelized melt flow through the cumulates was the dominant melt transport mechanism, but that some must have been transported through porous flow within the cumulates to form the interstitial Olivines.

In Figure 4.10 and Figure 4.6 the carbonates makes it clear that a highly carbonatite metasomatized pervasive magma (Grannes, 2016, Grant et al., 2016, Grant et al., in prep., Larsen et al., 2018, Nikolaisen, 2016) interacted with the Spinels; either re-equilibrating or crystallizing chromian Spinel, carbonates and probably the odd Olivine. The Amphibole in Figure 4.11 could also have crystallized from such a fluid-rich melt. The odd Olivine could however also have formed by re-equilibration with very high-Mg Spinels. Al rich (>40 wt% Al_2O_3) can be formed in low pressure systems (Allan et al., 1988). Irvine (1967) suggested they could be formed in very deep systems. It is likely that Al-rich chromian Spinel formation is not controlled by density but rather by chemistry of the crystallizing magma or the unit equilibrating with a Spinel.

Two types of Magnetite are present in the RUC lithologies: primary magmatic Magnetite (group 3) and metamorphic Ti-rich Magnetite called Fe-Ti (see Figure 4.4, Figure 4.7, Figure 4.10 and Figure 4.11). Ti-rich Magnetite is caused by a combination of extensive trapped liquid reaction and variable degrees of low-pressure fractionation (Barnes and Roeder, 2001).

Magnetite and Chromite lose more Al than Cr during metamorphism and reaction with silicates and metamorphic fluids, forming chlorite and Amphibole. Metamorphic Magnetite has a very high Cr/(Cr+Al) ratio because of this. Magnetite do not have either Cr or Al in its pure chemical formula, but do contain Fe^{3+}. Because of this, both metamorphic and primary Magnetite plots high on $Fe^{3+}/(Fe^{3+} + Cr+Al)$.

There is limited solid-solution between aluminate Spinels and ferrite Spinels at the temperatures found in nature (Sack and Ghiorso, 1991a). This is observed as sharp borders between Hercynite and primary Magnetite in all Spinels except for Figure 4.13. The borders between all Spinel phases and metamorphic Fe-Ti oxides are always sharp. This is another example of the limited solid-solution in the Spinel gap. Between Hercynite and Chromite, most chemical Spinel compositions are present in the analyzed Spinels (Appendix B and Appendix C).

As phrased by Barnes and Roeder (2001):

> *"Processes of high- and low-pressure crystal fractionation and crustal contamination are recorded by the Spinel chemistry... Chromium-rich, Mg-rich Chromites are the hallmark of primitive mantle-derived magmas that have not undergone these overprints... The global distribution of Spinel compositions is influenced greatly by the rarity of preservation of primitive mantle melts… Many factors must be taken into account, particularly the tendency of Chromites to re-equilibrate with surrounding siilicates during prolonged cooling and metamorphism."*

It is highly likely that re-equilibration of the Fe-number and Mg-number of the chromian Spinel took place with surrounding residual melt and silicate minerals post Spinel crystallization due to the slow cooling rate and great depth of the RUC as proposed by Larsen et al. (2018) and Orvik (2019). Roeder & Campbell (1985) found that the $Fe^{2+}/(Fe^{2+}+Mg^{2+})$ ratio found in disseminated low concentration Chromite grains would rise by slow cooling or equilibration with coexisting silicates (often Olivine) (Roeder and Campbell, 1985). Roeder (1994) proposed that the chemistry of a Spinel grain with a metamorphic rim will be strongly chemically affected by the rim-forming reaction. This last hypothesis is not supported by the results of this thesis. Most of the analyzed grains were small and only consisting of one Spinel type. Such grains should have a different chemical composition relative to the grains that have rims if Roeder is correct (Figure 4.18-Figure 4.28 and Figure 5.4-Figure 5.6).

5.4.4 Element plots in Spinel grains

The Ti-Al plot in Figure 4.20 is one of very few plots where there is no significant division in chemistry between the different types of chromian Spinel. In the Ti-Al plot there is a decreasing trend where increasing Ti decreases the Al in Spinels. This is a feature explained by Kamenetsky et al. (2001). Both Al and Ti have a positive correlation between concentration in melt and concentration in crystallized chromian Spinel. Kamenetsky et al (2001) found that with increased Ti available in mafic volcanic melts, the activity of Al into the chromian Spinel lattice decrease. The connection is not obviously also true for deep rooted ultramafic systems like the RUC, as the P-T conditions in the surface-near flood basalts Kamenetsky et al. (2001) studied are significantly different than the P-T conditions seen in Figure 1.2. As all Spinel types plot sub-linearly with a negative trend it appears that the general Kamenetsky et al. Al-Ti hypothesis can be extended to include deep ultramafic systems.

In the Ti-Cr Spinel plot (Figure 4.19), the Spinels plot in a trend like an offcut sinus curve. The Spinels of group 1 has up to ca 0,5 wt% TiO_2 with increasing Ti as Cr increase. Group 2 has quite stable, possibly decreasing Cr_2O_3 with increasing TiO_2. Group 2 has the highest Cr content of all the Spinel types. Group 3 have high Ti and medium-low Cr except for 3 outlier measurements. There is no conclusive Spinel correlation between Cr content and Ti content.

Mg-rich (and Cr rich) Spinels are generally interpreted (Barnes and Roeder, 2001, Kamenetsky et al., 2001, Roeder, 1994) to be associated with the most primitive Spinel compositions, as these are found associated with Fo in primitive basaltic rocks, mantle peridotite and chromitite rocks. As seen in Figure 4.21, group 1 is most Mg rich, followed by group 2. Group 2 is most Cr-rich, followed by group 3 and 1. Overall, then, it is not easy to interpret which Spinel group is the more primitive based on Cr and Mg ratios. Cr- and Mg enrichement in Chromites reflect primary crystallization from primitive, unfractionated mantle-derived magmas (Barnes and Roeder, 2001). Since no Spinel group in this thesis are most enriched in both those elements, these Spinels probably crystallized from primitive and mantle-derived but fractionated melts.

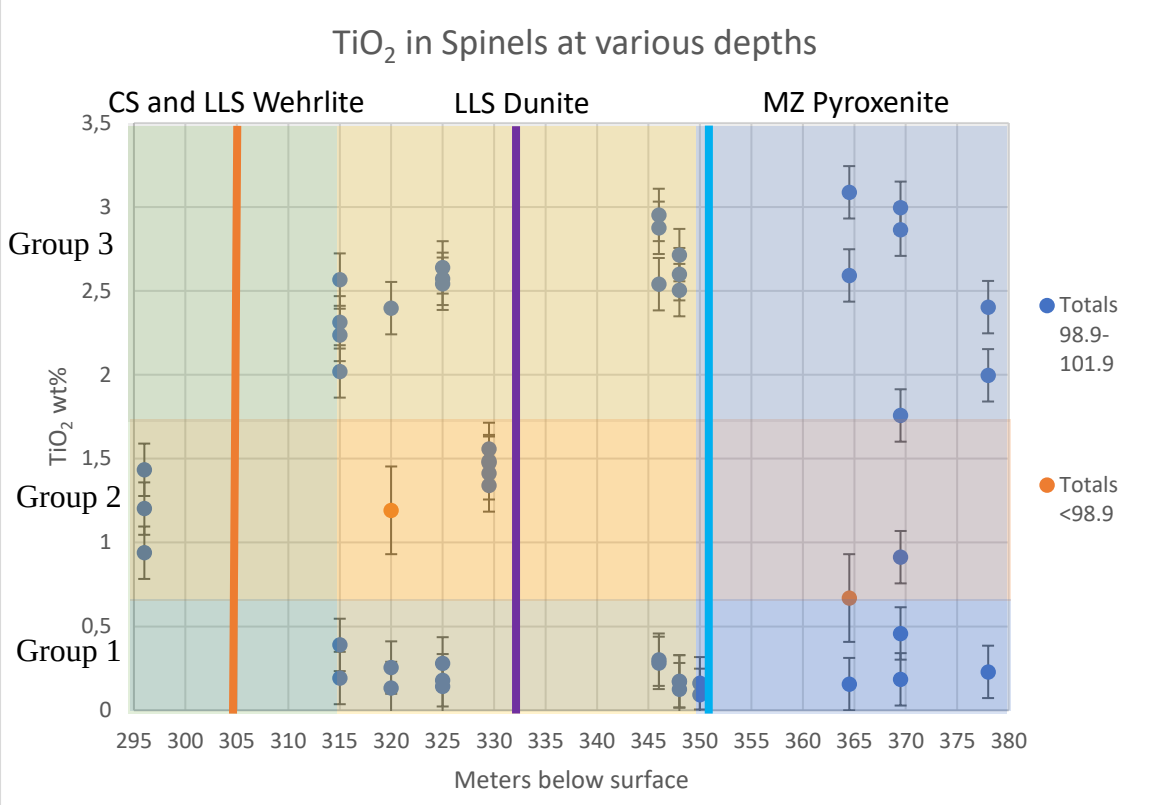

Figure 5.3

The average measured TiO_2 content in each analyzed Spinel mineral plotted with σ uncertainty bars. Two grains with outlier totals have been included as they are potentially important to understand the Spinel crystallization. Horizontal boxes mark the Spinel groups (bottom is group 1, middle is group 2 and highest is group 3) and vertical boxes mark the lithology.

The lack of lithological system in Spinel composition can be seen in Figure 5.3. All three RF4 lithologies have analyzed Spinels of group 1, 2 and 3 except for the upper wehrlite that only has one thin section. The rare type 2 Chromites appear with seeming randomness. Immediately above the blue fractionation line, at the bottom of the dunite section, both Hercynite and Magnetite appear to have increasing TiO_2 concentrations with decreasing depth. As there is a 15 meters gap and the purple fractionation line between the highest of these Spinel analyses and the next, no conclusion can be drawn due to lack of data points.

5.4.4.1 RUC Spinels compared to other Spinel compositions

The plot by Kamenetsky et al. (2001) consists of 19 000 Spinel compositional data points. The basis for all the density plots (9 completely different geological categories each with 2-6 sub-categories) are 40 000 data points (Barnes and Roeder, 2001). Most of them are probably from the commonly analyzed lithologies MORB, OIB and ARC. The few analyzed LIPs are likely from well known and not necessarily deeply formed basaltic flood-plains and intrusions. There is a high likelihood that unusual or otherwise geologically interesting rocks and minerals have been over-sampled instead of sampling to give as representative an image of the world's Spinels as possible. E.g. there are significantly more Chromites than Magnetites analyzed. Comparing to their data will therefore not necessarily give many decisive conclusions but is useful to give an indication of how similar the globally unique RUC is compared to what has been observed other places.

5.4.4.2 Spinel prism

In Figure 5.4 and Figure 5.5 the Spinel chemical plots have been overlain with part of the Spinel database from Barnes and Roeder (2001). The Barnes and Roeder category "Spinels from layered intrusions where chromitites, subvolcanic intrusions and flood basalts have been removed" is used. Most of this thesis' Spinels are from the ultramafic Lower Layered Series, and so this is the dataset from Kamenetsky et al. (2001) and Barnes and Roeder (2001) that best fit these Spinels for comparison.

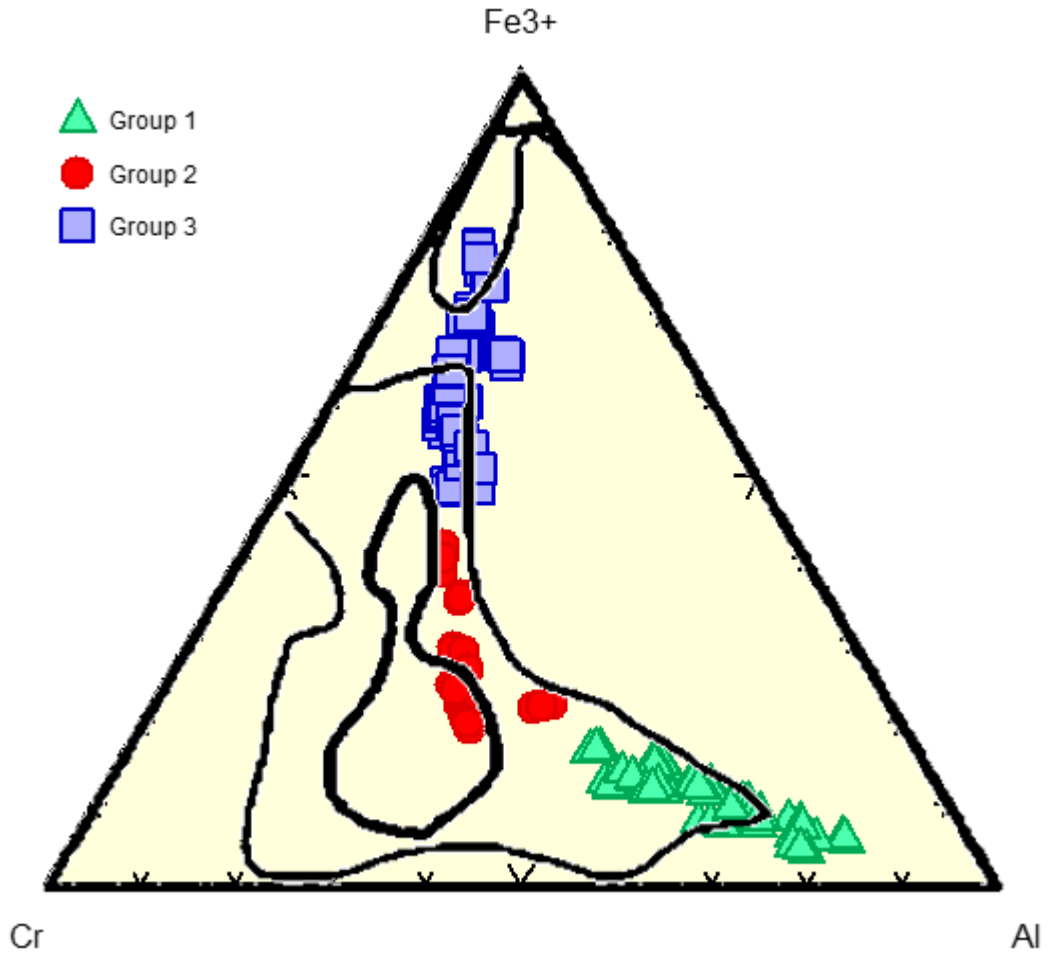

Figure 5.4

Ternary Spinel prism with Cr^{3+}, Al^{3+} and Fe^{3+} in the mineral formula as the input parameters. All EPMA analyses with reasonable oxide totals are plotted in this diagram, sorted by mineral group. The Spinel prism is overlain with a density plot of layered intrusions from Barnes and Roeder (2001). The thick areas cover 50% of the Barnes and Roeder (2001) Spinels, while the thinner areas cover 90% of their Spinels.

The area between the Fe^{3+} and Al endmembers in Figure 5.4 is the Spinel gap. The Spinel gap clearly appears in both the RF4 Spinels and the Barnes and Roeder (2001) Spinel database for layered intrusions. Most of the Spinels from the database density plot is less Al rich or endmember Fe^{3+} in composition than the Spinels from RUC. However, the RUC Spinels are for the most part within the 90% density area. As ca ¼ of the group 1 and ca ¼ of the group 3 Spinels are outside the thin area in the Spinel prism, the most endmember compositions of both group 1 and 3 are anomalous.

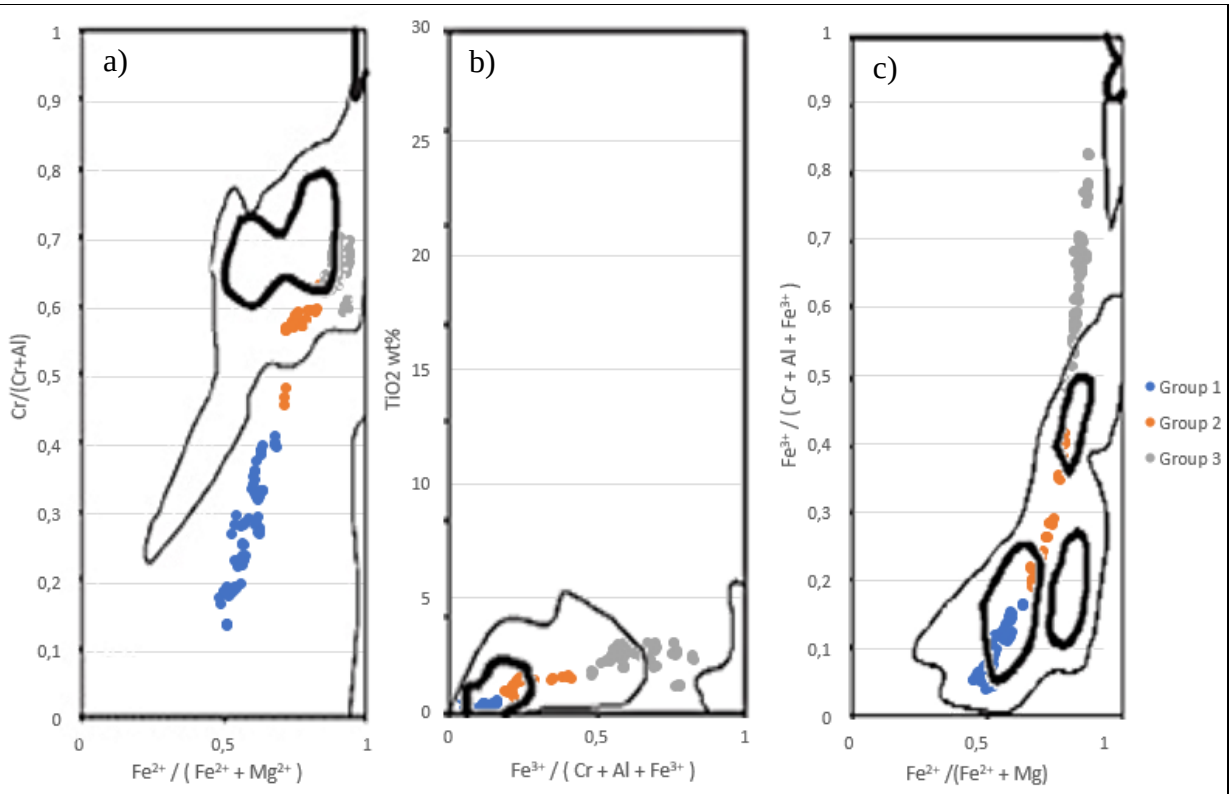

Figure 5.5

Spinel chemical diagrams from Barnes and Roeder (2001) with overlain Spinel compositions analyzed in this thesis.

a) Cr-number and Fe^{2+}-number overlain with density diagrams from layered mafic-ultramafic intrusions Spinels.

b) TiO_2 and Fe^{3+}-number overlain with density diagrams from layered mafic-ultramafic intrusions Spinel.

c) Fe^{3+}-number and Fe^{2+}-number overlain with density diagrams from layered mafic-ultramafic intrusions Spinel.

The Cr# vs. Fe^{2+}# in Figure 5.5 a) show the only of the Barnes and Roeder figures where the majority of Spinel measurements do not to some extent agree with the plots from Barnes and Roeder (2001). In fact, the RUC Spinels of group 1 and 2 do not fit with the Spinels in any of Barnes and Roeder's 40 000 Spinel database when plotting Fe^{2+}-number vs. Cr-number. In Figure 5.5 a) the entirety of group 1 and group 2 plot outside the 90% zone. More than that, group 1 and 2 plot in what Barnes and Roeder has claimed to be the Spinel gap in the Cr#-Fe^{2+}# diagram. The fact that the Spinel chemistry – which fits remarkably well with the Barnes and Roeder limited

data on layered intrusions – do not at all agree with the observed trend in the Cr#-Fe^{2+}# diagram suggest that the Fe^{2+}:Mg^{2+} and Cr:Al ratios could be different for Spinels formed in very deep layered intrusions formed in LIP setting compared to the "regular" layered mafic-ultramafic intrusion Barnes and Roeder (2001) have in their database. Spinels with compositions within the Spinel gap can be stable, but is rarely so in the presence of Cpx and melt (Roeder, 1994). The trend in Spinel composition and the Spinel gap will vary for different melts, fO_2 (Hill and L. Roeder, 1974) and pressure. At the distinctly uncharacteristically high pressure of RUC formation, it is plausible that the Spinel gap is significantly moved compared to that outlined by Barnes and Roeder (2001).

In the TiO_2-Fe^{3+}# and the Fe^{2+}#-Fe^{3+}# plots of Figure 5.5 b) and c) group 1 and part of group 2 are within the 50% density area of Barnes and Roeder's plot. In both diagrams part of the group 3 fall outside the 90% density area. The Spinels of group 3 outside the 90% density area do however bridge two segments of the 90% area. The group 3 Spinels would probably have equilibrated to separate into either of the two endmembers under more ordinary circumstances (i.e. shallower depth and with smaller degree of protolith melting).

The diagrams in Figure 5.4 and Figure 5.5 b) and c) strongly exhibit what Barnes and Roeder called the FeTi trend. They interpreted this trend to come from fractionation within the crust combined with chemical overprinting by reaction with accessory cumulus Spinels and evolving trapped intercumulus melt (Henderson, 1976, Henderson and Wood, 1982, Roeder and Campbell, 1985, Scowen et al., 1991).

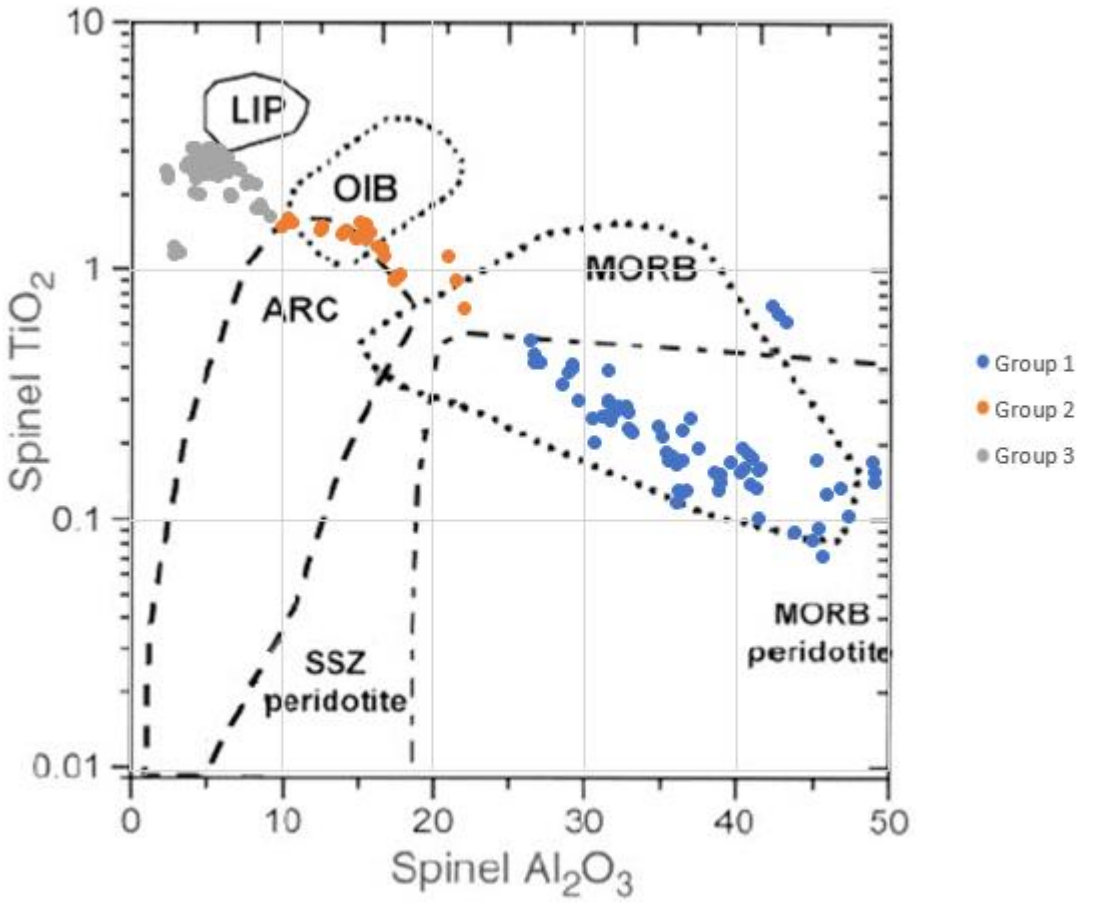

Figure 5.6

Spinel TiO_2 vs. AL_2O_3, where all Spinel measurements are included and organized into groups. The diagram is overlain with results from Kamenetsky et al. (2001) for their modeling of Spinels found as inclusions in primitive Olivine (Fo >84).

In Figure 5.6 the Spinel Ti:Al oxide ratio has been overlain by the Kamenetsky et al. (2001) Spinel type area diagram for Spinels crystallized in various geological settings. RUC being part of the SIP, it would be assumed that at least a significant portion of the Spinels plot inside the LIP area in Kamenetsky et al.'s diagram. Group 3 Magnetites plot just below the LIP area due to too low Ti content. Group 2 Chromites plots somewhere between Island Arc (Bosi et al.), Ocean Island Basalt (OIB) and Mid Ocean Ridge Basalts (MORB). Group 1 Hercynites plots in the MORB to MORB peridotite area. All in all the Kamenetsky et al. Spinel origin hypothesis do not fit well with what is observed in Reinfjord. The Spinels analyzed by Kamenetsky et al. (2001) were all from Spinel inclusions in Olivine that were found in rapidly cooled volcanic rocks. The "LIP" Spinels came from the flood basalts above LIPs – and not from the deeply formed and likely deeply

chemically re-equilibrated Spinels examined here. Most flood basalts have evolved compositions (<8 wt% MgO) (Jennings et al., 2017, Sobolev et al., 2009), while rare high-MgO (<12 wt% MgO) is considered the purest records of the most primitive magmas generated in the mantle beneath LIPs (Heinonen et al., 2015, Jennings et al., 2017, Kamenetsky et al., 2012, Thompson and Gibson, 2000). A <12 wt% MgO is modeled for the melt that formed the SIP (Grant et al., in prep.). It is however interesting to note that the group 1 Spinels that are anomalous in the Spinel prism, the Cr#-Fe^{2+}# and the Ti-Cr plots are persistently within the Kamenetsky et al. MORB Spinel composition. That indicates that whatever mechanism formed the group 1 Spinels has a similar formation in MORB Spinel crystallization.

MORBs, like LIPs, have a massive degree of protolith melting and influx of magma via mantle plume. A mantle plume origin has been suggested for SIP (Larsen et al., 2018). MORBs crystallize at high temperatures but low pressures. The Spinels found as inclusions in Olivine crystallize prior to the MORB magma abrupt cooling by ocean water. Because of this, the low pressure but high temperature setting is the only peculiar MORB crystallization feature. If we assume the group 1 Spinels formed under similar conditions, substantial heating while at shallow depths must have occurred. The only way that could have occurred is by influx of very warm magma (either the replacive CS magma or the low-viscosity calc-alkaline carbonate-forming magma) happened at a lower pressure than the CS cumulate formation. From Larsen et al. (2018) the CS formed by intrusion at great depth. From Orvik (2019) the RUC dyke swarm formed at approximately 10-14 kbar. Neither has found evidence of a low-P heated event in the RUC history. Another possibility is that Spinels of Hc composition have a very extensive stability field.

Another explanation for the observed gap between the extensive Spinel research by Kamenetsky et al. (Kamenetsky et al., 2001) and the RUC chemistry is that the Kamenetsky Spinels were all inclusions within Olivine while the Spinels analyzed in this thesis were mostly individual (interstitial or cumulate) crystals. Spinels inside an Olivine will, when equilibrating, be limited to the Olivine's chemistry for chemical substitutions. Individual Spinel crystals will equilibrate with whatever they contact; be that Olivine, pyroxene (a rare phenomenon according to Roeder (1994)), sulfides, Amphiboles, carbonates or magma. It is therefore possible that the Spinel compositions found by Kamenetsky et al. (2001) are more similar to the primary Spinel compositions than what is found in the RUC Spinels in this thesis. Group 3 Mt have the most similar composition to the

LIP area in Figure 5.6. Group 3 is in several cases surrounded by a rim of group 1 Spinel. Those grains would be chemically shielded from equilibrating far from the original Spinel chemistry. Most of the group 3 Spinels are however not, and whatever equilibration that group experienced seems to be equal for grains that have and do not have group 1 rims.

The Spinels of group 2 and 3 are found as inclusions in Olivine in RUC. It is strange then that Spinels of similar composition to group 2 Chromite is not also found as inclusions in continental flood basalts analyzed by Kamenetsky et al. (2001). Group 2 Chromite plots unexpectedly far from the LIP bubble in Figure 5.6, as these are hypothesized to have co-crystallized with cumulate Ol in the MZ and LLS. If the Kamenetsky et al. (2001) measurements are accurate, the RUC Chromites have undergone significant re-equilibration distancing it from its primary composition. Alternatively, the primitive Spinel inclusions from continental flood basalts in Figure 5.6 have Magnetite as inclusions in Olivine, not both Magnetite and Chromite as the RUC Olivines do.

The Ti-Al trend presented by Kamenetsky et al. for LIPs are a bubble, while it is a negative exponential to linear trend in the RUC.

Barnes and Roeder (2001) noted that there are relatively unaltered Chromites with very low Fe^{3+} composition found in essentially unmetamorphosed komatiitic dunites which indicate that they are primary liquidus compositions which records very primitive magmas. The only other similarly reduced Chromites are found in ophiolitic chromitites. They also preserve primitive liquidous compositions. Both komatiites and the parent magmas of ophiolitic cumulates formed by high degrees of melting of reduced depleted mantle (Barnes and Roeder, 2001), as the SIP did. It is unclear how low Fe^{3+} concentrations are in Barnes and Roeder's chromties, but they could be compared to the group 2 Chromites studied here.

Kamenetsky supports that Mg, Fe^{3+} and Ti decrease along an increasing Si and Al and decreasing P-T conditions for magma formation during source mantle melting (Kamenetsky et al., 2001). Most of the chemical components of this hypothesis is observed in our analyzed Spinels: Mg however is observed to increase with decreasing Fe^{3+} and Ti and increasing Si and Al. If the P-T part of the hypothesis still holds, group 3 crystallized deepest, followed by group 2 and finally group 1**.** This is not the Chr→Mt→Hc crystallization history assumed based on ternary

crystallization diagrams. The variation in $Fe^{2+}/(Fe^{2+}+Mg)$ has two sources: evolving melt composition and exchange of Fe^{2+} and Mg between Spinel and coexisting phases. Both favor increasing Fe-number in Spinel with decreasing temperature (Irvine, 1965). Low Fe-number in Spinels reflect the high temperature of equilibration with coexisting phases. As the expected evolution in Fe-number is not observed, it could be that the rocks were not slowly cooled after crystallizing, but rather heated by the intruding CS-forming warm, primitive magma. After that, though, it is likely the RUC experienced slow cooling until Caledonian uplift occurred.

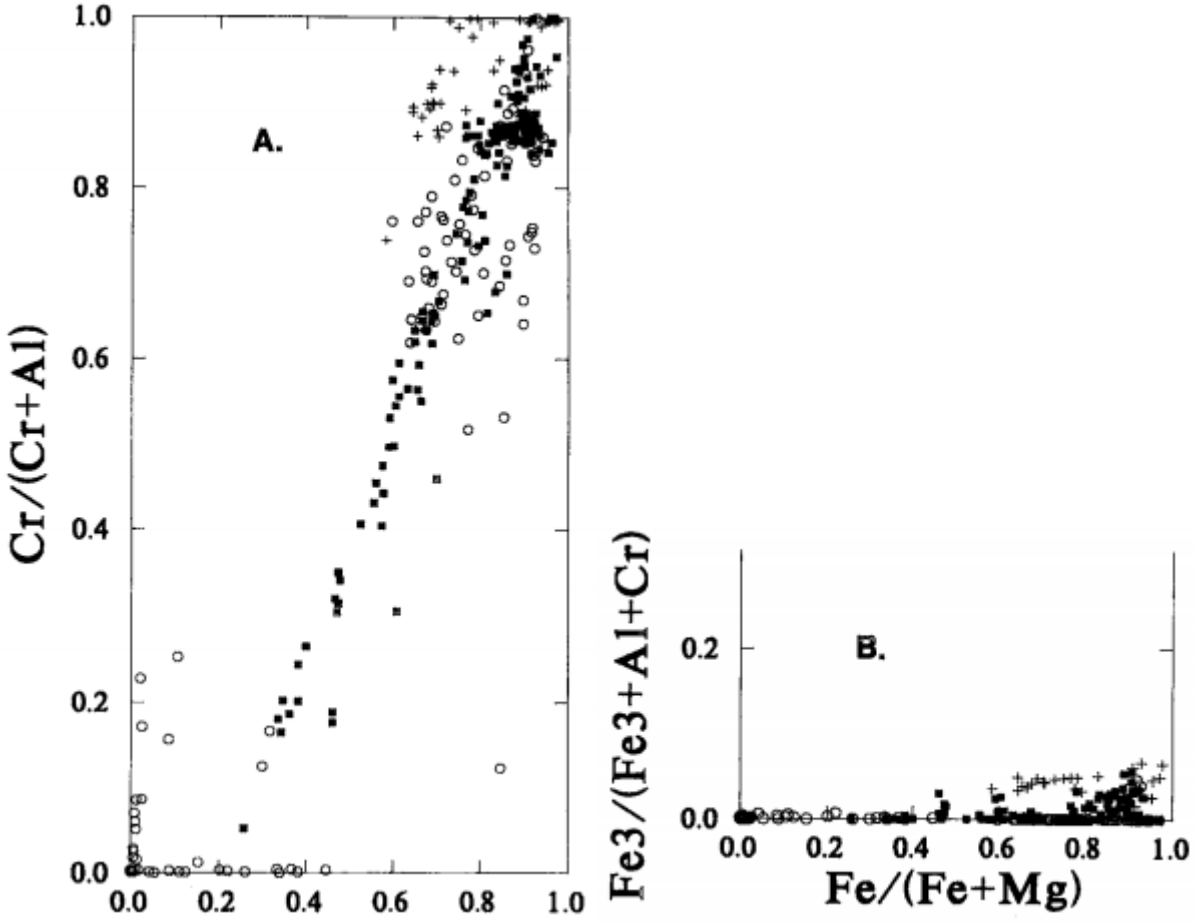

Figure 5.7

Spinel compositions from chondritic meteorites, from Roeder (1994). Open circles: CAI fragments in unequilibrated carbonaceous chondrites. Crosses: Unequilibrated ordinary chondrites. Filled squares: equilibrated ordinary chondrites.

Neither of the Spinel groups correlate with the equilibrated and unequilibrated chondrites in Figure 5.7. This gives the expected conclusion that the parental magmas from which the Spinels crystallized were part of the chemically segregated mantle.

5.5 Clinopyroxene crystallization

Grant et al. (2016) found that the RUC Olivines were abnormaly depleted in CaO. The depletion is found in other of the SIP intrusions: the Nedre Brumandfjord (Griffin, 2013, Yeo, 1984) as well as some of the mafic intrusions (C.Y. et al., 2014 , Jagoutz et al., 2007). They explain it by assuming that Olivine underwent sub-solidus re-equilibrated with Clinopyroxene during cooling, as the Ol/Cpx partitioning coefficient for Ca decrease with temperature (Coogan et al., 2007, Köhler and Brey, 1990). Sub-solidus elemental re-equilibration between major mineral components are assumed for the RUC. This process is rarely used in explaining chemical compositions in mafic-ultramafic melts for Clinopyroxene and Olivine. It would be very strange then if the abundantly noted re-equilibration between chromian Spinels and surrounding minerals has not taken place here.

5.6 Al, Na+K and Ca

Ca is mainly found in Clinopyroxene and carbonate minerals in the RF4. Al is mainly found in Clinopyroxene and Spinel minerals. The alkali metals Na and K are mainly found in Clinopyroxene, Orthopyroxene and Amphibole. The only common denominator mineral is that all the elements are found in Cpx. As all three graphs in Figure 4.45 and Figure 4.44 have a very good correlation, it is reasonable to assume that most of the chemical contributions of each element stem from the Cpx content. There are some exceptions, such as the Al and Na+K peaks at 309m and 338m almost reaching as high as the Ca peak at the same depths. This indicate that those rocks could contain plagioclase or Amphibole. Between 88m and 73m, the Al and Na+K graphs look similar while the Ca graph changes differently. Here it is also likely that either Ca or Al+Na+K in part comes from a non-Cpx mineral.

Generally speaking the Na+K is much lower in the CS lithologies than in the MZ and LLS lithologies. As metasomatism is observed throughout the RF4 drill core, it suggests that the

primary cumulate-forming magmas that formed the MZ and LLS were more calc-alkaline than the magmas that formed the CS.

A significant part of the Al could come from the Spinels, as group 1 and 2 Spinels have substantial Al in their chemical formulas. Group 3 has less Al in its chemical formula. In that case, the Cpx (responsible for Ca, Na+K and part of Al) has a good correlation with the Spinels of type 1 and 2. This indicate a primary magmatic origin for both Spinel types.

5.7 Nickel

When Ni is enriched or depleted relative to the Fo content, it is assumed to be explained by interaction with Ni-Fe-S liquid (Barnes and Naldrett, 1985, Li and Naldrett, 1999, Li et al., 2004). Iljina (2013) noted very high variations in NiO contents from the Ni-Cu-PGE reefs, indicating that this process is at work in some parts of the drill core. Grannes (2016) noted cryptic variations in Mn and Ni with Fo, but that the variations in Ni were too large to be explained by encasement in Fo (Grant et al., 2016). If sulfide saturation is reached after a significant portion of Olivine has been crystallized, most of the Ni will have already been incorporated into the Olivines. When sulfide immiscibility takes place early in a magma's intrusion and subsequent crystallization, then Ni will likely be enriched in sulfide due to its siderophile nature.

Nickel is present in trace amounts in the silicates Olivine and pyroxene, where it has substituted for other 2+ valence cations. It is also present in trace amounts in Spinels, and in substantial amounts in the sulfide pentlandite. As Ni in large parts of the RF3 (Figure 4.32 b) and RF4 (Figure 4.32 a) show little to no correlation to sulfide, herein the only mineral where it is a significant constituent, it must be concluded that the anomalous Ni in the rest of the drill cores comes from Ni in silicate constituents. As there are no identified Spinel seams in either drill core, this mineral is probably Olivine (and maybe pyroxene, though the Olivine concentration far supersedes the pyroxene concentration in most of the drill core).

Three major Ni enriched places are found in the RF4 drill core. The two shallowest peaks are also the highest, as seen in Table 16. They are both from rocks that are anomalously enriched in S. Because of this, it is likely the Ni peaks stem from pentlandite. The next large Ni anomaly is 45m wide and found below the green fractionation line. This Ni anomaly do not coincide with increased

S. On the contrary, there is almost no S in that interval. Ni in this CS dunite area is therefore believed to be encased in silicate minerals, mainly Olivine. The 45m wide Ni anomaly is found where the fractionation discrepancy is located and used as part of the evidence that the discrepancy actually indicate new influx of material rather than fractionation.

5.7.1 Ni and fractionation

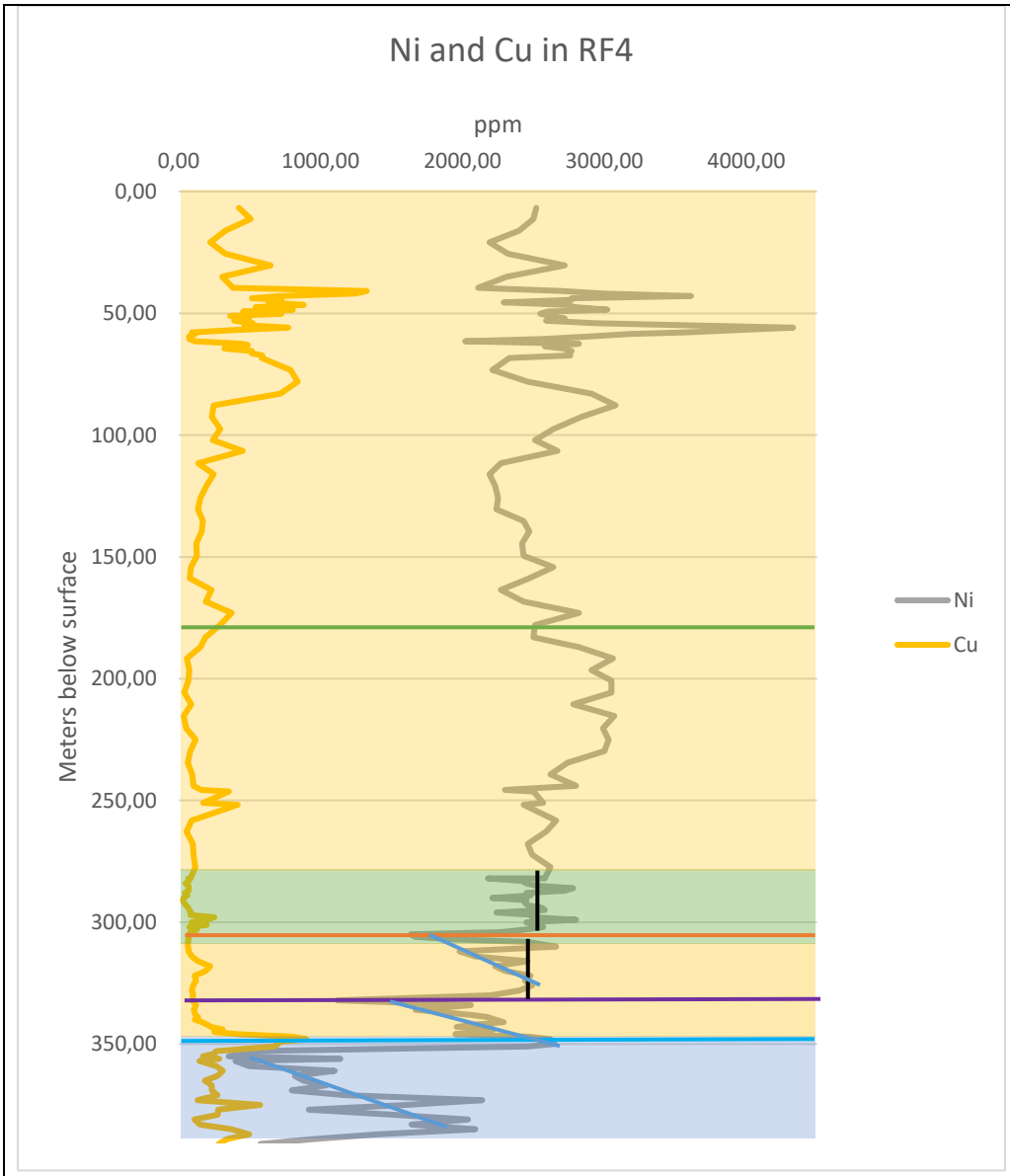

Figure 5.8

Diagram depicting how the Ni and Cu concentrations of the RF4 drill core correlate with the green, orange, purple and blue fractionation lines from Figure 4.39. Black horizontal lines mark areas where Ni is constant, blue lines mark where Ni decrease.

The Ni trends can be seen in Figure 5.8. As marked by blue arrows, Ni decrease when approaching a fractionation line. Immediately after the fractionation lines, Ni increases. As Ni is compatible and easily stubstitutes into Olivine, large scale decreasing trends such as is observed 390-350m, 350-335m and 335-305m supports that fractional crystallization of Olivine with gradual depletion in Ni occurred in those cumulate intervals.

Two intervals are marked with constant, black lines in Figure 5.8: 335-305m and 305-280m. The fact that the 335-305m interval has both a decreasing and a constant trend can be explained by sills of the CS magma that formed the 305-280m replacive wehrlite interval. Such sills were observed in the RF1 drill core by Nikolaisen (2016).

5.8 PGE

When a TEM scan intersected increased conductivity in RUC, a 600x600m open bowl shaped conductor between 60 and 110m deep was modeled (Schanche et al., 2012). When the RUC was sampled by drill core RF1 and RF2 a PGE-reef in RF1 appeared and is thought to account for the increased conductivity. When RF3 and RF4 were drilled and studied, a PGE reef in RF4 appeared. The spatial relationship between a Cu reef ca 20m above the PGE reefs is consistent in both RF1 and RF4. The PGE reef in RF1 has been studied by Nikolaisen (2016) and the PGE reef in RF4 has been studied by Tollefsrud (2018). Based on reef thickness it is believed that the RF1 reef is close to the center of the "bowl" while the RF4 reef is probably along the "bowl" edges (Tollefsrud, 2018). In RF1 the PGM are (bismutho)tellurides, while in RF4 they are(sulf)arsenides and antimonides. In RF1 the PGM are found as inclusions in sulfides while in RF4 mainly are found along the grain boundaries of sulfides. Some of the RF1 PGM are found associated with potentially post-magmatic concentration processes (e.g. native Au and PGM are found in a pyroxenite pegmatite with zoned Amphibole). Late processes (e.g. carbonate clots) are observed in the PGE reef in RF4 as well, but not in close relation to the PGM. Nikolaisen (2016) observed a textural PGM evolution from large grains at the bottom of the PGM reef and smaller grains upward; a sedimentary settling sequence. From this it is assumed that the PGE reef in RF1 is a stratigraphic PGE horizon settled on the floor of the magma chamber. From this is extrapolated that the PGM probably formed by sedimentary deposition of PGE enriched sulfide droplets in the cumulate slush

(Nikolaisen, 2016). Both the RF1 and RF4 PGE reefs appear in close relation to a sharp increase in MgO near the PGE anomaly. This is thought to represent a recharge event.

Generally speaking, PGE are thought to concentrate magmatically into viable ore deposits by sulfide immiscibility with a high R factor, usually caused by replenishment in large magma chambers in the Earth's crust (Daltry and Wilson, 1997).

5.8.1 Upper PGE reef: RF1 (540,8-541,55 m.a.s.l.) and RF4 (574,5-575,5 m.a.s.l. = 61,5-62,5m)

Nikolaisen (2016) proposed three main hypotheses on why RUC is PGE enriched:

1) Gradual in-situ enrichment in a magma chamber that eventually accumulated as a PGE horizon
2) Late melt recharge with immiscible sulfide liquid that was already PGE enriched
3) Late remobilization of PGE enriched sulfides

Tollefsrud (2018) proposed a fourth hypothesis, mainly to explain the lack of S-Pd correlation:

4) Intrusion of a more primitive, PGE depleted melt after formation of the PGE reef

A fifth, which is a combination of previous ideas is proposed here:

5) In situ enrichment of PGE in magma chamber until recharge of a S rich magma caused sulfide immiscibility.

All the hypotheses above (possibly except 2) assume a highly turbulent magma chamber where a liquid sulfide phase could be held in suspension.

If hypothesis 1 occurred, it should be visible in the fractionation graphs for RF1. If it is assumed that the same process formed both reefs, this is not plausible as both Fe/(Fe+Mg) and V/Cr graphs are constant in the upper RF4 PGE reef area. Tollefsrud (2018) pointed out that a magma of type 2 would be extremely heavy. A type 2) hypothesis is however believed to explain the Platreef (Holwell and Mcdonald, 2006), so it is plausible. Tollefsrud (2018) conclude that although hypothesis 3) might play a significant role for the PGE enrichment in RF1, it does likely not in RF4. Hypothesis 4 explains why there is a 20m thick enriched S and Cu zone immediately above the PGE reef, but not how the PGE reef itself formed. Hypothesis 5) would not have any major

drawbacks, but relies heavily on the assumption that a small volume of immiscible sulfide liquid was held in suspension significant PGE had been scavenged. This is the only way hypothesis 5) can explain that the PGE reef in RF4 coincides with a S minimum. Another possible process would be:

6) A suspended immiscible sulfide liquid scavenged PGE from large volumes of PGE-containing magma passing through the RUC conduit system, and then later depositing the sulfides in the entire magma chamber floor.

In proposition 1, 5 and 6 a hiatus could be implored. A hiatus period (e.g caused by increased temperature above Ol solidus temperature) in the magma chamber would allow for a long period of sulfide scavenging without cumulate growth.

Both Nikolaisen and Tollefsrud uses the increased MgO associated with their appropriate PGE reefs as proof of a recharge event. However, in the RF4 drill core, the Fe-Mg ratio do not increase (Figure 4.37). In the RF1 Fe/(Fe+Mg) ratio in Figure 4.41 there is a decrease just above the PGE reef. In the PGE reef and below it is a gradual increase in the fractionation ratio.

What Tollefsrud (2018) observe then is that there is more Mg and Fe in a constant proportion present in the cumulates relative to some other element – likely Si and Ca. Simply put, that observed "proof" of a recharging magma is faulty. In RF1, the observed increase in MgO corresponds with a smaller increase in Fe so that the Fe# decrease. This is an indication of recharge as Nikolaisen assume.

The CS forming magma(s) do not show any sign of fractional evolution in Figure 4.41, Figure 4.37, Figure 4.40 and Figure 4.51. This is likely due to the massive quantities of continuously influxing mama through the system in the CS forming period. Changes in element quantities must be considered for entire minerals for us to identify changes in magma constituents. So, when observing the MgO one must also consider the FeO and SiO (the entire Olivine chemical composition) to find chemical changes and not simple changes in mineral proportions of the cumulate.

5.8.1.1 PGE reef in RF1, RF2, RF3 and RF4

As seen in Figure 4.51, immediately above the upper PGE reef in RF4, there is a Ni peak in a small S+Cu reef. 10m above that is a large Cu+S reef coinciding with another Ni peak. This exact PGE – S+Ni(+Cu) – S+Ni+Cu sequence is observed in RF1 on the other side of the fault in Table 17. The sequence is also seen in the RF3 drill core, but here there is no elevated PGE values below the deeper Ni peak (see Figure 4.33 and Figure 4.34, below the purple areas). The same sequence of reefs is not observed in the chemically analyzed 4-168m of the RF2 drill core. Based on the depths of the reef sequence in RF1, RF3 and RF4 in Table 17, the expected altitude of the sequence in RF2 has been calculated in Table 18. The calculations are based on the assumption that the fault between RF1+RF3 and RF2+RF4 only has an extensional dimension without rotation of the hanging wall, as well as that the reef sequence is horizontal where cut by RF1, RF3 and RF4. The depth at which the PGE reef is expected to intersect RF3 is close to where a revision of the RUC profiles (Grannes, 2016) suggest the fault would cut RF3. If the fault is not discrete and linear, the PGE-reef block could have been crushed and partly relocated by the fault. Or if high abundances of fluids permeated the fault, the PGE could have become scavenged by them due to their closeness to the fault core in RF3. Either of these two explanations could be the reason for the substantially lower PGE enrichment in the RF3 where the PGE reef should be compared to the reefs in RF1 and RF4.

As seen in Table 17 and Table 18, the reef sequence has been eroded down in RF2. This would explain why neither the PGE reef nor the rest of the distinctive Cu+S+Ni – S+Ni – PGE sequence is observed in this drill core.

RF1 and RF4 are drilled on opposite sides of the fault from Figure 5.9. They both contain PGE reefs, and it is assumed in the revised profiles that the PGE reef in both were originally the same continuous feature. However, none of the proposed explanations above can explain why the PGM on one side are PGE-tellurides while they are PGE-(sulf)arsenites and antimonides in the other drill core.

As is discussed in the section “RF3 and RF4 displacement”, it is proposed that the fault cutting between RF1+3 and RF2+4 is steeper than previously modeled by Grannes (2016). If the fault inclination is increased, the fault will not cut RF3 immediately below the reef sequence. So if the

conclusion of this thesis is correct in section "RF3 and RF4 displacement", the explanation proposed here to explain the lack of PGE anomaly at 200-180m depth in RF3 must be wrong.

Nikolaisen (2016) proposed that the PGE reef slid down so it is thickest in the bowl center and thinnest near its edges. That is likely his explanation for the lack of PGE reef in RF3. But even so it would be expected to have some remnant of a positive PGE anomaly below the purple area in Figure 4.33. The complete lack of it suggest that something else entirely is causing the phenomenon. Also, Nikolaisen (2016) and Tollefsrud (2018) agree that the PGE and overlying Cu reef(s) has a bowl-shape where it is thickest in the center and thinnest near the edges. If the reason why the PGE reef is absent in RF3 is that RF3 cuts the lithologies near the bowl's edge, then the Cu reef(s) above the hypothetical RF3 PGE reef should be equally thinned. It is not, in fact the Cu reef in RF3 is 5m thicker and of 50-100% higher Cu concentrations than the Cu reef in RF4 where the PGE reef is present (Table 17). So why is there no PGE anomaly in RF3? Assuming that the fault explanation is wrong, these options remain:

1) The lithology below the reef sequence is different in RF3 than in RF1 and RF4.
2) The PGE reef and the rest of the reef sequence was formed during two separate magmatic incidents, where the PGE reef formed first. During the formation of the rest of the reef sequence, the PGE reef was resorbed by the reef-sequence-forming magma and removed in the RF3, but not in RF2 and RF4.
3) Metasomatic processes somehow removed all trace of the PGE reef in RF3

Neither explanation is very likely based on the other chemical data. A remapping of the RF3 drill core should be conducted to answer where the fault cuts the drill core to answer which of the presented fault-related hypotheses are correct.

5.8.2 Lower PGE reef: RF4 (339-336 m.a.s.l. = 297-300m)

The lower minor PGE reef has less than half the PGE concentration of the main reef – but goes over a larger area (3m instead of 1m). The total concentration of the enriched upper reef is only ca 300ppb higher in total than the entire enriched lower reef.

The lower PGE reef is part of the Wehrlite unit in RF4. It is found immediately above the orange fractionation line in Figure 4.51. There is a tiny S and Cu peak at the same place as the PGE reef. Other than that, no other elements change than the PGE and the fractionation ratios.

The fact that there is a PGE reef immediately above the orange fractionation graph gives significant support that the most uncertain of the fractionation indicator lines are correctly interpreted as recharge events. It is in the middle of a lithology with no drastic change in any other element. That the fractionation lines managed to predict where a recharge-formed PGE would be found is impressive. The Merensky and UG2 PGE reefs of the Bushveld intrusion are explained by turbulent recharge with pluming (Kinnaird et al., 2002).

5.8.3 PGE chemistry

When comparing PGE chemistry in PGE and Cu reefs in the RF drill cores it is pertinent to compare the RF4 Cu reef (the main Cu reef) and the RF4 PGE reef (the main PGE reef 20m below the main Cu reef) with the RF1 Cu and PGE reefs (Cu reef 20m above the PGE reef).

The PGE and Cu reefs in Table 17 show that the PGE and Cu reefs of the other Reinfjord drill cores have enrichment in Os relative to Ru and Rh; except for the RF4 PGE reef. The Os concentration in the PGE reef is actually lower than in the Cu reefs of RF1 and RF2. Overall the RF4 PGE reef is significantly more depleted in the IPGE than the RF1 PGE reef. The IPGE and PPGE have different partitioning coefficients between mineral-melt. The IPGE has higher $D_M^{Mineral/melt}$ than PPGE, implying that the IPGE prefer to be incorporated into a solid mineral prior to the PPGE, e.g. during early crystallization of Olivine and Orthopyroxene (Mungall, 2005). Assuming that the PGE reef in RF1 and RF4 is one continuous feature cut by the fault in Figure 5.9: it seems unlikely that the melt that enriched the RF4 PGE reef sulfides had endured more previous crystallization (where the IPGE could be incorporated) compared to the magma that enriched the PGE reef in RF1. The IPGE have low solubilities which decrease with increasing fO_2 that can be locally induced by crystallization of Chromite (Mungall, 2005). Another possibility is for the IPGE to be more/less metasomatically moved than the PPGE.

In an experiment Fleet et al. (1999) found that Os, Ir and Pd obtained higher partitioning coefficients when the S concentration increased. If we assume that PGE enrichment was carried

out by a small volume of sulfide melt, where the PGE reefs had a high degree of scavenging and the substantially more S-rich Cu reefs 20m above had a lower degree of scavenging, it should be expected that the PGE reefs and the Cu reefs have the same general PGE graph shape, but that the graph magnitude separates them. This is not the case, as the Cu reefs have lower Pd than the PGE reefs in their relative magnitudes. As Os and Pd are the anomalous elements, it seems that the observed S-dependant partitioning factor for Os and Pd observed by Fleet et al. is also observed here. Os is enriched relative to the other IPGE in both PGE- and Cu reefs. It therefore seems that the relatively low-S PGE reefs had sufficient S concentration to increase the Os partitioning, but not high enough to increase Ir partitioning.

Another peculiar RF4 feature not observed in the other drill cores is that in the RF4 Cu and PGE reefs it appears that Ru has been preferentially concentrated in the Cu reef rather than the PGE reef compared to the comparable concentrations found in the RF1 and RF2 reefs. Either this means that the RF4 drill core had a higher degree of interaction with the settled PGE reef when large quantities of immiscible sulfide formed the overlying S reef in RF4 than in RF1; or it means that substantial Ru (and possibly Os) were moved by metasomatic processes in the RF1 as those processes were significant in RF1 but not in RF4.

5.9 Remobilization of elements

From Larsen et al. (2018):

> *"... and like any other lithology at the ultramafic centers, they are modified, remobilized and sometimes refined by later igneous events entering the conduit system."*

Magmatic and/or metasomatic alteration processes have been observed in the RUC drill cores and are potential remobilization factors. The upper part of RUC contain more heavily metasomatically removed sulfides than RF1, though PGMs are found to remain in the altered sulfide crystals (Tollefsrud, 2018). In the upper RF1, part of the PGE are found associated with pyroxene pegmatite with zoned Amphibole believed to have formed through fluid reaction (Nikolaisen,

2016). The differences in metasomatism are suggested to be attributed to fault-valve mechanisms (Tollefsrud, 2018).

5.9.1 Magmatic remobilization processes

Post cumulate formation, magmatic remobilization of elements is plausible. A carbonatitic pervasive melt formed carbonate and silicate clots observed throughout the RUC. This melt likely contained high concentrations of CO_2 and possibly other fluids (such as S). This melt could have remobilized PGE+Au as well as sulfide phases, e.g. by Tollefsrud (2018). PGE have higher partitioning into hydrothermal fluids as bisulfide compared to chloride complexes under neutral-slightly alkaline pH and reducing conditions (Mungall, 2005). Under such conditions, the solubility of Pd is twice as high as for Pt, though both are low (Liu et al., 2016). Metasomatic mobilization of PGE are likely in RF1 (Nikolaisen, 2016), but not likely to have caused concentration of the PGE reef in RF4 (Tollefsrud, 2018). The metasomatic processes could have also added sulfides or PGE to the system. There is only one observation of increased sulfide mineralization in a carbonate clot in this study, so this appear to have occurred to a small degree. The PGMs in what appear to be metasomatically removed sulfides could also be crystallized from the volatile phase in a heavily altered area. Since the carbonaceous calc-alkaline melts have low viscosities and densities, they could have flowed through the cumulates through magmatic porosity. Only a small fraction of the melt would be deposited in the porosity and so the small area of the carbonate clots is likely misleading when considering the large volume of the melts that formed them.

The pervasive carbonatitic metasomatic magma or another late magmatic process is believed to have formed the group 1 Spinel, indicating that the magma was substantially Al enriched relative to Cr. Whether the melt formed Spinel group 1 by crystallization or re-equilibration is unclear. To explain the low-Cr, high-Al chemistry of the melt, low degrees of partial melting while forming the pervasive magma is suggested. Based on the primitive Ol crystals around some Spinels, the magma was more primitive than the one forming the cumulate Ol. By medium-low degrees of fractional melting, the magma would assume a very primitive Fo composition, but have low Cr.

There is a dyke swarm in the northern part of the RUC with some dykes found elsewhere in the complex. The dykes are believed to be contemporary with the carbonate clots (Orvik, 2019). The

dykes have variable compositions from gabbroic to pyroxenitic, lamporphyric, wherlitic and lherzolitic. They formed through variable melt influx during isobaric conditions after minor cooling of the CS (Orvik, 2019). The magma forming the dykes likely mixed in a deeper staging chamber from a heterogeneous (variable degrees of metasomatism) composition (Orvik, 2019). The dykes from the dyke swarm had a significant volatile component (Orvik, 2019). Dyke-forming magma could have also had a pervasive component. Since all the dykes have a significant volatile component, the carbonate clots could be the remnants of any one of them.

5.9.2 Serpentinization

Part of the reason why the RUC is such a great locality to observe the primary magmatism in very deep LIP systems is the generally low degree of serpentinization. Serpentine shows an obvious affinity to Olivine in RF4 as well as breaking down chalcopyrite to cubanite and eventually native Cu. Serpentinization appear to affect PGM to a vastly smaller degree than Cu sulfides (Tollefsrud, 2018). In an unaltered system, chalcopyrite would be the main Cu sulfide. In the RUC, chalcopyrite is partly to completely altered to cuprite (see Nikolaisen, 2016 for examples).

Serpentinization of Ol generates Dolomite by the following formula:

Equation 11

$$4Mg_2SiO_4 + 6H_2O + 4CO_2 + 2Ca^{2+} \leftrightarrow 2\,Mg_3Si_2O_5(OH)_4^- + 2\,CaMg(CO_3)_2 + 6H_2$$

The presence of carbonates could be caused by this rather than low-T serpentinization. However, the thin sections with the most carbonates have low degrees of serpentinization, so it is unlikely that serpentinization accounts for more than rare carbonate assemblages. Also, the carbonate assemblages are often related to anomalous Ol, a phase that would be destroyed rather than generated by a serpentinization reaction.

Tollefsrud (2018) concluded that the post-magmatic processes had affected the CS heterogeneously and proposed that e.g. fault-valve mechanisms (Sibson, 1990) or differences in fluid chemistry on each side of the fault could have caused the phenomenon.

5.10 RF3 and RF4 displacement

The fact that the largest PGE reef in RF3 corresponds with the area where the RF3 chemical signature deviates from the RF4 chemical signature (the red area in Figure 4.33 and Figure 4.34) is very curious. This indicate that whatever formed the discrepancy in the red/blue areas in RF3 and RF4 in Figure 4.33 had a PGE-concentrating and precipitating effect. The PGE anomaly is not very large – there are several peaks in RF4 with similar concentrations, but as it is the only anomalous PGE peak in RF3 it is worth investigating.

Three possible hypotheses are proposed that would explain the discrepancy in Cu, Ni, S and Cr and the anomaly in PGE in RF3 indicated by the transition to the red area in Figure 4.33.

1) Fault displacement and hydrothermal PGE concentration/precipitation
2) Local intrusive with PGE enrichement in sulfides in the intrusive roof
3) Variable deposition in one large magma chamber

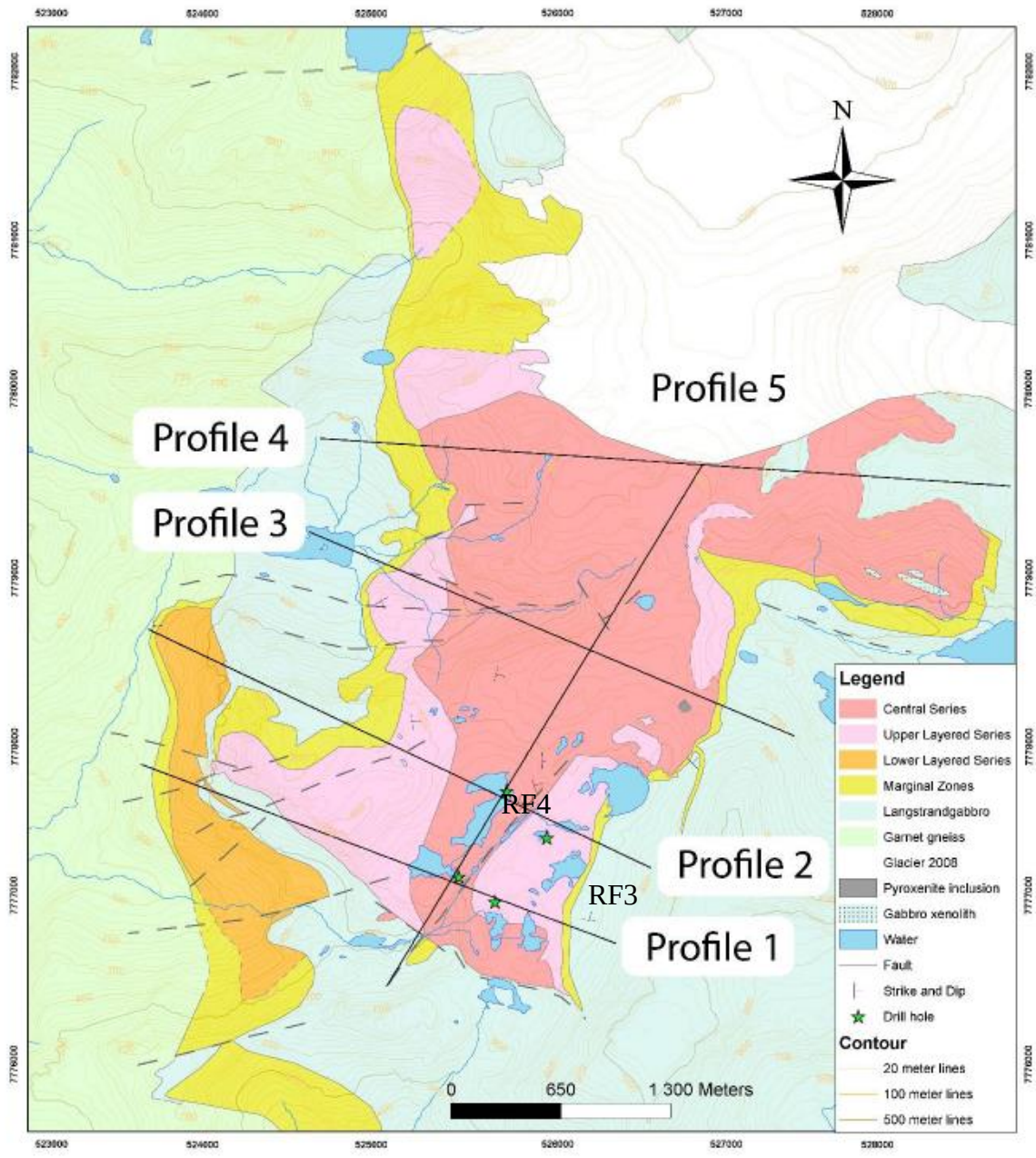

Figure 5.9

Geological map with profiles and drilling locations marked from Grannes (2016).

5.10.1 Fault displacement

One way to explain the chemical inconsistency is to assume fault displacement. If so, a fault with a significant displacement must cut one of the drill cores somewhere in the 45m interval between the green corresponding area and the blue/red differing area in Figure 4.33 a). Due to the PGE

anomaly at 298m in Figure 4.34, it would be reasonable to expect hydrothermal fluids in the fault to have relocated and precipitated the PGE anomaly. In such a case, the fault would be expected to cut RF3 where the PGE anomaly is. The geological map (Figure 5.9) and profiles made by Grannes (2016) include a large 40^{o} fault cutting between RF4 and RF3. When the fault is continued, it cuts RF3 somewhat above where the PGE reef is found. If the fault has a greater inclination than what is modeled by Grannes (2016), it would cut at the top of the red area in Figure 4.33 and Figure 4.34. Based on the displacement of RF1+3 and RF2+4 across the fault in Table 18, it is a normal fault. Normal faults normally have 45-60^{o} dip. This is a very strong support for the fault hypothesis, and strongly suggests that the fault in the profile should be extended to cut through RF3. This addition has been made in the reworked profile 2 in Figure 5.10 b).

In this hypothesis, the PGE are relocated and precipitated by late hydrothermal activity. The fault is modeled to have formed in an extensional regime.

The proposed reason for the lack of PGE anomaly below the reef sequence in RF3 is that the fault in the revised model cuts very close to the reef sequence, and that somehow removes the PGE anomaly via fault processes. However, the green area (Figure 4.33) is substantially below this. Either the green area is a random likeness between the drill cores; or the fault cuts 110m below where the expected upper PGE reef below purple zone (Figure 4.33) should have been.

5.10.2 Local intrusive

Another hypothesis is that the cumulates found in RF4 below 150m and in RF3 below 300m are intrusions deposited at different times by different melts. If a local intrusion cut one of the drill cores and said intrusion had a different chemical composition than the magma that formed the cumulates in the other drill core this would be what the drill cores would look like. As the blue area in RF4 in Figure 4.33a is best described as a continuation of the element trends above and below the marked area while all elements except Cr change in the red area of Rf3 in Figure 4.33b, it is more likely that such a local intrusive is what is observed in the RF3 drill core. To explain the PGE anomaly in RF3, enrichment of PGE either by sulfide minerals in a previously formed chamber roof, or by sulfides in the floor of the later overlying CS dunite is suggested. This explanation seems less likely than the fault hypothesis, as such an intrusion should have been visible other places in the RUC, e.g. the dyke swarm. The lithology in the deepest part of RF3 is

mapped as dunitic, but dunitic dykes are not found. If it is a part of the CS replacive magmatic event that formed the discrepancy it is strange that the chemical Ni-S-Cr signature is so different from what is observed in the rest of the CS.

5.10.3 One chamber – varying deposition

The last way to explain the inconsistency is by localized either increased volume of deposition or a local hiatus. In this hypothesis it is assumed that the cumulates found in both drill cores were deposited in the same magma chamber. If so it seems unlikely that one area in the chamber experienced a much higher degree of crystallization than another. If the chemistry changed in one part of the chamber, e.g. by assimilation of wall rock one place, the proximal crystallization would be different than the cumulates forming in the rest of the magma chamber. This could explain the different chemistry from S, Ni and Cu observed in RF3 compared to RF4. If assimilation of S rich, Ni poor rock, or even S rich rock where Ni could substitute into newly revealed Olivine, depleting it from the crystallizing magma, the resulting chemical graphs could look like Figure 4.33b. It would however not explain the PGE anomaly in RF3.

Of the three possibilities, the first seem by far the most likely as previous work (Grannes, 2016) has already hypothesized a fault where one would be needed to cause the observed chemistry. Nikolaisen (2016) suggested that metasomatic processes had a significant role in the (re)mobilization and crystallization of the PGM in RF1. Tollefsrud (2018) hypothesized that such hydrothermal fluids could originate from fault-valve mechanisms. For PGE to be enriched in or very close to the fault core by fault-driven hydrothermal processes is not only plausible, but support the work and hypotheses made in previous studies of the RUC.

5.11 Marginal Zone, Lower Layered Series or Central Series

5.11.1 LLS or CS: RF4- 305-350m below surface

Between the blue and orange fractionation lines are two dunite-wehrlite units characterized by fractional crystallization. According to the known RUC research, the CS consists of replacive dunites with a very distinct chemical signature. The CS consists of dunites and wehrlites with cumulate or oikocrystic Clinopyroxene (Grant et al., 2016). The Cs has discordant borders with

the modally layered LLS and ULS, and so intruded into previously formed (assumed mushy) cumulates, replacing them (Larsen et al., 2018). The unit has insignificant indications for fractional evolution as observed in this study, and it is generally believed that most of the CS-forming magma was not trapped in the RUC, but rather it intruded through the RUC giant plumbing system to shallower levels (Nikolaisen, 2016). All these things are true for the Upper CS body, as well as most of the CS Wehrlite body. But the fractionation graphs in Figure 5.1 show that it is distinctly not the case in the "CS Lower Dunite" body to the lower part of the "CS Wehrlite body" - where two fractionation lines are found.

Since the CS consists of a replacive lithology, observing traces of the chemistry of the original cumulate that was magmatically replaced would not be surprising. Finding strong indications of fractional evolution could therefore be a remnant of the replaced cumulate imprint on the replacive lithology. An explanation for why a similar feature is not observed in the rest of the CS could be that it is a sort of Marginal Zone between the CS and LLS/ULS cumulates where the replacing magma were faster cooled than in the center of the CS. If this were true, a similar feature would be expected in the other discordant borders of the CS. It is not observed in the RF3 ULS-CS-ULS-CS-ULS sequence in the upper drill core. Another argument against the "marginal zone between CS and LLS/ULS" hypothesis is that if the cumulates were melted there would have likely been a far greater degree of mixing that would at least partly destroy the fractionation graphs' fractional signature. Warm magma, and particularly the CS forming magma, rise and mix. There would be a maximum of one fractionation sequence in a CS marginal zone. If the CS forming magma intruded in two short bursts and then for full force, it would make sense. But that is not what is suggested for this massive intrusive event. So, is the CS Lower dunite body in reality two sequences of the same magmatic type as the Pyroxenite fractionation sequence below them?

As seen in Figure 4.31, the 305-350m interval plots more Ca rich and less Cr rich than the CS, yet distinctly not along the Gabbro-Cpx line as the 350-391m interval. It is therefore proposed that the 305-350m interval is a remnant of the original pre-CS formation cumulates, probably part of the LLS.

5.11.2 MZ or LLS: RF4 – 350-391m below surface

The pyroxenite in the 350-391m interval of RF4 is a magmatic cumulate sequence characterized by fractional crystallization. The unit consists of Olivine clinopyroxenite with small transitions to dunite (Grant et al., 2016). The unit share the RUC characteristic that there is a remarkable lack of plagioclase among the cumulate and interstitial assemblage. Yet this lithology is interpreted by Grannes (2016) and Grant (2016) to be a Marginal Zone lithology contaminated by partially melted Langstad-gabbronorite.

From the observation of the only LLS exposure along the SW facing cliff above Reinfjord village, the LLS is comprised of 4 cyclic units of Olivine and pyroxene-dominated cumulates (Bennett, 1986, Emblin, 1985). From the fractionation data, the 41 upper meters of the pyroxenite unit consists of 1 unit characterized by fractional crystallization.

Grant (2016) noted that there is a high abundance of Orthopyroxene in the MZ of the LLS. The pyroxenite thin sections had variable concentrations of Orthopyroxene, but in some cases there were more Opx present than Cpx.

A peritectic reaction between ultramafic melts and partially melted gabbro can form marginal pyroxenites in zoned ultramafic complexes (Burg et al., 2009, Jagoutz et al., 2006).

Grant et al.'s (2016) bulk rock data plot in Figure 4.31 b) clearly shows that there are MZ rocks sampled from the RUC drill cores. These are identified by plotting along the CPX Gabbro line due to their influence by the Langstad-gabbronorite. Though none of the RF4 samples in Figure 4.31 a) plot with as high Cr_2O_3 content as the MZ samples in Figure 4.31 b), the bulk rock chemical signature of most of the 350-391m interval rocks plot along the CPX Gabbro-line. This indicate that Grant et al. (2016) and Grannes (2016) were correct in their interpretation of the unit. As the lithologies above the MZ pyroxenite is likely LLS lithologies, it is pertinent to assume that the RF4 MZ pyroxenites are LLS in a marginal zone contaminated by Langstad-gabbronorite.

5.11.3 ULS and CS: RF3 – 0-100m below surface

According to Grannes (2016) and Grant et al. (2016), the RF3 drill core intersects the ULS three times in its upper 100m. This is visualized by Grannes in Profile 2 (a revised version of which is seen in Figure 5.10 b), where the ULS and CS undulate for the upper 100m of the drill core. As

the RF3 drill core has not been logged by this thesis' author, I am unable to verify the account, but Figure 4.36 d) show three large Ca-peaks in the CS wehrlite unit. If the "CS Wehrlite" unit is really 3 repetitions of "CS Wehrlite" and "ULS wehrlite" units, the two major S peaks in RF3 at 41m and 72m (Figure 4.36 a) could be explained by the units' contact relations. Neither reef is particularly enriched in Cu (Figure 4.36 b). There are segmentatious variations in the Ca graph (Figure 4.36 d), but no change in either fractionation indicator in Figure 5.2. The fact that the lithology change (see the lithology coded Ca variations in Figure 4.36 d) and the grey circles in Figure 4.31 b) without any change in either fractionation line can only be explained by that the ULS is less characterized by fractional evolution than the LLS as discussed in the two previous sections.

5.12 RF3 and RF1 evolved sill

Both RF1 and RF3 has an area where the fractionation graphs indicate a highly evolved composition. In RF1 the peak is found at 507 masl (Figure 4.41 a) while in RF3 it is found at 526 masl (Figure 4.40 b and c). If this is the same geological feature (e.g. a highly evolved sill that is only found on the ESE side of the fault), it does not have the same geologically modeled dip as the major Cu reef sequence in Figure 5.10. The Cu reef in Figure 5.10 is modeled to cut RF1 66m below it cuts RF3. This evolved sill cuts RF1 19m above it cuts RF3. Because the sill is only found on the ESE side of the fault, and not in either RF2 or RF4, it is suggested to have formed significantly later than the rest of the RUC, possibly changing its orientation by connecting with the fault.

5.13 Refined RUC profiles

A reinterpretation of Profile 1, 2 and 5 from the RUC mapping by Grannes (2016), where the reinterpretation of the magmatic series (CS-LLS-MZ in RF4, ULS-CS-LLS in RF1, CS-LLS in RF2 and ULS-CS in RF3) and modeled displacement across the fault, can be seen in Figure 5.10. The fault displacement is calculated based on the assumption that the fault only has extensional displacement without rotation of the hanging wall and the assumption that the major Cu reef is a horizontal horizon that once was continuous.

In the newly interpreted profiles, the fault (marked in green) is extended to not only cut through RF1 and RF3, but also the MZ and likely the gneiss country rocks. Because the fault displacement calculations based on the Cu reef displacement are 70-80m, the fault is a large tectonic feature with significant displacement. The fault is modeled to intersect RF1 at ca 200m depth below surface and RF3 at ca 300m depth below surface.

The major Cu reef is observed in RF1, RF3 and RF4. As seen in Figure 5.10 a) the fault displacement is such that the expected location of the reef in RF2 has been eroded. Below the Cu reef in RF1 and RF4 is a PGE reef. The reason for the absence of a similar reef in RF3 is not understood.

The newly interpreted model has added a segment of LLS cumulates at the bottom of the RUC. The borders between the LLS and CS are assumed to be discordant, like the borders between the ULS and CS (Grant et al., 2016). Elevated Ca concentration and evolving fractionation indicators has been used to pinpoint the initiation of the LLS in the RF1, RF2 and RF4. The profile revision agree with Grannes (2016) that the RF4 is the only drill core which penetrates into the MZ.

Based on the chemical signatures used in this thesis (Ca and fractionation indicators), the LLS and ULS differ in the fractionation indicator trends. The LLS have a clearly defined fractionation-based layering caused by influx of large magmatic volumes and uninterrupted fractional evolution in a closed magma chamber. The ULS is recognized by its elevated Ca content relative to the CS replacive lithologies, but show no sign of magmatic fractional evolution in the cumulates. Previous characterizations have not been able to separate the two series with certainty as their chemistry, modal layering and ages are quite similar. This is a significant separating factor between the two layered series, supporting the ULS, LLS and CS separation by Bennet (1986).

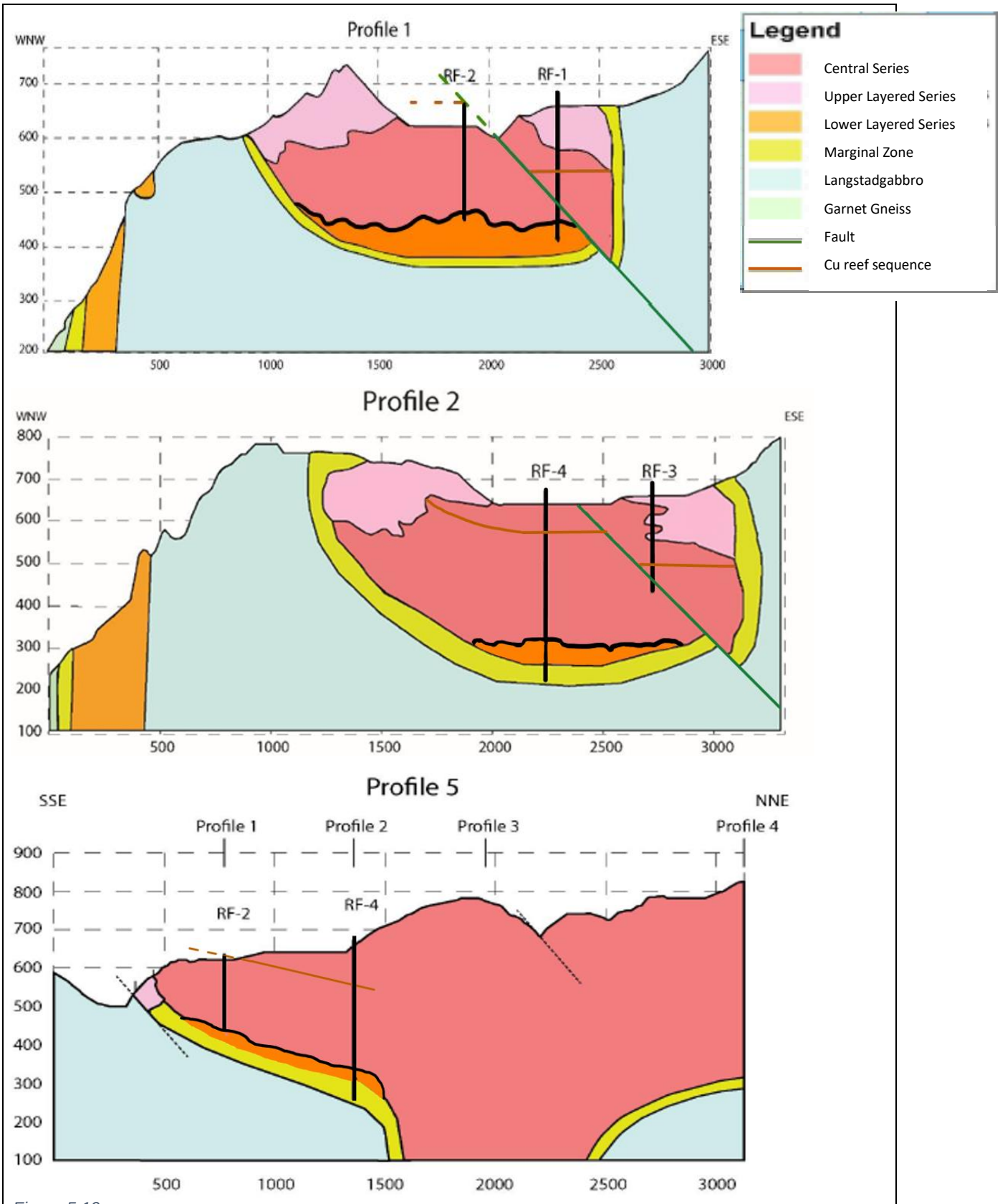
Profile 1
WNW
ESE
RF-2
RF-1
700
600
500
400
300
200
500
1000
1500
2000
2500
3000
Legend
Central Series
Upper Layered Series
Lower Layered Series
Marginal Zone
Langstadgabbro
Garnet Gneiss
Fault
Cu reef sequence
Profile 2
WNW
ESE
800
700
600
500
400
300
200
100
RF-4
RF-3
500
1000
1500
2000
2500
3000
Profile 5
SSE
NNE
Profile 1
Profile 2
Profile 3
Profile 4
900
800
700
600
500
400
300
200
100
RF-2
RF-4
500
1000
1500
2000
2500
3000

Figure 5.10

Revised profiles through the RF drill cores based on previous profiles made by Grannes (2016). The fault is marked in green and the main Cu reef (the "reef sequence") is marked in purple. A LLS unit has been added at the base of RF1, RF2 and RF4 based on fractionation indicators.

a) Profile 1 cuts through RF1, the fault and RF2.

b) Profile 2 cuts through RF3, the fault and RF4.

c) Profile 5 is parallel to the fault and cuts through RF2 and RF4.

5.14 Deep LIP processes - large implications

Why is it so important to understand the mineralization in Reinfjord?

During mantle intrusion up in the crust, a significant proportion of the intrusive melt's volume is crystallized in very deep systems. To understand the nature of crystallization in very deep systems gives valuable information on asthenosphere-lithosphere melt transfer. This means that to fully understand the fractional history of large volumes of magma intruding through the crust, the deepest localities must be studied. To understand e.g. the PGE chemical trace graph in deep systems will give valuable information on which elements are pertinent to look for in deeply formed intrusions due to poor mobility and which are expected to be found higher up.

The Chr chemical signatures from RUC is significantly different from the expected chemical compositions based on shallower layered intrusions and the most primitive Fo found in LIP continental flood basalts. Continental flood basalts give knowledge of how the extrusive magma crystallize. "Normal" mafic-ultramafic layered intrusions give information on how crystallization is at 3-5 kbar. But substantial proportions of the crystallization occur significantly deeper. The RUC formed at 8 kbar: 25-35 km depth (Larsen et al., 2018) or 10-14 kbar: 33-45km depth (Orvik, 2019). Ni, Cr and Fo are the parameters used to extrapolate degree of fractionation prior to cumulate formation/magma solidification. To correctly model that, how Cr partitions in very deep systems must be well understood. In the RUC, it is estimated that up to 15-20% fractionation occurred prior to cumulate formation. The chemistry of those 15-20% is unknown, as they formed even deeper in the crust.

Generally speaking, whichever mineral of a type is most Mg+Cr rich relative to Fe^{2+}+Al is considered the more primitive. As is shown in the RUC, that might be a too great simplification for very deep systems, at least for Spinels. The negative Ti-Al correlation in Spinels observed by

Kamenetsky et al. (2001) is observed here. This gives that Mg and Ti might be better indicators for very deep chromian Spinels, as Cr and Al substitute. It is assumed that in the Cr-Al substitution, Al is the limiting element rather than Cr. This would explain why the Cr content is not linearly connected with Mg in the RUC. The fact that the assumed latest formed chromian Spinel type (Hc) is the most Mg rich brings significant doubt about how Mg partition into chromian Spinels at great depth.

6 Further work

- The Spinels found as inclusions in Olivine should be analyzed: both primary Spinels and those found in inclusion trails made by the calcareous magma. Would be useful to compare the chemical signature between the chromite and magnetites formed by the two melts to see how large the calcareous magma's influence is on the cumulate minerals.
- RF3 should be re-logged where the location of the fault is the primary goal should be carried out to decide which of the fault-related hypotheses is likely correct: the upper-PGE-reef-absence hypothesis; or the Ni-Cu-S-discrepancy hypothesis.
- Thin sections of the area where the PGE-anomaly should have been in RF3 should be made and studied to uncover why the expected anomaly is absent.
- The V/Cr fractionation indicator should be tested for other, well known and understood mafic-ultramafic systems to study whether the method has potential to be an important tool for uncovering the magmatic history of cumulate lithologies.
- A comparison of the chromian Spinel compositions of RUC with other very deep systems should be conducted to see if there is a systematic breakdown of the "Mg and Cr rich Spinels are the most primitive" assumption that is universally accepted by the current scientific community.

7 Conclusions

Spinels:

- The group 3 Magnetite is a primary mineral.
- Group 2 Chromite is a primary mineral, possibly extensively re-equilibrated if Kamenetksy et al (2001) are a reliable means of comparison.
- Group 1 Hercynite is primary or secondary, likely formed at high T by crystallization from or interaction with a pervasive melt. Hercynite must have formed prior to the event that formed Mt-Hc mixing and the formation of Mt-Hc outshoots.
- All Spinels have strongly anomalous Cr# vs Mg#. This indicate that the assumtion that the most primitive Spinels have the highest Cr# and Mg# might not be valid in very deep magmatic systems. This could have major implications for fractionation models for the magmas forming shallower intrusions.
- The rounded Spinels were probably formed by sinking through hot, abrasive magma and mushy cumulates.
- A Spinel volume expansion by heating (possibly caused by the CS-forming melts) of chromian Spinels is suggested.
- The negative Al-Ti correlation observed by Kamenetsky et al (2001) is also observed in RUC, supporting that the hypothesis is valid for Spinel formation in general.
- It is assumed that the chromian Spinel compositions are not entirely primary, as chemical re-equilibration has likely taken place. However, there is significant evidence against different Spinel types re-equilibrating with each other.

Fault:

- The fault between RF1+RF3 and RF2+RF4 either cut RF3 at ca 300m or at ca 180m. Both are suggested to explain features from the RF3 PGE-diagram. Only one of these hypotheses can be correct.
- The lack of PGE anomaly below the major Cu reef in RF3 is a mystery that should be examined more closely.

Fractionation:

- The V/Cr indicator is a good supplement to Fe/(Fe+Mg) when studying fractionation in magmatic cumulates. During cases of fractional crystallization, the two indicators agree remarkably well. Using the V/Cr fractionation indicator will provide information for when a change in Fe/(Fe+Mg) is due to fractional evolution/recharge and when the observed trend is caused by assimilation of previously formed cumulates or other processes.
- The LLS is characterized by fractional crystallization in closed chambers, while the part of ULS seen from the RF3 drill core is characterized by crystallization in an open chamber setting. This is a significant difference between the two layered cumulate magmatic series.
- The RF4 is characterized by 3 fractional crystallization events interrupted by large recharge events. Above that, a 100m interval of an open conduit system with assimilation of wall rock is found. This lithology is interrupted by a chemically unchanging open system magmatic deposition.
- The CS formed by at least 2 major magmatic bursts through the RUC conduit system.
- The RF3 is mostly characterized by deposition in an open magmatic system with possible cases of cumulate assimilation.

PGE and other reefs:

- The deepest PGE reef in RF4 is found immediately above a fractionation event suggested by the Fe/(Fe+Mg) and V/Cr indicators, giving credence to their accuracy in interpreting fractional crystallization and recharge in the cumulate pile.
- From the revised model for the RUC profiles, the Cu (and PGE) reefs visible in RF1, RF3 and RF4 have been eroded from where RF2 is drilled.

Revision of magmatic cumulate series:

- The RF1, RF2 and RF4 intersect a LLS unit below the well known CS.
- The deepest section of RF4 is part of the MZ as proposed by Grant et al. (2016)

8 References

Alexander, C. M. O. D. 2007. *Chondrite* [Online]. Encyclopædia Britannica. Available: https://www.britannica.com/science/chondrite [Accessed May 23 2019].

Allan, J. F., Sack, R. O. & Batiza, R. 1988. Cr-rich spinels as petrogenetic indicators: MORB-type lavas from the Lamont seamount chain, eastern Pacific. *American Mineralogist,* 73**,** 741-753.

Als 2018. Schedule of Services & Fees.

Barnes, S.-J., Prichard, H. M., Cox, R. A., Fisher, P. C. & Godel, B. 2008. The location of the chalcophile and siderophile elements in platinum-group element ore deposits (a textural, microbeam and whole rock geochemical study): Implications for the formation of the deposits. *Chemical Geology,* 248**,** 295-317.

Barnes, S.-J. a. F., D. 1995. The distribution of the platinum-group elements, nickel, copper, and gold in the Muskox Layered Intrusion, Northwest Territories, Canada. *Economic Geology,* 90**,** 54-135.

Barnes, S. J. & Naldrett, A. J. 1985. Geochemistry of the J-M (Howland) Reef of the Stillwater Complex, Minneapolis Adit area; I, Sulfide chemistry and sulfide-olivine equilibrium. *Economic Geology,* 80**,** 627-645.

Barnes, S. J. & Roeder, P. L. 2001. The range of Spinel Compositions in Terrestrial Mafic and Ultramafic Rocks. *Journal of Petrology,* 42**,** 2279-2302.

Basu, A. R., Renne, P. R., Dasgupta, D. K., Teichann, F., Poreda, R. J. 1993. Early and late alkali igneous pulses and a high 3-He plume origin for the Deccan flood basalts. *Science,* 261.

Bates, R. L. & Jackson, J. A. 1987. *Glossary of Geology,* Alexandria, Virginia, USA, American Geological Institute.

Bell, K. a. R., A. S 2004. Carbonatites From the Kola Alkaline Province: Origin, Evolution and Source Characteristics. *Mineralogical Society Series,* 10.

Bennett, M. C. 1971. The Reinfjord ultramafic complex. *Norges geologiske undersøkelse Bulletin,* 269**,** 165-171.

Bennett, M. C. 1973. The geology and petrology of the Reinfjord ultramafic complex, Troms, North Norway. *University College of Swansea*.

Bennett, M. C. 1974. The emplacement of a high temperature peridotite in the Seiland province of the Norwegian caledonides. *Journal of the Geological Society,* 130**,** 205-226.

Bennett, M. C., Emblin, S.R., Robins, B., Yeo, W.J.A 1986. High-temperature ultramafic complexes in the North Norwegian Caledonides: I - regional setting and field relationships. *Norges Geologiske Undersøkelse Bulletin,* 405**,** 1-41.

Bosi, F., Biagioni, C. & Pasero, M. 2018. Nomenclature and classification of the spinel supergroup. *European Journal of Mineralogy,* 31**,** 183-192.

Bottinga, Y. & Meurer, W. P. 1990. The degassing of Hawaaian tholeiite. *Bulletin of Volcanology,* 53**,** 73-85.

Bouilhol, P., Schmidt, M. W. & Burg, J.-P. 2015. Magma Transfer and Evolution in Channels within the Arc Crust: the Pyroxenitic Feeder Pipes of Sapat (Kohistan, Pakistan). *Journal of Petrology,* 56**,** 1309-1342.

Bowen, N. 1922. The reaction principle in petrogenesis. *The Journal of Geology,* 30**,** 177-198.

Burg, J. P., Bodinier, J. L., Gerya, T., Bedini, R. M., Boudier, F., Dautria, J. M., Prikhodko, V., Efimov, A., Pupier, E. & Balanec, J. L. 2009. Translithosphericmantle diapirism: geological evidence and numerical modelling of the Kondyor zoned ultramafic complex (Russian Far-East). *Journal of Petrology* 50**,** 289–321.

C.Y., W., M, Z., S, Y. & Y, S. 2014 Geochemistry of the Abulangdang intrusion: cumulates of high-Ti picritic magmas in the Emeishan large igneous province, SW China. *Chemical Geology*, 378-379**,** 244-39.

Cabri, L. J. a. L., J.H.G 1976. The mineralogy of the platinum-group elements from some copper-nickel deposits of the Sudbury area. *Society of Economic Geologists*, 71.

Cadow, R. 1993. Sm-Nd and Rb-Sr ages of hornblende clinopyroxenite and metagabbro from the Lillebukt alkaline complex, Seiland Igneous Province. *Norsk Geologisk Tidsskrift*, 73**,** 243-249.

Cameca. 2017. *Introduction to EPMA* [Online]. CAMECA Science and Metrology Solutions. Available: https://www.cameca.com/products/epma/technique [Accessed 04:08 2019].

Campbell, I. a. N., A. 1979. The influence of silicate: sulfide ratios on the geochemistry of magmatic sulfides. *Economic Geology*, 74**,** 755-772.

Canil, D. 1999. Vanadium partitioning between orthopyroxene, spinel and silicate melt and the redox states of mantle source regions for primary magmas. *Geochimica et Csomochimica Acta*, 63**,** 557-572.

Central, M. 2019. *Motic BA310 POL Polarizing Light Microscope* [Online]. 325 Bustleton Pike, Feasterville, PA 19053: Microscope Central by Arenatheme. Available: https://microscopecentral.com/products/motic-ba310-pol-polarizing-light-microscope [Accessed].

Chatterjee, N. D., Leistner, H., Terhart, L., Abraham, K. & Klaska, R. 1982. Thermodynamic mixing properties of corundum–eskolaite, α–(Al, Cr+3)2O3, crystalline solutions at high temperatures and pressures. *American Mineralogist*, 67**,** 725-735.

Clark, J. 2019. *Chemistry of Vanadium* [Online]. Chemistry LibreTexts. Available: https://chem.libretexts.org/Bookshelves/Inorganic_Chemistry/Supplemental_Modules_(Inorganic_Chemistry)/Descriptive_Chemistry/Elements_Organized_by_Block/3_d-Block_Elements/Group_05%3A_Transition_Metals/Chemistry_of_Vanadium [Accessed].

Coogan, L. A., Jenkin, G. R. T. & Wilson, R. N. 2007. Contrasting Cooling Rates in the Lower Oceanic Crust at Fast- and Slow-spreading Ridges Revealed by Geospeedometry. *Journal of Petrology*, 48**,** 2211-2231.

Corfu, F., Robert, R. J., Torsvik, T. H., Ashwal, L. W., Ramsay, D. M. 2007. Peri-Gondwanan elements in the caledonian nappes of Finnmark, norther Norway: implications for the paleogeographic framework of the Scandinavian Caledonides. *American Journal of Science*, 307**,** 434-458.

Daltry, V. D. C. & Wilson, A. H. 1997. Review of platinum-group mineralogy: Compositions and elemental associations of the PG-minerals and unidentified PGE-phases. *Mineralogy and Petrology*, 60**,** 185-229.

Davidson, M. W. & Abramowitz, M. 2008. Optical Microscopy. Available: http://zeiss-campus.magnet.fsu.edu/referencelibrary/pdfs/Davidson_Abramowitz_Optical_Microscopy.pdf.

Dick, H. J. B. & Bullen, T. 1984. Chromian spinel as a petrogenetic indicator in abyssal and alpine-type peridotites and spatially associated lavas. *Contributions to Mineralogy and Petrology,* 86**,** 54-76.

Elvenvold, S., Andersen, T. 1993. Fluid evolution during metamorphism at increasing pressure: carbonic- and nitrogen-bearing fluid inclusions in granulites from Øksfjord, north Norwegian Caledonides. *European Journal of Mineralogy***,** 777-790.

Emblin, S. R. 1985. *The Reinfjord Ultramafic Complex, Seiland Province: Emplacement History and Magma Chamber Model.* Unpublished Ph.D thesis, University of Bristol, UK.

Ernst, R. E., Bell, K. 2010. Large igneous provinces (LIPs) and carbonatites. *Mineralogy and Petrology,* 98**,** 55-76.

Fairhead, J. D. 2015. Generating a high-resolution global gravity model for oil exploration: part 2 - marine satellite altimeter-derived gravity. *The Leading Edge,* 34**,** 566-571.

Fan, W., Zhang, C., Wang, Y., Guo, F. & Peng, T. 2008. *Geochronology and geochemistry of Permian basalts in western Guangxi Province, Southwest China: Evidence for plume-lithosphere interaction.*

Gellein, J. 2003. *Gravimetric Residual Map,* 1:250000. Norges Geologiske Undersøkelse.

Gibson, S. A., Thompson, R. N., Day, J. A. 2006. Timescales and mechanisms of plume-lithosphere interactions: 40Ar/39Ar geochronology and geochemistry of alkaline igneous rocks from the Praná-Etendeka large igneous province. *Earth and Planetary Science Letters,* 251**,** 1-17.

Goeke, E. 2011. *Mineralogy: optical mineralogy in crossed polars* [Online]. Life in Plane Light. Available: https://lifeinplanelight.wordpress.com/2011/02/28/mineralogy-optical-mineralogy-in-crossed-polars/ [Accessed 04:09 2019].

Goldschmidt, V. M. 1937. The Principles of Distribution of Chemical Elements in Minerals and Rocks. The seventh Hugo Müller Lecture, delivered before the Chemical Society. *Journal of the Chemical Society***,** 655-673.

Grannes, K. R. B. 2016. *Cryptic Variations of Olivene and Clinopyroxene in the RF-4 Drill-Core: A Geochemical Study of the Reinfjord Ultramafic Complex, Norway.* MSc Msc, Norwegian University of Science and Technology.

Grant, T. B., Larsen, R. B., Anker-Rasch, L., Grannes, K. R., Iljina, M., Mcenroe, S., Nikolaisen, E., Schanche, M. & Øen, E. 2016. Anatomy of a deep crustal volcanic conduit system; The Reinfjord Ultramafic Complex, Seiland Igneous Province, Northern Norway. *Lithos,* 252-253**,** 200-215.

Grant, T. E., Larsen, R. B., Brown, E. L., Müller, A. B. & Mcenroe, S. in prep. In-situ observations of ultramafic magma mixing at the base of the crust using trace elements in clinopyroxene from the Reinfjord Ultramafic intrusion: Implications for the chemical diversity of high-MgO magmas.

Griffin, W. L., Sturt, B.A., O'neill, C.J., Kirkland, C.L., O'reilly, S.Y. 2013. Intrusion and contamination of high-temperature dunitic magma: the Nordre Bumandsfjord pluton, Seiland, Arctic Norway. *Contributions to Mineralogy and Petrology,* 165**,** 903-930.

Harmer, R. E. 2000. New precise dates on the acid phase of the Bushveld and their implications.

Harris, D. C. & Cabri, L. J. 1991. Nomenclature of Platinum-Group-Element alloys: Review and Revision[1]. *Canadian Mineralogist,* 29**,** 231-237.

Heinonen, J. S., Jennings, E. S. & Riley, T. R. 2015. Crystallisation temperatures of the most Mg-rich magmas of the Karoo LIP on the basis of Al-in-olivine thermometry. *Chemical Geology,* 411**,** 26-35.

Henderson, P. 1976. Reaction trends shown by chrome-spinels of the Rhum layered intrusion. *In:* IRVINE, T. N. (ed.) *Chromium: its Physicochemical Behavior and Petrologic Significance.* Pergamon.

Henderson, P. & Wood, R. J. 1982. Reaction relationships of chrome-spinels in igneous rocks — further evidence from the layered intrusions of Rhum and Mull, Inner Hebrides, Scotland. *Contributions to Mineralogy and Petrology,* 78**,** 225-229.

Higgins, M. D., Van Breemen, O. 1998. The age of the Sept Iles layered mafic intrusion, Canada: implications for the late Neoproterozoic/Cambrian history of souteastern Canada. *Journal of Geology,* 106**,** 421-431.

Hill, R. & L. Roeder, P. 1974. *The Crystallization of Spinel from Basaltic Liquid as a Function of Oxygen Fugacity*.

Hjelen, J. 2016a. JEOL JXA-8500F Electron Probe Micro analyzer (EPMA) EM Lab, Department of Materials Technology, NTNU.

Hjelen, J. 2016b. Overview for Hitachi Analytical Variable Pressure SU6600 SEM. EM Lab, Department of Materials Science and Engineering, NTNU.

Holwell, D. A. & Mcdonald, I. 2006. Petrology, geochemistry and the mechanisms determining the distribution of platinum-group element and base metal sulphide mineralisation in the Platreef at Overysel, northern Bushveld Complex, South Africa. *Mineralium Deposita,* 41**,** 575.

Hooper, P. 1971. The mafic and ultramafic intrusions of SW Finnmark and North Troms. Norges Geologiske Undersøkelse.

Iljina, M. 2013. Reinfjord drilling and mapping campaigns in 2012 - geochemical observations, discussion on ore enesis and exploration implications. *Report for Nordic Mining ASA.*

Irvine, T. N. 1965. Chromian spinel as a petrogenetic indicator: Part 1. Theory. *Canadian Journal of Earth Sciences,* 2**,** 648-672.

Irvine, T. N. 1967. Chromian spinel as a petrogenetic indicator. Part 2. Petrogenetic applications. *Canadian Journal of Earth Sciences,* 4**,** 71-103.

Irvine, T. N. 1977. Origin of chromitite layers in the Muskox Intrusion and other stratiform intrusions: a new interpretation. *Geology,* 5**,** 273-277.

J. Wood, B. & Virgo, D. 1989. Upper mantle oxidation state: Ferric iron contents of Iherzolite spinels by 57Fe Mössbauer spectroscopy and resultant oxygen fugacities. *Geochimica et Cosmochimica Acta,* 53**,** 1277-1291.

Jacob, K. T. 1978. Electrochemical Determination of Activities in Cr2O3-Al2O3 Solid Solution. *Journal of the Electrochemical Society,* 125**,** 175-179.

Jagoutz, O., Müntener, O., Burg, J. P., Ulmer, P. & Jagoutz, E. 2006. Lower continental crust formation through focused flow in km-scale melt conduits: The zoned ultramafic bodies of the Chilas Complex in the Kohistan island arc (NW Pakistan). *Earth and Planetary Science Letters,* 242**,** 320-342.

Jagoutz, O., Müntener, O., Ulmer, P., Pettke, T., Burg, J.-P., Dawood, H. & Hussain, S. 2007. Petrology and Mineral Chemistry of Lower Crustal Intrusions: the Chilas Complex, Kohistan (NW Pakistan). *Journal of Petrology,* 48**,** 1895-1953.

Jennings, E., Gibson, S., Maclennan, J. & Heinonen, J. 2017. *Deep mixing of mantle melts beneath continental flood basalt provinces: Constraints from olivine-hosted melt inclusions in primitive magmas*.

Kamenetsky, V., Sobolev, A., Eggins, S., Crawford, A. J. & Arculus, R. 2002. *Olivine-enriched melt inclusions in chromites from low-Ca boninites, Cape Vogel, Papua New Guinea:*

Evidence for ultramafic primary magma, refractory mantle source and enriched components.

Kamenetsky, V. S., Chung, S.-L., Kamenetsky, M. B. & Kuzmin, D. V. 2012. Picrites from the Emeishan Large Igneous Province, SW China: a Compositional Continuum in Primitive Magmas and their Respective Mantle Sources. *Journal of Petrology,* 53**,** 2095-2113.

Kamenetsky, V. S., Crawford, A. J. & Meffre, S. 2001. Factors Controlling Chemistry of Magmatic Spinel: an Empirical Study of Associated Olivine, Cr-spinel and Melt Inclusions from Primitive Rocks. *Journal of Petrology,* 42**,** 655-671.

Kinnaird, J. A. 2005. The Bushveld Large Igneous Province. *Review paper, The University of the Witwatersrand, Johannesburg, South Africa***,** 39p.

Kinnaird, J. A., Kruger, F. J., Nex, P. a. M. & Cawthorn, R. G. 2002. Chromitite formation—a key to understanding processes of platinum enrichment. *Applied Earth Science,* 111**,** 23-35.

Krill, A. G. & Zwaan, K. 1987. Reinterpretation of Finnmarkian deformation on western Sørøy, northern Norway. *Norsk Geologisk Tidsskrift,* 67**,** 15-24.

Kullerud, G., Yund, R.A. And Moh, G.H. 1969. Phase relations in the Cu-Fe-S, Cu-Ni-S and Fe-Ni-S systems. *Economic Geology Monograph,* 4**,** 323-343.

Köhler, T. P. & Brey, G. P. 1990. Calcium exchange between olivine and clinopyroxene calibrated as a geothermobarometer for natural peridotites from 2 to 60 kb with applications. *Geochimica et Cosmochimica Acta,* 54**,** 2375-2388.

Larsen, R. B., Grant, T., Sorensen, B. E., Tegner, C., Mcenroe, S., Pastore, Z., Fichler, C., Nikolaisen, E., Grannes, K. R., Church, N., Ter Maat, G. W. & Michels, A. 2018. Portrait of a giant deep-seated magmatic conduit system: The Seiland Igneous Province. *Lithos,* 296**,** 600-622.

Larsen, R. B., Grant, T. B., Sørensen, B. E., Nikolaisen, E., Grannes, K. R. B. PGE-Ni-Cu formation in a deep-crustal ultramafic conduit system: the Seiland Igneous Province, North Norway. 35th International Geological Congress, 2016 Cape Town. S. African Rep.

Larsen, R. B. a. T., C. 2006. Pressure conditions for the solidification of the Skaergaard intrusion: eruption of East Greenland flood basalts in less than 300,000 years. *Lithos,* 92**,** 181-197.

Levy, D. & Artioli, G. 1998. Thermal Expansion of Chromites and Zinc Spinels.

Li, C. & Naldrett, A. J. 1999. Geology and petrology of the Voisey's Bay intrusion: reaction of olivine with sulfide and silicate liquids. *Lithos,* 47**,** 1-31.

Li, C., Tao, Y., Qi, L. & Ripley, E. M. 2012. Controls on PGE fractionation in the Emeishan picrites and basalts: Constraints from integrated lithophile–siderophile elements and Sr–Nd isotopes. *Geochimica et Cosmochimica Acta,* 90**,** 12-32.

Li, C., Xu, Z., De Waal, S. A., Ripley, E. M. & Maier, W. D. 2004. Compositional variations of olivine from the Jinchuan Ni–Cu sulfide deposit, western China: implications for ore genesis. *Mineralium Deposita,* 39**,** 159-172.

Lipin, B. R. 1993. Pressure increases, the formation of chromite seams, and the development of the Ultramafic Series in the Stillwater Complex, Montana. *Journal of Petrology,* 34**,** 76-955.

Liu, Y., Mungall, J. E. & Ames, D. E. 2016. Hydrothermal Redistribution and Local Enrichment of Platinum Group Elements in the Tootoo and Mequillon Magmatic Sulfide Deposits, South Raglan Trend, Cape Smith Belt, New Quebec Orogen*. *Economic Geology,* 111**,** 467-485.

Maclean, W. H. 1969. Liquidus phase relations in the FeS-FeO-Fe30•-SiO• system, and their application in geology. *Economic Geology,* 64**,** 865-884.

Mcdonough, W. & Sun, S. S. 1995. *The composition of the Earth*.
Mindat.Org. 1993-2019a. *Alumoberezovite* [Online]. mindat.org: Hudson Institute of Mineralogy. Available: https://www.mindat.org/min-9090.html [Accessed May 6 2019].
Mindat.Org. 1993-2019b. *Picotite* [Online]. Hudson Institute of Mineralogy: Mindat.org. Available: https://www.mindat.org/min-9769.html [Accessed May 6 2019].
Mindat.Org. 2019. *Clinopyroxene Subgroup* [Online]. Mindat.org. Available: https://www.mindat.org/min-7630.html [Accessed May 23 2019].
Mukherjee, R., Mondal, S. K., González-Jiménez, J. M., Griffin, W. L., Pearson, N. J. & O'reilly, S. Y. 2015. Trace-element fingerprints of chromite, magnetite and sulfides from the 3.1 Ga ultramafic–mafic rocks of the Nuggihalli greenstone belt, Western Dharwar craton (India). *Contributions to Mineralogy and Petrology,* 169**,** 59.
Mungall, J. E. 2005. *Exploration for Platinum-Group Element Deposits*.
Naldrett, A. J. 1989. Association of platinum-group elements with chromitite in layered intrusions and ophiolite complexes. *Economic Geology,* 84**,** 7-180.
Naldrett, A. J. 2004. *Magmatic sulfide deposits: geology, geochemistry and exploration*, Springer Science & Business Media.
Nesse, W. D. 2009. *Introduction to Mineralogy,* Oxford, UK, Oxford University Press.
Ngu. 2015. *(LA)-ICP-MS* [Online]. Norway: NGU. Available: https://www.ngu.no/fagomrade/icp-ms [Accessed 04:08 2019].
Nielsen, T. F. D., Turkov, V. A., Solovova, I. P., Kogarko, L. N. & Ryabchikov, I. D. 2006. A Hawaiian beginning for the Iceland plume: Modelling of reconnaissance data for olivine-hosted melt inclusions in Palaeogene picrite lavas from East Greenland. *Lithos,* 92**,** 83-104.
Nikolaisen, E. 2016. *Platinum Group Elements in the Reinfjord Ultramafic Complex.* MsC MsC, Norwegian University of Science and Technology.
Oen, E. N. 2013. *Formation of Sulphide-deposits in Reinfjord and Lokkarfjord, Seiland Igneous Province. A Sulphur Isotope Study of Economically Interesting Sulphide Deposits Formed in Conjunction with Ultramafic Magmatism (in Norwegian).* MsC MsC, Norwegian University of Science and Technology.
Olesen, O., Brönner, M., Ebbing, J., Gellein, J., Gernigon, L., Koziel, J., Lauritsen, T., Myklebust, R., Sand, M., Solheim, D., Usov, S. 2010. New aeromagnetic and gravity compilations from Norway and adjacent areas - methods and applications. *Petroleum Geology Conference Series,* 7**,** 559-586.
Oosterom, M. G. 1963. The ultramafites and layered gabbro sequences. *Leidse Geologische Mededelingen,* 28**,** 177-296.
Orvik, A. A. 2019. *The dyke swarm in the Reinfjord Ultramafic Complex - A window into the terminal stages forming the Seiland Igneous Province.* Msc, Norwegian University of Science and Technology.
Pastore, Z., Fichler, C. & Mcenroe, S. A. 2016. The deep crustal structure of the mafic-ultramafic Seiland Igneous Province of Norway from 3-D gravity modelling and geological implications. *Geophysical Journal International,* 207**,** 1653-1666.
Peregoedova, A. V. 1999. *Physicochemical Behabiour of Pt and Pd in the Process of the Crystallization of Fe, Ni, Cu-Bearing Sulphide Melts and Following Subsolidus Transformations (According to Experimental Data).* Ph.D Ph.D., UIGGM SB RAS.
Reginiussen, H., Ravna, E. & Berglund, K. 1995. *Mafic dykes from Øksfjord, Seiland Igneous Province, northern Norway: geochemistry and palaeotectonic significance*.
Robb, L. 2005. *Introduction to Ore-Forming Processes,* Oxford, UK, Blackwell Publishing.

Roberts, D. 2007. *Palaeocurrent data from the Kalak Nappe Complex, northern Norway: A key element in models of terrane affiliation*.
Roberts, R. J. 2008. *The Seiland Igneous Province, Northern Norway : age, provenance, and tectonic significance.*
Roberts, R. J., Corfu, F., Torsvik, T. H., Ashwal, L. D. & Ramsay, D. M. 2006. Short-lived mafic magmatism at 560-570 Ma in the northern Norwegian Caledonides: U-Pb zircon ages from the Seiland Igneous Province. *Geological Magazine,* 143**,** 887-903.
Roberts, R. J., Corfu, F., Torsvik, T.H., Ashwal, L.D., Hetherington, C.J. 2010. Age of alkaline rocks in the Seiland Igneous Province, Northern Norway. *Journal of the Geological Society,* 167**,** 71-81.
Robins, B. & Gardner, P. M. 1975. The magmatic evolution of the Seiland province, and Caledonian plate boundaries in northern Norway. *Earth and Planetary Science Letters,* 26**,** 167-78.
Roeder, P. L. 1994. Chromite: From the Fiery Rain of Chondrules to the Kilauea Iki Lava Lake. *Journal of the Mineralogical Association of Canada,* 32**,** 729-746.
Roeder, P. L. & Campbell, I. H. 1985. The Effect of Postcumulus Reactions on Composition of Chrome-spinels from the Jimberlana Intrusion. *Journal of Petrology,* 26**,** 763-786.
Rottenfusser, R., Wilson, E. E. & Davidson, M. W. *Reflected Light Microscopy* [Online]. ZEISS - Education in Microscopy and Digital Imaging. Available: http://zeiss-campus.magnet.fsu.edu/articles/basics/reflected.html [Accessed 04:08 2019].
Sack, R. O. & Ghiorso, M. S. 1991a. Chromian spinels as petrogenetic indicators: thermodynamic and petrological applicaions. *American Mineralogist,* 76**,** 827-847.
Sack, R. O. & Ghiorso, M. S. 1991b. Chromian spinels as petrogenetic indicators: Thermodynamics and petrological applications. *American Mineralogist,* 76**,** 827-847.
Salters V.J.M. And Stracke, A. 2004. Composition of the depleted mantle. *Geochemistry, Geophysics, Geosystems,* 5**,** 469-484.
Schanche, M., Iljina, M. & Larsen, R. B. 2012. New nickel-copper-platinum group element deposits in N. Norway. *Mineralproduksjon,* 2**,** 91-99.
Schorn, S. 1999-2019. *Alumoberezovite* [Online]. Available: https://www.mineralienatlas.de/lexikon/index.php/MineralData?lang=en&mineral=Alumoberezovite [Accessed May 6th 2019].
Scotese, C. R. 2002. *Earth Climate Past and Future,* NY, Freeman and Sonns.
Scowen, P. a. H., Roeder, P. L. & Heltz, R. T. 1991. Reequilibration of chromite within Kilauea Iki lava lake, Hawaii. *Contributions to Mineralogy and Petrology,* 107**,** 8-20.
Sibson, R. H. 1990. Conditions for fault-valve behaviour. *Geological Society, London, Special Publications,* 54**,** 15.
Siivola, J. & Schmid, R. 2007. *List of Mineral Abbreviations* [Online]. Available: https://www.bgs.ac.uk/scmr/docs/papers/paper_12.pdf [Accessed].
Sobolev, A. V., Sobolev, S. V., Kuzmin, D. V., Malitch, K. N. & Petrunin, A. G. 2009. Siberian meimechites: origin and relation to flood basalts and kimberlites. *Russian Geology and Geophysics,* 50**,** 999-1033.
Stevens, R. E. 1944. Composition of some chromites of the Western Hemisphere. *American Mineralogist,* 29**,** 1-34.
Streckheisen, A. 1973. Plutonic Rocks. Classification and nomenclature reccommended by the IUGS Subcommission on the Systematics of Igneous Rocks. *Geotimes,* 18**,** 26-30.

Streckheisen, A., Zanettin, B., Le Bas, M. J., Bonin, B., Bateman, G., Bellieni, G., Dudek, A., Schmid, R., Sørensen, A. & Woolley, A. R. 2002. *Igneous Rocks. A Classification and Glossary Terms,* Cambridge, UK, Cambridge University Press.

Sturt, B. A., Speedyman, D. L. & Griffin, W. 1980. *The Nordre Bumandsfjord ultramafic pluton, Seiland, north Norway. Part 1: field relations*.

Sørensen, B. E., Grant, T. B. & Larsen, R. B. 2015. Coupled reaction driven deformation, strain softening and CO_2 metasomatism in peridotites from the Reinfjord ultramafic complex, Northern Norway. *Geological Society of America, Annual Meeting* Baltimore, USA.

Søyland-Hansen, T. 1971. *An Investigation of Ni-Cu mineralization's in the Reinfjord-Jøkelfjord Area (in Norwegian).* MsC MsC thesis, Norwegian University of Science and Technology.

Tang, Q., Ma, Y., Zhang, M., Li, C., Zhu, D. & Tao, Y. 2013. The Origin of Ni-Cu-PGE Sulfide Mineralization in the Margin of the Zhubu Mafic-Ultramafic Intrusion in te Emeishan Large Igneous Province, Southwestern China. *Society of Economic Geologists,* 108**,** 1889-1901.

Tappe, S., Pearson, D.G, Nowell, G., Nielsen, T., Milstead, P., Muehlenbachs, K. 2011. A fresh isotopic look at Greenland Kimberlites: cratonic mantle lithosphere imprint on deep source signals. *Earth and Planetary Science Letters,* 305**,** 235-248.

Tegner, C., Robins, B., Reginiussen, H., Grundvig, S. 1999. Assimilation of crustal xenoliths in a basaltic magma chamber: Sr and Nd isotopic constraints from the Hasvik layered intrusion, Norway. *Journal of Petrology,* 40**,** 363-380.

Tgt-Ybgr 1970. (Third Geological Team, Yunnan Bureaus of Geology and Resources). Reserves report of Zhubu Pt deposit in Yuanmou of Yunnan Province: Internal Report.

Thompson, R. N. & Gibson, S. A. 2000. Transient high temperatures in mantle plume heads inferred from magnesian olivines in Phanerozoic picrites. *Nature,* 407**,** 502.

Thomson, G. P. & Davisson, C. 1937. Electronic waves. *Nobel prize in physics.* Sweden.

Tollefsrud, L. 2018. *Platinum Group Element Mineralization in the Reinfjord Ultramafic Complex.* MsC MsC, Norwegian University of Science and Technology.

Tredoux, M., Lindsay, N.M., Davies, G. And Mcdonald, I. 1995. The fractionation of platinum group elements n magmatic systems with the suggestion of a novel casual mechanism. *South African Journal of Geology,* 98**,** 67-157.

Ulmer, G. C. 1969. Experimental investigation on chromite spinels. *Economic Geology Monograph,* 4**,** 31-114.

Usepa 2000. Guidance for Data Quality Assessment: Practical Methods for Data Analyses.

Vakhromeev, A. S., Zimin, L. A. & Kozhevnikov, K. E. 1936. Uralskie mestorozhdeniya khromita *VIMS, Moskva-Leningrad,* 85**,** 240.

Vegvesen, S., Nibio & Kartverket. 2019. *Norge i bilder* [Online]. Available: https://norgeibilder.no/?x=752504&y=7792065&level=11&utm=33&projects=&layers=2&plannedOmlop=0&plannedGeovekst=0 [Accessed June 6th 2019].

Vernon-Parry, K. D. 2000. Scanning electron microscopy: an introduction. *III-Vs Review, Elsevier,* 13**,** 40-44.

Wang, C., Zhou, M.-F. & Qi, L. 2007. *Permian flood basalts and mafic intrusions in the Jinping (SW China)–Song Da (northern Vietnam) district: Mantle sources, crustal contamination and sulfide segregation.*

Wang, C. Y., Zhou, M., Yang, S. & Sun, Y. 2014 Geochemistry of the Abulangdang intrusion: cumulates of high-Ti picritic magmas in the Emeishan large igneous province, SW China. *Chemical Geology* 378-379**,** 244-39.

White, W. M. 2005. *Geochemistry*, Wiley-Blackwell.
Yaxley, G. M. & Brey, G. P. 2004. Phase relations of carbonate-bearing eclogite assemblages from 2.5 to 5.5 GPa: implications for petrogenesis of carbonatites. *Contributions to Mineralogy and Petrology,* 146**,** 606-619.
Yeo, W. J. A. 1984 The Melkvann Ultramafic Complex, Seiland igneous province, North Norway: intrusive mechanisms and petrological evolution. . *Unpublished Ph.D. thesis.* University of Bristol, U.K
Yu, X., Lee, C.-T. A., Chen, L.-H. & Zeng, G. 2015. Magmatic recharge in continental flood basalts: insights from the Chifeng igneous province in Inner Mongolia. *Geochemistry, Geophysics, Geosystems,* 16**,** 2082–2096.

9 Appendix A

9.1 Thin section scans and descriptions

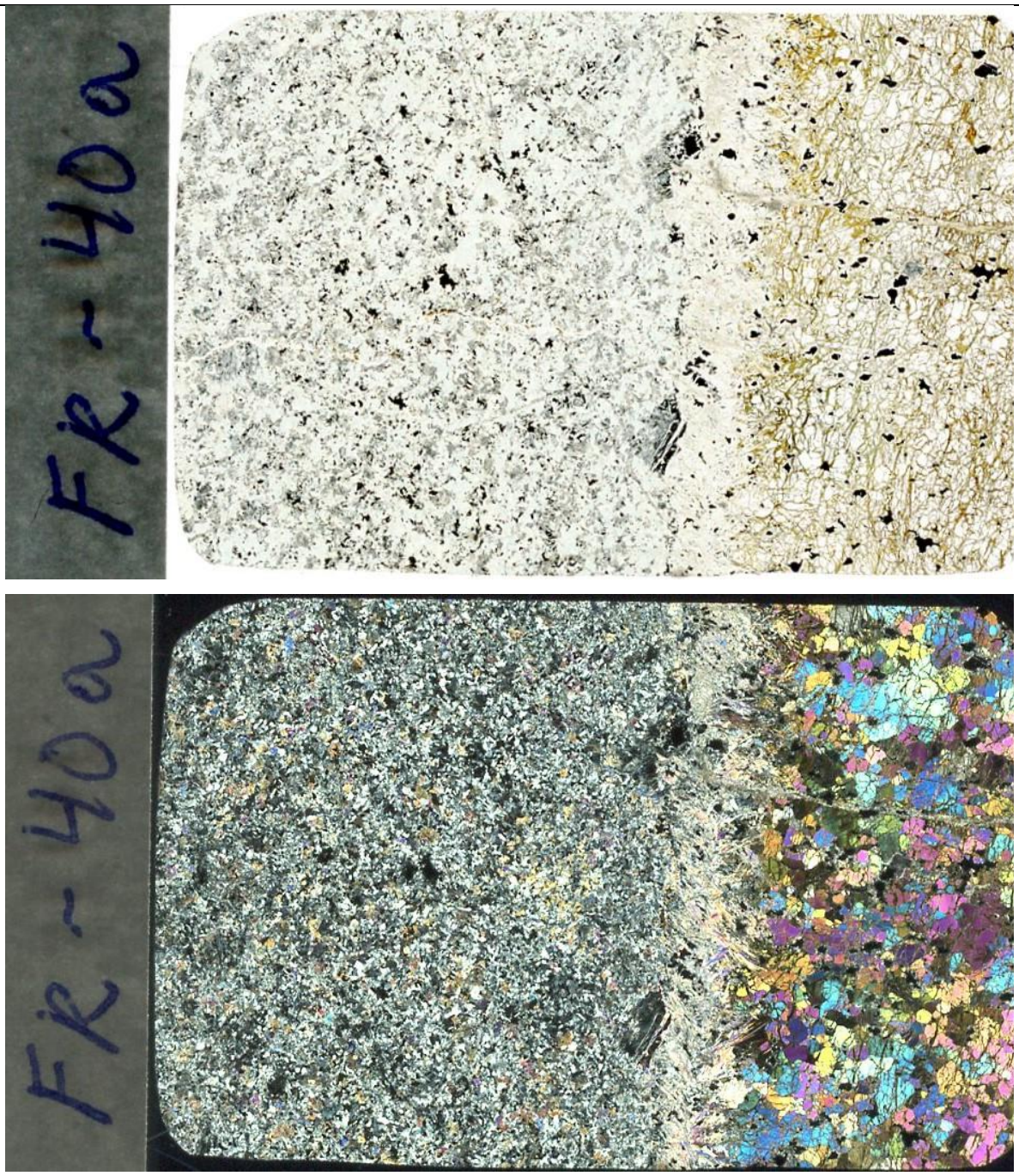

Figure 9.1

Thin section FR-40a scanned in transmitted plane polarized light (Figure 9.1 a) and crossed polarized light (Figure 9.1 b).

The thin section FR-40a is from a highly sulfide rich dyke with a contact reaction rim. This is the only surface sample thin section in this study, originally taken by Reinhardt (2019). The sample has not undergone further research than to note that substantial sulfide occurrences can be found in dykes from the area.

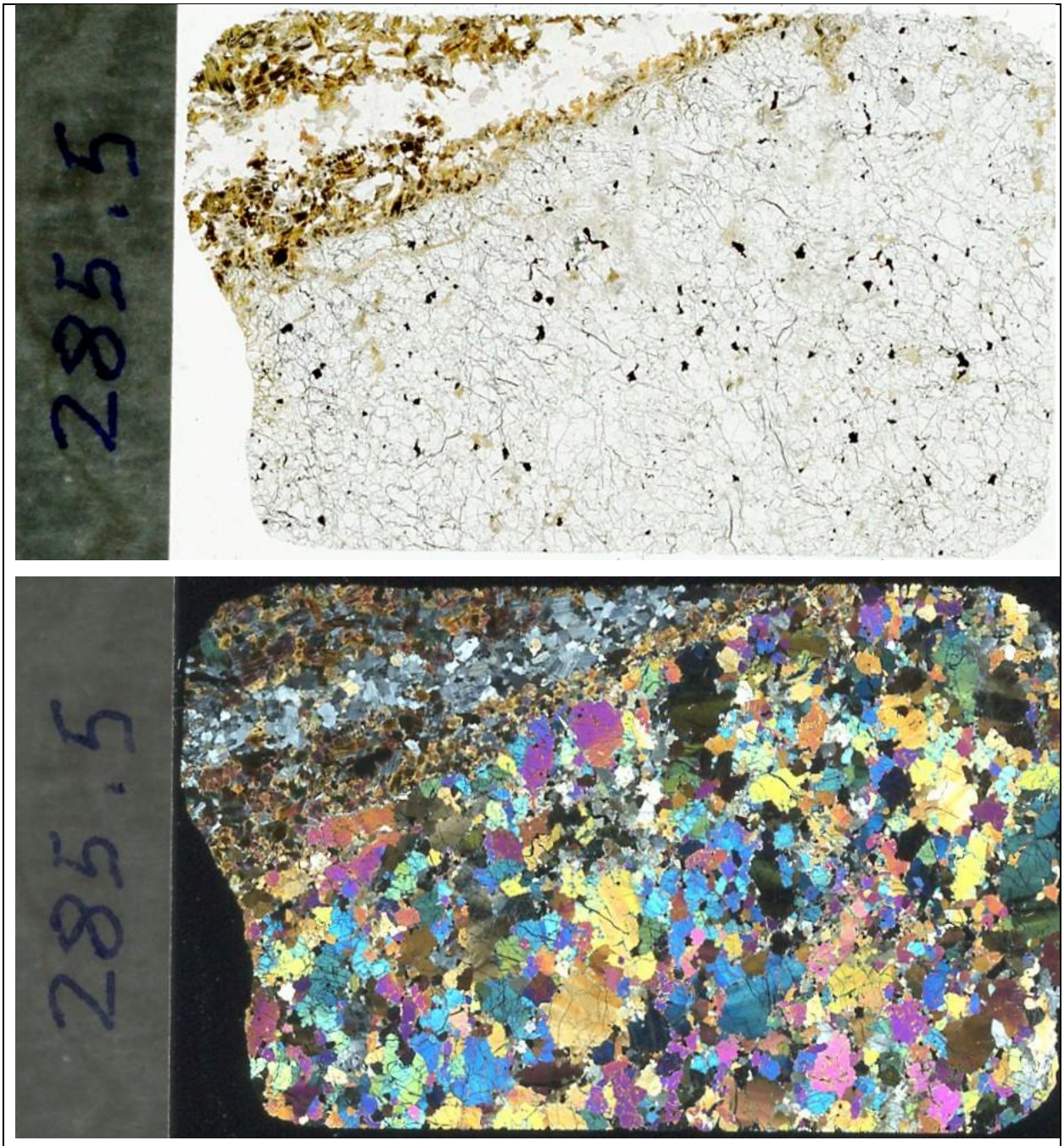

Figure 9.2

Thin section 285,5 scanned in transmitted plane polarized light (Figure 9.2 a) and crossed polarized light (Figure 9.2 b).

The thin section 285,5 shows a pyroxenitic dyke cutting a dunite in a contact with a ca 0,5 cm contact reaction rim. The pyroxenitic dyke is in turn cut by a plagioclase dominated dyke. Most of the sulfide minerals are interstitial and found in the pyroxenite dyke. The dunite host most of the

chromian Spinels of which 2 types are identified. The dunite contain Olivine of type 1. The sample shows low degrees of serpentinization.

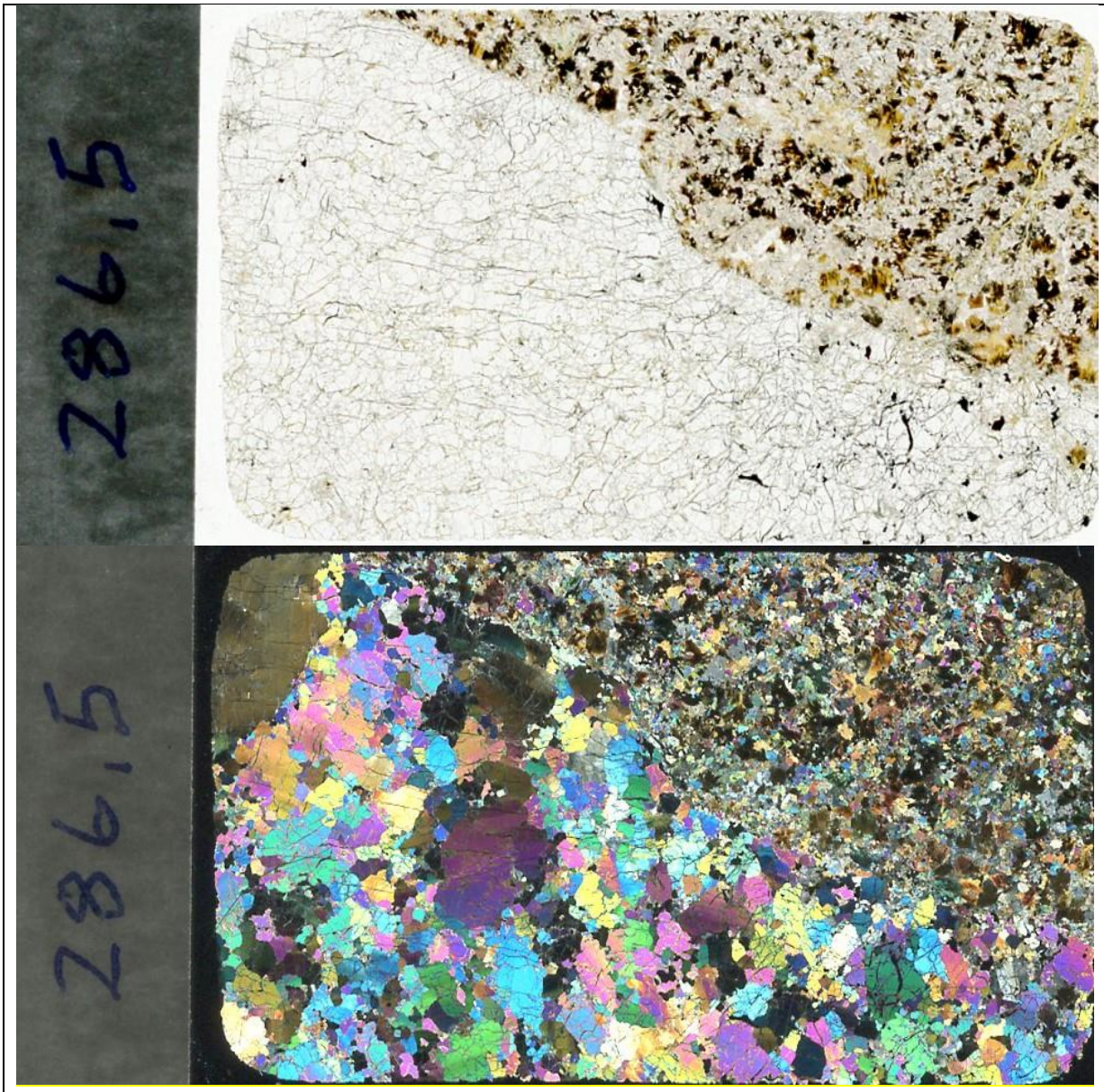

Figure 9.3

Thin section 286,5 scanned in transmitted plane polarized light (Figure 9.3 a) and crossed polarized light (Figure 9.3 b).

Thin section 286,5 depicts a sharp contact between a dunite and a gabbroic dyke. The contact has a small contact reaction rim which mostly affect the dyke by a more finely grained and more Olivine rich configuration. The dyke has a greater concentration of sulfide minerals than the host rock dunite. There are only one Spinel phase in the dyke and three Spinel types in the dunite. The

dunite has Olivine of type 1 and 3 with varying grain size and shape. The sample has undergone low degrees of serpentinization.

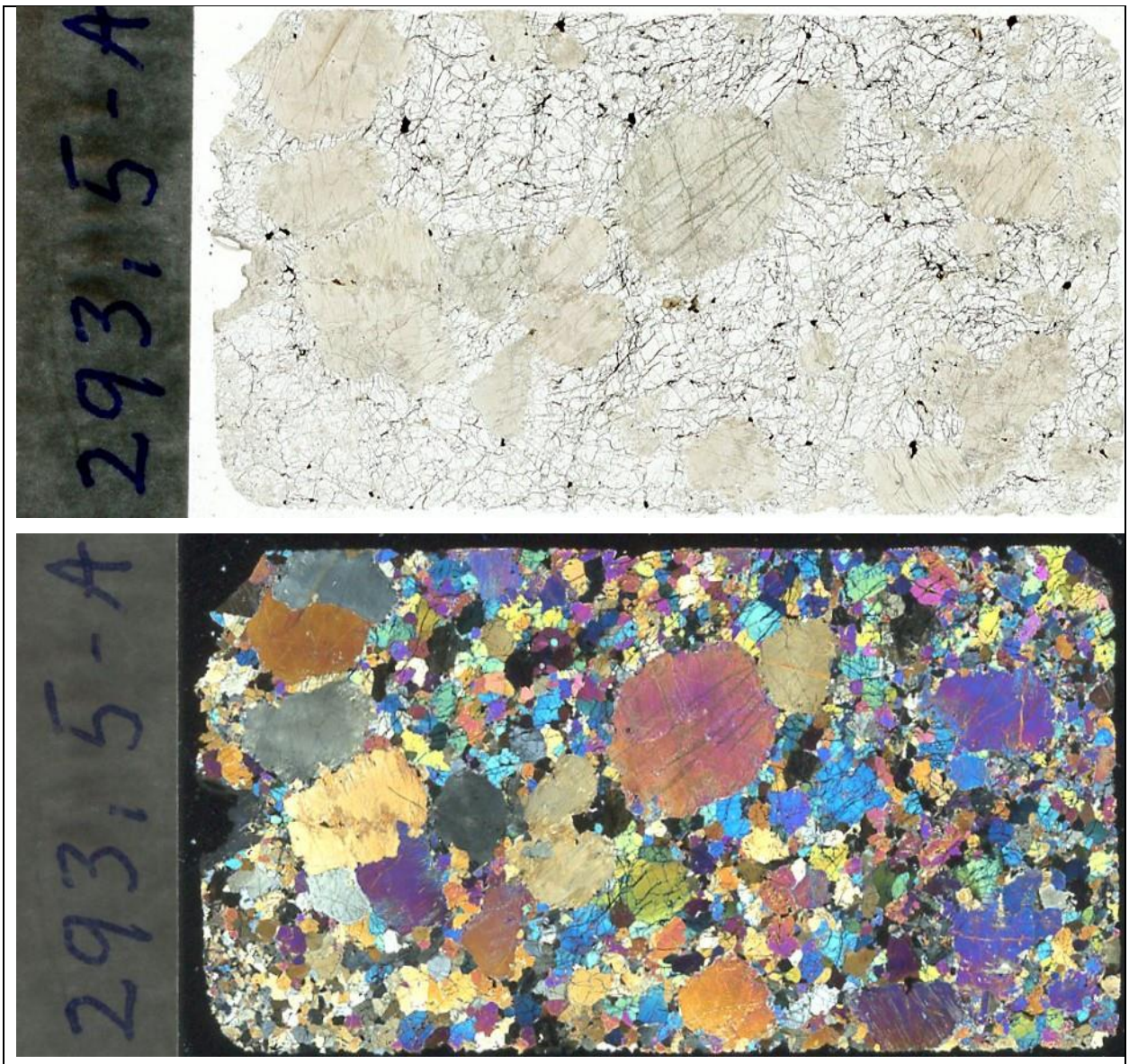

Figure 9.4

Thin section 293,5-A scanned with transmitted plane polarized light (Figure 9.4 a) and crossed polarized light (Figure 9.4 b).

Thin section 293,5-A contain a wehrlite with substantially larger pyroxene crystals than Olivine. Sulfides are mostly found as interstitial crystals but one sulfide grain is found alog a crack in a large pyroxene grain. There are observed inclusions of Olivine in pyroxene crystals. Two types of chromian Spinels were identified; the brighter is mostly found as euhedral inclusions in Olivine. The sample is homogenous and shows low degrees of serpentinization.

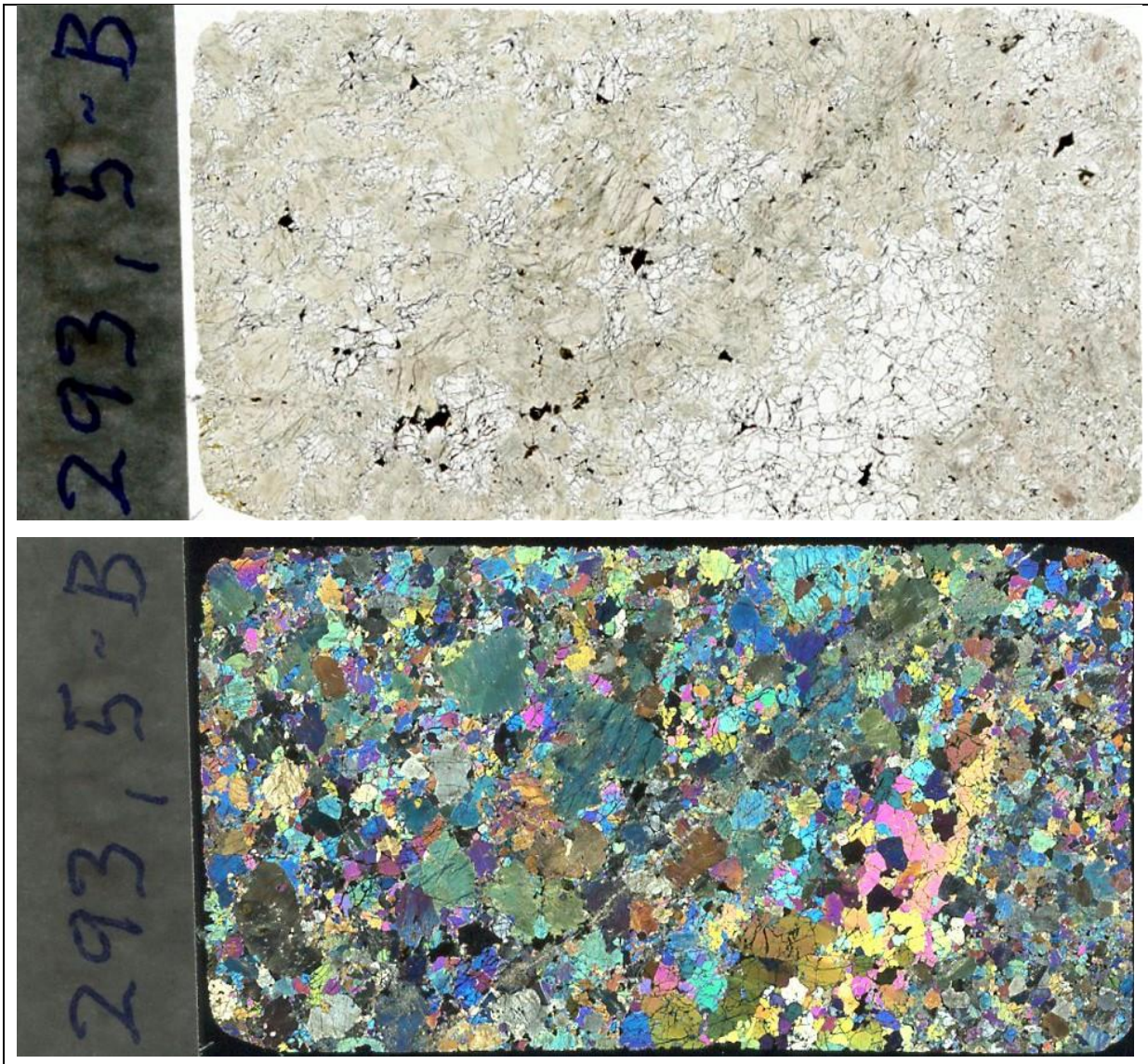

Figure 9.5

Thin section 293,5-B scanned in transmitted plane polarized light (Figure 4.2 a) and crossed polarized light (Figure 4.2 b).

Sample 293,5-B shows a pyroxenite being intruded by a replacive dunite in the lower right part. The process is most easily observed in plane polarized light, but is also apparent in cross-polarized light when looking for the phenomenon. The replacive dunite and pyroxenite both contain chromian Spinels. The pyroxenite have both Clinopyroxene and Orthopyroxene. The sulfides are mostly found in the pyroxenite as both interstitial crystals and as inclusions in pyroxene. The largest sulfide minerals are found in the replacive dunite, though sulfides are rarer in the dunite. The dunite contain type 1 Olivine. The rock has been subject to low degrees of serpentinization.

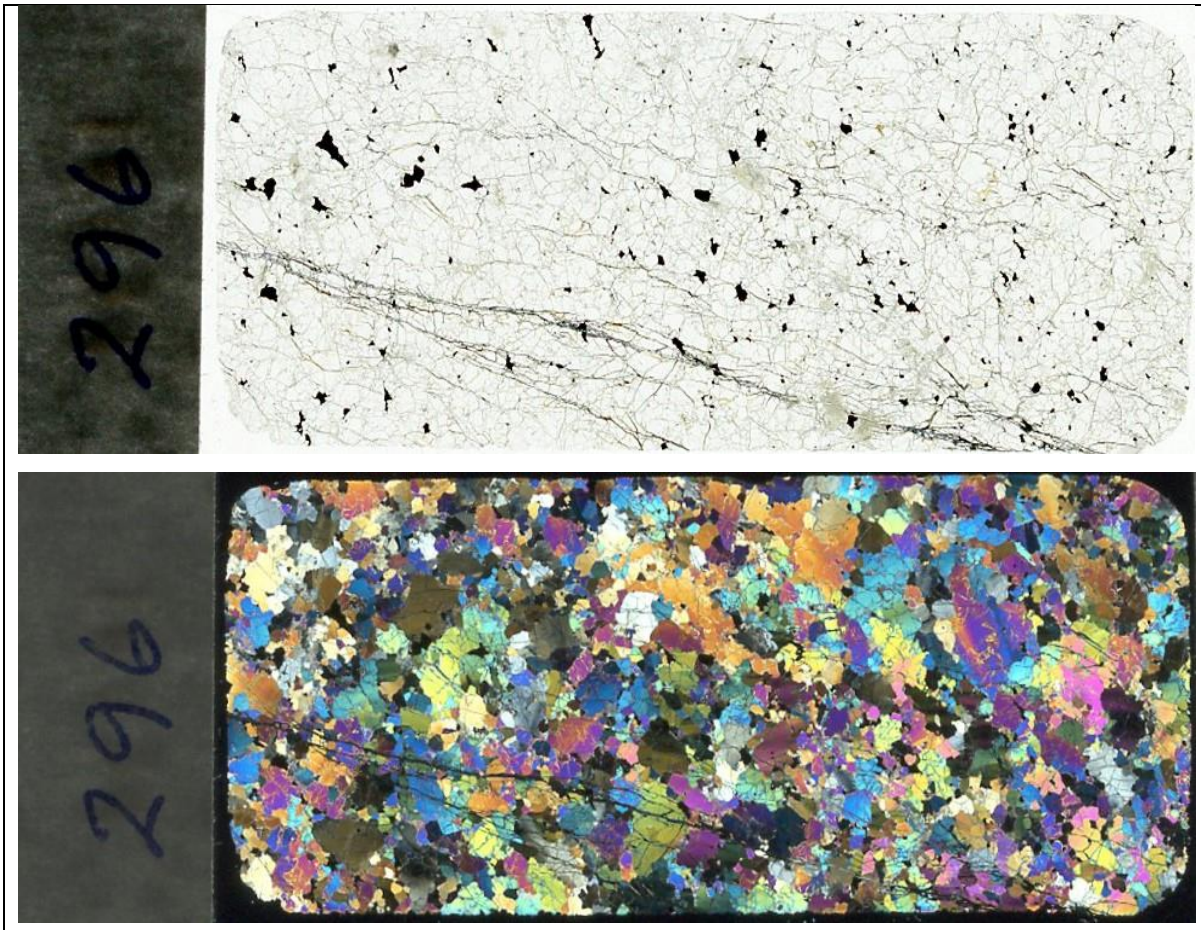

Figure 9.6

Thin section 296 scanned in transmitted plane polarized light (Figure 9.6 a) and crossed polarized light (Figure 9.6 b).

Thin section 296 is a homogenous dunite cut by localized serpentinization in a W-SE orientation. Sulfide minerals are interstitial in the sample. Two types of chromian Spinels (medium and bright) are present, the brighter occurring as inclusions in the darker type. Carbonate splotches are observed several places, and Spinels appear to be associated with them. The serpentinized fractures cutting through the sample cuts all minerals, including sulfides and Spinels. The rest of the sample has low degrees of serpentinization.

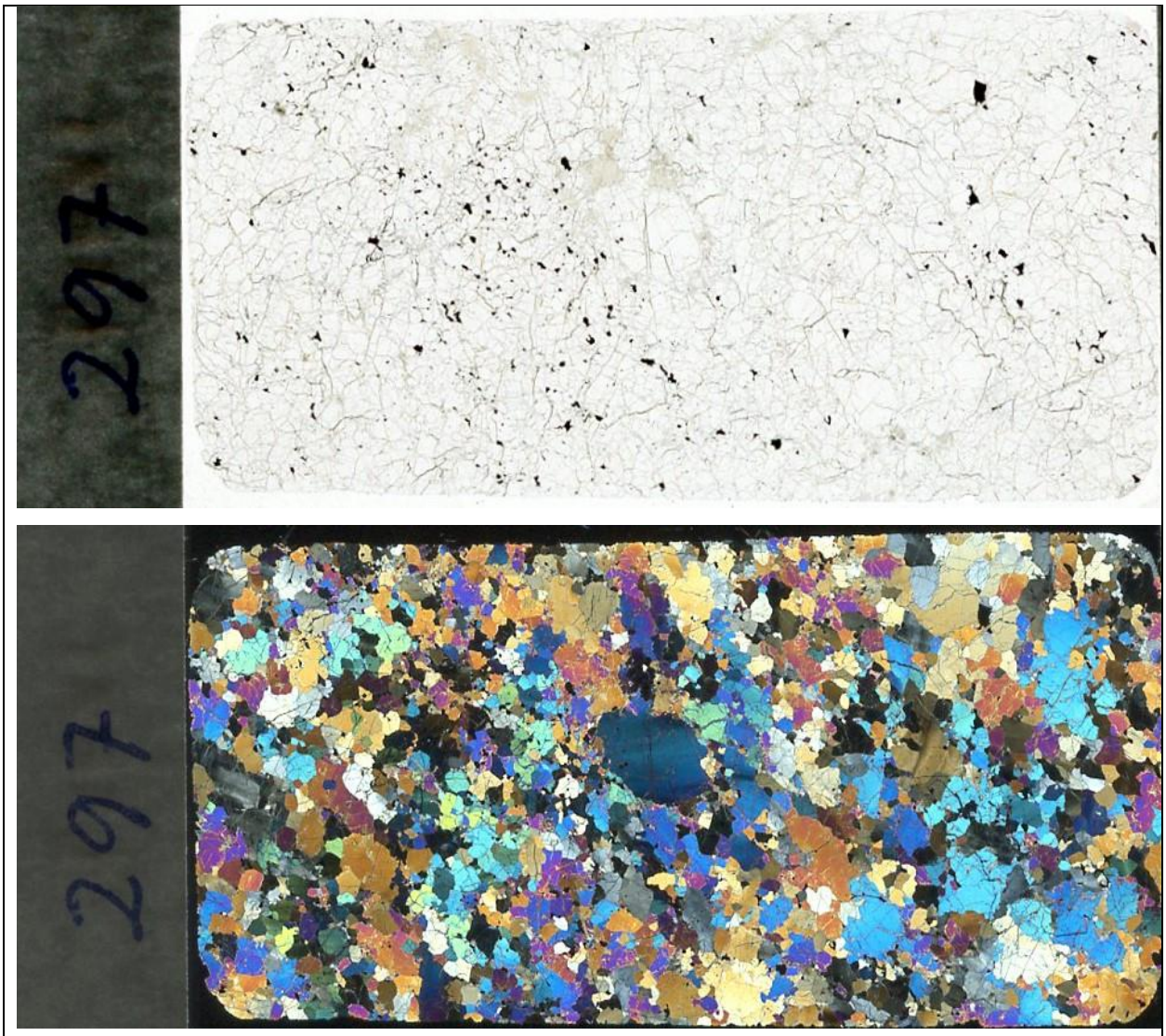

Figure 9.7

Thin section 297 scanned using transmitted plane polarized light (Figure 9.7 a) and crossed polarized light (Figure 9.7 b).

Sample 297 is a dunite with heterogeneously distributed opaque minerals. The main chromian Spinel phase occurs as interstitial crystals. There are two other chromian Spinel types in the section. The brighter type is found as inclusions in the main phase. The darker phase is found as inclusions in sulfide minerals and with sulfide minerals as inclusions in the Spinel. Some carbonate splotches are present in the rock. The sample contain type 1 ***(and 2??)*** Olivine.

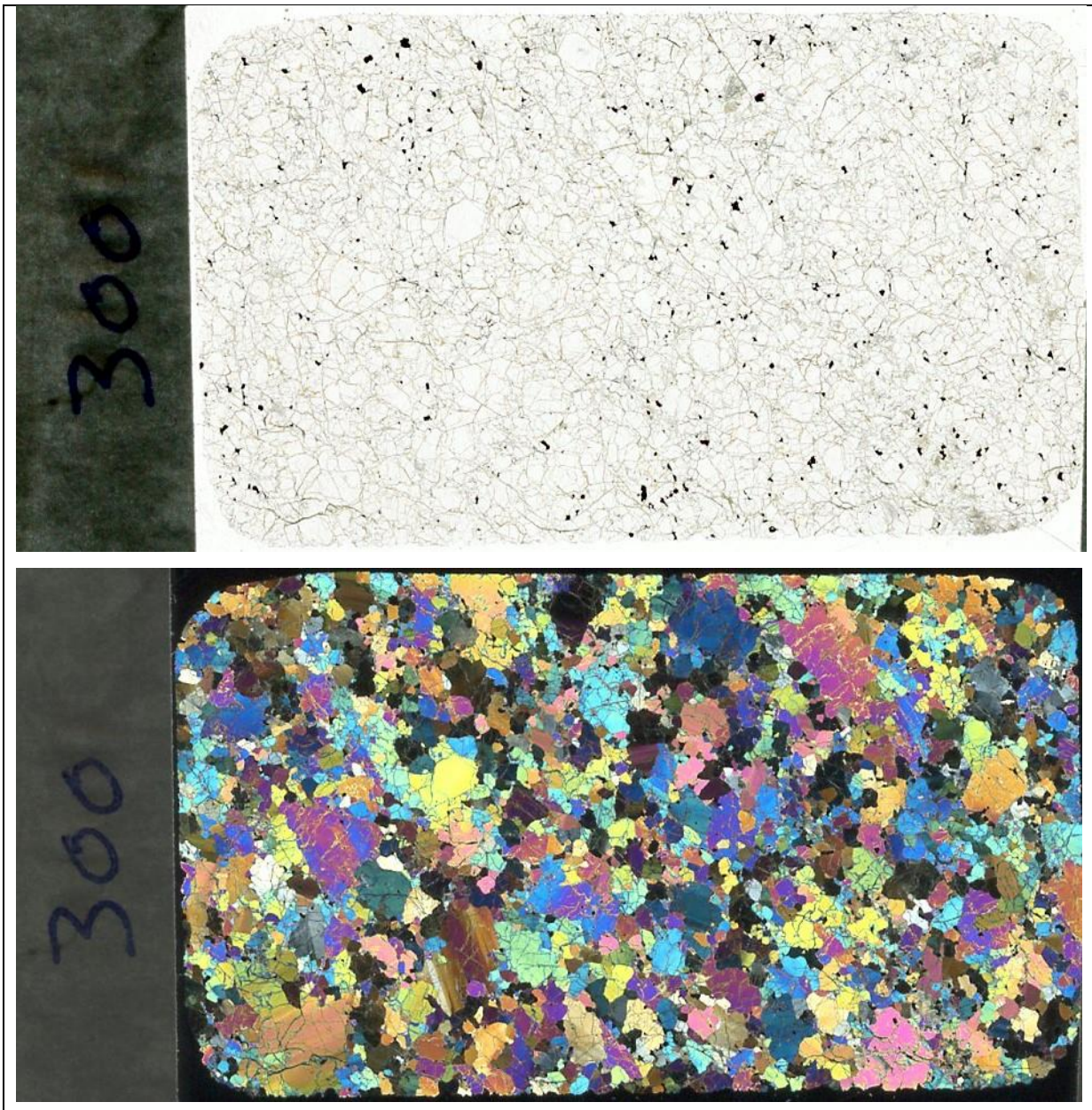

Figure 9.8

Thin section 300 scanned using transmitted plane polarized light (Figure 9.8 a) and crossed polarized light (Figure 9.8 b).

Thin section 300 is a homogeneous dunite with interstitial chromian Spinels and sulfides. Type 1 and ⅔ Olivine is present. 4 types of chromian Spinels have been observed in optical microscopy, all in contact with the other types. The main chromian Spinel and the darkest variant are sometimes found as inclusions in Olivine. The Spinel crystals are most commonly interstitial. The darkest chromian Spinel is also found in association with carbonate clusters. There are very few sulfides in the thin section. The sample has undergone low degrees of serpentinization.

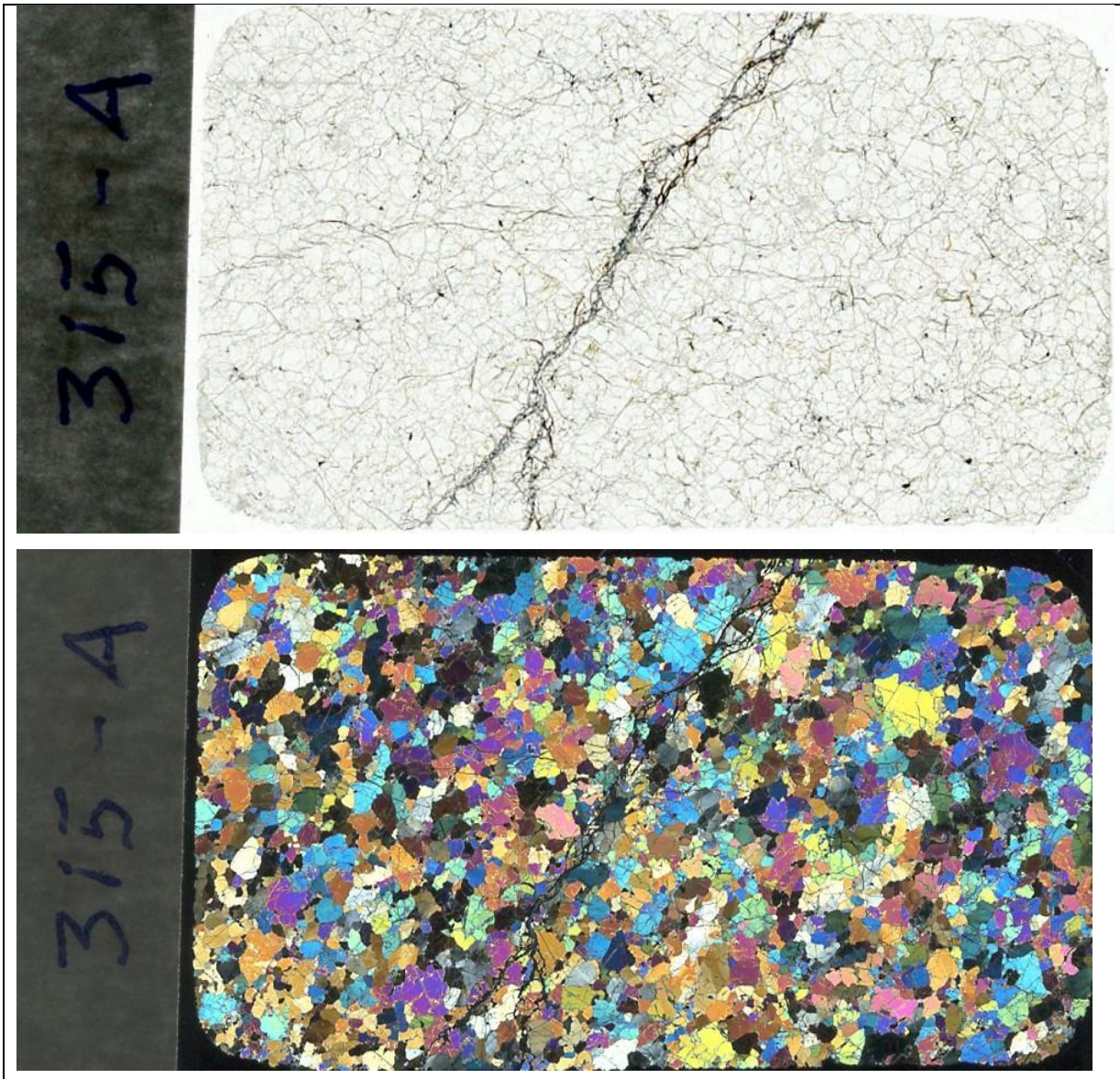

Figure 9.9

Thin section 315-A scanned using transmitted plane polarized light (Figure 9.9 a) and crossed polarized light (Figure 9.9 b).

Thin section 315-A contains a dunite cut by a chaotic serpentine vein. There are 3 chromian Spinel types present in the thin section. There are few sulfides in the rock. 2 types of chromian Spinels have been recognized, and are found as inclusions in each other. Most of the Spinel grains are interstitial, though some are found as inclusions in Olivine and in the calcareous spots of the thin section.

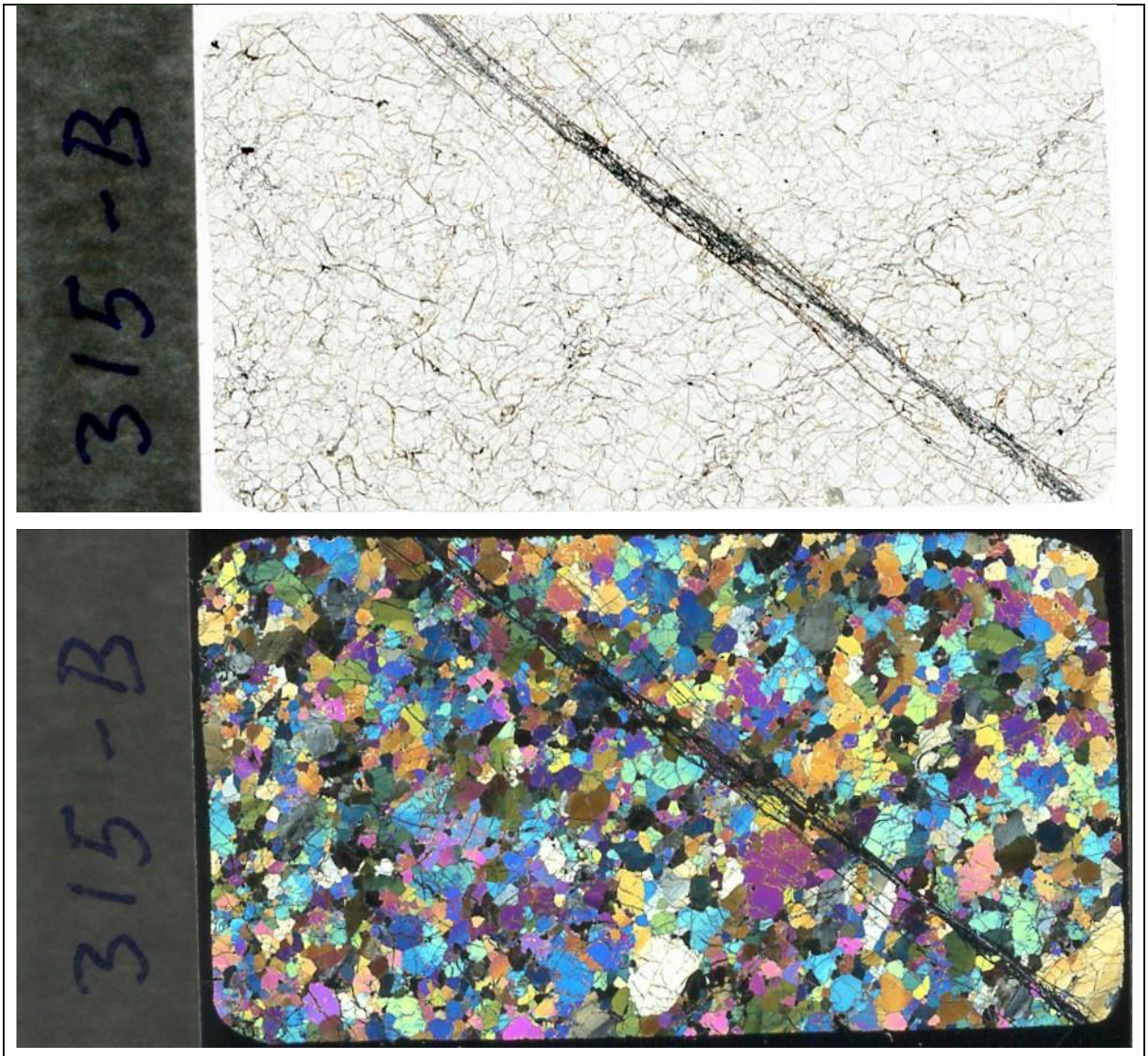

Figure 9.10

Thin section 315-B scanned using transmitted plane polarized light (Figure 9.10 a) and crossed polarized light (Figure 9.10 b).

The thin section 315-B contains a dunite cut by a discrete and even serpentine vein that is perpendicular to the vein in 315-A. 3 types of chromian Spinels have been identified in the thin section. The dominant type is the “wolf grey” Spinel. It hosts inclusions of a brighter and darker Spinel and is mostly found as interstitial crystals. The dominant and darkest Spinel types are also found as inclusions in Olivine. The sulfide minerals are evenly distributed in the section. The vein appears to be filled with serpentine, an opaque mineral and carbonates. The rest of the sample has undergone low degrees of serpentinization.

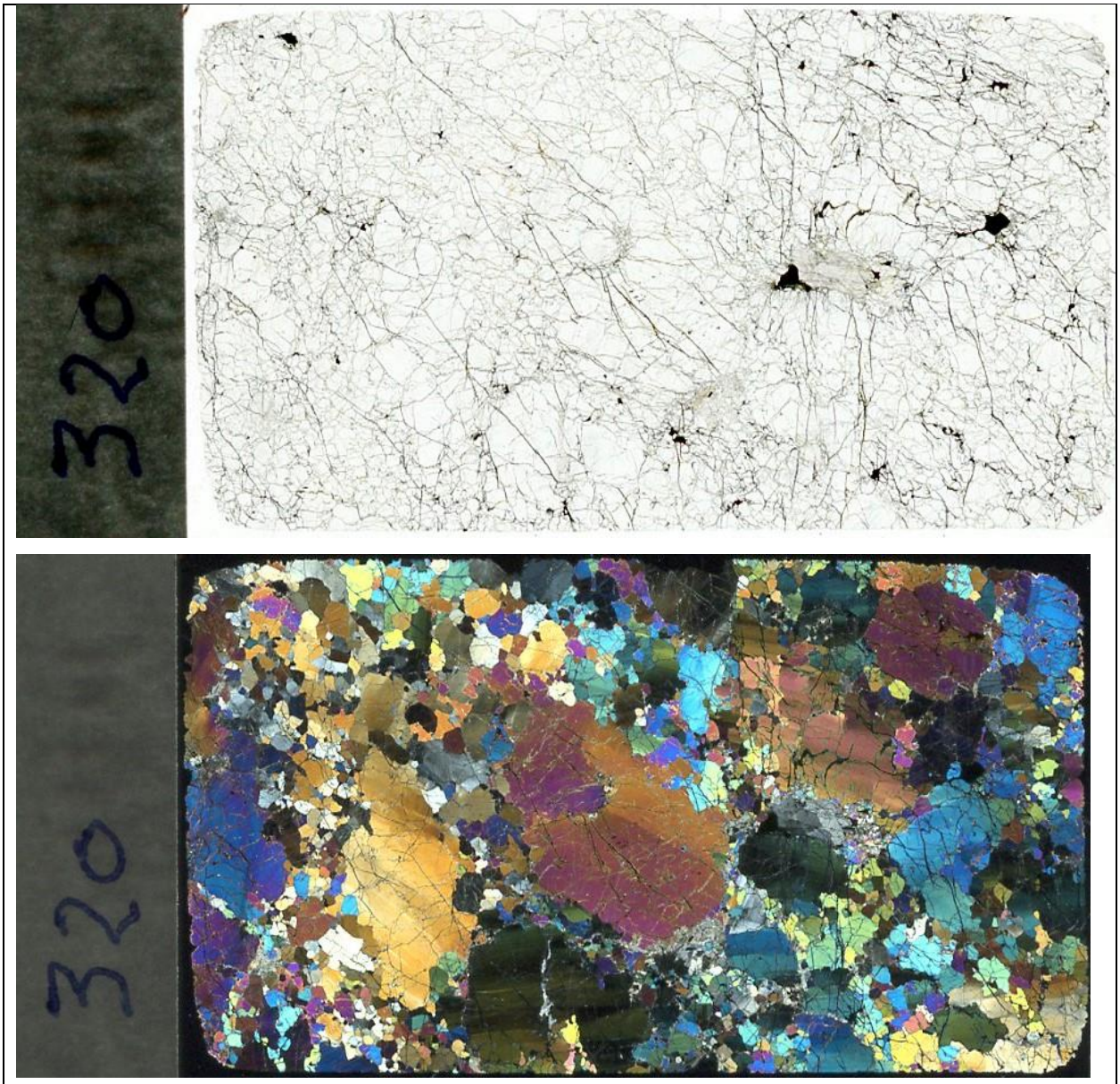

Figure 9.11

Thin section 320 scanned using transmitted plane polarized light (Figure 4.1 a) and crossed polarized light (Figure 4.1).

Thin section 320 displays a dunite with large variation in grain size of the Olivine crystals. There are calcareous spots with a relative enrichment in sulfide minerals compared to the rest of the sample. The sample contain few sulfide minerals. Most sulfide minerals and chromian Spinel grains are interstitial. Two types of Spinels have been identified in the section. Only type 1 Olivine is present, though in varying grain size. The sample has undergone low to medium grades of serpentinization.

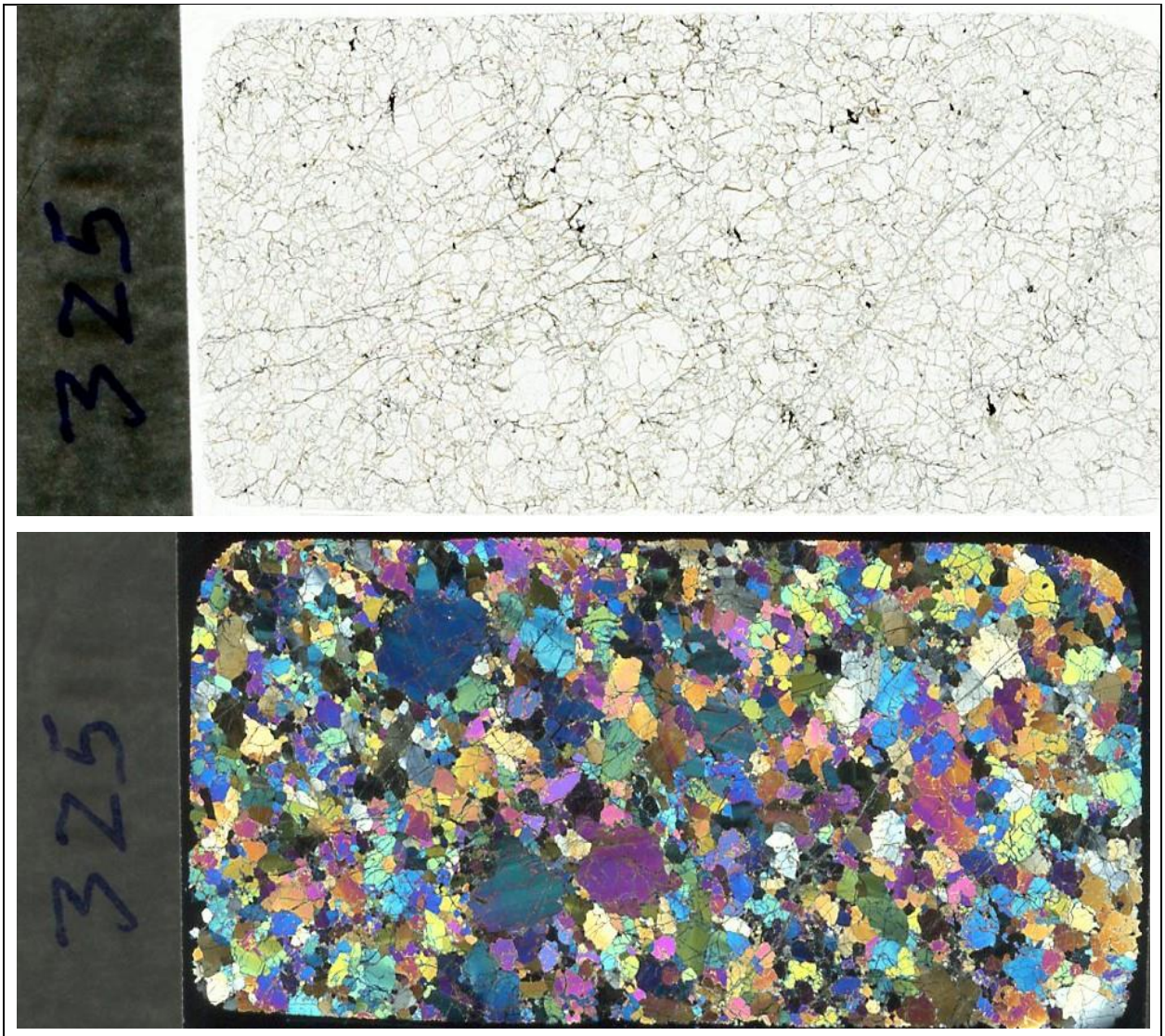

Figure 9.12

Thin section 325 scanned using transmitted plane polarized light (Figure 9.12 a) and crossed polarized light (Figure 9.12 b).

Thin section 325 is a homogeneous fine grained dunite. Three types of chromian Spinels are observed in contact with each other. Most occur as interstitial crystals, though some are found as inclusions in Olivine. Rutile is found in serpentinized veins and appear to be connected to the chromian Spinels. The sulfide minerals in the sample are interstitial crystals, mostly primary sulfides. The section contain clusters of carbonate minerals. The sample has undergone low to medium grade serpentinization.

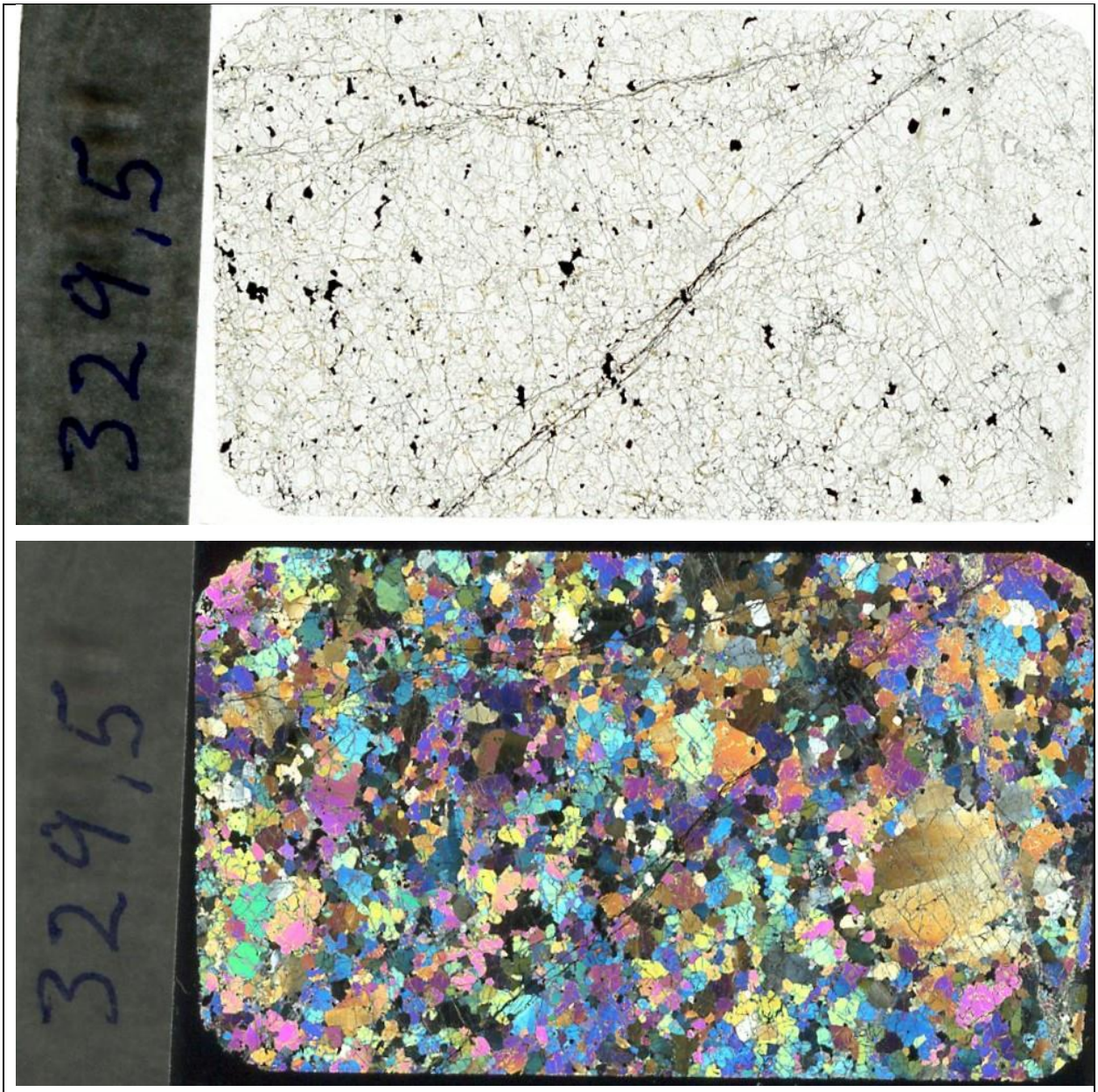

Figure 9.13

Thin section 329,5 scanned using transmitted plane polarized light (Figure 9.13 a) and crossed polarized light (Figure 9.13 b).

Thin section 329,5 is a homogenous dunite. Approximately ⅓ of the sulfide minerals are found as inclusions in Olivine (and pyroxene), the rest as interstitial crystals. Sulfide minerals are often found in contact with the main chromian Spinel in the sample. Three chromian Spinels are present, though the main "wolf grey" phase is much more abundant than the darker and brighter variants. The main chromian Spinel phase is found as large interstitial crystals, sometimes with inclusions of the minor, darker, chromian Spinel type or the brighter type. Olivine type 1 and 3 are present in

the section. Carbonate clusters are present several places. So is rutile, though it does not appear to have any connection to other mineralization in this sample. The sample is cut by serpentine veins and carbonate veins, the serpentine veins cutting the carbonate veins. The sample has undergone low to medium grade serpentinization.

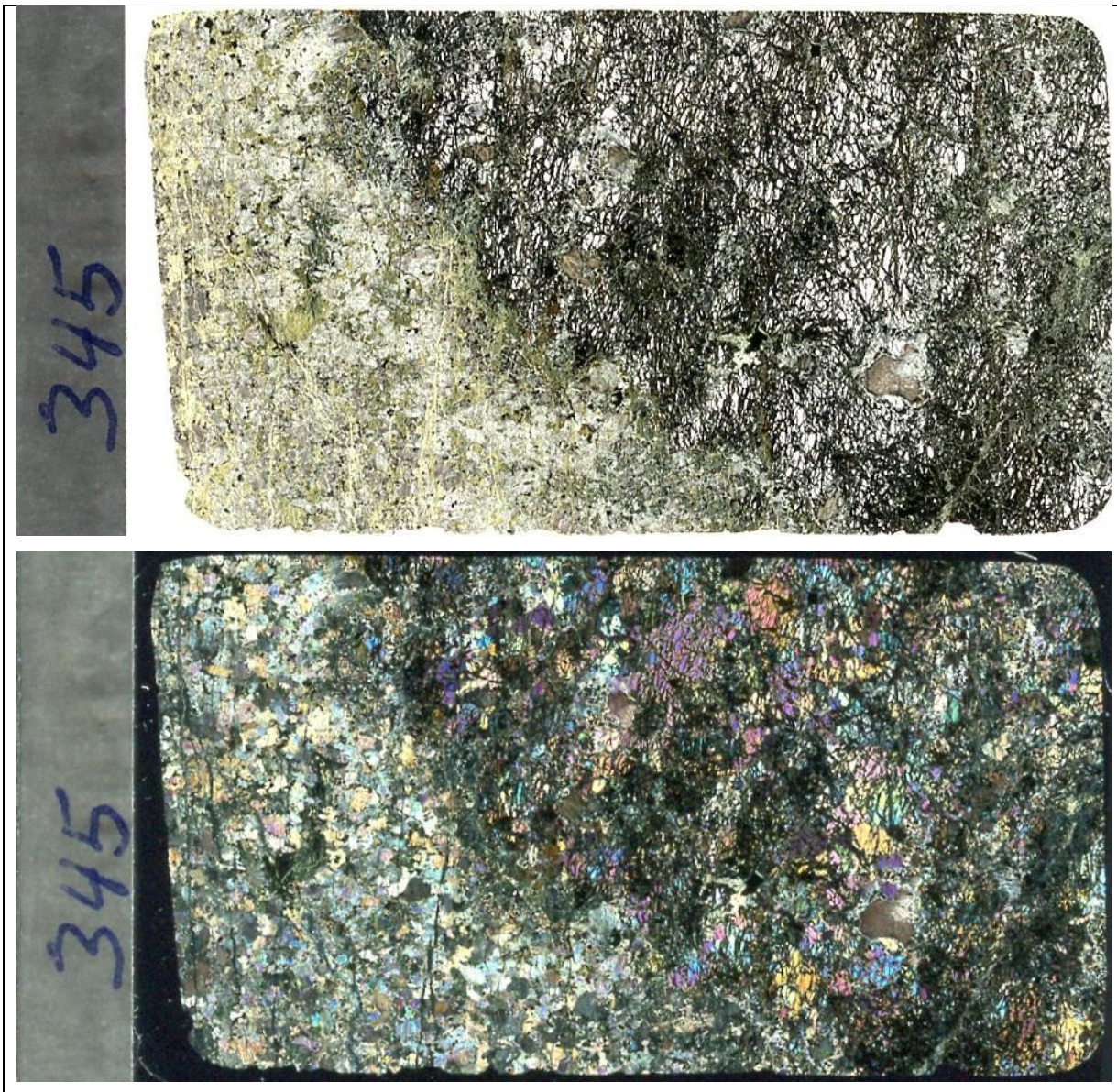

Figure 9.14

Thin section 345 scanned using transmitted plane polarized light (Figure 9.14 a) and crossed polarized light (Figure 9.14 b).

Sample 345 is of a pyroxenite (left) cut by a dunitic dyke (right). One type of chromian Spinel is observed in the sample. The number of sulfide mineral grains in this sample is greater than in the

previous. Pentlandite is the main sulfide mineral. The sample has undergone heavy serpentinization. All grains in the sample has also undergone some brittle deformation.

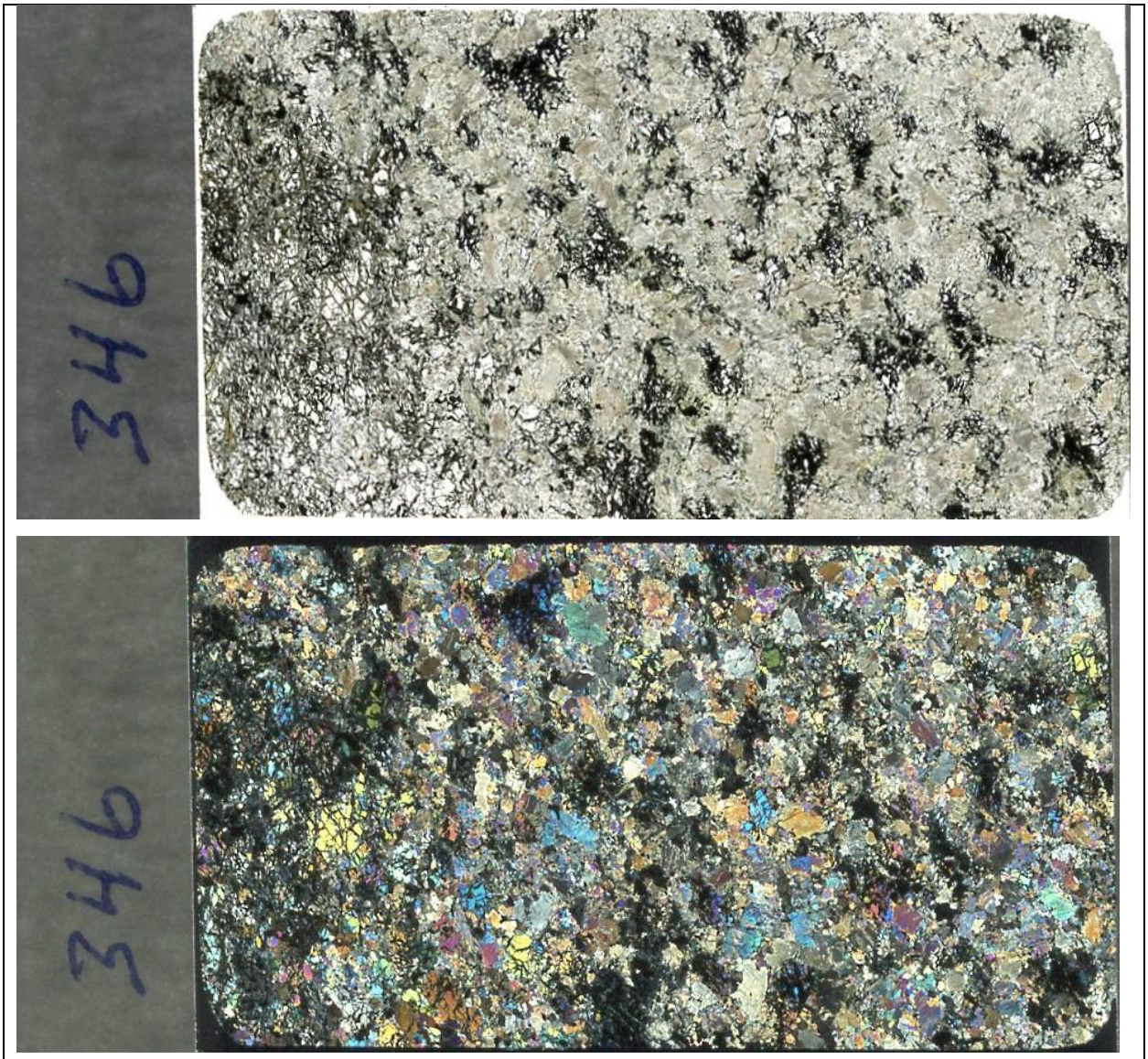

Figure 9.15

Thin section 346 scanned using transmitted plane polarized light (Figure 9.15 a) and crossed polarized light (Figure 9.15 b).

Sample 346 is the first sample of the main copper reef in this study. It is a wehrlite to pyroxenite with heterogeneous distribution of pyroxenes (more in the right of the scanned thin sections) and serpentinization (more extensive in the left side of the thin section). The sample contains many sulfide grains, primarily pentlandite and chalcopyrite. The sulfide grains are several places cut by

chromian Spinel, often in irregular bands. Chromian Spinel more often occur as interstitial crystals. The sample has undergone high grade of serpentinization.

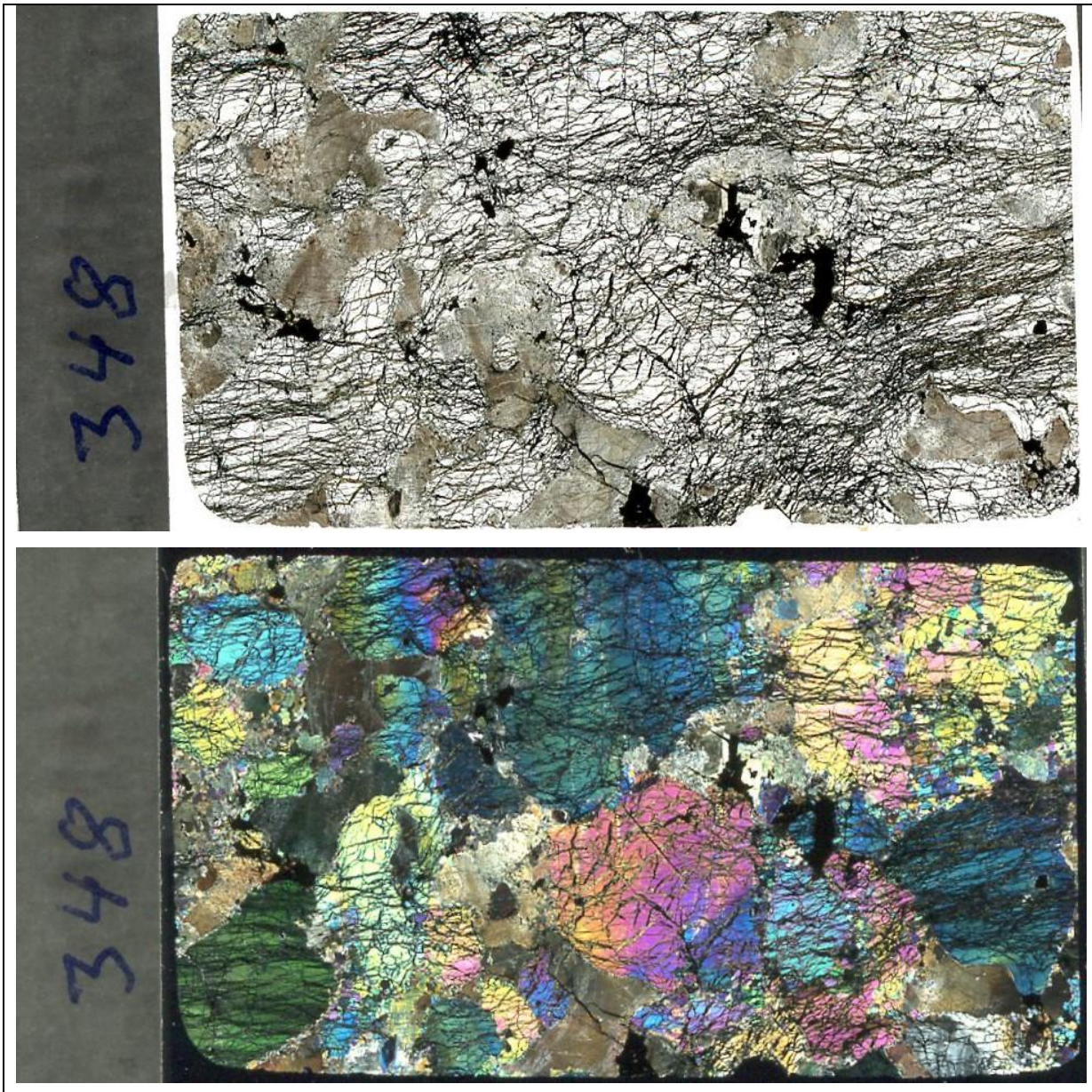

Figure 9.16

Thin section 348 scanned using transmitted plane polarized light (Figure 9.16 a) and crossed polarized light (Figure 9.16 b).

Thin section 348 is a dunite with large massive sulfide grains and cm sized type 1 Olivine grains. It also contain smaller type 3 Olivine grains. The sample contain both Clinopyroxene and Orthopyroxene. Two types of chromian Spinels are found in the sample. The main, “wolf grey”, phase occur as euhedral to subhedral interstitial crystals, some places in contact with sulfide grains.

The less common, darker variant occur as inclusions in pyroxene, Olivine and the main chromian Spinel. The sample has undergone medium grade serpentinization.

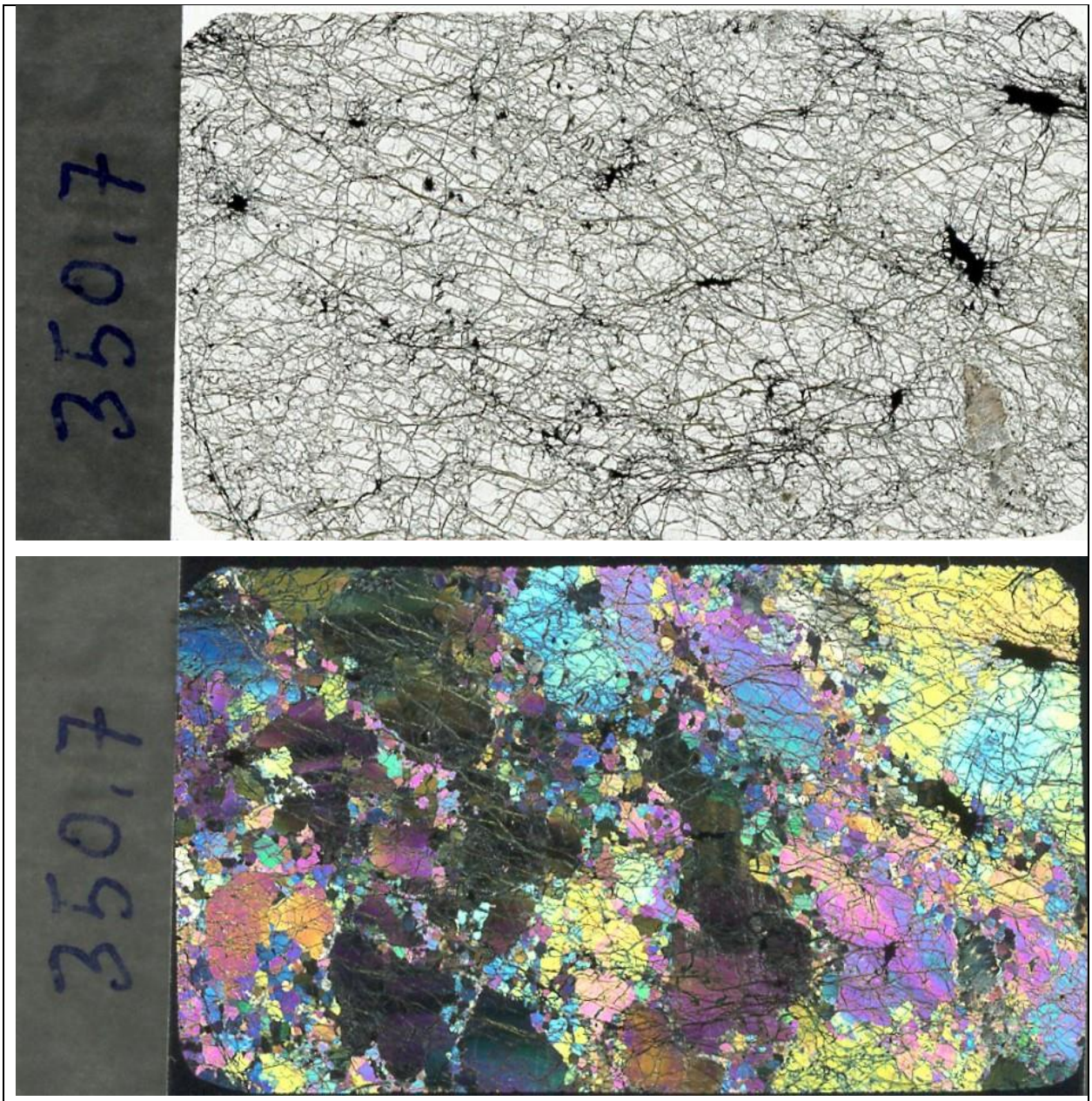

Figure 9.17

Thin section 350,7 scanned using transmitted plane polarized light (Figure 9.17 a) and crossed polarized light (Figure 9.17 b).

Thin section 350,7 is the deepest thin section in the copper reef. It is a homogenous dunite with massive sulfides and two main grain sizes; either cm scale Olivine type 1 and pyroxene grains; or 50 micro meter scale Olivine type 2 grains. All sulfide grains are surrounded by serpentine veins,

so it is unclear whether the grains have a magmatic or a hydrothermal origin. 1 type of chromian Spinel is observed in the sample, it is rare and only found in small grains as interstitial crystals. The Spinel grains are in places surrounded by a halo of smaller Spinel grains. The sample contain both Clinopyroxene, Orthopyroxene and Amphibole in approximately similar quantities. The sample has undergone medium grade serpentinization.

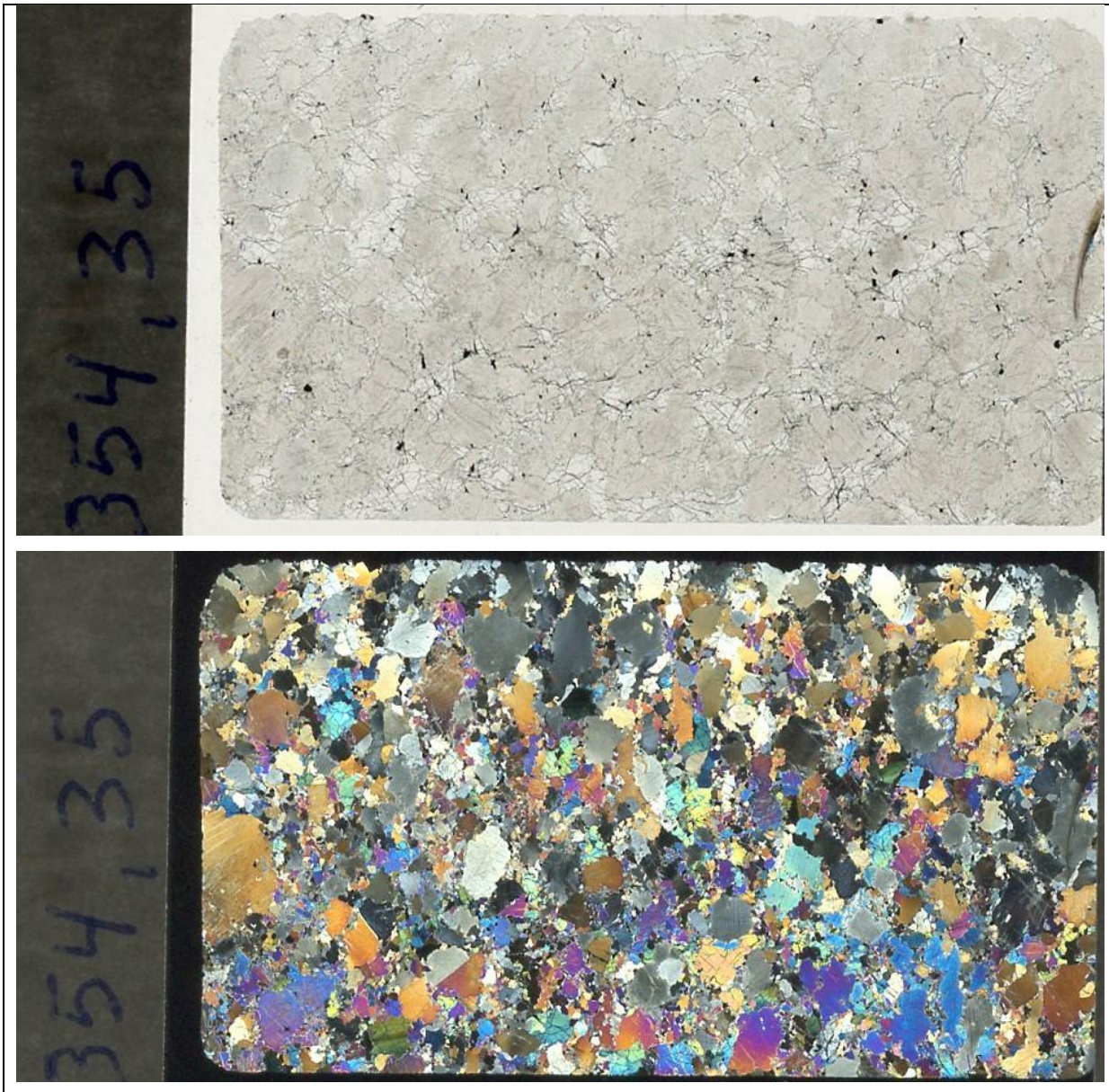

Figure 9.18

Thin section 354,35 scanned using transmitted plane polarized light (Figure 9.18 a) and crossed polarized light (Figure 9.18 b).

Thin section 354,35 is a homogenous medium grained pyroxenite 4 meters below the copper reef. The sulfide grains are small, evenly distributed, interstitial crystals. Two types of chromian Spinels are present, and are found in close association with each other. Both occur as both inclusions and interstitial crystals. There is generally much less Spinels than sulfide crystals in the sample. The sample has undergone a very low grade serpentinization.

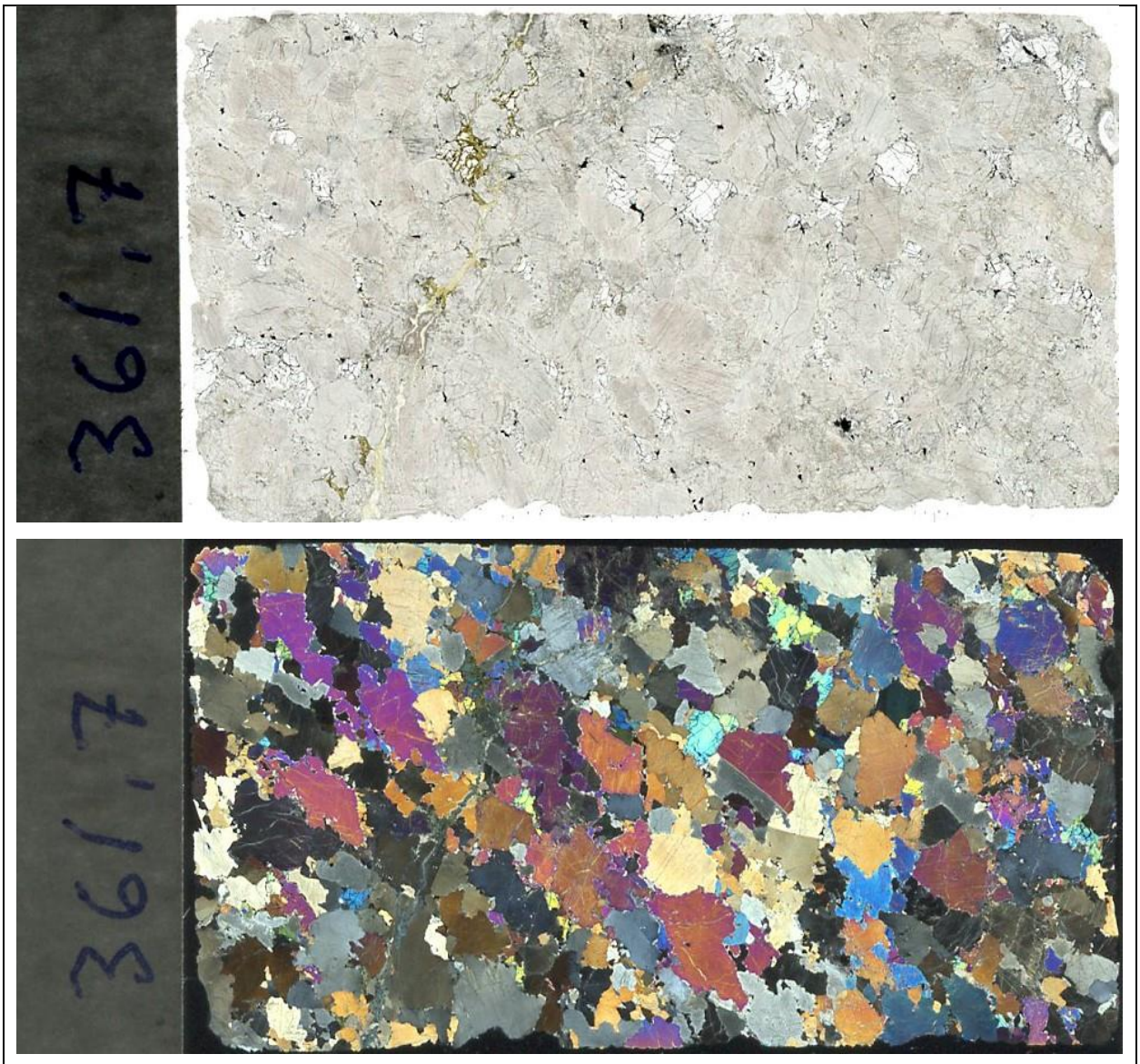

Figure 9.19

Thin section 361,7 scanned using transmitted plane polarized light (Figure 9.19 a) and crossed polarized light (Figure 9.19 b).

Sample 361,7 is a homogeneous, weakly foliated pyroxenite with evenly distributed small sulfide and chromian Spinel grains. Two types of chromian Spinels are present, the darker kind is found

as a halo around the main “wolf grey” phase. The Olivine crystals are of type 2. The sample has undergone little serpentinization. A migrating vein cuts through all crystals in the center left part of the thin section.

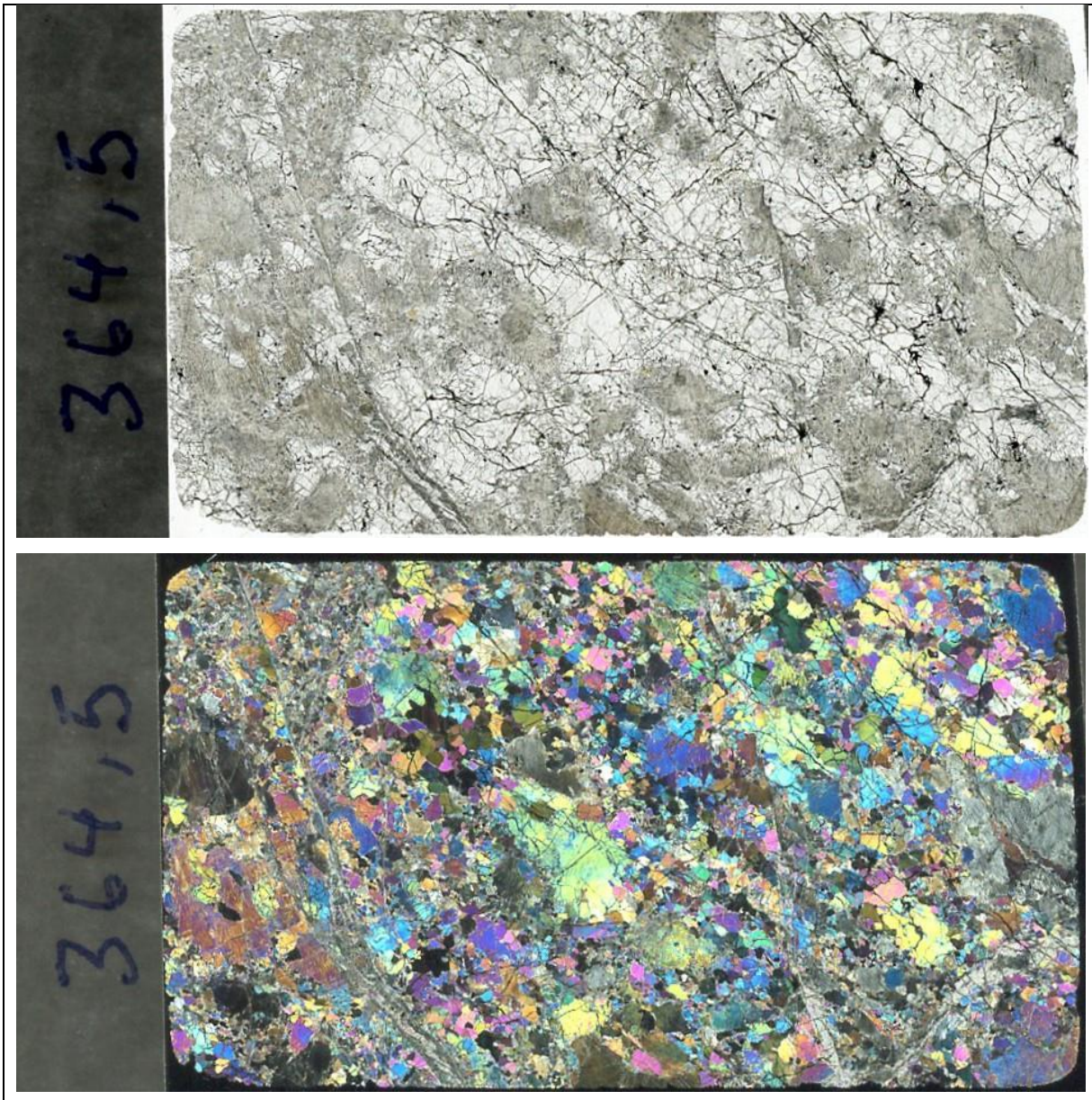

Figure 9.20

Thin section 364,5 scanned using transmitted plane polarized light (Figure 9.20 a) and crossed polarized light (Figure 9.20 b).

Thin section 364,5 is a heterogeneous medium to fine grained gabbro cut by veins and vein-parallel textures. There are remarkably few chromian Spinels present in the thin section compared to the others. The sample has layering with varying grain sizes. The opaque minerals are generally evenly

distributed. There are both serpentine and calcareous veins. The sample has undergone medium degrees of serpentinization.

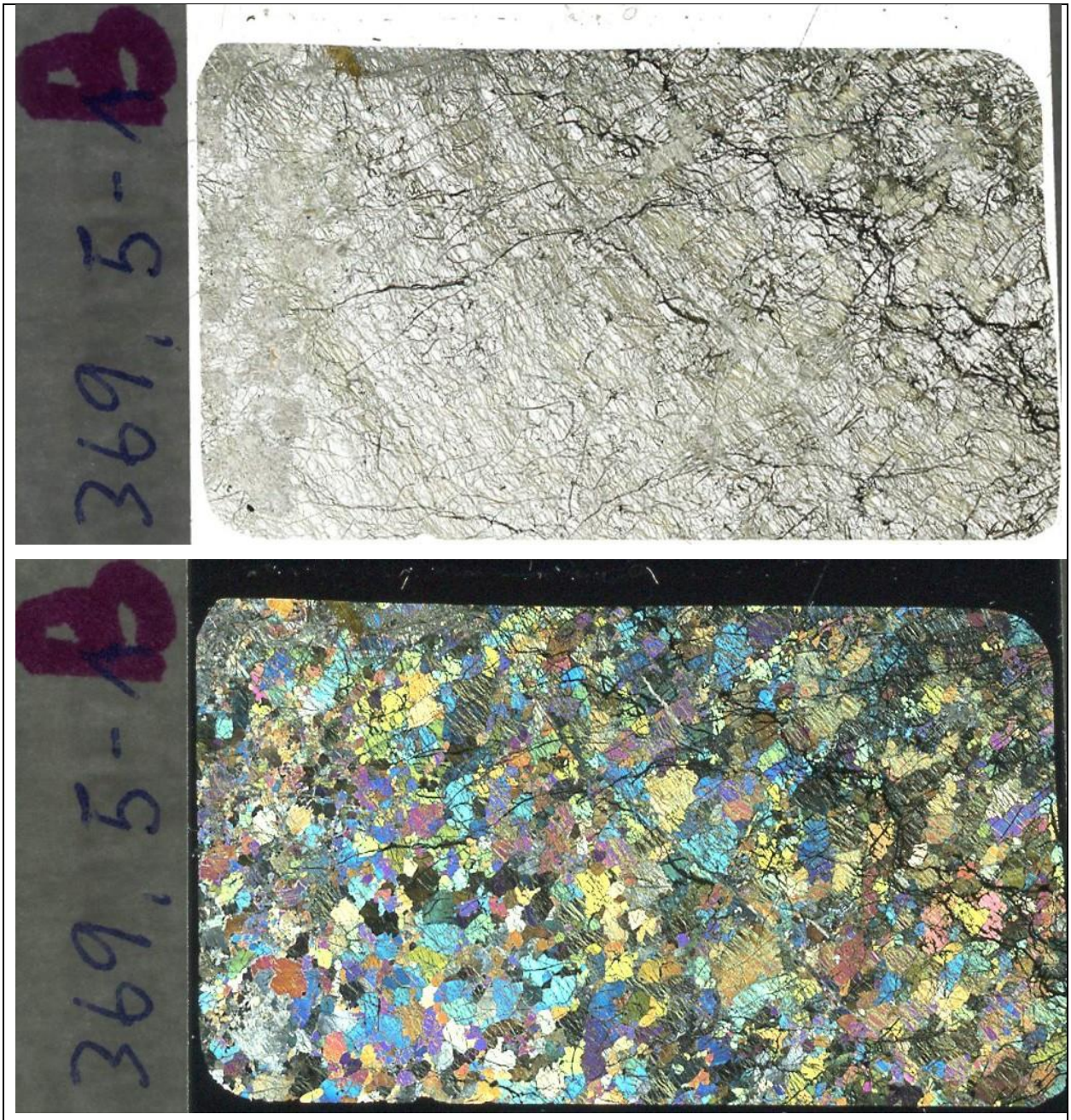

Figure 9.21

Thin section 369,5-B scanned using transmitted plane polarized light (Figure 9.21 a) and crossed polarized light (Figure 9.21 b).

369,5-B is a heterogeneous wehrlite with increasing pyroxene occurrence to the left in the thin section and increasing dunite and serpentinization to the right in the thin section. The dunitic side

(right) of the thin section have fewer chromian Spinels and more abundant sulfide minerals than in the pyroxenitic part (left). Up to two chromian Spinel types are observed in the same grain. Other than that Spinels are rare and are found in small interstitial crystals. The sample contain type 1 and 2 Olivine and both Clinopyroxene and Orthopyroxene. The sample is heavily to medium grade serpentinized.

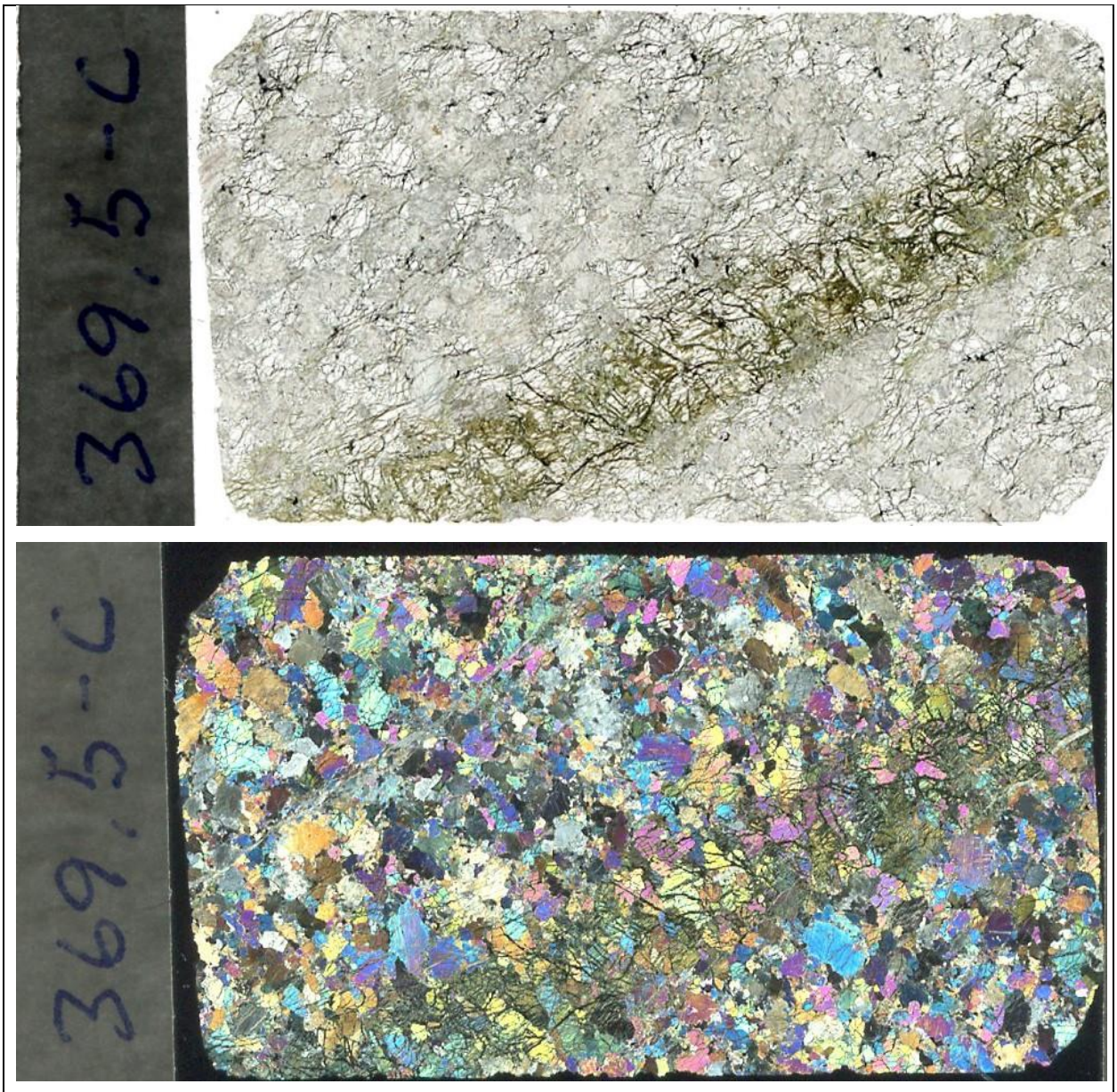

Figure 9.22

Thin section 369,5-C scanned using transmitted plane polarized light (Figure 9.22 a) and crossed polarized light (Figure 9.22 b).

Thin section 369,5-C is a layered pyroxenite with a more dunite and serpentine band. The sulfides are mostly interstitial crystals evenly distributed in the pyroxenite, though some places sulfide minerals are found as inclusions in pyroxene. There is substantially less opaque minerals in the dunittic band. Two chromian Spinels are found; the “wolf grey” phase are present as interstitial crystals and the darker variant as inclusions in the “wolf grey” Spinel, Olivines and pyroxenes. In this sample it is unclear wether the darker phase is more abundant than the “wolf grey” one due to technical difficulty in locating the crystals. The dunittic band is strongly serpentinized, and tensional crystal growth is observed in one of the serpentine veins. A large pyroxene crystal appear to be “bent”, possibly by plastic deformation. The sample does not contain any carbonates. Some feldspar crystals are present.

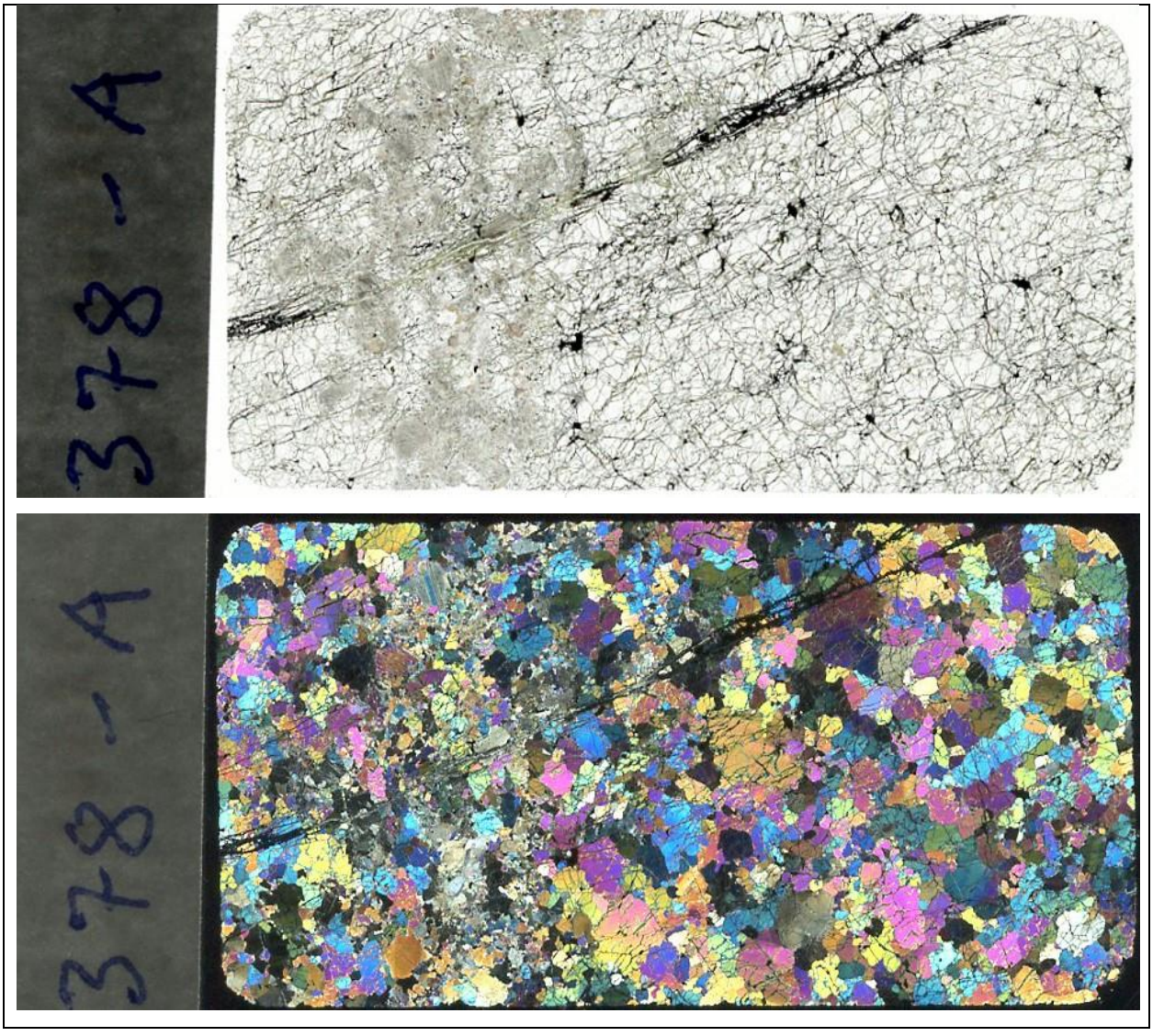

Figure 9.23

Thin section 378-A scanned using transmitted plane polarized light (Figure 9.23 a) and crossed polarized light (Figure 9.23 b).

Thin section 378-A is a heterogeneous dunite cut by serpentinized sub horizontal fractures and by a pyroxene rich vertical dyke. The sulfide grains are numerous and generally larger above the serpentine vein than below it. The sulfide grains occur as interstitial crystals and are surrounded by a spider web of serpentinization. Two Spinel types are identified; the “wolf grey” (main) and a darker phase (minor). The main phase is mostly found as interstitial crystals but are also present as inclusions. The darker phase is only found as inclusions, in the main Spinel and in Olivine. A Spinel inclusion in Olivine has both of the phases present. The sample has Olivine crystals of type 1 and 2 and 3, as well as carbonate spots. The sample has undergone medium grade serpentinization.

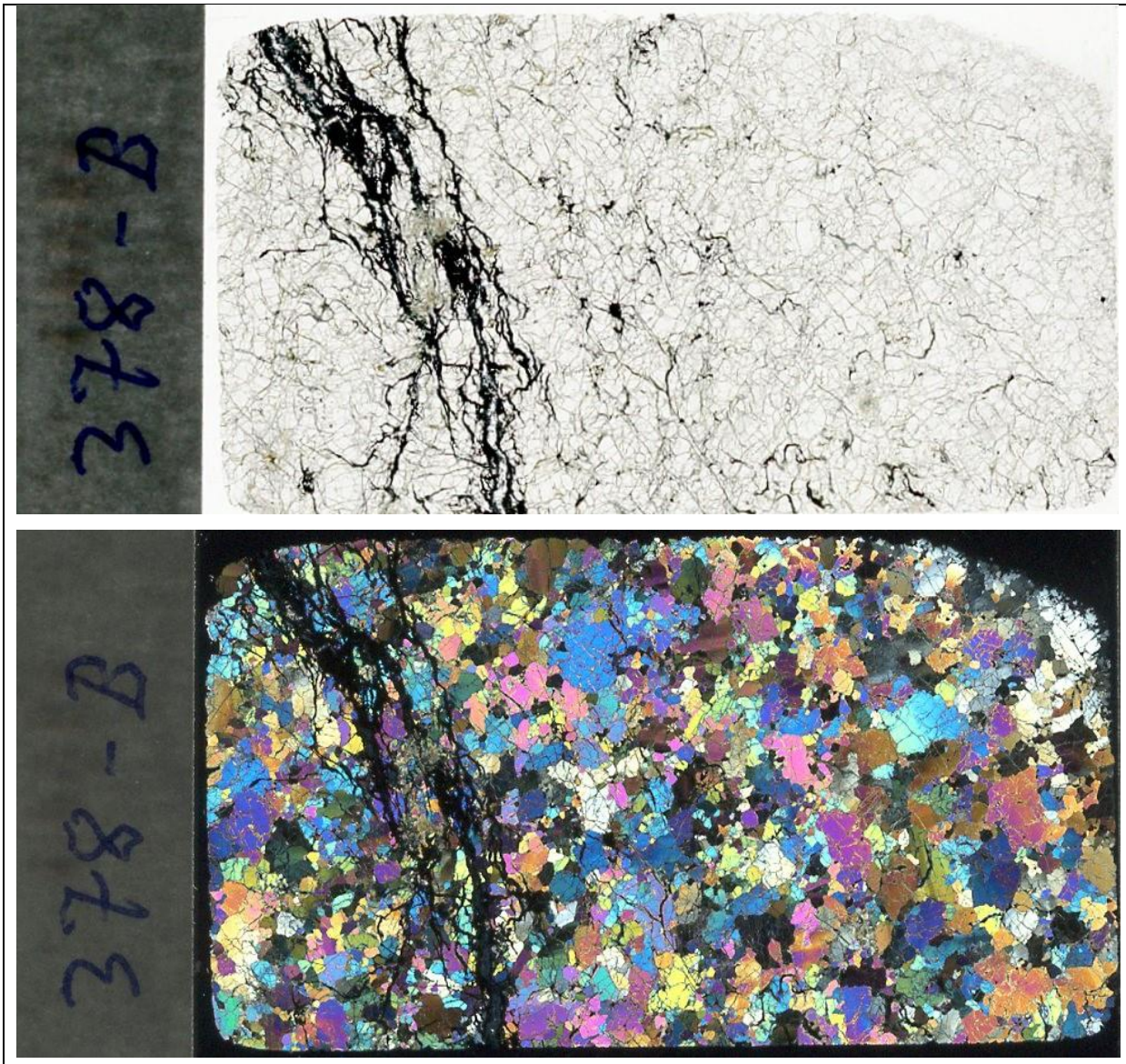

Figure 9.24

Thin section 378-B scanned using transmitted plane polarized light (Figure 9.24 a) and crossed polarized light (Figure 9.24 b).

Thin section 378-B is a homogenous dunite cut by very discrete and concentrated serpentine (or pseudotachylyte) veins in the left part of the thin section. There appear to be more sulfide minerals in a 1,5 cm band from the shear zone. The sample contain Olivine of type 1 and 2. One type of chromian Spinel has been observed, both as circular inclusions in Olivine and as interstitial crystals. The sample has undergone low to medium grade serpentinization.

10 Appendix B

10.1 EPMA results

10.1.1 Spinels – measured oxides, wt%

10.1.1.1 Group 1:

Table 19: EPMA raw data from the analyses of Spinel group 1: Hercynite

No.	Comment	SiO2	MgO	TiO2	MnO	Al2O3	V2O3	FeO	Cr2O3	NiO	Total
15	315-A.5	0.58	10.83	0.16	0.23	38.51	0.09	27.68	21.36	0.09	99.52
16	315-A.6	0.54	10.43	0.23	0.32	36.48	0.11	28.21	23.12	0.06	99.48
B	315	0.56	10.63	0.19	0.27	37.49	0.10	27.94	22.24	0.08	99.50
23	315-A.13	0.27	8.08	0.42	0.33	29.19	0.16	34.03	27.51	0.04	100.01
24	315-A.14	0.19	8.11	0.40	0.40	29.18	0.08	33.69	28.16	0.05	100.26
25	315-A.15	0.29	7.92	0.35	0.43	28.48	0.09	34.45	28.32	0.04	100.35
E	315	0.25	8.04	0.39	0.38	28.95	0.11	34.06	27.99	0.04	100.21
32	320.4	0.05	8.64	0.26	0.39	31.13	0.18	33.38	25.49	0.06	99.58
33	320.5	0.20	8.50	0.30	0.40	29.61	0.28	34.97	26.73	0.08	101.07
34	320.6	0.00	8.58	0.20	0.33	30.63	0.20	33.77	26.02	0.07	99.78
B	320	0.08	8.57	0.25	0.37	30.45	0.22	34.04	26.08	0.07	100.14
41	320.13	0.07	10.43	0.14	0.20	40.90	0.12	29.81	18.51	0.14	100.32
42	320.14	0.13	10.43	0.16	0.24	41.43	0.10	29.41	17.84	0.09	99.83
43	320.15	0.15	10.65	0.10	0.27	41.49	0.07	28.07	18.73	0.06	99.58
C	320	0.12	10.50	0.13	0.24	41.27	0.10	29.10	18.36	0.10	99.91
47	325.4	0.07	8.95	0.29	0.32	32.75	0.13	33.54	24.77	0.16	100.98
48	325.5	0.09	8.70	0.27	0.28	32.00	0.11	32.: 90	25.79	0.10	100.23

B	325	0.08	8.82	0.28	0.30	32.38	0.12	33.22	25.28	0.13	100.61
53	325.1	0.35	10.04	0.15	0.19	38.96	0.08	30.88	20.08	0.20	100.93
55	325.12	0.07	9.78	0.13	0.25	38.84	0.10	30.90	19.90	0.19	100.17
D	325	0.21	9.91	0.14	0.22	38.90	0.09	30.89	19.99	0.19	100.55
59	325.16	0.13	10.03	0.13	0.25	36.68	0.12	31.75	21.48	0.09	100.66
60	325.17	0.06	9.68	0.17	0.30	36.00	0.07	32.87	21.51	0.21	100.86
61	325.18	0.15	9.17	0.24	0.27	34.81	0.12	33.44	21.63	0.17	100.00
F	325	0.12	9.63	0.18	0.27	35.83	0.10	32.69	21.54	0.16	100.50
70	346.7	0.09	8.52	0.27	0.30	32.87	0.20	35.85	23.21	0.19	101.49
71	346.8	0.08	8.26	0.30	0.29	31.61	0.20	37.42	23.45	0.14	101.74
C	346	0.09	8.39	0.28	0.30	32.24	0.20	36.64	23.33	0.17	101.62
76	346.13	0.25	8.19	0.40	0.28	31.59	0.20	36.85	23.62	0.15	101.52
77	346.14	0.23	8.01	0.26	0.32	31.36	0.15	37.27	23.55	0.18	101.33
78	346.15	0.11	8.14	0.25	0.27	31.75	0.22	36.20	23.84	0.11	100.91
E	346	0.20	8.11	0.30	0.29	31.57	0.19	36.77	23.67	0.15	101.25
82	348.4	0.06	8.41	0.13	0.27	36.16	0.12	34.63	20.96	0.03	100.77
83	348.5	0.09	8.47	0.13	0.32	36.38	0.11	34.91	20.27	0.08	100.75
84	348.6	0.02	8.58	0.26	0.30	36.91	0.08	34.06	20.67	0.10	100.97
B	348	0.06	8.49	0.17	0.30	36.48	0.10	34.53	20.63	0.07	100.83
88	348.1	0.06	11.81	0.07	0.27	45.70	0.08	26.94	15.69	0.11	100.72
89	348.11	0.08	12.27	0.13	0.24	46.80	0.11	25.52	15.23	0.09	100.46
90	348.12	0.07	11.61	0.17	0.26	45.29	0.10	26.82	16.35	0.07	100.74
D	348	0.07	11.89	0.13	0.25	45.93	0.10	26.42	15.75	0.09	100.64
94	348.16	0.00	8.57	0.22	0.26	35.17	0.12	34.91	22.01	0.14	101.39
95	348.17	0.05	8.64	0.19	0.28	35.42	0.09	34.89	21.50	0.14	101.18
96	348.18	0.07	8.82	0.12	0.29	36.08	0.16	34.24	21.36	0.14	101.29
F	348	0.04	8.68	0.17	0.27	35.56	0.12	34.68	21.62	0.14	101.29
103	350,7.7	0.04	10.07	0.16	0.23	41.55	0.06	30.80	18.01	0.14	101.06
104	350,7.8	0.00	9.87	0.15	0.23	40.24	0.05	31.68	18.44	0.10	100.74

105	350,7.9	0.05	9.66	0.17	0.20	39.64	0.08	32.02	18.75	0.11	100.67
A	350	0.03	9.87	0.16	0.22	40.47	0.06	31.50	18.40	0.11	100.83
109	350,7.13	0.15	12.26	0.10	0.18	47.37	0.09	25.70	14.51	0.16	100.52
110	350,7.14	0.14	10.71	0.09	0.24	43.88	0.11	29.21	15.75	0.15	100.27
111	350,7.15	0.18	11.18	0.08	0.21	45.05	0.05	28.41	14.96	0.16	100.27
B	350	0.15	11.38	0.09	0.21	45.43	0.08	27.77	15.07	0.16	100.35
22	364,5.3	0.83	10.88	0.62	0.20	43.23	0.18	25.34	14.80	0.10	96.17
23	364,5.4	0.77	10.20	0.72	0.23	42.36	0.18	27.13	15.81	0.10	97.47
Y	364	0.80	10.54	0.67	0.22	42.79	0.18	26.23	15.30	0.10	96.82
24	364,5.5	0.10	11.79	0.17	0.19	48.96	0.08	26.97	12.00	0.08	100.35
25	364,5.6	0.15	11.64	0.14	0.15	49.11	0.09	26.57	11.75	0.10	99.70
A	364.5	0.13	11.71	0.16	0.17	49.03	0.08	26.77	11.88	0.09	100.02
8	369,5B.7	0.32	10.30	0.18	0.27	41.06	0.05	29.13	18.61	0.07	99.99
9	369,5B.8	0.34	10.09	0.19	0.24	40.42	0.10	29.73	18.90	0.07	100.07
C	369.5	0.33	10.19	0.18	0.25	40.74	0.07	29.43	18.76	0.07	100.03
17	369,5B.16	0.21	6.91	0.43	0.30	27.08	0.15	39.12	26.78	0.11	101.08
18	369,5B.17	0.31	6.95	0.43	0.31	26.73	0.16	38.78	26.63	0.11	100.41
19	369,5B.18	0.13	6.91	0.52	0.38	26.36	0.21	38.82	27.76	0.09	101.17
F	369.5	0.22	6.92	0.46	0.33	26.72	0.17	38.91	27.06	0.10	100.89
32	378-A.1	0.26	9.25	0.21	0.27	37.45	0.06	31.93	21.23	0.08	100.75
33	378-A.2	0.24	9.88	0.19	0.27	39.36	0.11	30.80	19.58	0.13	100.55
34	378-A.3	0.23	8.80	0.15	0.28	35.37	0.04	32.67	22.73	0.11	100.36
A	378	0.25	9.31	0.18	0.27	37.39	0.07	31.80	21.18	0.11	100.56
38	378-A.7	0.43	8.63	0.23	0.30	32.92	0.16	34.79	23.80	0.08	101.34
39	378-A.8	0.43	8.85	0.22	0.31	33.19	0.12	33.43	24.28	0.13	100.97
C	378	0.43	8.74	0.23	0.31	33.06	0.14	34.11	24.04	0.10	101.15

10.1.1.2 Group 2:

Table 20: EPMA raw data from the analyses of Spinel group 2: Chromite

No.	Comment	SiO2	MgO	TiO2	MnO	Al2O3	V2O3	FeO	Cr2O3	NiO	Total
2	296.1	0.00	5.42	1.25	0.42	16.37	0.35	43.31	33.98	0.14	101.24
3	296.2	0.02	5.33	1.14	0.35	16.73	0.36	42.74	33.80	0.21	100.67
4	296.3	0.00	5.31	1.21	0.41	16.68	0.35	43.43	33.35	0.22	100.96
A	296	0.01	5.35	1.20	0.39	16.59	0.35	43.16	33.71	0.19	100.96
5	296.4	0.00	5.23	1.35	0.46	15.61	0.34	44.92	33.52	0.19	101.61
6	296.5	0.03	5.00	1.55	0.41	15.21	0.36	45.66	33.25	0.12	101.60
7	296.6	0.00	5.15	1.41	0.44	15.91	0.37	44.38	33.25	0.16	101.07
B	296	0.01	5.12	1.43	0.44	15.58	0.36	44.99	33.34	0.16	101.43
8	296.7	0.10	5.93	0.95	0.33	17.71	0.29	41.42	34.77	0.15	101.63
9	296.8	0.00	5.86	0.97	0.41	17.79	0.31	40.48	34.68	0.14	100.63
10	296.9	0.00	5.84	0.90	0.35	17.39	0.31	41.30	34.58	0.17	100.84
C	296	0.03	5.88	0.94	0.36	17.63	0.30	41.06	34.68	0.15	101.04
50	329,5.1	0.04	4.07	1.40	0.44	14.03	0.29	49.82	31.15	0.21	101.45
52	329,5.3	0.06	4.26	1.43	0.40	14.24	0.34	49.09	31.38	0.08	101.27
A	329.5	0.05	4.16	1.41	0.42	14.14	0.31	49.45	31.27	0.14	101.36
53	329,5.4	0.14	3.70	1.50	0.41	12.67	0.36	54.13	27.69	0.20	100.80
54	329,5.5	0.13	3.61	1.45	0.36	12.62	0.36	53.90	28.12	0.19	100.74
B	329.5	0.13	3.66	1.48	0.38	12.65	0.36	54.02	27.91	0.19	100.77
55	329,5.6	0.00	3.12	1.62	0.36	10.42	0.34	57.85	26.94	0.27	100.92
56	329,5.7	0.01	3.25	1.55	0.45	10.65	0.34	55.16	27.59	0.30	99.29
57	329,5.8	0.14	3.12	1.51	0.36	10.11	0.34	58.80	26.59	0.21	101.17
C	329.5	0.05	3.16	1.56	0.39	10.39	0.34	57.27	27.04	0.26	100.46
58	329,5.9	0.00	4.44	1.34	0.38	14.87	0.30	49.18	31.04	0.22	101.76
D	329.5	0.00	4.44	1.34	0.38	14.87	0.30	49.18	31.04	0.22	101.76

62	329,5.13	0.11	4.79	1.52	0.39	15.55	0.33	47.40	31.20	0.16	101.44
63	329,5.14	0.03	4.66	1.45	0.36	15.48	0.31	47.28	31.35	0.18	101.11
E	329.5	0.07	4.72	1.49	0.38	15.52	0.32	47.34	31.28	0.17	101.27
5	369,5B.4	0.10	6.12	1.13	0.42	20.96	0.55	43.32	29.22	0.08	101.90
6	369,5B.5	0.20	6.19	0.70	0.39	22.05	0.39	43.40	27.87	0.11	101.30
B	369.5	0.15	6.16	0.91	0.41	21.51	0.47	43.36	28.55	0.10	101.60

10.1.1.3 Group 3:

Table 21: EPMA raw data from analyses of Spinel group 3: Magnetite

No.	Comment	SiO2	MgO	TiO2	MnO	Al2O3	V2O3	FeO	Cr2O3	NiO	Total
11	315-A.1	0.52	2.35	2.31	0.38	4.43	0.48	74.64	14.44	0.30	99.85
A	315	0.52	2.35	2.31	0.38	4.43	0.48	74.64	14.44	0.30	99.85
17	315-A.7	0.30	2.04	2.04	0.30	4.28	0.74	75.77	13.26	0.31	99.03
18	315-A.8	0.29	1.92	2.00	0.30	4.69	0.79	75.98	13.80	0.35	100.10
C	315	0.29	1.98	2.02	0.30	4.48	0.76	75.87	13.53	0.33	99.57
20	315-A.10	0.03	2.51	2.19	0.44	8.30	0.40	64.38	20.70	0.20	99.15
21	315-A.11	0.01	2.37	2.30	0.39	7.85	0.49	67.13	20.45	0.20	101.19
22	315-A.12	0.00	2.35	2.22	0.43	7.62	0.49	66.99	19.67	0.23	100.00
D	315	0.01	2.41	2.24	0.42	7.92	0.46	66.17	20.27	0.21	100.11
26	315-A.16	0.06	2.21	2.68	0.43	5.79	0.47	68.79	19.82	0.20	100.46
27	315-A.17	0.07	2.30	2.40	0.38	5.60	0.44	69.40	19.68	0.20	100.46
28	315-A.18	0.15	2.26	2.62	0.44	6.01	0.45	68.06	20.29	0.15	100.43
F	315	0.09	2.26	2.57	0.41	5.80	0.45	68.75	19.93	0.18	100.45
29	320.1	0.00	2.19	2.42	0.34	5.51	0.75	69.25	19.10	0.11	99.67
30	320.2	0.05	2.34	2.40	0.37	5.90	0.71	69.02	18.79	0.10	99.68
31	320.3	0.10	2.31	2.37	0.45	5.85	0.72	67.99	19.31	0.15	99.24
A	320	0.05	2.28	2.40	0.39	5.75	0.72	68.75	19.07	0.12	99.53
44	325.1	0.07	2.35	2.56	0.37	6.66	0.44	68.04	19.27	0.35	100.12
45	325.2	0.01	2.57	2.54	0.40	7.21	0.48	66.81	19.59	0.29	99.90
46	325.3	0.17	2.51	2.53	0.36	7.27	0.50	66.53	19.43	0.33	99.64
A	325	0.09	2.48	2.54	0.38	7.05	0.47	67.13	19.43	0.32	99.88
50	325.7	0.04	2.03	2.76	0.32	5.05	0.52	72.71	15.36	0.32	99.11
52	325.9	0.16	1.86	2.52	0.33	5.23	0.48	72.90	15.51	0.29	99.26
C	325	0.10	1.94	2.64	0.33	5.14	0.50	72.80	15.43	0.30	99.19

56	325.13	0.02	2.05	2.63	0.32	5.41	0.63	70.26	17.85	0.24	99.41
57	325.14	0.09	1.99	2.58	0.35	4.98	0.59	71.24	17.11	0.23	99.16
58	325.15	0.05	1.90	2.50	0.30	4.56	0.61	72.51	16.10	0.25	98.78
E	325	0.05	1.98	2.57	0.33	4.99	0.61	71.34	17.02	0.24	99.12
64	346.1	0.00	1.73	3.05	0.29	4.42	0.55	76.37	13.38	0.15	99.94
65	346.2	0.01	1.79	2.69	0.34	4.41	0.59	76.52	13.39	0.16	99.90
66	346.3	0.00	1.77	2.89	0.34	4.37	0.58	76.13	12.92	0.17	99.18
A	346	0.00	1.76	2.88	0.32	4.40	0.58	76.34	13.23	0.16	99.67
67	346.4	0.00	2.41	2.60	0.36	6.15	0.70	68.30	19.14	0.29	99.93
68	346.5	0.00	2.39	2.55	0.35	6.28	0.69	68.42	19.37	0.28	100.34
69	346.6	0.00	2.45	2.48	0.32	6.53	0.68	67.95	19.15	0.26	99.82
B	346	0.00	2.42	2.54	0.34	6.32	0.69	68.22	19.22	0.28	100.03
73	346.1	0.18	2.36	3.00	0.41	5.46	0.71	69.87	17.30	0.23	99.51
74	346.11	0.10	2.20	2.89	0.42	5.34	0.74	70.71	17.30	0.26	99.97
75	346.12	0.17	2.27	2.97	0.33	5.46	0.72	70.40	17.31	0.27	99.90
D	346	0.15	2.28	2.95	0.39	5.42	0.72	70.33	17.30	0.25	99.79
79	348.1	0.00	1.47	2.72	0.31	4.89	0.54	75.49	13.94	0.15	99.51
80	348.2	0.00	1.45	2.75	0.29	4.91	0.50	75.32	13.82	0.18	99.21
81	348.3	0.00	1.46	2.67	0.37	5.10	0.54	75.25	14.14	0.15	99.65
A	348	0.00	1.46	2.71	0.32	4.96	0.53	75.35	13.96	0.16	99.46
85	348.7	0.00	1.35	2.60	0.25	3.69	0.67	80.28	10.81	0.17	99.82
C	348	0.00	1.35	2.60	0.25	3.69	0.67	80.28	10.81	0.17	99.82
91	348.13	0.00	1.74	2.63	0.33	5.02	0.63	73.30	15.45	0.22	99.32
92	348.14	0.00	1.71	2.46	0.35	5.32	0.61	73.72	15.48	0.26	99.91
93	348.15	0.00	1.75	2.42	0.37	4.99	0.61	73.98	15.33	0.19	99.62
E	348	0.00	1.73	2.50	0.35	5.11	0.61	73.67	15.42	0.22	99.62
2	369,5B.1	0.03	2.85	1.77	0.40	8.39	0.70	63.18	23.06	0.24	100.63
3	369,5B.2	0.11	2.98	1.85	0.33	8.56	0.71	62.78	23.29	0.14	100.74
4	369,5B.3	0.06	3.07	1.65	0.40	9.29	0.68	63.61	22.76	0.16	101.67

A	369.5	0.07	2.97	1.76	0.38	8.74	0.70	63.19	23.04	0.18	101.01
10	369,5B.9	0.30	2.03	2.98	0.33	5.04	0.51	75.65	13.48	0.28	100.59
11	369,5B.10	0.30	1.98	3.09	0.28	5.20	0.50	75.78	13.86	0.23	101.23
12	369,5B.11	0.23	2.01	2.91	0.32	5.38	0.47	75.35	13.91	0.22	100.79
D	369.5	0.28	2.01	2.99	0.31	5.21	0.49	75.59	13.75	0.24	100.87
13	369,5B.12	0.19	2.49	2.80	0.35	6.54	0.52	67.96	20.35	0.23	101.44
14	369,5B.13	0.13	2.23	3.07	0.35	5.38	0.59	70.41	19.16	0.26	101.58
15	369,5B.14	0.22	2.44	3.01	0.33	5.92	0.60	68.66	19.46	0.26	100.90
16	369,5B.15	0.19	2.47	2.57	0.31	6.12	0.47	68.71	19.37	0.26	100.45
E	369.5	0.18	2.41	2.86	0.33	5.99	0.54	68.94	19.58	0.25	101.09
40	378-A.9	0.29	2.24	2.03	0.29	6.68	0.50	70.12	17.91	0.29	100.35
41	378-A.10	0.23	2.33	1.97	0.32	6.58	0.55	69.77	18.35	0.34	100.43
42	378-A.11	0.21	2.35	1.99	0.33	6.75	0.59	70.27	17.99	0.30	100.77
D	378	0.24	2.31	2.00	0.31	6.67	0.55	70.05	18.08	0.31	100.51
35	320.7	0.06	1.19	1.16	0.17	2.95	0.33	81.70	10.25	0.10	97.90
36	320.8	0.07	1.18	1.24	0.17	2.99	0.32	81.60	10.37	0.16	98.09
37	320.9	0.06	1.34	1.17	0.20	3.39	0.29	80.76	10.75	0.17	98.12
X	320	0.06	1.24	1.19	0.18	3.11	0.31	81.35	10.45	0.14	98.04
28	364,5.9	0.11	1.32	3.09	0.25	4.14	0.64	80.65	9.22	0.18	99.59
B	364.5	0.11	1.32	3.09	0.25	4.14	0.64	80.65	9.22	0.18	99.59
30	364,5.11	0.18	1.40	2.70	0.23	3.91	0.50	81.01	9.25	0.17	99.33
31	364,5.12	0.29	1.65	2.48	0.36	4.18	0.41	80.79	9.13	0.18	99.46
C	364.5	0.23	1.52	2.59	0.29	4.04	0.45	80.90	9.19	0.18	99.40
35	378-A.4	0.06	1.82	2.98	0.31	4.69	0.53	75.92	13.97	0.27	100.55
36	378-A.5	0.11	2.08	2.61	0.34	5.67	0.55	72.97	15.27	0.23	99.84
37	378-A.6	0.32	2.24	2.61	0.33	5.32	0.53	73.63	14.30	0.27	99.53
B	378	0.17	2.05	2.73	0.33	5.23	0.54	74.17	14.51	0.26	99.98
43	378-A.12	0.15	1.21	2.40	0.24	2.54	0.39	85.62	7.97	0.23	100.74
44	378-A.13	0.11	1.24	2.32	0.25	2.57	0.35	84.36	7.65	0.26	99.10

45	378-A.14	0.11	1.22	2.49	0.17	2.46	0.43	84.78	7.93	0.21	99.80
C	378	0.12	1.22	2.40	0.22	2.52	0.39	84.92	7.85	0.23	99.88

10.1.2 Spinels – calculated elements in chemical formula

10.1.2.1 Group 1:

Table 22: Calculated EPMA data into cation units in mineral formula for Spinels of group 1: Hercynite

No.	Comment	Si4+	Ti4+	Al3+	V3+	Fe3+	Cr3+	Mg2+	Mn2+	Fe2+	Ni2+	Total	Charge
15	315-A.5	0.01	0.00	1.33	0.00	0.14	0.49	0.47	0.01	0.54	0.00	3	8
16	315-A.6	0.01	0.01	1.27	0.00	0.15	0.54	0.46	0.01	0.55	0.00	3	8
B	315	0.01	0.00	1.30	0.00	0.15	0.52	0.47	0.01	0.54	0.00	3	8
23	315-A.13	0.01	0.01	1.06	0.00	0.24	0.67	0.37	0.01	0.64	0.00	3	8
24	315-A.14	0.00	0.01	1.05	0.00	0.23	0.68	0.37	0.01	0.63	0.00	3	8
25	315-A.15	0.01	0.01	1.03	0.00	0.25	0.69	0.36	0.01	0.64	0.00	3	8
E	315	0.01	0.01	1.05	0.00	0.24	0.68	0.37	0.01	0.64	0.00	3	8
32	320.4	0.00	0.01	1.12	0.00	0.25	0.61	0.39	0.01	0.60	0.00	3	8
33	320.5	0.00	0.01	1.06	0.01	0.27	0.64	0.38	0.01	0.62	0.00	3	8
34	320.6	0.00	0.00	1.10	0.00	0.26	0.63	0.39	0.01	0.60	0.00	3	8
B	320	0.00	0.01	1.09	0.01	0.26	0.63	0.39	0.01	0.61	0.00	3	8
41	320.13	0.00	0.00	1.39	0.00	0.17	0.42	0.45	0.00	0.55	0.00	3	8
42	320.14	0.00	0.00	1.41	0.00	0.16	0.41	0.45	0.01	0.55	0.00	3	8
43	320.15	0.00	0.00	1.42	0.00	0.14	0.43	0.46	0.01	0.54	0.00	3	8
C	320	0.00	0.00	1.41	0.00	0.16	0.42	0.45	0.01	0.54	0.00	3	8
47	325.4	0.00	0.01	1.15	0.00	0.24	0.59	0.40	0.01	0.60	0.00	3	8
48	325.5	0.00	0.01	1.14	0.00	0.22	0.62	0.39	0.01	0.61	0.00	3	8
B	325	0.00	0.01	1.15	0.00	0.23	0.60	0.40	0.01	0.60	0.00	3	8
53	325.1	0.01	0.00	1.33	0.00	0.18	0.46	0.43	0.00	0.57	0.00	3	8
55	325.12	0.00	0.00	1.34	0.00	0.19	0.46	0.43	0.01	0.57	0.00	3	8
D	325	0.00	0.00	1.34	0.00	0.19	0.46	0.43	0.01	0.57	0.00	3	8
59	325.16	0.00	0.00	1.27	0.00	0.22	0.50	0.44	0.01	0.56	0.00	3	8
60	325.17	0.00	0.00	1.25	0.00	0.24	0.50	0.42	0.01	0.57	0.00	3	8

61	325.18	0.00	0.01	1.22	0.00	0.24	0.51	0.41	0.01	0.59	0.00	3	8
F	325	0.00	0.00	1.25	0.00	0.23	0.50	0.42	0.01	0.57	0.00	3	8
70	346.7	0.00	0.01	1.16	0.00	0.28	0.55	0.38	0.01	0.62	0.00	3	8
71	346.8	0.00	0.01	1.12	0.00	0.31	0.55	0.37	0.01	0.63	0.00	3	8
C	346	0.00	0.01	1.14	0.00	0.29	0.55	0.37	0.01	0.62	0.00	3	8
76	346.13	0.01	0.01	1.12	0.00	0.29	0.56	0.37	0.01	0.64	0.00	3	8
77	346.14	0.01	0.01	1.11	0.00	0.30	0.56	0.36	0.01	0.64	0.00	3	8
78	346.15	0.00	0.01	1.13	0.01	0.28	0.57	0.37	0.01	0.63	0.00	3	8
E	346	0.00	0.01	1.12	0.00	0.29	0.56	0.36	0.01	0.64	0.00	3	8
82	348.4	0.00	0.00	1.26	0.00	0.23	0.49	0.37	0.01	0.63	0.00	3	8
83	348.5	0.00	0.00	1.27	0.00	0.24	0.47	0.37	0.01	0.62	0.00	3	8
84	348.6	0.00	0.01	1.28	0.00	0.22	0.48	0.38	0.01	0.62	0.00	3	8
B	348	0.00	0.00	1.27	0.00	0.23	0.48	0.37	0.01	0.62	0.00	3	8
88	348.1	0.00	0.00	1.51	0.00	0.13	0.35	0.49	0.01	0.50	0.00	3	8
89	348.11	0.00	0.00	1.54	0.00	0.11	0.34	0.51	0.01	0.49	0.00	3	8
90	348.12	0.00	0.00	1.50	0.00	0.12	0.36	0.49	0.01	0.51	0.00	3	8
D	348	0.00	0.00	1.52	0.00	0.12	0.35	0.50	0.01	0.50	0.00	3	8
94	348.16	0.00	0.00	1.23	0.00	0.25	0.51	0.38	0.01	0.62	0.00	3	8
95	348.17	0.00	0.00	1.24	0.00	0.25	0.50	0.38	0.01	0.61	0.00	3	8
96	348.18	0.00	0.00	1.25	0.00	0.24	0.50	0.39	0.01	0.61	0.00	3	8
F	348	0.00	0.00	1.24	0.00	0.24	0.51	0.38	0.01	0.61	0.00	3	8
103	350,7.7	0.00	0.00	1.41	0.00	0.18	0.41	0.43	0.01	0.56	0.00	3	8
104	350,7.8	0.00	0.00	1.37	0.00	0.20	0.42	0.43	0.01	0.57	0.00	3	8
105	350,7.9	0.00	0.00	1.36	0.00	0.20	0.43	0.42	0.00	0.58	0.00	3	8
A	350	0.00	0.00	1.38	0.00	0.19	0.42	0.43	0.01	0.57	0.00	3	8
109	350,7.13	0.00	0.00	1.56	0.00	0.11	0.32	0.51	0.00	0.49	0.00	3	8
110	350,7.14	0.00	0.00	1.48	0.00	0.16	0.36	0.46	0.01	0.54	0.00	3	8
111	350,7.15	0.00	0.00	1.50	0.00	0.15	0.34	0.47	0.01	0.52	0.00	3	8
B	350	0.00	0.00	1.51	0.00	0.14	0.34	0.48	0.01	0.52	0.00	3	8

22	364,5.3	0.02	0.01	1.51	0.00	0.08	0.35	0.48	0.01	0.55	0.00	3	8
23	364,5.4	0.02	0.02	1.47	0.00	0.09	0.37	0.45	0.01	0.58	0.00	3	8
Y	364	0.02	0.01	1.49	0.00	0.09	0.36	0.46	0.01	0.56	0.00	3	8
24	364,5.5	0.00	0.00	1.61	0.00	0.12	0.26	0.49	0.00	0.51	0.00	3	8
25	364,5.6	0.00	0.00	1.62	0.00	0.11	0.26	0.49	0.00	0.51	0.00	3	8
A	364.5	0.00	0.00	1.61	0.00	0.11	0.26	0.49	0.00	0.51	0.00	3	8
8	369,5B.7	0.01	0.00	1.40	0.00	0.15	0.43	0.44	0.01	0.56	0.00	3	8
9	369,5B.8	0.01	0.00	1.38	0.00	0.16	0.43	0.44	0.01	0.57	0.00	3	8
C	369.5	0.01	0.00	1.39	0.00	0.15	0.43	0.44	0.01	0.56	0.00	3	8
17	369,5B.16	0.00	0.01	0.99	0.00	0.33	0.65	0.32	0.01	0.69	0.00	3	8
18	369,5B.17	0.01	0.01	0.98	0.00	0.33	0.66	0.32	0.01	0.68	0.00	3	8
19	369,5B.18	0.00	0.01	0.96	0.01	0.32	0.68	0.32	0.01	0.68	0.00	3	8
F	369.5	0.01	0.01	0.98	0.00	0.32	0.66	0.32	0.01	0.68	0.00	3	8
32	378-A.1	0.01	0.00	1.30	0.00	0.19	0.49	0.41	0.01	0.60	0.00	3	8
33	378-A.2	0.01	0.00	1.35	0.00	0.18	0.45	0.43	0.01	0.57	0.00	3	8
34	378-A.3	0.01	0.00	1.24	0.00	0.21	0.54	0.39	0.01	0.61	0.00	3	8
A	378	0.01	0.00	1.30	0.00	0.19	0.49	0.41	0.01	0.59	0.00	3	8
38	378-A.7	0.01	0.01	1.16	0.00	0.25	0.56	0.38	0.01	0.62	0.00	3	8
39	378-A.8	0.01	0.01	1.17	0.00	0.23	0.57	0.39	0.01	0.61	0.00	3	8
C	378	0.01	0.01	1.16	0.00	0.24	0.57	0.39	0.01	0.62	0.00	3	8

10.1.2.2 Group 2:

Table 23: Calculated EPMAdata into cation units in mineral formula for Spinel group 2: Chromite

No.	Comment	Si4+	Ti4+	Al3+	V3+	Fe3+	Cr3+	Mg2+	Mn2+	Fe2+	Ni2+	Total	Charge
2	296.1	0.00	0.03	0.63	0.01	0.43	0.87	0.26	0.01	0.75	0.00	3	8
3	296.2	0.00	0.03	0.64	0.01	0.42	0.87	0.26	0.01	0.75	0.01	3	8
4	296.3	0.00	0.03	0.64	0.01	0.43	0.86	0.26	0.01	0.75	0.01	3	8
A	296	0.00	0.03	0.64	0.01	0.42	0.87	0.26	0.01	0.75	0.00	3	8
5	296.4	0.00	0.03	0.60	0.01	0.46	0.86	0.25	0.01	0.76	0.01	3	8
6	296.5	0.00	0.04	0.59	0.01	0.47	0.86	0.24	0.01	0.78	0.00	3	8
7	296.6	0.00	0.03	0.61	0.01	0.45	0.86	0.25	0.01	0.77	0.00	3	8
B	296	0.00	0.04	0.60	0.01	0.46	0.86	0.25	0.01	0.77	0.00	3	8
8	296.7	0.00	0.02	0.67	0.01	0.39	0.88	0.28	0.01	0.73	0.00	3	8
9	296.8	0.00	0.02	0.68	0.01	0.37	0.89	0.28	0.01	0.73	0.00	3	8
10	296.9	0.00	0.02	0.67	0.01	0.40	0.89	0.28	0.01	0.73	0.00	3	8
C	296	0.00	0.02	0.67	0.01	0.39	0.89	0.28	0.01	0.73	0.00	3	8
50	329,5.1	0.00	0.03	0.55	0.01	0.56	0.81	0.20	0.01	0.82	0.01	3	8
52	329,5.3	0.00	0.04	0.55	0.01	0.54	0.82	0.21	0.01	0.81	0.00	3	8
A	329.5	0.00	0.04	0.55	0.01	0.55	0.82	0.21	0.01	0.82	0.00	3	8
53	329,5.4	0.00	0.04	0.50	0.01	0.68	0.73	0.18	0.01	0.84	0.01	3	8
54	329,5.5	0.00	0.04	0.50	0.01	0.67	0.75	0.18	0.01	0.84	0.00	3	8
B	329.5	0.00	0.04	0.50	0.01	0.67	0.74	0.18	0.01	0.84	0.01	3	8
55	329,5.6	0.00	0.04	0.42	0.01	0.77	0.72	0.16	0.01	0.87	0.01	3	8
56	329,5.7	0.00	0.04	0.43	0.01	0.73	0.75	0.17	0.01	0.85	0.01	3	8
57	329,5.8	0.00	0.04	0.40	0.01	0.79	0.71	0.16	0.01	0.87	0.01	3	8
C	329.5	0.00	0.04	0.42	0.01	0.77	0.73	0.16	0.01	0.86	0.01	3	8
58	329,5.9	0.00	0.03	0.57	0.01	0.55	0.80	0.22	0.01	0.80	0.01	3	8
D	329.5	0.00	0.03	0.57	0.01	0.55	0.80	0.22	0.01	0.80	0.01	3	8

62	329,5.13	0.00	0.04	0.60	0.01	0.50	0.81	0.23	0.01	0.79	0.00	3	8
63	329,5.14	0.00	0.04	0.60	0.01	0.51	0.81	0.23	0.01	0.79	0.00	3	8
E	329.5	0.00	0.04	0.60	0.01	0.51	0.81	0.23	0.01	0.79	0.00	3	8
5	369,5B.4	0.00	0.03	0.78	0.01	0.42	0.73	0.29	0.01	0.73	0.00	3	8
6	369,5B.5	0.00	0.02	0.82	0.01	0.43	0.70	0.29	0.01	0.72	0.00	3	8
B	369.5	0.00	0.02	0.80	0.01	0.42	0.71	0.29	0.01	0.72	0.00	3	8

10.1.2.3 Group 3:

Table 24: Calculated EPMA data into cation units in mineral formula for Spinel group 3: Magnetite

No.	Comment	Si4+	Ti4+	Al3+	V3+	Fe3+	Cr3+	Mg2+	Mn2+	Fe2+	Ni2+	Total	Charge
11	315-A.1	0.01	0.06	0.18	0.01	1.25	0.40	0.12	0.01	0.93	0.01	3	8
A	315	0.01	0.06	0.18	0.01	1.25	0.40	0.12	0.01	0.93	0.01	3	8
17	315-A.7	0.01	0.05	0.18	0.02	1.30	0.37	0.11	0.01	0.94	0.01	3	8
18	315-A.8	0.01	0.05	0.19	0.02	1.28	0.38	0.10	0.01	0.94	0.01	3	8
C	315	0.01	0.05	0.19	0.02	1.29	0.38	0.10	0.01	0.94	0.01	3	8
20	315-A.10	0.00	0.06	0.34	0.01	0.96	0.57	0.13	0.01	0.91	0.01	3	8
21	315-A.11	0.00	0.06	0.32	0.01	1.00	0.55	0.12	0.01	0.92	0.01	3	8
22	315-A.12	0.00	0.06	0.31	0.01	1.02	0.54	0.12	0.01	0.92	0.01	3	8
D	315	0.00	0.06	0.32	0.01	0.99	0.55	0.12	0.01	0.92	0.01	3	8
26	315-A.16	0.00	0.07	0.24	0.01	1.06	0.54	0.11	0.01	0.94	0.01	3	8
27	315-A.17	0.00	0.06	0.23	0.01	1.09	0.54	0.12	0.01	0.93	0.01	3	8
28	315-A.18	0.00	0.07	0.25	0.01	1.04	0.56	0.12	0.01	0.94	0.00	3	8
F	315	0.00	0.07	0.24	0.01	1.06	0.55	0.12	0.01	0.94	0.01	3	8
29	320.1	0.00	0.06	0.23	0.02	1.09	0.53	0.11	0.01	0.94	0.00	3	8
30	320.2	0.00	0.06	0.24	0.02	1.09	0.52	0.12	0.01	0.93	0.00	3	8
31	320.3	0.00	0.06	0.24	0.02	1.07	0.54	0.12	0.01	0.93	0.00	3	8
A	320	0.00	0.06	0.24	0.02	1.08	0.53	0.12	0.01	0.93	0.00	3	8
44	325.1	0.00	0.07	0.27	0.01	1.05	0.53	0.12	0.01	0.93	0.01	3	8
45	325.2	0.00	0.07	0.29	0.01	1.02	0.54	0.13	0.01	0.91	0.01	3	8
46	325.3	0.00	0.07	0.30	0.01	1.01	0.53	0.13	0.01	0.92	0.01	3	8
A	325	0.00	0.07	0.29	0.01	1.03	0.53	0.13	0.01	0.92	0.01	3	8
50	325.7	0.00	0.07	0.21	0.01	1.20	0.43	0.11	0.01	0.95	0.01	3	8
52	325.9	0.00	0.07	0.22	0.01	1.19	0.43	0.10	0.01	0.96	0.01	3	8
C	325	0.00	0.07	0.21	0.01	1.20	0.43	0.10	0.01	0.95	0.01	3	8

56	325.13	0.00	0.07	0.22	0.02	1.12	0.50	0.11	0.01	0.95	0.01	3	8
57	325.14	0.00	0.07	0.21	0.02	1.16	0.48	0.10	0.01	0.95	0.01	3	8
58	325.15	0.00	0.07	0.19	0.02	1.20	0.45	0.10	0.01	0.95	0.01	3	8
E	325	0.00	0.07	0.21	0.02	1.16	0.48	0.10	0.01	0.95	0.01	3	8
64	346.1	0.00	0.08	0.18	0.02	1.27	0.37	0.09	0.01	0.98	0.00	3	8
65	346.2	0.00	0.07	0.18	0.02	1.29	0.37	0.09	0.01	0.96	0.00	3	8
66	346.3	0.00	0.08	0.18	0.02	1.29	0.36	0.09	0.01	0.97	0.00	3	8
A	346	0.00	0.08	0.18	0.02	1.28	0.37	0.09	0.01	0.97	0.00	3	8
67	346.4	0.00	0.07	0.25	0.02	1.06	0.53	0.13	0.01	0.92	0.01	3	8
68	346.5	0.00	0.07	0.26	0.02	1.06	0.53	0.12	0.01	0.92	0.01	3	8
69	346.6	0.00	0.06	0.27	0.02	1.06	0.53	0.13	0.01	0.92	0.01	3	8
B	346	0.00	0.07	0.26	0.02	1.06	0.53	0.13	0.01	0.92	0.01	3	8
73	346.1	0.00	0.08	0.23	0.02	1.11	0.48	0.12	0.01	0.94	0.01	3	8
74	346.11	0.00	0.08	0.22	0.02	1.12	0.48	0.11	0.01	0.94	0.01	3	8
75	346.12	0.00	0.08	0.22	0.02	1.11	0.48	0.12	0.01	0.95	0.01	3	8
D	346	0.00	0.08	0.22	0.02	1.11	0.48	0.12	0.01	0.94	0.01	3	8
79	348.1	0.00	0.07	0.20	0.02	1.25	0.39	0.08	0.01	0.98	0.00	3	8
80	348.2	0.00	0.07	0.20	0.01	1.25	0.39	0.08	0.01	0.98	0.01	3	8
81	348.3	0.00	0.07	0.21	0.02	1.24	0.39	0.08	0.01	0.98	0.00	3	8
A	348	0.00	0.07	0.21	0.01	1.24	0.39	0.08	0.01	0.98	0.00	3	8
85	348.7	0.00	0.07	0.15	0.02	1.39	0.30	0.07	0.01	0.99	0.00	3	8
C	348	0.00	0.07	0.15	0.02	1.39	0.30	0.07	0.01	0.99	0.00	3	8
91	348.13	0.00	0.07	0.21	0.02	1.20	0.43	0.09	0.01	0.96	0.01	3	8
92	348.14	0.00	0.06	0.22	0.02	1.20	0.43	0.09	0.01	0.96	0.01	3	8
93	348.15	0.00	0.06	0.21	0.02	1.22	0.43	0.09	0.01	0.96	0.01	3	8
E	348	0.00	0.07	0.21	0.02	1.21	0.43	0.09	0.01	0.96	0.01	3	8
2	369,5B.1	0.00	0.05	0.34	0.02	0.93	0.62	0.15	0.01	0.88	0.01	3	8
3	369,5B.2	0.00	0.05	0.34	0.02	0.91	0.63	0.15	0.01	0.89	0.00	3	8
4	369,5B.3	0.00	0.04	0.37	0.02	0.92	0.61	0.15	0.01	0.87	0.00	3	8

A	369.5	0.00	0.04	0.35	0.02	0.92	0.62	0.15	0.01	0.88	0.00	3	8
10	369,5B.9	0.01	0.08	0.21	0.01	1.24	0.37	0.11	0.01	0.96	0.01	3	8
11	369,5B.10	0.01	0.08	0.21	0.01	1.22	0.38	0.10	0.01	0.97	0.01	3	8
12	369,5B.11	0.01	0.08	0.22	0.01	1.22	0.38	0.10	0.01	0.96	0.01	3	8
D	369.5	0.01	0.08	0.21	0.01	1.23	0.38	0.10	0.01	0.97	0.01	3	8
13	369,5B.12	0.01	0.07	0.26	0.01	1.02	0.55	0.13	0.01	0.93	0.01	3	8
14	369,5B.13	0.00	0.08	0.22	0.02	1.08	0.52	0.11	0.01	0.95	0.01	3	8
15	369,5B.14	0.01	0.08	0.24	0.02	1.04	0.53	0.13	0.01	0.94	0.01	3	8
16	369,5B.15	0.00	0.07	0.25	0.01	1.06	0.53	0.13	0.01	0.93	0.01	3	8
E	369.5	0.00	0.07	0.24	0.02	1.05	0.53	0.12	0.01	0.94	0.01	3	8
40	378-A.9	0.01	0.05	0.27	0.01	1.10	0.49	0.12	0.01	0.93	0.01	3	8
41	378-A.10	0.01	0.05	0.27	0.02	1.10	0.50	x	0.01	0.92	0.01	3	8
42	378-A.11	0.01	0.05	0.27	0.02	1.11	0.49	0.12	0.01	0.92	0.01	3	8
D	378	0.01	0.05	0.27	0.02	1.10	0.49	0.12	0.01	0.92	0.01	3	8
35	320.7	0.00	0.03	0.13	0.01	1.51	0.29	0.06	0.01	0.96	0.00	3	8
36	320.8	0.00	0.03	0.13	0.01	1.50	0.30	0.06	0.01	0.96	0.00	3	8
37	320.9	0.00	0.03	0.14	0.01	1.48	0.31	0.07	0.01	0.95	0.00	3	8
X	320	0.00	0.03	0.13	0.01	1.49	0.30	0.07	0.01	0.96	0.00	3	8
28	364,5.9	0.00	0.08	0.17	0.02	1.38	0.26	0.07	0.01	1.00	0.01	3	8
B	364.5	0.00	0.08	0.17	0.02	1.38	0.26	0.07	0.01	1.00	0.01	3	8
30	364,5.11	0.00	0.07	0.16	0.01	1.41	0.26	0.07	0.01	0.99	0.00	3	8
31	364,5.12	0.01	0.07	0.17	0.01	1.41	0.25	0.09	0.01	0.97	0.01	3	8
C	364.5	0.01	0.07	0.17	0.01	1.41	0.26	0.08	0.01	0.98	0.01	3	8
35	378-A.4	0.00	0.08	0.19	0.01	1.25	0.39	0.09	0.01	0.97	0.01	3	8
36	378-A.5	0.00	0.07	0.23	0.02	1.19	0.42	0.11	0.01	0.95	0.01	3	8
37	378-A.6	0.01	0.07	0.22	0.01	1.21	0.40	0.12	0.01	0.94	0.01	3	8
B	378	0.00	0.07	0.22	0.02	1.22	0.40	0.11	0.01	0.95	0.01	3	8
43	378-A.12	0.00	0.06	0.11	0.01	1.53	0.22	0.06	0.01	0.99	0.01	3	8
44	378-A.13	0.00	0.06	0.11	0.01	1.54	0.22	0.07	0.01	0.98	0.01	3	8

45	378-A.14	0.00	0.07	0.10	0.01	1.52	0.22	0.06	0.00	0.99	0.01	3	8
C	378	0.00	0.06	0.11	0.01	1.53	0.22	0.06	0.01	0.99	0.01	3	8

10.1.3 Clinopyroxene – measured oxides, wt%

Table 25: EPMA raw data from the analyzed Clinopyroxenes

Analysis No.	Name	SiO2	TiO2	Al2O3	FeOt	MnO	MgO	CaO	Na2O	K2O	Cr2O3	Total
1	296.1	50.853	0.725	4.025	3.946	0.096	15.917	22.112	0.84	0	1.02	99.53
2	296.2	50.88	0.61	3.561	2.945	0.07	15.612	23.066	0.769	0.002	0.728	98.24
3	296.3	50.779	0.76	4.091	3.324	0.099	15.497	22.613	0.859	0.008	1.006	99.03
4	296.4	52.282	0.739	4.121	3.622	0.073	15.678	22.452	0.898	0.022	0.836	100.72
5	296.5	50.96	0.74	4.152	3.694	0.166	15.853	22.14	0.89	0	0.964	99.55
average	296	51.1508	0.7148	3.99	3.5062	0.1008	15.7114	22.4766	0.8512	0.0064	0.9108	99.41
6	296.6	51.88	0.571	3.616	2.49	0.083	15.499	23.003	0.922	0.003	0.902	98.96
7	296.7	51.719	0.723	3.541	3.054	0.032	15.996	23.234	0.736	0.014	0.867	99.91
8	296.8	51.774	0.652	3.84	2.613	0.122	15.359	22.648	0.876	0	1.172	99.05
9	296.9	51.491	0.617	3.875	3.176	0.084	15.499	22.865	0.891	0	0.995	99.49
10	296.1	51.651	0.577	3.58	2.412	0.083	15.605	23.305	0.823	0.019	1.042	99.09
average	296	51.703	0.628	3.6904	2.749	0.0808	15.5916	23.011	0.8496	0.0072	0.9956	99.306
11	296.11	51.412	0.568	3.802	3.379	0.111	16.224	22.465	0.705	0	1.069	99.73
12	296.12	51.66	0.568	3.516	2.234	0.105	15.882	23.609	0.656	0.007	0.719	98.95
13	296.13	51.484	0.678	3.76	3.227	0.07	15.697	23.224	0.797	0.01	0.875	99.82
14	296.14	51.544	0.705	3.897	2.45	0.124	15.983	22.842	0.777	0	0.978	99.
15	296.15	51.51	0.825	4.111	3.988	0.15	16.075	21.872	0.78	0	1.387	100.69
average	296	51.522	0.6688	3.8172	3.0556	0.112	15.9722	22.8024	0.743	0.0034	1.0056	99.702
36	325.1	50.744	0.697	4.98	3.533	0.095	16.04	23.18	0.628	0.015	0.597	100.50
37	325.2	50.124	0.75	4.74	2.649	0.09	15.918	23.508	0.56	0.011	0.624	98.97
38	325.3	50.301	0.726	4.585	3.432	0.078	15.849	23.416	0.524	0	0.638	99.54
39	325.4	50.447	0.711	4.75	3.13	0.088	16.108	23.358	0.552	0.028	0.82	99.99
40	325.5	50.735	0.544	4.233	3.446	0.14	16.362	22.957	0.574	0.019	0.504	99.51
average	325	50.4702	0.6856	4.6576	3.238	0.0982	16.0554	23.2838	0.5676	0.0146	0.6366	99.707
41	325.6	51.301	0.449	7.869	4.516	0.091	20.597	12.518	1.786	0.02	0.19	99.33

42	325.7	50.797	0.451	8.464	4.513	0.071	20.533	12.469	1.941	0	0.201	99.4
43	325.8	51.554	0.343	6.357	4.142	0.134	21.199	12.516	1.512	0.022	0.228	98.00
44	325.9	49.051	0.54	8.378	4.649	0.052	20.425	12.806	1.965	0.022	0.277	98.16
45	325.1	49.144	0.536	9.099	4.892	0.059	20.254	12.45	1.941	0	0.179	98.55
average	325	50.3694	0.4638	8.0334	4.5424	0.0814	20.6016	12.5518	1.829	0.0128	0.215	98.700
46	325.11	50.298	0.614	5.43	3.579	0.102	16.158	22.438	0.884	0.021	0.668	100.19
47	325.12	50.755	0.696	4.839	3.565	0.087	16.029	23.488	0.658	0	0.693	100.8
48	325.13	50.757	0.72	4.916	4.123	0.1	15.576	23.551	0.583	0	0.677	101.00
49	325.14	51.022	0.597	4.188	3.424	0.14	16.417	23.057	0.625	0.001	0.673	100.14
50	325.15	50.962	0.559	4.203	3.383	0.087	16.029	23.544	0.532	0.003	0.624	99.92
average	325	50.7588	0.6372	4.7152	3.6148	0.1032	16.0418	23.2156	0.6564	0.005	0.667	100.41
73	329,5.11	51.484	0.649	3.929	3.559	0.069	16.077	23.021	0.64	0.018	0.783	100.22
74	329,5.12	51.341	0.837	3.953	3.49	0.121	15.84	23.626	0.648	0.01	0.761	100.62
75	329,5.13	51.285	0.88	4.122	3.561	0.104	15.649	23.622	0.71	0.025	0.89	100.84
76	329,5.14	51.418	0.603	3.853	3.837	0.098	15.563	23.331	0.704	0.005	0.813	100.22
77	329,5.15	51.686	0.601	3.415	3.298	0.091	15.902	24.131	0.594	0	0.696	100.41
average	329.5	51.4428	0.714	3.8544	3.549	0.0966	15.8062	23.5462	0.6592	0.0116	0.7886	100.468
83	346.1	49.702	0.979	5.592	4.116	0.11	14.996	23.428	0.477	0.01	0.568	99.97
84	346.2	49.641	0.974	5.881	4.244	0.109	15.056	22.909	0.613	0.021	0.641	100.08
85	346.3	49.53	1.031	5.602	4.309	0.134	15.726	22.684	0.638	0	0.517	100.17
86	346.4	49.361	1.004	5.666	4.225	0.156	15.547	23.091	0.498	0.008	0.661	100.21
87	346.5	49.363	0.992	5.51	3.767	0.104	15.371	23.264	0.471	0	0.661	99.50
average	346	49.5194	0.996	5.6502	4.1322	0.1226	15.3392	23.0752	0.5394	0.0078	0.6096	99.991
88	346.6	49.819	0.915	4.921	3.68	0.099	15.594	23.287	0.52	0.012	0.665	99.51
89	346.7	49.643	0.787	5.29	4.475	0.103	16.528	22.234	0.479	0.013	0.759	100.31
90	346.8	49.788	0.86	4.89	3.811	0.094	15.764	23.502	0.434	0.018	0.492	99.65
91	346.9	49.648	0.842	4.831	3.606	0.102	15.735	23.703	0.412	0	0.622	99.50
92	346.1	49.941	0.794	4.687	3.85	0.136	15.729	23.088	0.478	0	0.707	99.4
average	346	49.7678	0.8396	4.9238	3.8844	0.1068	15.87	23.1628	0.4646	0.0086	0.649	99.677

93	346.11	49.418	0.851	5.127	3.901	0.07	15.851	23.74	0.419	0.003	0.546	99.92
94	346.12	49.267	0.936	5.098	3.75	0.112	15.498	23.926	0.407	0.009	0.67	99.67
95	346.13	49.272	0.94	4.936	3.779	0.061	15.661	23.536	0.497	0	0.786	99.46
96	346.14	49.426	0.81	4.806	3.741	0.08	15.618	23.59	0.381	0	0.604	99.05
97	346.15	49.367	0.924	5.279	3.741	0.093	15.547	23.647	0.428	0.004	0.674	99.70
average	346	49.35	0.8922	5.0492	3.7824	0.0832	15.635	23.6878	0.4264	0.0032	0.656	99.565
98	346.16	49.684	0.764	4.808	3.767	0.093	15.883	23.033	0.55	0	0.681	99.26
99	346.17	49.18	0.877	5.168	3.73	0.092	15.684	23.347	0.434	0.018	0.832	99.36
100	346.18	49.5	0.98	5.076	3.712	0.107	15.814	23.231	0.527	0	0.719	99.66
101	346.19	50.121	0.826	4.656	3.927	0.108	16.405	22.825	0.458	0	0.592	99.91
102	346.2	50.299	0.723	4.682	3.558	0.096	15.851	23.715	0.425	0	0.5	99.84
average	346	49.7568	0.834	4.878	3.7388	0.0992	15.9274	23.2302	0.4788	0.0036	0.6648	99.611
103	346.21	49.979	0.678	4.219	3.573	0.084	15.969	24.479	0.299	0.014	0.829	100.12
104	346.22	49.71	0.647	4.581	3.635	0.095	16.033	23.816	0.279	0.012	0.711	99.51
105	346.23	49.632	0.639	4.669	3.626	0.133	15.752	24.153	0.297	0	0.84	99.74
106	346.24	50.021	0.652	4.638	3.807	0.062	15.898	23.646	0.319	0	0.847	99.8
107	346.25	49.684	0.77	5.347	3.652	0.124	15.896	23.344	0.481	0	0.585	99.88
average	346	49.8052	0.6772	4.6908	3.6586	0.0996	15.9096	23.8876	0.335	0.0052	0.7624	99.831
108	348.1	50.881	0.707	4.875	4.338	0.103	15.425	23.236	0.571	0	0.665	100.80
109	348.2	50.419	0.838	5.184	4.495	0.114	15.236	23.475	0.553	0.018	0.691	101.02
110	348.3	50.446	1.324	4.332	6.426	0.157	17.213	19.28	0.472	0	0.492	100.14
111	348.4	50.271	0.817	5.141	4.239	0.135	15.163	23.678	0.469	0	0.754	100.66
112	348.5	50.215	0.804	4.898	3.951	0.121	15.196	23.541	0.55	0	0.713	99.98
average	348	50.4464	0.898	4.886	4.6898	0.126	15.6466	22.642	0.523	0.0036	0.663	100.524
113	348.6	48.931	0.972	5.907	4.078	0.121	15.554	23.554	0.45	0.017	0.666	100.2
114	348.7	48.928	0.92	6.323	4.217	0.093	15.453	23.734	0.294	0	0.677	100.63
115	348.8	49.21	1.125	5.904	3.949	0.097	15.577	23.392	0.526	0	0.738	100.51
116	348.9	49.456	1.12	5.908	3.837	0.135	15.565	23.211	0.558	0	0.692	100.48
117	348.1	49.584	1.02	5.827	3.858	0.099	15.604	23.357	0.479	0	0.637	100.46

average	348	49.2218	1.0314	5.9738	3.9878	0.109	15.5506	23.4496	0.4614	0.0034	0.682	100.470
118	348.11	50.467	0.834	4.611	4.277	0.149	16.15	22.653	0.414	0	0.716	100.27
119	348.12	50.432	0.763	4.948	4.072	0.092	15.754	23.691	0.482	0.003	0.783	101.0
120	348.13	50.373	0.864	4.791	3.907	0.162	15.56	23.715	0.427	0	0.793	100.59
121	348.14	50.735	0.782	4.268	4.05	0.166	16.089	23.257	0.34	0	0.628	100.31
122	348.15	50.372	0.86	4.341	4.112	0.11	15.655	23.357	0.357	0	0.722	99.88
average	348	50.4758	0.8206	4.5918	4.0836	0.1358	15.8416	23.3346	0.404	0.0006	0.7284	100.416
123	348.16	50.277	0.969	5.328	3.783	0.099	15.762	23.87	0.42	0.002	0.485	100.99
124	348.17	49.932	0.845	5.603	4.038	0.069	15.765	23.326	0.373	0	0.522	100.47
125	348.18	50.273	0.846	5.383	3.947	0.107	15.844	23.803	0.371	0.01	0.552	101.13
126	348.19	50.353	0.617	5.172	4.152	0.098	15.753	24.237	0.279	0	0.515	101.17
127	348.2	51.054	0.477	4.322	3.682	0.072	16.348	23.615	0.428	0.012	0.348	100.35
average	348	50.3778	0.7508	5.1616	3.9204	0.089	15.8944	23.7702	0.3742	0.0048	0.4844	100.827
128	350,7.1	47.628	0.994	6.344	5.635	0.283	16.123	20.55	0.606	0.011	0.515	98.68
129	350,7.2	49.291	1.121	5.873	4.881	0.134	16.444	21.619	0.472	0.001	1.009	100.84
130	350,7.3	48.857	1.177	6.415	4.179	0.085	15.633	22.358	0.657	0.004	0.711	100.07
131	350,7.4	48.005	1.231	6.594	4	0.105	15.633	22.582	0.754	0.008	0.52	99.43
132	350,7.5	48.627	1.157	6.337	3.872	0.06	15.597	22.493	0.644	0	0.512	99.29
average	350.7	48.4816	1.136	6.3126	4.5134	0.1334	15.886	21.9204	0.6266	0.0048	0.6534	99.668
133	350,7.6	49.259	0.754	5.666	3.757	0.106	15.831	23.414	0.478	0	0.477	99.74
134	350,7.7	48.996	0.991	5.706	3.404	0.079	15.647	23.551	0.434	0	0.55	99.35
135	350,7.8	49.163	0.827	5.683	3.904	0.095	15.652	23.219	0.416	0.017	0.522	99.49
136	350,7.9	49.17	0.922	5.712	3.921	0.131	15.647	23.355	0.568	0	0.522	99.94
137	350,7.10	49.455	0.928	5.507	3.88	0.11	16	22.897	0.485	0	0.558	99.8
average	350.7	49.2086	0.8844	5.6548	3.7732	0.1042	15.7554	23.2872	0.4762	0.0034	0.5258	99.673
138	350,7.11	50.658	0.944	5.009	4.193	0.102	15.599	22.561	0.644	0	0.664	100.37
139	350,7.12	50.636	0.749	4.842	4.91	0.151	16.689	21.214	0.537	0.009	0.754	100.49
140	350,7.13	50.393	0.801	4.876	3.938	0.126	15.794	23.316	0.647	0	0.719	100.6
141	350,7.14	49.874	0.897	5	3.967	0.074	15.766	22.78	0.556	0	0.657	99.57

142	350,7.15	50.319	0.794	4.88	3.847	0.099	15.756	23.255	0.514	0.009	0.561	100.03
average	350.7	50.376	0.837	4.9214	4.171	0.1104	15.9208	22.6252	0.5796	0.0036	0.671	100.21
143	350,7.16	49.046	1.193	5.934	3.829	0.121	15.471	22.932	0.64	0.011	0.781	99.95
144	350,7.17	49.065	1.117	6.034	3.904	0.113	15.848	22.088	0.733	0.007	0.753	99.66
145	350,7.18	49.42	1.003	5.651	3.867	0.037	15.749	22.927	0.624	0	0.616	99.89
146	350,7.19	48.957	0.966	5.966	4.019	0.102	15.464	23.1	0.557	0.02	0.842	99.99
147	350,7.20	48.899	1.013	5.202	4.318	0.114	15.753	22.696	0.53	0	0.726	99.25
average	350.7	49.0774	1.0584	5.7574	3.9874	0.0974	15.657	22.7486	0.6168	0.0076	0.7436	99.751
2	354,35.1	51.574	0.839	4.135	4.696	0.117	16.99	22.261	0.423	0.034	0.14	101.20
3	354,35.2	51.328	0.958	4.417	4.148	0.136	15.653	23.622	0.464	0	0.163	100.88
4	354,35.3	51.113	1.086	4.621	3.457	0.088	15.436	23.762	0.439	0	0.208	100.2
5	354,35.4	51.522	0.948	4.533	5.718	0.108	17.987	19.731	0.405	0	0.21	101.16
6	354,35.5	51.136	1.093	4.639	4.537	0.091	17.578	20.276	0.378	0.007	0.155	99.8
average	354.35	51.3346	0.9848	4.469	4.5112	0.108	16.7288	21.9304	0.4218	0.0082	0.1752	100.67
7	354,35.6	52.003	0.754	3.901	3.932	0.101	15.914	23.989	0.427	0	0.206	101.22
8	354,35.7	51.851	0.787	3.769	3.933	0.103	15.89	24.134	0.382	0	0.175	101.02
9	354,35.8	52.13	0.712	3.27	3.854	0.117	16.108	24.066	0.363	0.007	0.17	100.79
10	354,35.9	52.053	0.591	3.336	3.842	0.085	15.981	23.87	0.384	0	0.195	100.33
11	354,35.10	51.646	0.906	3.847	4.063	0.111	15.739	24.115	0.401	0.005	0.213	101.04
average	354.35	51.9366	0.75	3.6246	3.9248	0.1034	15.9264	24.0348	0.3914	0.0024	0.1918	100.886
12	354,35.11	51.714	0.923	4.139	4.132	0.069	15.662	23.648	0.455	0.006	0.185	100.93
13	354,35.12	51.886	0.878	3.985	4.656	0.098	16.493	22.531	0.385	0.006	0.2	101.11
14	354,35.13	51.451	0.922	4.057	4.293	0.098	15.785	23.945	0.429	0.01	0.267	101.25
15	354,35.14	51.519	0.841	4.045	4.263	0.139	16.185	23.409	0.46	0.004	0.112	100.97
16	354,35.15	51.326	1.011	4.402	3.956	0.132	15.599	23.815	0.456	0.012	0.157	100.86
average	354.35	51.5792	0.915	4.1256	4.26	0.1072	15.9448	23.4696	0.437	0.0076	0.1842	101.030
32	364,5.1	49.649	1.203	6.036	4.059	0.106	14.756	23.568	0.501	0.002	0.365	100.24
33	364,5.2	49.194	1.086	5.603	4.412	0.102	15.178	23.11	0.436	0.01	0.464	99.59
34	364,5.3	49.341	1.005	5.792	4.113	0.095	15.045	23.762	0.476	0.013	0.343	99.98

35	364,5.4	48.792	1.089	5.959	4.392	0.08	14.949	23.251	0.508	0.002	0.457	99.47
36	364,5.5	49.877	1.023	5.733	4.657	0.066	14.726	23.626	0.547	0.009	0.446	100.7
average	364.5	49.3706	1.0812	5.8246	4.3266	0.0898	14.9308	23.4634	0.4936	0.0072	0.415	100.002
37	364,5.6	49.553	1.265	6.167	4.283	0.095	14.891	23.132	0.528	0.015	0.501	100.4
38	364,5.7	51.266	0.819	4.299	3.977	0.143	15.325	23.615	0.538	0.019	0.564	100.56
39	364,5.8	50.848	0.819	4.442	4.593	0.098	15.174	23.475	0.568	0	0.546	100.56
40	364,5.9	51.707	0.601	3.941	4.359	0.127	16.953	20.994	0.421	0	0.466	99.56
41	364,5.10	51.059	0.689	4.435	4.22	0.142	15.339	23.667	0.533	0	0.549	100.63
42	364,5.11	51.257	0.572	4.119	4.165	0.123	15.384	23.873	0.477	0	0.611	100.58
average	364.5	50.94833	0.794167	4.567167	4.266167	0.121333	15.511	23.126	0.510833	0.005667	0.5395	100.390
43	364,5.12	51.574	0.586	3.954	4.161	0.127	15.496	23.628	0.398	0.005	0.607	100.53
44	364,5.13	51.334	0.673	4.07	4.226	0.12	15.436	23.551	0.412	0	0.485	100.30
45	364,5.14	51.412	0.594	3.865	3.66	0.098	15.449	23.745	0.42	0	0.508	99.75
46	364,5.15	51.284	0.734	4.336	4.18	0.142	15.451	24.12	0.466	0	0.486	101.19
47	364,5.16	51.448	0.624	4.069	4.422	0.108	15.954	22.632	0.485	0	0.558	100.
average	364.5	51.4104	0.6422	4.0588	4.1298	0.119	15.5572	23.5352	0.4362	0.001	0.5288	100.418
17	369,5B.1	51.712	0.765	3.766	3.703	0.113	16.263	22.527	0.677	0	0.852	100.37
18	369,5B.2	52.117	0.529	2.757	3.208	0.137	16.191	23.707	0.611	0	0.728	99.98
19	369,5B.3	51.732	0.754	3.459	4.391	0.118	17.017	21.337	0.647	0.011	0.806	100.27
20	369,5B.4	51.57	0.777	3.804	2.908	0.133	15.806	23.742	0.694	0.014	0.77	100.21
21	369,5B.5	51.537	0.828	4.066	3.107	0.117	15.701	23.206	0.76	0.01	0.804	100.13
average	369.5	51.7336	0.7306	3.5704	3.4634	0.1236	16.1956	22.9038	0.6778	0.007	0.792	100.197
22	369,5B.6	51.584	0.797	4.081	3.836	0.1	15.49	23.159	0.735	0.013	0.791	100.58
23	369,5B.7	51.677	0.854	4.028	3.837	0.116	15.607	23.339	0.745	0.007	0.845	101.05
24	369,5B.8	51.58	0.792	4.082	4.205	0.087	16.885	21.216	0.608	0.002	0.826	100.28
25	369,5B.9	50.986	0.981	4.535	3.883	0.127	15.991	22.528	0.713	0	0.729	100.47
26	369,5B.10	51.045	0.865	4.431	3.959	0.163	15.516	23.136	0.703	0.002	0.805	100.62
average	369.5	51.3744	0.8578	4.2314	3.944	0.1186	15.8978	22.6756	0.7008	0.0048	0.7992	100.604
27	369,5B.11	51.388	0.89	4	3.7	0.115	15.66	23.772	0.598	0.018	0.782	100.92

28	369,5B.12	51.721	0.77	3.88	3.797	0.11	15.687	23.476	0.617	0.018	0.786	100.86
29	369,5B.13	51.682	0.822	3.968	3.582	0.097	15.811	23.223	0.647	0.001	0.838	100.67
30	369,5B.14	51.784	0.74	3.839	3.873	0.12	16.105	22.81	0.613	0	0.777	100.66
31	369,5B.15	51.959	0.674	3.658	4.146	0.108	17.018	21.672	0.615	0	0.781	100.63
average	369.5	51.7068	0.7792	3.869	3.8196	0.11	16.0562	22.9906	0.618	0.0074	0.7928	100.749
48	378-A.1	50.692	1.117	4.917	3.864	0.102	15.36	23.755	0.642	0.027	0.671	101.14
49	378-A.2	50.14	0.987	5.121	3.945	0.104	15.41	23.287	0.688	0.012	0.582	100.27
50	378-A.3	50.955	1.053	4.968	3.591	0.119	15.359	23.369	0.624	0	0.574	100.61
51	378-A.4	50.978	1.004	4.863	3.876	0.125	15.245	23.536	0.632	0	0.643	100.90
52	378-A.5	50.686	1.045	4.933	3.714	0.108	15.417	23.402	0.595	0.021	0.733	100.65
average	378	50.6902	1.0412	4.9604	3.798	0.1116	15.3582	23.4698	0.6362	0.012	0.6406	100.718
53	378-A.6	50.729	0.983	4.623	3.806	0.107	15.867	22.754	0.679	0.02	0.754	100.32
54	378-A.7	50.698	0.845	4.914	4.225	0.098	15.534	22.655	0.671	0.004	0.792	100.43
55	378-A.8	50.535	0.969	4.682	4.14	0.105	15.277	23.344	0.682	0.022	0.692	100.44
56	378-A.9	50.499	1.021	4.87	3.865	0.134	15.264	23.479	0.655	0.002	0.761	100.5
57	378-A.10	50.542	0.98	4.808	3.834	0.148	15.15	23.425	0.678	0.007	0.709	100.28
average	378	50.6006	0.9596	4.7794	3.974	0.1184	15.4184	23.1314	0.673	0.011	0.7416	100.407
58	378-A.11	50.402	1.066	5.012	4.167	0.094	15.291	23.259	0.688	0.019	0.701	100.69
59	378-A.12	50.36	1.125	4.986	4.247	0.141	15.17	23.559	0.734	0	0.806	101.12
60	378-A.13	50.081	1.055	5.045	4.488	0.089	15.308	22.911	0.703	0	0.811	100.49
61	378-A.14	50.047	1.146	4.988	4.132	0.152	14.892	23.082	0.698	0.003	0.77	99.9
62	378-A.15	50.171	1.032	5.055	4.224	0.126	15.142	23.471	0.762	0	0.842	100.82
average	378	50.2122	1.0848	5.0172	4.2516	0.1204	15.1606	23.2564	0.717	0.0044	0.786	100.610

10.1.4 Clinopyroxene – calculated elements in chemical formula

Table 26: Calculated EPMA data into cation units in mineral formula for Clinopyroxenes.

No.	Name	Si4+	Ti4+	Al(IV)	AL(VI)	Al (total)	Cr3+	Fe2+	Mn2+	Mg2+	Ca2+	Na+	K+
1	296.1	1.869	0.023	0.131	0.046	0.177	0.004	0.142	0.004	0.918	0.865	0.030	0.002
2	296.2	1.869	0.026	0.131	0.059	0.190	0.005	0.126	0.004	0.850	0.922	0.033	0.000
3	296.3	1.868	0.030	0.132	0.067	0.199	0.006	0.106	0.003	0.841	0.931	0.031	0.000
4	296.4	1.863	0.026	0.137	0.056	0.193	0.006	0.173	0.003	0.969	0.764	0.028	0.000
5	296.5	1.865	0.030	0.135	0.065	0.199	0.004	0.138	0.003	0.956	0.793	0.027	0.000
average	*296*	*1.867*	*0.027*	*0.133*	*0.059*	*0.192*	*0.005*	*0.137*	*0.003*	*0.907*	*0.855*	*0.030*	*0.000*
6	296.6	1.885	0.021	0.115	0.052	0.167	0.006	0.119	0.003	0.860	0.932	0.030	0.000
7	296.7	1.885	0.022	0.115	0.046	0.161	0.005	0.120	0.003	0.861	0.940	0.027	0.000
8	296.8	1.898	0.019	0.102	0.038	0.140	0.005	0.117	0.004	0.874	0.939	0.026	0.000
9	296.9	1.902	0.016	0.098	0.046	0.144	0.006	0.117	0.003	0.871	0.935	0.027	0.000
10	296.1	1.879	0.025	0.121	0.044	0.165	0.006	0.124	0.003	0.854	0.940	0.028	0.000
average	*296*	*1.890*	*0.021*	*0.110*	*0.045*	*0.155*	*0.006*	*0.119*	*0.003*	*0.864*	*0.937*	*0.028*	*0.000*
11	296.11	1.881	0.025	0.119	0.058	0.177	0.005	0.126	0.002	0.849	0.921	0.032	0.000
12	296.12	1.882	0.024	0.118	0.052	0.170	0.006	0.141	0.003	0.892	0.875	0.027	0.000
13	296.13	1.870	0.025	0.130	0.044	0.174	0.008	0.131	0.003	0.855	0.933	0.030	0.000
14	296.14	1.874	0.023	0.126	0.048	0.173	0.003	0.130	0.004	0.878	0.912	0.032	0.000
15	296.15	1.869	0.028	0.131	0.058	0.189	0.005	0.120	0.004	0.847	0.929	0.032	0.001
average	*296*	*1.875*	*0.025*	*0.125*	*0.052*	*0.177*	*0.005*	*0.130*	*0.003*	*0.864*	*0.914*	*0.031*	*0.000*
36	325.1	1.886	0.021	0.114	0.048	0.162	0.025	0.113	0.003	0.884	0.881	0.048	0.000
37	325.2	1.910	0.015	0.090	0.029	0.119	0.021	0.098	0.004	0.885	0.931	0.043	0.000
38	325.3	1.889	0.021	0.111	0.038	0.149	0.023	0.134	0.004	0.926	0.835	0.046	0.001
39	325.4	1.885	0.021	0.115	0.049	0.164	0.022	0.089	0.004	0.861	0.930	0.049	0.001
40	325.5	1.884	0.023	0.116	0.059	0.175	0.023	0.095	0.004	0.855	0.909	0.054	0.000
average	*325*	*1.891*	*0.020*	*0.109*	*0.045*	*0.154*	*0.023*	*0.106*	*0.004*	*0.882*	*0.897*	*0.048*	*0.000*
41	325.6	1.882	0.022	0.118	0.058	0.175	0.023	0.117	0.003	0.843	0.905	0.052	0.001

42	325.7	1.878	0.023	0.122	0.051	0.173	0.024	0.117	0.004	0.846	0.909	0.053	0.000
43	325.8	1.880	0.022	0.120	0.055	0.175	0.024	0.128	0.003	0.917	0.828	0.043	0.000
44	325.9	1.861	0.027	0.139	0.056	0.195	0.021	0.119	0.004	0.870	0.881	0.050	0.000
45	325.1	1.865	0.024	0.135	0.056	0.191	0.023	0.121	0.005	0.845	0.906	0.050	0.000
average	*325*	*1.873*	*0.024*	*0.127*	*0.055*	*0.182*	*0.023*	*0.120*	*0.004*	*0.864*	*0.886*	*0.050*	*0.000*
46	325.11	1.872	0.024	0.128	0.044	0.172	0.023	0.113	0.004	0.850	0.928	0.042	0.001
47	325.12	1.883	0.021	0.117	0.049	0.166	0.023	0.116	0.003	0.851	0.916	0.044	0.001
48	325.13	1.882	0.023	0.118	0.052	0.170	0.024	0.109	0.003	0.858	0.906	0.046	0.000
49	325.14	1.886	0.020	0.114	0.050	0.165	0.022	0.118	0.004	0.874	0.890	0.043	0.000
50	325.15	1.889	0.018	0.111	0.045	0.157	0.022	0.126	0.003	0.922	0.844	0.043	0.000
average	*325*	*1.882*	*0.021*	*0.118*	*0.048*	*0.166*	*0.023*	*0.116*	*0.003*	*0.871*	*0.897*	*0.044*	*0.000*
73	329,5.11	1.823	0.033	0.177	0.084	0.261	0.011	0.125	0.003	0.808	0.927	0.036	0.000
74	329,5.12	1.821	0.030	0.179	0.066	0.244	0.014	0.137	0.003	0.838	0.917	0.031	0.000
75	329,5.13	1.819	0.028	0.181	0.071	0.252	0.010	0.127	0.003	0.827	0.939	0.034	0.001
76	329,5.14	1.810	0.030	0.190	0.071	0.261	0.013	0.136	0.003	0.827	0.924	0.037	0.000
77	329,5.15	1.828	0.028	0.172	0.076	0.248	0.013	0.143	0.002	0.805	0.928	0.039	0.000
average	*329.5*	*1.820*	*0.030*	*0.180*	*0.073*	*0.253*	*0.012*	*0.133*	*0.003*	*0.821*	*0.927*	*0.035*	*0.000*
83	346.1	1.817	0.035	0.183	0.083	0.266	0.015	0.131	0.003	0.814	0.909	0.038	0.001
84	346.2	1.874	0.023	0.126	0.059	0.185	0.016	0.122	0.004	0.835	0.925	0.038	0.001
85	346.3	1.864	0.023	0.136	0.056	0.192	0.016	0.141	0.003	0.829	0.922	0.040	0.000
86	346.4	1.894	0.017	0.106	0.065	0.170	0.013	0.134	0.004	0.926	0.824	0.030	0.000
87	346.5	1.868	0.019	0.132	0.059	0.191	0.016	0.129	0.004	0.836	0.928	0.038	0.000
average	*346*	*1.876*	*0.016*	*0.124*	*0.054*	*0.178*	*0.018*	*0.127*	*0.004*	*0.839*	*0.936*	*0.034*	*0.000*
88	346.6	1.865	0.022	0.135	0.062	0.197	0.016	0.131	0.004	0.847	0.907	0.036	0.000
89	346.7	1.885	0.016	0.115	0.056	0.170	0.018	0.127	0.004	0.844	0.925	0.028	0.000
90	346.8	1.881	0.019	0.119	0.057	0.176	0.014	0.130	0.004	0.843	0.925	0.029	0.000
91	346.9	1.890	0.016	0.110	0.058	0.167	0.015	0.113	0.003	0.847	0.935	0.030	0.000
92	346.1	1.866	0.020	0.134	0.052	0.186	0.014	0.127	0.004	0.838	0.941	0.033	0.000
average	*346*	*1.882*	*0.017*	*0.118*	*0.058*	*0.175*	*0.016*	*0.135*	*0.003*	*0.870*	*0.887*	*0.034*	*0.000*

93	346.11	1.881	0.018	0.119	0.056	0.175	0.015	0.126	0.004	0.849	0.923	0.031	0.000
94	346.12	1.845	0.031	0.155	0.056	0.211	0.019	0.118	0.003	0.833	0.926	0.045	0.001
95	346.13	1.840	0.027	0.160	0.062	0.221	0.017	0.121	0.003	0.843	0.916	0.049	0.001
96	346.14	1.857	0.029	0.143	0.071	0.213	0.017	0.109	0.004	0.835	0.913	0.044	0.000
97	346.15	1.857	0.028	0.143	0.066	0.209	0.019	0.118	0.004	0.828	0.919	0.045	0.000
average	*346*	*1.850*	*0.029*	*0.150*	*0.062*	*0.212*	*0.021*	*0.113*	*0.003*	*0.839*	*0.915*	*0.042*	*0.001*
98	346.16	1.850	0.029	0.150	0.063	0.213	0.018	0.116	0.003	0.836	0.918	0.045	0.001
99	346.17	1.856	0.027	0.144	0.056	0.199	0.022	0.116	0.003	0.865	0.892	0.048	0.001
100	346.18	1.855	0.023	0.145	0.067	0.212	0.023	0.129	0.003	0.847	0.888	0.048	0.000
101	346.19	1.853	0.027	0.147	0.055	0.202	0.020	0.127	0.003	0.835	0.917	0.048	0.001
102	346.2	1.848	0.028	0.152	0.058	0.210	0.022	0.118	0.004	0.833	0.921	0.046	0.000
average	*346*	*1.854*	*0.027*	*0.146*	*0.062*	*0.208*	*0.021*	*0.118*	*0.005*	*0.828*	*0.921*	*0.048*	*0.000*
103	346.21	1.853	0.026	0.147	0.060	0.206	0.021	0.122	0.004	0.842	0.908	0.048	0.001
104	346.22	1.843	0.029	0.157	0.059	0.216	0.020	0.127	0.003	0.834	0.911	0.049	0.001
105	346.23	1.838	0.031	0.162	0.052	0.214	0.023	0.130	0.004	0.825	0.921	0.052	0.000
106	346.24	1.838	0.029	0.162	0.056	0.218	0.024	0.138	0.003	0.837	0.901	0.050	0.000
107	346.25	1.845	0.032	0.155	0.062	0.217	0.022	0.127	0.005	0.818	0.912	0.050	0.000
average	*346*	*1.836*	*0.028*	*0.164*	*0.054*	*0.218*	*0.024*	*0.129*	*0.004*	*0.826*	*0.920*	*0.054*	*0.000*
108	348.1	1.840	0.030	0.160	0.057	0.217	0.023	0.130	0.004	0.828	0.913	0.051	0.000
109	348.2	1.882	0.018	0.118	0.051	0.169	0.023	0.109	0.002	0.876	0.902	0.045	0.001
110	348.3	1.874	0.023	0.126	0.044	0.170	0.022	0.107	0.004	0.862	0.924	0.046	0.000
111	348.4	1.869	0.024	0.131	0.046	0.177	0.026	0.109	0.003	0.850	0.922	0.050	0.001
112	348.5	1.885	0.017	0.115	0.051	0.166	0.024	0.118	0.003	0.850	0.916	0.050	0.000
average	*348*	*1.890*	*0.017*	*0.110*	*0.037*	*0.147*	*0.020*	*0.101*	*0.003*	*0.867*	*0.945*	*0.042*	*0.000*
113	348.6	1.880	0.020	0.120	0.046	0.166	0.023	0.108	0.003	0.861	0.922	0.047	0.001
114	348.7	1.831	0.027	0.169	0.073	0.243	0.017	0.127	0.003	0.823	0.925	0.034	0.000
115	348.8	1.826	0.027	0.174	0.081	0.255	0.019	0.131	0.003	0.825	0.903	0.044	0.001
116	348.9	1.821	0.029	0.179	0.064	0.243	0.015	0.132	0.004	0.862	0.893	0.045	0.000
117	348.1	1.816	0.028	0.184	0.061	0.246	0.019	0.130	0.005	0.853	0.910	0.036	0.000

average	*348*	*1.825*	*0.028*	*0.175*	*0.065*	*0.240*	*0.019*	*0.116*	*0.003*	*0.847*	*0.922*	*0.034*	*0.000*
118	348.11	1.824	0.028	0.176	0.069	0.245	0.018	0.127	0.004	0.842	0.911	0.039	0.000
119	348.12	1.841	0.025	0.159	0.055	0.214	0.019	0.114	0.003	0.859	0.922	0.037	0.001
120	348.13	1.822	0.022	0.178	0.051	0.229	0.022	0.137	0.003	0.904	0.874	0.034	0.001
121	348.14	1.839	0.024	0.161	0.051	0.213	0.014	0.118	0.003	0.868	0.930	0.031	0.001
122	348.15	1.837	0.023	0.163	0.047	0.211	0.018	0.112	0.003	0.868	0.939	0.030	0.000
average	*348*	*1.848*	*0.022*	*0.152*	*0.052*	*0.204*	*0.021*	*0.119*	*0.004*	*0.867*	*0.915*	*0.034*	*0.000*
123	348.16	1.837	0.023	0.163	0.051	0.214	0.019	0.120	0.003	0.873	0.916	0.033	0.000
124	348.17	1.823	0.024	0.177	0.046	0.223	0.016	0.120	0.002	0.872	0.938	0.030	0.000
125	348.18	1.823	0.026	0.177	0.046	0.222	0.020	0.116	0.004	0.855	0.949	0.029	0.000
126	348.19	1.826	0.026	0.174	0.042	0.216	0.023	0.117	0.002	0.865	0.935	0.036	0.000
127	348.2	1.837	0.023	0.163	0.048	0.211	0.018	0.116	0.003	0.865	0.940	0.027	0.000
average	*348*	*1.824*	*0.026*	*0.176*	*0.054*	*0.230*	*0.020*	*0.116*	*0.003*	*0.856*	*0.936*	*0.031*	*0.000*
128	350,7.1	1.827	0.025	0.173	0.047	0.220	0.019	0.117	0.003	0.863	0.940	0.031	0.000
129	350,7.2	1.841	0.021	0.159	0.051	0.210	0.020	0.117	0.003	0.877	0.914	0.040	0.000
130	350,7.3	1.823	0.024	0.177	0.049	0.226	0.024	0.116	0.003	0.867	0.927	0.031	0.001
131	350,7.4	1.828	0.027	0.172	0.049	0.221	0.021	0.115	0.003	0.871	0.919	0.038	0.000
132	350,7.5	1.843	0.023	0.157	0.045	0.202	0.017	0.121	0.003	0.899	0.899	0.033	0.000
average	*350.7*	*1.851*	*0.020*	*0.149*	*0.054*	*0.203*	*0.015*	*0.109*	*0.003*	*0.869*	*0.935*	*0.030*	*0.000*
133	350,7.6	1.837	0.023	0.163	0.050	0.212	0.019	0.115	0.003	0.877	0.919	0.034	0.000
134	350,7.7	1.842	0.019	0.158	0.025	0.183	0.024	0.110	0.003	0.877	0.967	0.021	0.001
135	350,7.8	1.839	0.018	0.161	0.039	0.200	0.021	0.112	0.003	0.884	0.944	0.020	0.001
136	350,7.9	1.835	0.018	0.165	0.039	0.203	0.025	0.112	0.004	0.868	0.957	0.021	0.000
137	350,7.10	1.843	0.018	0.157	0.045	0.201	0.025	0.117	0.002	0.873	0.934	0.023	0.000
average	*350.7*	*1.829*	*0.021*	*0.171*	*0.061*	*0.232*	*0.017*	*0.112*	*0.004*	*0.872*	*0.921*	*0.034*	*0.000*
138	350,7.11	1.838	0.019	0.162	0.042	0.204	0.022	0.113	0.003	0.875	0.944	0.024	0.000
139	350,7.12	1.857	0.019	0.143	0.067	0.210	0.019	0.132	0.003	0.839	0.909	0.040	0.000
140	350,7.13	1.841	0.023	0.159	0.064	0.223	0.020	0.137	0.004	0.829	0.918	0.039	0.001
141	350,7.14	1.852	0.037	0.148	0.040	0.187	0.014	0.197	0.005	0.942	0.759	0.034	0.000

142	350,7.15	1.841	0.023	0.159	0.063	0.222	0.022	0.130	0.004	0.828	0.929	0.033	0.000
average	*350.7*	*1.849*	*0.022*	*0.151*	*0.061*	*0.213*	*0.021*	*0.122*	*0.004*	*0.834*	*0.929*	*0.039*	*0.000*
143	350,7.16	1.848	0.025	0.152	0.059	0.211	0.019	0.144	0.004	0.855	0.889	0.037	0.000
144	350,7.17	1.802	0.027	0.198	0.058	0.256	0.019	0.126	0.004	0.854	0.929	0.032	0.001
145	350,7.18	1.795	0.025	0.205	0.068	0.273	0.020	0.129	0.003	0.845	0.933	0.021	0.000
146	350,7.19	1.805	0.031	0.195	0.060	0.255	0.021	0.121	0.003	0.852	0.919	0.037	0.000
147	350,7.20	1.812	0.031	0.188	0.067	0.255	0.020	0.118	0.004	0.850	0.911	0.040	0.000
average	*350.7*	*1.816*	*0.028*	*0.184*	*0.068*	*0.252*	*0.018*	*0.118*	*0.003*	*0.852*	*0.917*	*0.034*	*0.000*
2	354,35.1	1.806	0.028	0.194	0.064	0.258	0.020	0.122	0.003	0.850	0.922	0.033	0.000
3	354,35.2	1.850	0.023	0.150	0.050	0.199	0.021	0.131	0.005	0.883	0.890	0.029	0.000
4	354,35.3	1.839	0.021	0.161	0.052	0.213	0.023	0.124	0.003	0.857	0.926	0.034	0.000
5	354,35.4	1.844	0.024	0.156	0.051	0.207	0.023	0.120	0.005	0.849	0.930	0.030	0.000
6	354,35.5	1.860	0.022	0.140	0.044	0.184	0.018	0.124	0.005	0.879	0.913	0.024	0.000
average	*354.35*	*1.856*	*0.024*	*0.144*	*0.045*	*0.189*	*0.021*	*0.127*	*0.003*	*0.860*	*0.922*	*0.026*	*0.000*
7	354,35.6	1.850	0.023	0.150	0.048	0.198	0.021	0.125	0.004	0.866	0.916	0.029	0.000
8	354,35.7	1.831	0.027	0.169	0.060	0.229	0.014	0.115	0.003	0.856	0.932	0.030	0.000
9	354,35.8	1.827	0.023	0.173	0.069	0.242	0.015	0.124	0.002	0.860	0.915	0.026	0.000
10	354,35.9	1.830	0.023	0.170	0.060	0.231	0.016	0.120	0.003	0.860	0.928	0.026	0.000
11	354,35.10	1.835	0.017	0.165	0.057	0.222	0.015	0.127	0.003	0.856	0.946	0.020	0.000
average	*354.35*	*1.867*	*0.013*	*0.133*	*0.053*	*0.186*	*0.010*	*0.113*	*0.002*	*0.891*	*0.925*	*0.030*	*0.001*
12	354,35.11	1.838	0.021	0.162	0.060	0.222	0.014	0.120	0.003	0.864	0.929	0.026	0.000
13	354,35.12	1.784	0.028	0.216	0.064	0.280	0.015	0.177	0.009	0.900	0.825	0.044	0.001
14	354,35.13	1.801	0.031	0.199	0.054	0.253	0.029	0.149	0.004	0.896	0.847	0.033	0.000
15	354,35.14	1.797	0.033	0.203	0.075	0.278	0.021	0.129	0.003	0.857	0.881	0.047	0.000
16	354,35.15	1.780	0.034	0.220	0.068	0.288	0.015	0.124	0.003	0.864	0.897	0.054	0.000
average	*354.35*	*1.800*	*0.032*	*0.200*	*0.077*	*0.276*	*0.015*	*0.120*	*0.002*	*0.861*	*0.892*	*0.046*	*0.000*
32	364,5.1	1.793	0.032	0.207	0.068	0.275	0.019	0.140	0.004	0.876	0.868	0.045	0.000
33	364,5.2	1.817	0.021	0.183	0.064	0.246	0.014	0.116	0.003	0.871	0.926	0.034	0.000
34	364,5.3	1.813	0.028	0.187	0.062	0.249	0.016	0.105	0.002	0.863	0.934	0.031	0.000

35	364,5.4	1.819	0.023	0.181	0.066	0.248	0.015	0.121	0.003	0.863	0.920	0.030	0.001
36	364,5.5	1.813	0.026	0.187	0.061	0.248	0.015	0.121	0.004	0.860	0.923	0.041	0.000
average	*364.5*	*1.822*	*0.026*	*0.178*	*0.061*	*0.239*	*0.016*	*0.120*	*0.003*	*0.879*	*0.904*	*0.035*	*0.000*
37	364,5.6	1.817	0.025	0.183	0.063	0.246	0.015	0.116	0.003	0.867	0.921	0.034	0.000
38	364,5.7	1.853	0.026	0.147	0.069	0.216	0.019	0.128	0.003	0.851	0.884	0.046	0.000
39	364,5.8	1.850	0.021	0.150	0.059	0.208	0.022	0.150	0.005	0.909	0.830	0.038	0.000
40	364,5.9	1.843	0.022	0.157	0.054	0.210	0.021	0.120	0.004	0.861	0.914	0.046	0.000
41	364,5.10	1.841	0.025	0.159	0.058	0.218	0.019	0.122	0.002	0.868	0.901	0.040	0.000
42	364,5.11	1.848	0.022	0.152	0.060	0.211	0.016	0.118	0.003	0.863	0.915	0.037	0.000
average	*364.5*	*1.847*	*0.023*	*0.153*	*0.060*	*0.213*	*0.019*	*0.128*	*0.003*	*0.870*	*0.889*	*0.041*	*0.000*
43	364,5.12	1.807	0.033	0.193	0.064	0.258	0.023	0.118	0.004	0.850	0.905	0.046	0.001
44	364,5.13	1.809	0.031	0.191	0.071	0.262	0.022	0.120	0.004	0.871	0.873	0.052	0.000
45	364,5.14	1.819	0.028	0.181	0.065	0.245	0.018	0.119	0.001	0.864	0.904	0.045	0.000
46	364,5.15	1.805	0.027	0.195	0.065	0.259	0.025	0.124	0.003	0.850	0.913	0.040	0.001
47	364,5.16	1.818	0.028	0.182	0.046	0.228	0.021	0.134	0.004	0.873	0.904	0.038	0.000
average	*364.5*	*1.812*	*0.029*	*0.188*	*0.062*	*0.250*	*0.022*	*0.123*	*0.003*	*0.862*	*0.900*	*0.044*	*0.000*
17	369,5B.1	1.875	0.020	0.125	0.050	0.175	0.030	0.122	0.003	0.875	0.874	0.060	0.000
18	369,5B.2	1.895	0.017	0.105	0.051	0.156	0.021	0.092	0.002	0.867	0.920	0.056	0.000
19	369,5B.3	1.879	0.021	0.121	0.057	0.178	0.029	0.103	0.003	0.855	0.896	0.062	0.000
20	369,5B.4	1.897	0.020	0.103	0.073	0.176	0.024	0.110	0.002	0.848	0.873	0.063	0.001
21	369,5B.5	1.876	0.020	0.124	0.056	0.180	0.028	0.114	0.005	0.870	0.873	0.064	0.000
average	*369.5*	*1.884*	*0.020*	*0.116*	*0.058*	*0.173*	*0.027*	*0.108*	*0.003*	*0.863*	*0.887*	*0.061*	*0.000*
22	369,5B.6	1.911	0.016	0.089	0.068	0.157	0.026	0.077	0.003	0.851	0.908	0.066	0.000
23	369,5B.7	1.894	0.020	0.106	0.047	0.153	0.025	0.094	0.001	0.873	0.912	0.052	0.001
24	369,5B.8	1.906	0.018	0.094	0.072	0.167	0.034	0.080	0.004	0.843	0.893	0.063	0.000
25	369,5B.9	1.894	0.017	0.106	0.062	0.168	0.029	0.098	0.003	0.850	0.901	0.064	0.000
26	369,5B.10	1.903	0.016	0.097	0.058	0.155	0.030	0.074	0.003	0.857	0.920	0.059	0.001
average	*369.5*	*1.901*	*0.017*	*0.099*	*0.061*	*0.160*	*0.029*	*0.085*	*0.003*	*0.855*	*0.907*	*0.061*	*0.000*
27	369,5B.11	1.886	0.016	0.114	0.051	0.164	0.031	0.104	0.003	0.887	0.883	0.050	0.000

28	369,5B.12	1.904	0.016	0.096	0.056	0.153	0.021	0.069	0.003	0.873	0.932	0.047	0.000
29	369,5B.13	1.889	0.019	0.111	0.052	0.163	0.025	0.099	0.002	0.859	0.913	0.057	0.000
30	369,5B.14	1.893	0.019	0.107	0.061	0.169	0.028	0.075	0.004	0.875	0.899	0.055	0.000
31	369,5B.15	1.875	0.023	0.125	0.052	0.176	0.040	0.121	0.005	0.873	0.853	0.055	0.000
average	*369.5*	*1.890*	*0.018*	*0.110*	*0.054*	*0.165*	*0.029*	*0.094*	*0.003*	*0.873*	*0.896*	*0.053*	*0.000*
48	378-A.1	1.851	0.019	0.149	0.066	0.214	0.017	0.108	0.003	0.872	0.906	0.044	0.001
49	378-A.2	1.854	0.021	0.146	0.060	0.207	0.018	0.082	0.003	0.878	0.931	0.040	0.001
50	378-A.3	1.855	0.020	0.145	0.054	0.199	0.019	0.106	0.002	0.871	0.925	0.037	0.000
51	378-A.4	1.850	0.020	0.150	0.055	0.205	0.024	0.096	0.003	0.881	0.918	0.039	0.001
52	378-A.5	1.868	0.015	0.132	0.052	0.184	0.015	0.106	0.004	0.898	0.906	0.041	0.001
average	*378*	*1.856*	*0.019*	*0.144*	*0.057*	*0.202*	*0.019*	*0.100*	*0.003*	*0.880*	*0.917*	*0.040*	*0.001*
53	378-A.6	1.842	0.012	0.158	0.175	0.333	0.005	0.136	0.003	1.102	0.482	0.124	0.001
54	378-A.7	1.823	0.012	0.177	0.181	0.358	0.006	0.135	0.002	1.099	0.480	0.135	0.000
55	378-A.8	1.872	0.009	0.128	0.144	0.272	0.007	0.126	0.004	1.148	0.487	0.106	0.001
56	378-A.9	1.794	0.015	0.206	0.155	0.361	0.008	0.142	0.002	1.113	0.502	0.139	0.001
57	378-A.10	1.788	0.015	0.212	0.178	0.390	0.005	0.149	0.002	1.098	0.485	0.137	0.000
average	*378*	*1.824*	*0.013*	*0.176*	*0.167*	*0.343*	*0.006*	*0.138*	*0.002*	*1.112*	*0.487*	*0.128*	*0.001*
58	378-A.11	1.840	0.017	0.160	0.074	0.234	0.019	0.110	0.003	0.881	0.880	0.063	0.001
59	378-A.12	1.849	0.019	0.151	0.057	0.208	0.020	0.109	0.003	0.871	0.917	0.046	0.000
60	378-A.13	1.850	0.020	0.150	0.061	0.211	0.020	0.126	0.003	0.846	0.920	0.041	0.000
61	378-A.14	1.868	0.016	0.132	0.048	0.181	0.019	0.105	0.004	0.896	0.904	0.044	0.000
62	378-A.15	1.870	0.015	0.130	0.052	0.182	0.018	0.104	0.003	0.877	0.926	0.038	0.000
average	*378*	*1.855*	*0.018*	*0.145*	*0.059*	*0.203*	*0.019*	*0.110*	*0.003*	*0.874*	*0.909*	*0.047*	*0.000*

11 Appendix C

11.1 EDS chemical mapping

11.1.1 Thin section 369.5

Table 27: EDS mapping of Spinel grain in thin section 369.5B with compositions varying between Chromite and Magnetite.

No.	cps/eV	O	C	Mg	Al	Ti	Cr	Fe	Total
232	0.06	25.67	10.23	2.67	8.81	0	20.64	31.75	99.77
233	0.17	20.08		1.61	3.45	2.08	14.45	55.72	97.39
234	0.08	28.54		1.58	3.76	1.87	20.39	70.5	126.64
235	0.05	19		3.08	9.66		19.04	25.52	76.3
236	0.06	15.6	2.64	1	2.76		12.05	38.87	72.92
237	0.02	18.91		1.55	2.65	1.53	12.53	55.44	92.61
238	0.12	21.25		2.02	5.14	1.4	17.58	51.54	98.93
239	0.13	17.2		1	4.14		11.4	53.75	87.49
240	0.16	20.39	2.78	1.54	3.19		11.52	56.54	95.96
241	0.12	19.12		1.6	4.92	1.4	16.12	40.66	83.82
242	0.06	16.73		1.49	3.23		24.86	41.52	87.83
243	0.1	20.74		1.39	2.96		14.76	54.69	94.54
244	0.1	20.42		2.92	9.5		17	36.66	86.5
245	0.1	19.98		1.99	5.93		13.44	43.31	84.65
246	0.17	18.34		1.32	3.79		12.9	52.3	88.65
247	0.11	15.67		1.78	3.03		12.05	43.36	75.89
248	0.04	20.9		1.28	5.52		17.06	50.01	94.77
249	0.03	13.27		2.23	7.91		18.94	39.05	81.4
250	0.12	21.63	2.64	1.37	3.53	1.78	15.24	54.95	101.14
251	0.23	21.26		2.31	3.28		14	47.31	88.16
252	0.1	21.02		1.44	3.55	1.71	14.56	50.37	92.65

11.1.1.1 Mapped Chromite-Magnetite:

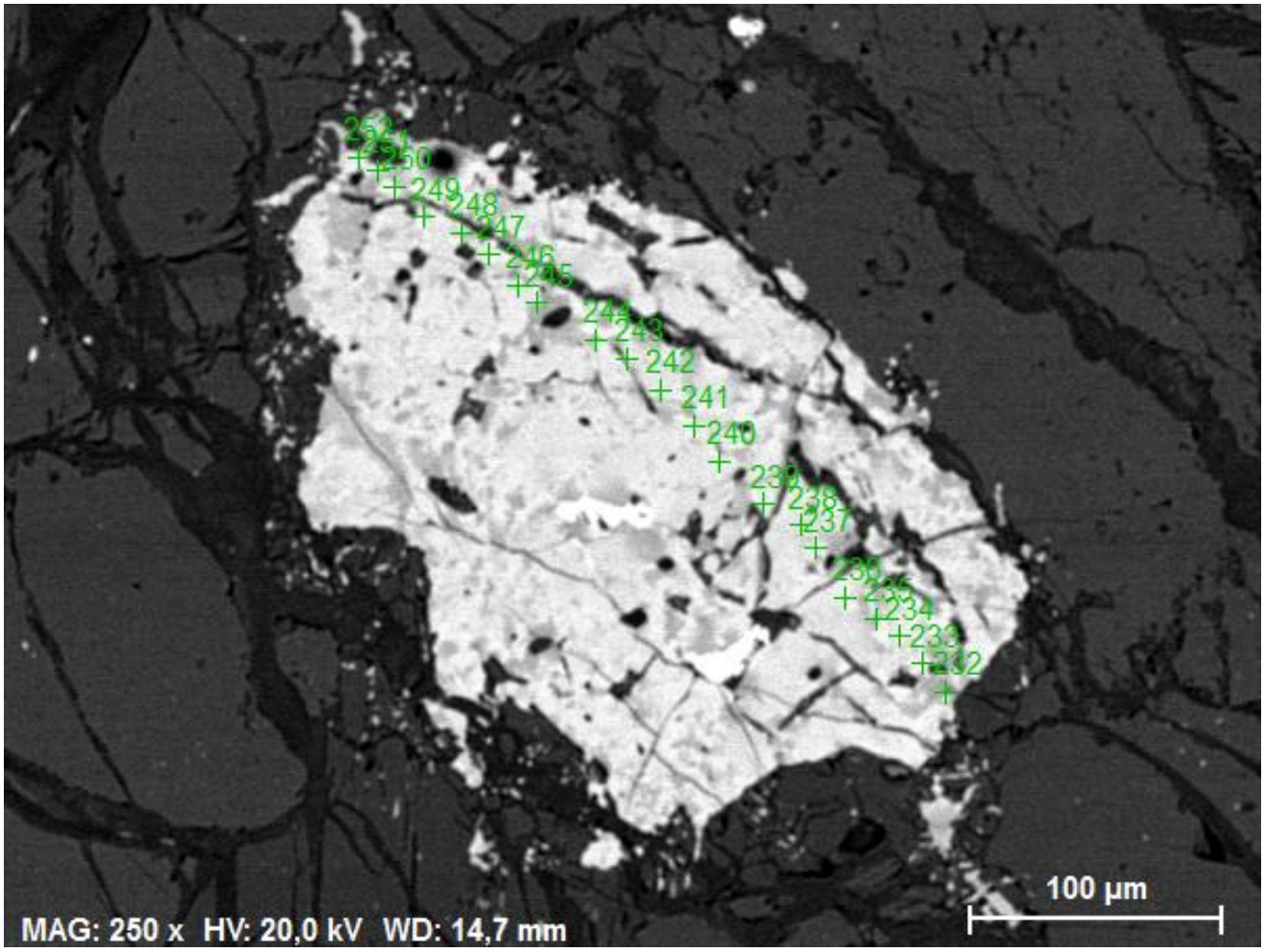

Table 28: EDS mapping of Spinel grain in thin section 369.5B with compositions varying between Hercynite and Magnetite.

No.	cps/eV	O	C	Mg	Al	Ti	Si	Cr	Fe	Total
255	0.12	22.58		3.01	12.46			19.49	25.37	82.91
256	0.09	20.74		1.25	4.33			15.64	50.74	92.7
257	0.13	16.9	2.1	1.07	4			10.79	40.62	75.48
258	0.08	18.58		0.89	4.3			13.6	47.13	84.5
259	0.09	20.44	6.38	1.42	5.83	1.65		16.92	36.48	89.12
260	0.13	19.69		1.24	3.25			12.61	56.75	93.54
261	0.1	28.35		2.88	9.61			20.13	51.96	112.93
262	0.15	22.11		3.83	13.21			19.04	23.49	81.68
263	0.1	15.51		1.31	3.71	1.56		12.75	40.26	75.1
264	0.07	23.64		3.19	12.41			18.08	30.25	87.57
265	0.22	19.99	4.44	2.28	5.89		0.79	11.58	27.23	72.2
266	0.06	16.34		0.75	4.29			14.68	38.69	74.75
267	0.2	26.66		2.12	6.11			17.11	64.17	116.17
268	0.15	20.08		1.4	2.78			11.03	61.5	96.79
269	0.12	23.57		0.84	2.72	1.9		14.32	51.19	94.54

11.1.1.2 Mapped Hercynite-Magnetite:

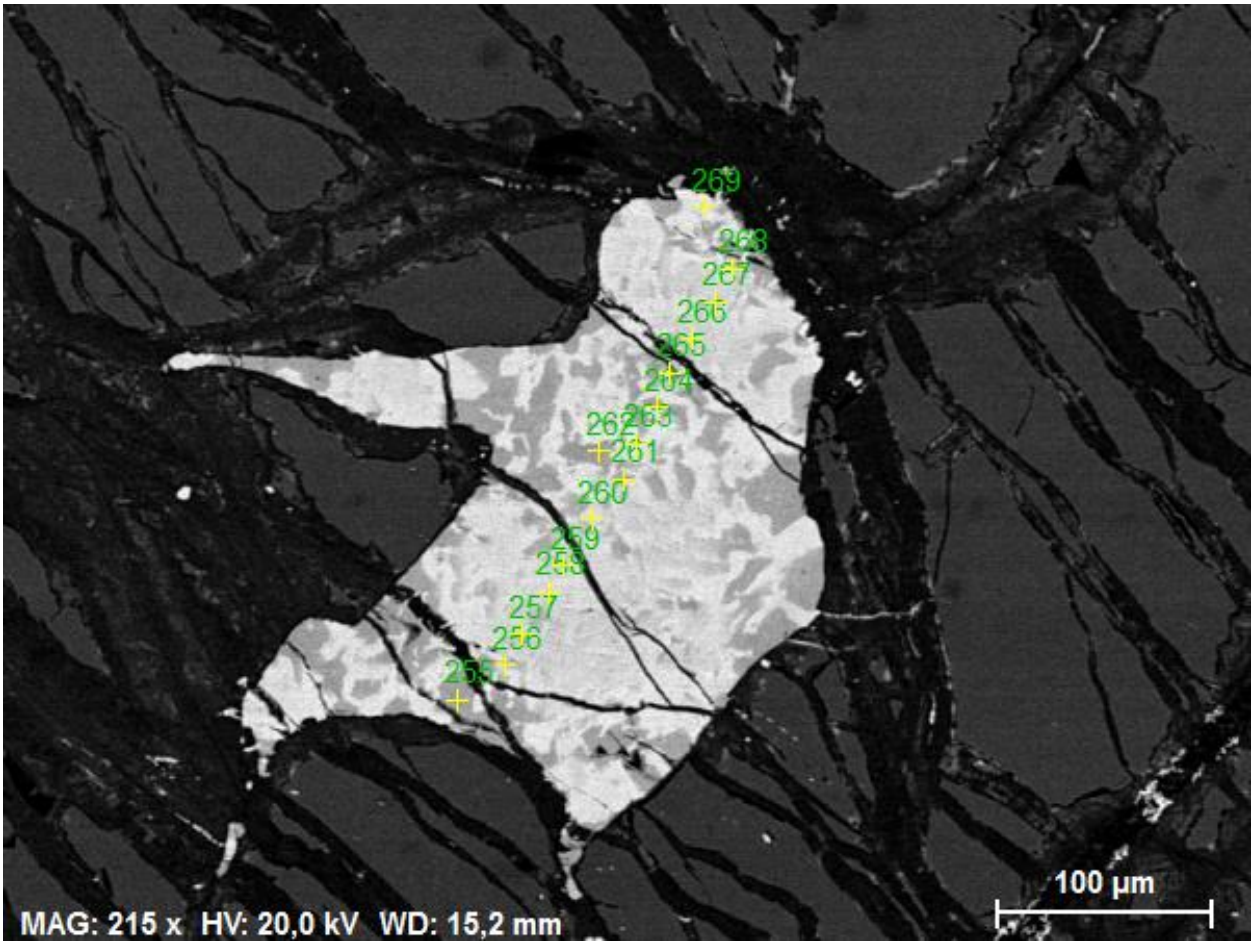

12 Appendix D

12.1 LA-ICP-MS bulk rock chemistry

12.1.1 Dunite

Table 29: Bulk rock chemistry for the upper dunite body in RF4.

			RF4 281-282	**RF4 282-283**	**RF4 283-284**	**RF4 284-285**
		from [m]	281,00	282,00	283,00	284,00
		to [m]	282,00	283,00	284,00	285,00
ME-ICP61	Ag	ppm	0,03	0,03	0,02	0,03
ME-ICP61	Al	%	0,24	0,15	0,15	0,12
ME-ICP61	As	ppm	<0.2	<0.2	<0.2	<0.2
ME-ICP61	Ba	ppm	5	5	10	5
ME-ICP61	Be	ppm	<0.05	<0.05	0,05	<0.05
ME-ICP61	Bi	ppm	0,01	0,06	0,01	0,01
ME-ICP61	Ca	%	1,47	0,81	0,45	0,48
ME-ICP61	Cd	ppm	0,03	0,03	0,02	0,03
ME-MS61	Ce	ppm	0,85	0,55	1,32	0,56
ME-ICP61	Co	ppm	149	158,5	158	160,5
ME-ICP61	Cr	ppm	540	378	266	298
ME-MS61	Cs	ppm	<0.05	<0.05	<0.05	<0.05
ME-ICP61	Cu	ppm	68,4	72,3	49,4	67,4
ME-ICP61	Fe	%	10,75	11,2	11,35	11,65
ME-ICP61	Ga	ppm	0,98	0,7	0,67	0,63
ME-MS61	Ge	ppm	0,09	0,05	0,025	0,05
ME-MS61	Hf	ppm	0,1	0,1	0,1	0,05
ME-MS61	In	ppm	0,012	0,011	0,01	0,01
ME-ICP61	K	%	0,01	0,01	0,03	0,01

ME-ICP61	La	ppm	0,6	0,5	1	0,6
ME-MS61	Li	ppm	1,8	1,7	1,8	1,7
ME-ICP61	Mg	%	21,8	23,5	23,5	23,9
ME-ICP61	Mn	ppm	1360	1420	1420	1440
ME-ICP61	Mo	ppm	0,4	0,37	0,42	0,36
ME-ICP61	Na	%	0,05	0,03	0,03	0,02
ME-MS61	Nb	ppm	0,1	0,1	0,5	0,2
ME-ICP61	Ni	ppm	2180	2420	2450	2520
ME-ICP61	P	ppm	30	40	40	40
ME-ICP61	Pb	ppm	<0.5	<0.5	<0.5	<0.5
ME-MS61	Rb	ppm	0,3	0,3	0,9	0,4
ME-MS61	Re	ppm	0,001	0,001	0,001	0,001
ME-ICP61	S	%	0,04	0,05	0,04	0,05
ME-ICP61	Sb	ppm	<0.05	<0.05	<0.05	<0.05
ME-ICP61	Sc	ppm	10,2	7,6	6	6,2
ME-MS61	Se	ppm	0,5	1	0,5	1
ME-MS61	Sn	ppm	0,10	0,10	0,10	0,10
ME-ICP61	Sr	ppm	5,5	2,9	4,6	2,5
ME-MS61	Ta	ppm	0,025	0,025	0,025	0,025
ME-MS61	Te	ppm	0,025	0,17	0,025	0,025
ME-ICP61	Th	ppm	0,08	0,08	0,16	0,09
ME-ICP61	Ti	%	0,057	0,039	0,027	0,027
ME-ICP61	Tl	ppm	<0.02	<0.02	<0.02	<0.02
ME-ICP61	U	ppm	0,1	0,2	0,2	0,1
ME-ICP61	V	ppm	23	16	10	13
ME-ICP61	W	ppm	0,1	0,1	0,1	0,1
ME-MS61	Y	ppm	1,1	0,7	0,6	0,5
ME-ICP61	Zn	ppm	102	103	105	108
ME-MS61	Zr	ppm	2,9	2	2,3	1,3

PGM-ICP23	Au	ppm	0,00	0,00	0,00	0,00
PGM-ICP23	Pt	ppm	0,0036	0,002	0,0018	0,0019
PGM-ICP23	Pd	ppm	0,003	0,002	0,001	0,001
PGM-MS25NS	Au	ppb	0,5	0,5	0,5	0,5

12.1.2 Wehrlite

Table 30: Bulk rock chemistry for the Wehrlite body in RF4, part 1

			RF4 285-286	**RF4 286-287**	**RF4 287-288**	**RF4 288-289**	**RF4 289-290**	**RF4 290-291**	**RF4 291-292**	**RF4 292-293**	**RF4 293-294**	**RF4 294-295**
		from [m]	285,00	286,00	287,00	288,00	289,00	290,00	291,00	292,00	293,00	294,00
		to [m]	286,00	287,00	288,00	289,00	290,00	291,00	292,00	293,00	294,00	295,00
ME-ICP61	Ag	ppm	0,02	0,03	0,01	0,02	0,01	0,02	0,01	0,02	0,03	0,03
ME-ICP61	Al	%	0,09	0,17	0,3	0,26	0,78	0,17	0,21	0,27	0,28	0,29
ME-ICP61	As	ppm	<0.2	<0.2	<0.2	<0.2	<0.2	<0.2	<0.2	<0.2	<0.2	<0.2
ME-ICP61	Ba	ppm	5	5	5	5	10	5	5	5	5	5
ME-ICP61	Be	ppm	<0.05	<0.05	<0.05	<0.05	0,11	<0.05	<0.05	<0.05	<0.05	<0.05
ME-ICP61	Bi	ppm	0,01	0,01	0,01	0,01	<0.01	0,01	0,01	0,01	0,01	0,01
ME-ICP61	Ca	%	0,51	0,44	0,57	0,64	1,13	0,31	0,57	1,12	0,71	0,66
ME-ICP61	Cd	ppm	0,03	0,03	0,03	0,03	0,04	0,02	0,02	0,03	0,03	0,03
ME-MS61	Ce	ppm	0,27	0,39	1,01	0,56	3,92	0,46	0,41	0,64	0,53	0,68
ME-ICP61	Co	ppm	151,5	155	152	155,5	143	156	150,5	150,5	154,5	155
ME-ICP61	Cr	ppm	358	1680	1900	1640	1250	1520	1740	1930	2840	3280
ME-MS61	Cs	ppm	<0.05	<0.05	<0.05	<0.05	<0.05	<0.05	<0.05	<0.05	<0.05	<0.05
ME-ICP61	Cu	ppm	71,2	70	43,5	61,9	32,3	28,9	38	49,8	69,2	74
ME-ICP61	Fe	%	11,45	11,85	11,8	11,95	11,35	11,2	10,9	11,3	11,8	11,75
ME-ICP61	Ga	ppm	0,53	1,16	1,62	1,44	2,87	1,09	1,35	1,47	1,71	1,89
ME-MS61	Ge	ppm	0,05	0,05	0,05	0,07	0,05	0,05	0,05	0,05	0,05	0,05
ME-MS61	Hf	ppm	0,05	0,05	0,1	0,1	0,4	0,05	0,1	0,1	0,1	0,1
ME-MS61	In	ppm	0,009	0,01	0,01	0,011	0,016	0,008	0,01	0,011	0,012	0,012
ME-ICP61	K	%	0,01	0,01	0,01	0,01	0,06	0,01	0,01	0,01	0,01	0,01
ME-ICP61	La	ppm	<0.5	0,5	0,6	0,5	1,6	0,5	<0.5	0,5	0,5	0,6
ME-MS61	Li	ppm	1,8	1,7	1,8	1,8	2,3	1,7	1,7	1,6	1,6	1,7
ME-ICP61	Mg	%	24,4	24,2	23,5	24,6	22,7	25	24,2	23,9	24,3	24,2
ME-ICP61	Mn	ppm	1470	1460	1440	1500	1410	1430	1370	1420	1460	1460

ME-ICP61	Mo	ppm	0,34	0,32	0,33	0,35	0,34	0,24	0,3	0,31	0,29	0,34
ME-ICP61	Na	%	0,02	0,02	0,05	0,03	0,18	0,02	0,02	0,04	0,03	0,03
ME-MS61	Nb	ppm	<0.1	<0.1	0,7	0,1	2,8	0,2	0,1	0,1	0,1	0,2
ME-ICP61	Ni	ppm	2780	2720	2450	2480	2210	2450	2440	2460	2560	2580
ME-ICP61	P	ppm	20	30	40	30	80	30	30	30	40	50
ME-ICP61	Pb	ppm	<0.5	<0.5	<0.5	<0.5	<0.5	<0.5	<0.5	<0.5	<0.5	<0.5
ME-MS61	Rb	ppm	0,1	0,1	0,2	0,2	0,6	0,2	0,1	0,1	0,1	0,2
ME-MS61	Re	ppm	0,001	0,001	0,001	0,001	0,001	0,001	0,001	0,001	0,001	0,001
ME-ICP61	S	%	0,07	0,06	0,04	0,04	0,05	0,03	0,04	0,04	0,05	0,05
ME-ICP61	Sb	ppm	<0.05	<0.05	<0.05	<0.05	<0.05	<0.05	<0.05	<0.05	<0.05	<0.05
ME-ICP61	Sc	ppm	6	5,8	6,4	7,3	8,9	5,3	6,6	8,8	6,9	6,9
ME-MS61	Se	ppm	1	0,5	0,5	0,5	0,5	0,5	0,5	1	0,5	1
ME-MS61	Sn	ppm	0,10	0,10	0,10	0,10	0,2	0,10	0,10	0,10	0,10	0,10
ME-ICP61	Sr	ppm	1,6	2,3	12,3	2,7	53,5	2,5	2,5	4,3	3,4	4,8
ME-MS61	Ta	ppm	0,025	0,025	0,025	0,025	0,15	0,025	0,025	0,025	0,025	0,025
ME-MS61	Te	ppm	0,025	0,025	0,025	0,025	0,025	0,025	0,025	0,025	0,025	0,025
ME-ICP61	Th	ppm	0,04	0,08	0,05	0,08	0,09	0,06	0,05	0,06	0,05	0,06
ME-ICP61	Ti	%	0,026	0,041	0,091	0,053	0,268	0,034	0,05	0,067	0,07	0,073
ME-ICP61	Tl	ppm	<0.02	<0.02	<0.02	<0.02	<0.02	<0.02	<0.02	<0.02	<0.02	<0.02
ME-ICP61	U	ppm	0,1	0,1	0,1	0,2	0,2	0,2	0,1	0,1	0,1	0,1
ME-ICP61	V	ppm	12	24	33	30	51	20	27	35	39	40
ME-ICP61	W	ppm	<0.1	<0.1	<0.1	<0.1	<0.1	<0.1	<0.1	<0.1	<0.1	<0.1
ME-MS61	Y	ppm	0,4	0,4	0,9	0,7	3	0,3	0,6	1	0,7	0,7
ME-ICP61	Zn	ppm	109	114	117	121	110	113	113	111	118	119
ME-MS61	Zr	ppm	1,3	0,9	3,2	1,9	12,6	1,4	1,7	2,4	1,9	2
PGM-ICP23	Au	ppm	0,00	0,00	0,00	0,00	0,00	0,00	0,00	0,001	0,001	0,00
PGM-ICP23	Pt	ppm	0,0082	0,0102	0,0034	0,0038	0,0009	0,0052	0,0025	0,0277	0,0734	0,0108
PGM-ICP23	Pd	ppm	0,005	0,007	0,002	0,003	0,001	0,002	0,001	0,009	0,036	0,006
PGM-MS25NS	Au	ppb	0,5	0,5	0,5	0,5	0,5	0,5	0,5	1	1	0,5

Table 31: Bulk rock chemistry of the Wehrlite in RF4, part 2

			RF4 295-296	RF4 296-297	RF4 297-298	RF4 298-299	RF4 299-300	RF4 300-301	RF4 301-302	RF4 302-303	RF4 303-304	RF4 304-305
		from [m]	295,00	296,00	297,00	298,00	299,00	300,00	301,00	302,00	303,00	304,00
		to [m]	296,00	297,00	298,00	299,00	300,00	301,00	302,00	303,00	304,00	305,00
ME-ICP61	Ag	ppm	0,03	0,03	0,15	0,08	0,03	0,06	0,02	0,02	0,03	0,02
ME-ICP61	Al	%	0,63	0,27	0,5	0,2	0,26	0,28	0,2	0,23	0,38	2,1
ME-ICP61	As	ppm	<0.2	<0.2	<0.2	<0.2	<0.2	<0.2	<0.2	<0.2	<0.2	<0.2
ME-ICP61	Ba	ppm	5	5	5	5	5	5	5	5	5	50
ME-ICP61	Be	ppm	0,06	<0.05	<0.05	<0.05	<0.05	<0.05	<0.05	<0.05	<0.05	0,31
ME-ICP61	Bi	ppm	0,01	0,01	0,04	0,02	0,02	0,01	0,01	0,01	0,01	0,01
ME-ICP61	Ca	%	2,39	0,97	2,55	0,39	1,12	1,28	0,56	1,12	1,63	3,61
ME-ICP61	Cd	ppm	0,05	0,04	0,07	0,05	0,04	0,04	0,03	0,03	0,03	0,08
ME-MS61	Ce	ppm	1,72	0,57	1,37	0,28	0,46	0,62	0,31	0,51	0,84	14,7
ME-ICP61	Co	ppm	141	152,5	139	156,5	159,5	159	158	155,5	150	121,5
ME-ICP61	Cr	ppm	2440	1810	1220	2140	1910	1400	1780	1210	2260	1580
ME-MS61	Cs	ppm	<0.05	<0.05	<0.05	<0.05	<0.05	<0.05	<0.05	<0.05	<0.05	<0.05
ME-ICP61	Cu	ppm	88,8	81,7	250	197,5	91,7	198	74,1	128	82,9	72
ME-ICP61	Fe	%	11,25	11,3	10	11,3	10,9	11,45	11,45	11,05	11,1	11,05
ME-ICP61	Ga	ppm	2,83	1,49	1,87	1,28	1,37	1,35	1,33	1,14	1,89	8,82
ME-MS61	Ge	ppm	0,06	0,07	0,1	0,11	0,09	0,05	0,025	0,05	0,05	0,08
ME-MS61	Hf	ppm	0,3	0,1	0,2	0,05	0,1	0,1	0,05	0,1	0,1	1,5
ME-MS61	In	ppm	0,023	0,014	0,017	0,011	0,011	0,015	0,009	0,012	0,015	0,047
ME-ICP61	K	%	0,01	0,01	0,01	0,01	0,01	0,01	0,01	0,01	0,01	0,18
ME-ICP61	La	ppm	0,7	0,5	<0.5	<0.5	<0.5	0,5	<0.5	0,5	0,5	4,7
ME-MS61	Li	ppm	1,7	1,6	1,6	1,7	1,7	1,7	1,7	1,7	1,6	1,9
ME-ICP61	Mg	%	21,7	23,5	22,2	24,6	24	23,4	23,9	23,5	22,8	16,65
ME-ICP61	Mn	ppm	1390	1410	1300	1380	1380	1410	1400	1390	1380	1310
ME-ICP61	Mo	ppm	0,29	0,26	0,28	0,22	0,18	0,27	0,29	0,29	0,25	0,38

ME-ICP61	Na	%	0,08	0,04	0,09	0,02	0,04	0,04	0,02	0,04	0,05	0,55
ME-MS61	Nb	ppm	0,2	0,1	0,2	0,1	0,1	0,1	0,1	0,1	0,1	9,5
ME-ICP61	Ni	ppm	2240	2510	2490	2800	2450	2510	2570	2440	2270	1635
ME-ICP61	P	ppm	50	40	50	40	40	40	40	30	30	180
ME-ICP61	Pb	ppm	<0.5	<0.5	0,8	<0.5	<0.5	<0.5	<0.5	<0.5	<0.5	<0.5
ME-MS61	Rb	ppm	0,1	0,1	0,2	0,1	0,1	0,2	0,1	0,1	0,1	1,8
ME-MS61	Re	ppm	0,001	0,001	0,001	0,001	0,001	0,001	0,001	0,001	0,001	0,001
ME-ICP61	S	%	0,07	0,06	0,15	0,12	0,06	0,1	0,05	0,05	0,06	0,16
ME-ICP61	Sb	ppm	<0.05	<0.05	<0.05	<0.05	<0.05	<0.05	<0.05	<0.05	<0.05	<0.05
ME-ICP61	Sc	ppm	15,8	8,4	15,6	5,2	8,1	9,5	6	8,2	11,2	17
ME-MS61	Se	ppm	1	1	1	1	0,5	1	0,5	0,5	1	1
ME-MS61	Sn	ppm	0,2	0,10	0,2	0,10	0,10	0,10	0,10	0,10	0,10	0,7
ME-ICP61	Sr	ppm	10,4	3,6	9,8	1,7	3,9	4,4	2,1	4	5,7	151
ME-MS61	Ta	ppm	0,025	0,025	0,025	0,025	0,025	0,025	0,025	0,025	0,025	0,52
ME-MS61	Te	ppm	0,025	0,025	0,14	0,11	0,08	0,025	0,025	0,025	0,025	0,025
ME-ICP61	Th	ppm	0,05	0,05	0,05	0,07	0,04	0,05	0,04	0,05	0,04	0,24
ME-ICP61	Ti	%	0,198	0,072	0,129	0,044	0,06	0,07	0,052	0,059	0,103	0,946
ME-ICP61	Tl	ppm	<0.02	<0.02	<0.02	<0.02	<0.02	<0.02	<0.02	<0.02	<0.02	<0.02
ME-ICP61	U	ppm	0,1	0,1	<0.1	<0.1	<0.1	0,1	0,1	0,1	0,1	0,2
ME-ICP61	V	ppm	73	35	53	28	33	33	28	27	46	171
ME-ICP61	W	ppm	<0.1	0,1	0,7	<0.1	0,1	<0.1	<0.1	<0.1	<0.1	0,1
ME-MS61	Y	ppm	2,8	1	2,3	0,4	0,8	1,1	0,5	0,9	1,5	9,2
ME-ICP61	Zn	ppm	103	106	93	108	98	101	105	99	100	102
ME-MS61	Zr	ppm	8,2	2,2	5,9	0,9	1,6	2,4	1,2	1,9	3,6	47,2
PGM-ICP23	Au	ppm	0,0005	0,0005	0,0290	0,0330	0,0010	0,0010	0,0005	0,0005	0,0010	0,0005
PGM-ICP23	Pt	ppm	0,0035	0,0216	0,1840	0,0901	0,0571	0,0076	0,0070	0,0881	0,0085	0,0048
PGM-ICP23	Pd	ppm	0,0030	0,0070	0,2130	0,1080	0,0370	0,0060	0,0040	0,0660	0,0050	0,0030
PGM-MS25NS	Au	ppb	0,5	0,5	29	33	1	1	0,5	0,5	1	0,5

Table 32: Bulk rock chemistry for the Wehrlite in RF4, part 3

			RF4 305-306	RF4 306-307	RF4 307-308	RF4 308-309	RF4 309-310	RF4 310-312	RF4 312-314	RF4 314-316
		from [m]	305,00	306,00	307,00	308,00	309,00	310,00	312,00	314,00
		to [m]	306,00	307,00	308,00	309,00	310,00	312,00	314,00	316,00
ME-ICP61	Ag	ppm	0,02	0,03	0,03	0,02	0,04	0,04	0,04	0,04
ME-ICP61	Al	%	2,14	1,69	0,42	0,35	0,19	0,80	1,01	0,09
ME-ICP61	As	ppm	<0.2	<0.2	<0.2	<0.2	0,2	<0.2	<0.2	<0.2
ME-ICP61	Ba	ppm	60	40	10	10	5	10,00	20,00	5,00
ME-ICP61	Be	ppm	0,36	0,29	<0.05	<0.05	<0.05	0,07	0,15	<0.05
ME-ICP61	Bi	ppm	0,01	0,01	0,01	0,02	0,01	0,01	0,02	0,01
ME-ICP61	Ca	%	3,06	2,58	0,93	0,55	0,48	1,98	2,06	0,39
ME-ICP61	Cd	ppm	0,06	0,06	0,03	0,04	0,02	0,04	0,07	0,03
ME-MS61	Ce	ppm	17,9	11,45	1,74	1,49	0,26	3,11	5,44	0,40
ME-ICP61	Co	ppm	124,5	133	155,5	160	156,5	146,00	150,00	168,00
ME-ICP61	Cr	ppm	1200	1250	1340	2420	1650	562,00	490,00	227,00
ME-MS61	Cs	ppm	<0.05	<0.05	<0.05	<0.05	<0.05	<0.05	<0.05	<0.05
ME-ICP61	Cu	ppm	75,7	66,9	67,3	63,1	65,2	71,20	93,50	136,00
ME-ICP61	Fe	%	10,8	11,1	11,25	11,6	11,2	11,15	11,65	11,70
ME-ICP61	Ga	ppm	7,75	6	1,81	1,79	1,11	2,67	3,09	0,48
ME-MS61	Ge	ppm	0,07	0,06	0,09	0,1	0,09	0,025	0,11	0,025
ME-MS61	Hf	ppm	1,5	1,1	0,2	0,1	0,1	0,40	0,50	0,05
ME-MS61	In	ppm	0,04	0,036	0,014	0,012	0,013	0,02	0,02	0,01
ME-ICP61	K	%	0,22	0,15	0,02	0,02	0,01	0,03	0,07	0,01
ME-ICP61	La	ppm	6,7	3,9	0,9	0,7	<0.5	1,20	2,20	<0.5
ME-MS61	Li	ppm	2,8	2,2	1,8	1,9	2,1	1,90	2,10	1,70
ME-ICP61	Mg	%	17,45	19,4	23,1	24,6	23,9	21,20	22,10	24,60
ME-ICP61	Mn	ppm	1320	1350	1380	1420	1410	1400,00	1450,00	1480,00
ME-ICP61	Mo	ppm	0,57	0,37	0,31	0,25	0,21	0,50	0,46	0,47
ME-ICP61	Na	%	0,62	0,47	0,09	0,06	0,02	0,19	0,26	0,02

ME-MS61	Nb	ppm	11,3	8,4	1,1	0,7	0,1	1,40	2,90	0,10
ME-ICP61	Ni	ppm	1665	1940	2460	2550	2660	1980,00	2090,00	2460,00
ME-ICP61	P	ppm	440	130	30	80	50	130,00	190,00	50,00
ME-ICP61	Pb	ppm	0,5	0,7	<0.5	<0.5	<0.5	<0.5	0,80	<0.5
ME-MS61	Rb	ppm	4,9	1,5	0,4	0,5	0,1	0,70	0,90	0,20
ME-MS61	Re	ppm	0,001	0,001	0,001	0,001	0,001	0,001	0,00	0,001
ME-ICP61	S	%	0,13	0,1	0,05	0,03	0,05	0,06	0,09	0,07
ME-ICP61	Sb	ppm	<0.05	<0.05	<0.05	<0.05	<0.05	<0.05	0,05	<0.05
ME-ICP61	Sc	ppm	14	12,3	7,5	5,4	5,2	11,70	11,30	5,60
ME-MS61	Se	ppm	1	1	0,5	1	1	1,00	1,00	1,00
ME-MS61	Sn	ppm	0,6	0,5	0,10	0,10	0,10	0,20	0,30	0,10
ME-ICP61	Sr	ppm	188	142,5	21,6	15,2	1,6	35,00	56,30	2,00
ME-MS61	Ta	ppm	0,64	0,46	0,07	0,025	0,18	0,09	0,18	0,025
ME-MS61	Te	ppm	0,025	0,025	0,025	0,025	0,025	0,025	0,05	0,025
ME-ICP61	Th	ppm	0,57	0,21	0,08	0,08	0,06	0,13	0,16	0,06
ME-ICP61	Ti	%	0,838	0,661	0,142	0,083	0,045	0,18	0,26	0,03
ME-ICP61	Tl	ppm	<0.02	<0.02	<0.02	<0.02	<0.02	<0.02	<0.02	<0.02
ME-ICP61	U	ppm	0,3	0,2	0,1	<0.1	<0.1	0,10	0,10	<0.1
ME-ICP61	V	ppm	127	101	37	34	24	45,00	57,00	12,00
ME-ICP61	W	ppm	0,2	0,1	0,1	0,1	0,1	4,50	6,90	3,80
ME-MS61	Y	ppm	8,7	6,9	1,6	0,8	0,4	3,20	3,70	0,40
ME-ICP61	Zn	ppm	100	100	103	110	103	104,00	108,00	106,00
ME-MS61	Zr	ppm	54,6	37,4	6,6	2,9	0,9	11,20	16,60	1,50
PGM-ICP23	Au	ppm	0,0005	0,0005	0,0005	0,0010	0,0005	0,0005	0,0005	0,0005
PGM-ICP23	Pt	ppm	0,0042	0,0030	0,0044	0,0058	0,0050	0,0025	0,0045	0,0057
PGM-ICP23	Pd	ppm	0,0040	0,0040	0,0040	0,0040	0,0030	0,0020	0,0030	0,0040
PGM-MS25NS	Au	ppb	0,5	0,5	0,5	1	0,5	0,5	0,5	0,5

12.1.3 Dunite

Table 33: Bulk rock chemistry for the lower Dunite in RF4, part 1

			RF4 316-318	RF4 318-320	RF4 320-322	RF4 322-324	RF4 324-326	RF4 326-328	RF4 328-330	RF4 330-332	RF4 332-334	RF4 334-336	RF4 336-338
		from [m]	316,00	318,00	320,00	322,00	324,00	326,00	328,00	330,00	332,00	334,00	336,00
		to [m]	318,00	320,00	322,00	324,00	326,00	328,00	330,00	332,00	334,00	336,00	338,00
ME-ICP61	Ag	ppm	0,07	0,07	0,04	0,05	0,04	0,06	0,04	0,03	0,04	0,04	0,09
ME-ICP61	Al	%	0,36	0,26	0,07	0,25	0,16	0,27	0,40	3,47	0,39	1,75	0,17
ME-ICP61	As	ppm	0,20	<0.2	<0.2	<0.2	0,20	<0.2	<0.2	<0.2	<0.2	0,20	<0.2
ME-ICP61	Ba	ppm	5,00	5,00	5,00	5,00	5,00	5,00	5,00	70,00	5,00	30,00	5,00
ME-ICP61	Be	ppm	<0.05	<0.05	<0.05	<0.05	<0.05	<0.05	<0.05	0,39	<0.05	0,21	<0.05
ME-ICP61	Bi	ppm	0,02	0,02	0,01	0,01	0,01	0,01	0,01	0,01	0,01	0,01	0,01
ME-ICP61	Ca	%	1,71	1,17	0,38	1,50	1,01	1,10	1,74	4,75	1,64	2,86	0,98
ME-ICP61	Cd	ppm	0,05	0,05	0,03	0,04	0,03	0,03	0,04	0,09	0,04	0,06	0,03
ME-MS61	Ce	ppm	0,92	0,57	0,23	0,70	0,49	0,72	0,88	22,90	0,75	11,50	0,62
ME-ICP61	Co	ppm	158,00	161,50	165,00	147,00	155,00	149,00	151,00	103,50	156,00	136,00	162,00
ME-ICP61	Cr	ppm	1210,00	919,00	181,00	554,00	376,00	490,00	1630,00	1310,00	3020,00	615,00	394,00
ME-MS61	Cs	ppm	<0.05	<0.05	<0.05	<0.05	<0.05	<0.05	<0.05	<0.05	<0.05	<0.05	<0.05
ME-ICP61	Cu	ppm	223,00	190,00	113,00	121,00	102,50	92,80	101,50	96,20	121,50	107,00	118,50
ME-ICP61	Fe	%	11,60	11,70	12,10	11,35	11,70	11,85	11,55	10,35	11,50	11,15	11,50
ME-ICP61	Ga	ppm	1,70	1,28	0,39	1,08	0,73	1,04	1,83	11,15	2,18	5,81	0,75
ME-MS61	Ge	ppm	0,05	0,05	0,025	0,025	0,025	0,05	0,025	0,07	0,025	0,06	0,08
ME-MS61	Hf	ppm	0,20	0,10	0,05	0,10	0,10	0,10	0,20	1,50	0,10	0,70	0,10
ME-MS61	In	ppm	0,02	0,02	0,01	0,02	0,01	0,01	0,02	0,05	0,01	0,03	0,01
ME-ICP61	K	%	0,01	0,01	0,01	0,01	0,01	0,01	0,01	0,21	0,01	0,09	0,01
ME-ICP61	La	ppm	<0.5	<0.5	<0.5	<0.5	<0.5	<0.5	<0.5	9,30	<0.5	4,10	<0.5
ME-MS61	Li	ppm	1,80	1,70	1,70	1,70	1,70	1,90	1,70	2,30	1,70	2,10	1,70
ME-ICP61	Mg	%	22,30	23,00	24,20	22,40	22,60	22,70	22,20	13,35	21,40	18,00	22,20
ME-ICP61	Mn	ppm	1470,00	1470,00	1480,00	1460,00	1450,00	1450,00	1460,00	1380,00	1440,00	1410,00	1420,00

ME-ICP61	Mo	ppm	0,46	0,43	0,48	0,49	0,51	0,69	0,42	0,54	0,46	0,58	0,62
ME-ICP61	Na	%	0,06	0,04	0,02	0,05	0,04	0,06	0,07	0,89	0,05	0,43	0,04
ME-MS61	Nb	ppm	0,10	0,10	0,10	0,10	0,10	0,30	0,30	13,10	0,10	7,00	0,20
ME-ICP61	Ni	ppm	2230,00	2300,00	2480,00	2440,00	2490,00	2400,00	2200,00	1120,00	2060,00	1670,00	2060,00
ME-ICP61	P	ppm	50,00	50,00	50,00	50,00	40,00	50,00	50,00	680,00	40,00	400,00	40,00
ME-ICP61	Pb	ppm	<0.5	<0.5	<0.5	<0.5	<0.5	<0.5	<0.5	<0.5	<0.5	<0.5	<0.5
ME-MS61	Rb	ppm	0,10	0,10	0,10	0,10	0,10	0,20	0,20	1,80	0,10	0,80	0,20
ME-MS61	Re	ppm	0,001	0,00	0,001	0,001	0,001	0,001	0,001	0,00	0,00	0,001	0,001
ME-ICP61	S	%	0,14	0,12	0,08	0,08	0,07	0,07	0,07	0,15	0,07	0,12	0,08
ME-ICP61	Sb	ppm	<0.05	<0.05	<0.05	<0.05	<0.05	<0.05	<0.05	<0.05	<0.05	<0.05	<0.05
ME-ICP61	Sc	ppm	11,70	9,60	5,70	11,00	8,70	9,00	11,90	24,90	11,80	16,20	8,30
ME-MS61	Se	ppm	1,00	1,00	1,00	1,00	1,00	1,00	1,00	1,00	1,00	1,00	1,00
ME-MS61	Sn	ppm	0,10	0,10	0,10	0,10	0,10	0,10	0,10	0,80	0,10	0,40	0,10
ME-ICP61	Sr	ppm	7,80	4,20	1,30	5,30	3,70	11,20	11,30	234,00	5,60	133,50	5,20
ME-MS61	Ta	ppm	0,025	0,025	0,025	0,025	0,025	0,025	0,025	0,75	0,025	0,45	0,025
ME-MS61	Te	ppm	0,06	0,025	0,05	0,025	0,025	0,025	0,025	0,025	0,025	0,025	0,025
ME-ICP61	Th	ppm	0,05	0,05	0,06	0,05	0,05	0,04	0,06	0,30	0,06	0,15	0,06
ME-ICP61	Ti	%	0,09	0,06	0,02	0,07	0,04	0,08	0,12	0,80	0,09	0,50	0,04
ME-ICP61	Tl	ppm	<0.02	<0.02	<0.02	<0.02	<0.02	<0.02	<0.02	<0.02	<0.02	<0.02	<0.02
ME-ICP61	U	ppm	<0.1	<0.1	<0.1	<0.1	<0.1	<0.1	<0.1	0,10	<0.1	0,10	<0.1
ME-ICP61	V	ppm	42,00	32,00	11,00	30,00	21,00	25,00	46,00	155,00	52,00	94,00	18,00
ME-ICP61	W	ppm	3,90	4,10	4,10	4,00	3,90	5,30	4,20	5,30	3,40	4,10	3,00
ME-MS61	Y	ppm	1,70	1,10	0,30	1,30	0,80	1,10	1,80	14,00	1,40	7,20	0,80
ME-ICP61	Zn	ppm	103,00	103,00	106,00	101,00	102,00	105,00	107,00	109,00	109,00	107,00	102,00
ME-MS61	Zr	ppm	3,90	2,40	0,80	3,00	1,90	3,10	3,90	43,90	3,10	17,50	2,20
PGM-ICP23	Au	ppm	0,0020	0,0030	0,0005	0,0020	0,0020	0,0005	0,0010	0,0005	0,0010	0,0005	0,0005
PGM-ICP23	Pt	ppm	0,0085	0,0094	0,0061	0,0154	0,0131	0,0070	0,0085	0,0042	0,0050	0,0050	0,0107
PGM-ICP23	Pd	ppm	0,0080	0,0100	0,0060	0,0160	0,0110	0,0090	0,0100	0,0040	0,0030	0,0030	0,0050
PGM-MS25NS	Au	ppb	2	3	0,5	2	2	0,5	1	0,5	1	0,5	0,5

Table 34: Bulk rock chemistry of the lower Dunite in RF4, part 2

			RF4 339-338	RF4 339-340	RF4 340-341	RF4 342-341	RF4 342-343	RF4 344-343	RF4 345-344	RF4 346-345	RF4 347-346	RF4 348-347	RF4 349-348	RF4 350-349
		from [m]	338,00	339,00	340,00	341,00	342,00	343,00	344,00	345,00	346,00	347,00	348,00	349,00
		to [m]	339,00	340,00	341,00	342,00	343,00	344,00	345,00	346,00	347,00	348,00	349,00	350,00
ME-ICP61	Ag	ppm	0,06	0,06	0,07	0,07	0,09	0,10	0,08	0,14	0,30	0,31	0,25	0,24
ME-ICP61	Al	%	0,20	0,28	0,21	0,38	1,25	0,29	0,19	0,43	0,31	0,32	0,21	0,20
ME-ICP61	As	ppm	<0.2	<0.2	<0.2	<0.2	<0.2	<0.2	<0.2	<0.2	<0.2	<0.2	<0.2	0,20
ME-ICP61	Ba	ppm	5,00	5,00	5,00	5,00	30,00	5,00	5,00	5,00	5,00	5,00	5,00	5,00
ME-ICP61	Be	ppm	<0.05	<0.05	<0.05	<0.05	0,15	<0.05	<0.05	<0.05	<0.05	<0.05	<0.05	<0.05
ME-ICP61	Bi	ppm	0,01	0,01	0,02	0,02	0,03	0,03	0,02	0,03	0,05	0,05	0,04	0,05
ME-ICP61	Ca	%	1,24	1,37	1,40	2,16	2,64	1,55	1,02	2,05	1,81	1,64	1,05	0,87
ME-ICP61	Cd	ppm	0,04	0,04	0,05	0,05	0,06	0,05	0,03	0,06	0,11	0,12	0,09	0,09
ME-MS61	Ce	ppm	0,65	0,86	0,80	1,06	8,77	0,74	0,82	1,25	0,84	1,01	0,59	0,61
ME-ICP61	Co	ppm	159,00	159,50	160,50	145,50	142,50	152,00	149,50	150,50	170,50	174,50	179,00	185,00
ME-ICP61	Cr	ppm	555,00	578,00	635,00	1340,00	738,00	1250,00	510,00	1090,00	796,00	631,00	654,00	733,00
ME-MS61	Cs	ppm	<0.05	<0.05	<0.05	<0.05	<0.05	<0.05	<0.05	<0.05	<0.05	<0.05	<0.05	<0.05
ME-ICP61	Cu	ppm	136,50	113,00	163,50	203,00	227,00	309,00	251,00	411,00	803,00	898,00	714,00	700,00
ME-ICP61	Fe	%	11,35	10,95	10,80	10,15	10,30	10,20	10,10	10,60	11,95	12,40	12,80	13,10
ME-ICP61	Ga	ppm	0,94	1,12	1,01	1,77	4,46	1,46	0,88	1,87	1,37	1,42	1,02	1,11
ME-MS61	Ge	ppm	0,025	0,025	0,025	0,025	0,025	0,025	0,025	0,025	0,025	0,05	0,05	0,05
ME-MS61	Hf	ppm	0,10	0,10	0,10	0,20	0,40	0,10	0,10	0,20	0,10	0,20	0,10	0,10
ME-MS61	In	ppm	0,01	0,01	0,01	0,02	0,03	0,02	0,01	0,02	0,02	0,02	0,02	0,02
ME-ICP61	K	%	0,01	0,01	0,01	0,01	0,09	0,01	0,01	0,01	0,01	0,01	0,01	0,01
ME-ICP61	La	ppm	<0.5	<0.5	<0.5	<0.5	3,60	<0.5	<0.5	<0.5	<0.5	<0.5	<0.5	<0.5
ME-MS61	Li	ppm	1,60	2,10	1,40	1,60	4,70	1,10	1,10	1,10	1,40	1,50	1,70	1,70
ME-ICP61	Mg	%	22,50	22,40	22,50	20,20	18,80	20,50	20,60	19,00	20,30	20,40	21,60	22,00
ME-ICP61	Mn	ppm	1410,00	1310,00	1320,00	1280,00	1330,00	1260,00	1260,00	1340,00	1440,00	1470,00	1510,00	1560,00
ME-ICP61	Mo	ppm	0,88	0,42	0,38	0,45	0,48	0,35	0,44	0,41	0,43	0,47	0,42	0,51

ME-ICP61	Na	%	0,04	0,06	0,05	0,07	0,28	0,05	0,04	0,06	0,05	0,06	0,04	0,04
ME-MS61	Nb	ppm	0,10	0,30	0,10	0,10	4,50	0,10	0,20	0,20	0,10	0,20	0,10	0,10
ME-ICP61	Ni	ppm	2180,00	2230,00	2290,00	2080,00	1960,00	2220,00	2140,00	1950,00	2470,00	2620,00	2610,00	2650,00
ME-ICP61	P	ppm	60,00	50,00	40,00	60,00	310,00	40,00	60,00	60,00	40,00	60,00	70,00	60,00
ME-ICP61	Pb	ppm	<0.5	0,50	0,50	<0.5	0,50	<0.5	0,50	0,50	0,80	0,70	0,50	<0.5
ME-MS61	Rb	ppm	0,10	0,20	0,20	0,30	1,60	0,20	0,20	0,40	0,20	0,20	0,10	0,20
ME-MS61	Re	ppm	0,001	0,001	0,001	0,001	0,00	0,00	0,00	0,00	0,00	0,00	0,00	0,00
ME-ICP61	S	%	0,09	0,09	0,11	0,13	0,16	0,18	0,21	0,33	0,43	0,50	0,37	0,37
ME-ICP61	Sb	ppm	<0.05	0,05	<0.05	<0.05	<0.05	<0.05	0,05	<0.05	0,05	<0.05	<0.05	<0.05
ME-ICP61	Sc	ppm	8,70	9,10	9,00	13,00	12,50	9,60	8,00	14,30	12,60	11,80	9,10	8,10
ME-MS61	Se	ppm	1,00	1,00	1,00	1,00	1,00	1,00	1,00	1,00	2,00	2,00	2,00	2,00
ME-MS61	Sn	ppm	0,10	0,10	0,10	0,10	0,30	0,10	0,10	0,20	0,20	0,20	0,20	0,20
ME-ICP61	Sr	ppm	5,00	14,40	6,80	11,30	103,50	7,40	5,50	8,00	8,30	7,90	4,50	3,70
ME-MS61	Ta	ppm	0,025	0,025	0,025	0,025	0,30	0,025	0,025	0,025	0,025	0,025	0,025	0,025
ME-MS61	Te	ppm	0,025	0,025	0,025	0,05	0,05	0,05	0,07	0,09	0,18	0,21	0,14	0,16
ME-ICP61	Th	ppm	0,10	0,08	0,10	0,09	0,27	0,06	0,10	0,11	0,06	0,06	0,04	0,09
ME-ICP61	Ti	%	0,05	0,09	0,06	0,10	0,32	0,08	0,05	0,12	0,08	0,09	0,06	0,06
ME-ICP61	Tl	ppm	<0.02	<0.02	<0.02	<0.02	<0.02	<0.02	<0.02	<0.02	<0.02	<0.02	<0.02	<0.02
ME-ICP61	U	ppm	<0.1	<0.1	<0.1	0,10	0,10	<0.1	<0.1	0,10	<0.1	<0.1	<0.1	<0.1
ME-ICP61	V	ppm	25,00	27,00	25,00	46,00	67,00	37,00	22,00	50,00	38,00	39,00	29,00	29,00
ME-ICP61	W	ppm	2,70	3,00	2,70	2,20	1,80	1,00	0,70	0,90	1,60	1,60	2,40	2,40
ME-MS61	Y	ppm	1,10	1,40	1,20	1,90	5,30	1,40	1,10	2,20	1,60	1,70	1,00	0,90
ME-ICP61	Zn	ppm	102,00	104,00	106,00	92,00	94,00	94,00	92,00	99,00	108,00	107,00	113,00	119,00
ME-MS61	Zr	ppm	2,30	3,30	2,40	3,50	11,10	2,50	1,70	4,50	3,50	4,10	2,30	2,00
PGM-ICP23	Au	ppm	0,0010	0,0005	0,0010	0,0010	0,0010	0,0030	0,0010	0,0050	0,0200	0,0110	0,0080	0,0090
PGM-ICP23	Pt	ppm	0,0067	0,0060	0,0064	0,0083	0,0155	0,0207	0,0214	0,0116	0,0195	0,0223	0,0157	0,0141
PGM-ICP23	Pd	ppm	0,0070	0,0070	0,0060	0,0070	0,0140	0,0210	0,0280	0,0130	0,0220	0,0260	0,0180	0,0150
PGM-MS25NS	Au	ppb	1	0,5	1	1	1	3	1	5	20	11	8	9

12.1.4 Olivine clinopyroxenite

Table 35: Bulk rock chemistry from the Olivine Clinopyroxenite in RF4, part 1

			RF4 351-350	**RF4 352-351**	**RF4 353-352**	**RF4 354-353**	**RF4 355-354**	**RF4 356-355**	**RF4 357-356**	**RF4 359-357**	**RF4 361-359**	**RF4 363-361**	**RF4 365-363**	**RF4 367-365**
		from [m]	350,00	351,00	352,00	353,00	354,00	355,00	356,00	357,00	359,00	361,00	363,00	365,00
		to [m]	351,00	352,00	353,00	354,00	355,00	356,00	357,00	359,00	361,00	363,00	365,00	367,00
ME-ICP61	Ag	ppm	0,20	0,15	0,09	0,09	0,07	0,10	0,04	0,10	0,11	0,11	0,09	0,08
ME-ICP61	Al	%	0,28	1,18	1,76	1,60	1,54	0,95	4,87	1,73	1,17	1,51	2,59	0,88
ME-ICP61	As	ppm	<0.2	0,80	0,40	<0.2	0,40	0,60	0,30	<0.2	0,20	0,60	0,70	0,30
ME-ICP61	Ba	ppm	5,00	10,00	5,00	5,00	5,00	5,00	90,00	10,00	5,00	5,00	40,00	5,00
ME-ICP61	Be	ppm	<0.05	0,05	0,05	<0.05	0,05	<0.05	0,51	0,07	<0.05	0,05	0,30	<0.05
ME-ICP61	Bi	ppm	0,04	0,04	0,04	0,03	0,03	0,03	0,02	0,03	0,03	0,02	0,02	0,02
ME-ICP61	Ca	%	1,40	6,56	12,15	11,55	11,80	6,47	7,42	11,40	7,84	9,39	5,49	5,94
ME-ICP61	Cd	ppm	0,08	0,12	0,13	0,13	0,12	0,10	0,11	0,13	0,10	0,10	0,11	0,10
ME-MS61	Ce	ppm	0,99	3,45	5,39	4,23	5,06	3,15	29,60	6,73	3,26	4,34	17,10	2,25
ME-ICP61	Co	ppm	178,50	119,00	57,80	62,70	61,20	115,50	68,00	65,30	107,00	88,60	112,50	126,00
ME-ICP61	Cr	ppm	640,00	777,00	888,00	1030,00	888,00	744,00	702,00	816,00	1320,00	1340,00	889,00	1070,00
ME-MS61	Cs	ppm	<0.05	<0.05	<0.05	<0.05	<0.05	<0.05	<0.05	<0.05	<0.05	<0.05	<0.05	<0.05
ME-ICP61	Cu	ppm	677,00	447,00	263,00	252,00	172,00	286,00	146,00	264,00	311,00	273,00	184,00	233,00
ME-ICP61	Fe	%	13,70	9,78	5,62	5,94	5,59	9,38	8,85	5,83	8,33	7,66	10,75	10,05
ME-ICP61	Ga	ppm	1,37	4,49	6,72	6,06	5,88	3,70	14,80	6,20	4,40	5,73	9,16	3,47
ME-MS61	Ge	ppm	0,18	0,15	0,11	0,11	0,11	0,14	0,07	0,10	0,14	0,14	0,18	0,15
ME-MS61	Hf	ppm	0,10	0,60	0,90	0,80	0,80	0,50	1,80	0,90	0,60	0,80	1,10	0,40
ME-MS61	In	ppm	0,02	0,03	0,06	0,05	0,05	0,04	0,07	0,05	0,04	0,06	0,05	0,03
ME-ICP61	K	%	0,01	0,01	0,01	0,01	0,01	0,02	0,24	0,02	0,01	0,01	0,12	0,01
ME-ICP61	La	ppm	<0.5	0,90	1,30	1,00	1,20	0,90	11,80	1,90	0,80	1,10	6,00	0,60
ME-MS61	Li	ppm	1,90	1,70	1,20	1,10	1,20	1,70	1,60	1,50	1,30	1,40	1,80	1,50
ME-ICP61	Mg	%	22,10	15,80	10,45	11,05	10,95	16,15	8,04	11,20	15,75	13,50	14,20	17,10
ME-ICP61	Mn	ppm	1580,00	1300,00	983,00	1020,00	953,00	1220,00	1280,00	959,00	1160,00	1140,00	1360,00	1300,00

ME-ICP61	Mo	ppm	0,24	0,26	0,22	0,24	0,32	0,38	0,72	0,38	0,28	0,34	0,47	0,67
ME-ICP61	Na	%	0,05	0,20	0,28	0,25	0,26	0,17	1,27	0,32	0,18	0,25	0,61	0,14
ME-MS61	Nb	ppm	0,20	0,90	0,30	0,20	0,10	0,50	19,60	1,50	0,20	0,60	10,80	0,20
ME-ICP61	Ni	ppm	2460,00	1390,00	462,00	474,00	353,00	1140,00	401,00	493,00	1100,00	819,00	879,00	1040,00
ME-ICP61	P	ppm	70,00	60,00	40,00	30,00	40,00	60,00	960,00	80,00	50,00	40,00	530,00	10,00
ME-ICP61	Pb	ppm	0,70	0,60	0,70	0,50	0,80	0,60	0,70	0,70	0,80	0,60	0,70	0,70
ME-MS61	Rb	ppm	0,20	0,20	0,30	0,30	0,30	0,40	1,50	0,40	0,20	0,40	0,90	0,10
ME-MS61	Re	ppm	0,00	0,00	0,00	0,001	0,00	0,00	0,00	0,00	0,00	0,00	0,00	0,00
ME-ICP61	S	%	0,41	0,32	0,25	0,21	0,18	0,18	0,24	0,21	0,20	0,19	0,20	0,20
ME-ICP61	Sb	ppm	0,06	<0.05	0,05	<0.05	0,05	0,07	<0.05	0,06	0,05	0,06	<0.05	0,05
ME-ICP61	Sc	ppm	11,20	37,50	67,30	64,40	66,80	38,00	34,00	66,40	45,90	55,50	29,90	37,70
ME-MS61	Se	ppm	2,00	2,00	2,00	1,00	2,00	1,00	1,00	1,00	1,00	2,00	1,00	1,00
ME-MS61	Sn	ppm	0,20	0,30	0,40	0,40	0,30	0,30	1,00	0,40	0,30	0,30	0,80	0,20
ME-ICP61	Sr	ppm	6,50	50,10	46,50	40,90	45,30	27,70	356,00	67,00	27,50	42,90	177,00	20,20
ME-MS61	Ta	ppm	0,025	0,06	0,025	0,025	0,025	0,025	1,07	0,10	0,025	0,05	0,64	0,025
ME-MS61	Te	ppm	0,18	0,12	0,06	0,05	0,025	0,08	0,025	0,05	0,06	0,06	0,06	0,05
ME-ICP61	Th	ppm	0,08	0,03	0,04	0,03	0,11	0,05	0,26	0,09	0,06	0,06	0,19	0,04
ME-ICP61	Ti	%	0,08	0,36	0,51	0,44	0,47	0,26	1,26	0,49	0,32	0,43	0,77	0,23
ME-ICP61	Tl	ppm	<0.02	<0.02	<0.02	<0.02	<0.02	<0.02	<0.02	<0.02	<0.02	<0.02	<0.02	<0.02
ME-ICP61	U	ppm	<0.1	<0.1	<0.1	<0.1	0,10	<0.1	0,10	<0.1	<0.1	<0.1	0,10	<0.1
ME-ICP61	V	ppm	35,00	124,00	215,00	200,00	192,00	111,00	232,00	183,00	138,00	169,00	155,00	102,00
ME-ICP61	W	ppm	5,70	4,90	7,00	8,60	6,00	5,80	12,60	8,40	5,70	7,80	9,80	3,90
ME-MS61	Y	ppm	1,50	6,30	10,60	9,10	9,20	5,40	18,30	9,40	6,60	8,40	11,90	4,90
ME-ICP61	Zn	ppm	116,00	77,00	37,00	40,00	38,00	76,00	98,00	43,00	62,00	59,00	100,00	80,00
ME-MS61	Zr	ppm	3,20	14,30	20,70	16,40	18,20	9,90	35,60	20,20	12,70	17,20	22,10	9,30
PGM-ICP23	Au	ppm	0,0080	0,0040	0,0005	0,0005	0,0005	0,0010	0,0005	0,0010	0,0020	0,0010	0,0010	0,0010
PGM-ICP23	Pt	ppm	0,0177	0,0094	0,0011	0,0003	0,0006	0,0033	0,0019	0,0032	0,0040	0,0027	0,0025	0,0025
PGM-ICP23	Pd	ppm	0,0210	0,0110	0,0020	0,0010	0,0010	0,0050	0,0020	0,0040	0,0040	0,0030	0,0030	0,0030
PGM-MS25NS	Au	ppb	8	4	0,5	0,5	0,5	1	0,5	1	2	1	1	1

Table 36: Bulk rock chemistry for the Olivine Clinopyroxenite unit in RF4, part 2

			RF4 369-367	RF4 371-369	RF4 373-371	RF4 375-373	RF4 377-375	RF4 379-377	RF4 381-379	RF4 383-381	RF4 385-383	RF4 385-387	RF4 387-389	RF4 389-391
		from [m]	367,00	369,00	371,00	373,00	375,00	377,00	379,00	381,00	383,00	385,00	387,00	389,00
		to [m]	369,00	371,00	373,00	375,00	377,00	379,00	381,00	383,00	385,00	387,00	389,00	391,00
ME-ICP61	Ag	ppm	0,11	0,11	0,06	0,21	0,10	0,13	0,06	0,05	0,14	0,18	0,11	0,09
ME-ICP61	Al	%	1,77	0,97	0,22	1,00	1,92	0,76	0,34	1,25	0,36	1,34	1,70	1,76
ME-ICP61	As	ppm	<0.2	<0.2	<0.2	0,50	0,80	0,30	0,30	0,20	<0.2	1,10	0,20	<0.2
ME-ICP61	Ba	ppm	20,00	5,00	5,00	10,00	20,00	5,00	5,00	10,00	5,00	5,00	10,00	5,00
ME-ICP61	Be	ppm	0,15	0,05	<0.05	0,07	0,13	<0.05	<0.05	0,08	<0.05	0,05	0,07	<0.05
ME-ICP61	Bi	ppm	0,02	0,03	0,01	0,03	0,02	0,02	0,02	0,01	0,03	0,04	0,03	0,03
ME-ICP61	Ca	%	7,58	6,76	0,75	6,14	8,54	5,02	1,28	2,83	1,94	7,35	8,73	11,05
ME-ICP61	Cd	ppm	0,11	0,09	0,04	0,12	0,12	0,09	0,04	0,05	0,07	0,13	0,12	0,14
ME-MS61	Ce	ppm	8,91	3,86	1,10	4,12	8,43	2,31	0,78	3,02	0,91	3,88	4,45	4,75
ME-ICP61	Co	ppm	112,00	115,50	165,50	116,00	95,80	123,50	157,50	139,00	155,50	113,00	94,10	72,50
ME-ICP61	Cr	ppm	856,00	1150,00	800,00	1640,00	1310,00	964,00	715,00	879,00	1110,00	1320,00	1560,00	1250,00
ME-MS61	Cs	ppm	<0.05	<0.05	<0.05	<0.05	<0.05	<0.05	<0.05	<0.05	<0.05	<0.05	<0.05	<0.05
ME-ICP61	Cu	ppm	234,00	274,00	132,50	575,00	278,00	275,00	111,50	149,50	373,00	497,00	341,00	283,00
ME-ICP61	Fe	%	8,56	8,42	11,40	8,78	8,35	9,11	11,20	10,70	11,25	9,09	7,51	6,02
ME-ICP61	Ga	ppm	6,43	3,91	1,29	4,04	6,82	3,25	1,56	4,61	1,85	5,19	5,48	6,18
ME-MS61	Ge	ppm	0,14	0,14	0,18	0,15	0,15	0,14	0,17	0,16	0,17	0,17	0,025	0,025
ME-MS61	Hf	ppm	1,00	0,50	0,10	0,60	1,00	0,40	0,10	0,60	0,20	0,60	0,80	0,90
ME-MS61	In	ppm	0,04	0,03	0,02	0,04	0,06	0,04	0,02	0,03	0,02	0,05	0,04	0,05
ME-ICP61	K	%	0,07	0,01	0,02	0,02	0,07	0,01	0,01	0,01	0,01	0,01	0,02	0,01
ME-ICP61	La	ppm	3,10	1,20	0,50	1,40	2,90	0,60	<0.5	0,80	<0.5	1,10	1,30	1,20
ME-MS61	Li	ppm	1,80	1,60	1,90	1,90	1,50	1,50	1,80	1,90	1,70	2,10	1,70	1,30
ME-ICP61	Mg	%	14,85	17,00	24,40	17,15	13,50	18,25	23,40	19,70	21,60	14,95	13,40	11,20
ME-ICP61	Mn	ppm	1140,00	1140,00	1370,00	1210,00	1200,00	1220,00	1360,00	1350,00	1380,00	1200,00	1110,00	1010,00
ME-ICP61	Mo	ppm	0,36	0,30	0,26	0,35	0,42	0,23	0,24	0,32	0,24	0,38	0,40	0,41

ME-ICP61	Na	%	0,36	0,19	0,05	0,20	0,38	0,13	0,05	0,21	0,06	0,23	0,29	0,29
ME-MS61	Nb	ppm	3,40	0,80	0,40	0,70	2,80	0,20	0,20	1,30	0,10	0,30	0,40	0,20
ME-ICP61	Ni	ppm	796,00	1170,00	2140,00	1600,00	916,00	1510,00	2040,00	1640,00	2090,00	1400,00	953,00	577,00
ME-ICP61	P	ppm	210,00	90,00	70,00	80,00	190,00	40,00	60,00	110,00	60,00	60,00	40,00	10,00
ME-ICP61	Pb	ppm	0,90	0,70	<0.5	0,90	0,90	0,60	<0.5	0,80	0,90	1,00	0,80	0,70
ME-MS61	Rb	ppm	1,00	0,40	0,50	0,90	1,10	0,20	0,10	0,20	0,10	0,70	0,70	0,30
ME-MS61	Re	ppm	0,00	0,00	0,00	0,00	0,00	0,00	0,00	0,00	0,00	0,00	0,00	0,00
ME-ICP61	S	%	0,20	0,17	0,09	0,27	0,22	0,17	0,07	0,12	0,17	0,32	0,25	0,25
ME-ICP61	Sb	ppm	0,05	0,05	<0.05	0,05	0,06	<0.05	<0.05	0,05	0,05	0,05	0,06	<0.05
ME-ICP61	Sc	ppm	48,60	42,10	7,70	34,90	50,50	33,60	11,00	18,30	13,70	45,30	48,60	65,50
ME-MS61	Se	ppm	1,00	1,00	1,00	2,00	1,00	1,00	1,00	1,00	1,00	2,00	1,00	1,00
ME-MS61	Sn	ppm	0,50	0,20	0,10	0,30	0,40	0,20	0,10	0,30	0,10	0,40	0,30	0,40
ME-ICP61	Sr	ppm	80,00	32,70	6,60	27,70	73,60	18,60	8,90	65,00	7,20	46,10	68,30	45,40
ME-MS61	Ta	ppm	0,21	0,06	0,025	0,06	0,18	0,025	0,025	0,11	0,025	0,025	0,025	0,025
ME-MS61	Te	ppm	0,07	0,07	0,07	0,14	0,08	0,06	0,025	0,025	0,11	0,11	0,07	0,025
ME-ICP61	Th	ppm	0,19	0,07	0,07	0,16	0,19	0,06	0,02	0,08	0,03	0,10	0,14	0,06
ME-ICP61	Ti	%	0,46	0,27	0,06	0,26	0,50	0,22	0,10	0,41	0,10	0,32	0,39	0,49
ME-ICP61	Tl	ppm	<0.02	<0.02	<0.02	<0.02	<0.02	<0.02	<0.02	<0.02	<0.02	<0.02	<0.02	<0.02
ME-ICP61	U	ppm	0,10	<0.1	<0.1	0,10	0,10	<0.1	<0.1	<0.1	<0.1	<0.1	0,10	<0.1
ME-ICP61	V	ppm	146,00	113,00	23,00	107,00	173,00	92,00	35,00	90,00	46,00	135,00	168,00	202,00
ME-ICP61	W	ppm	5,10	5,80	4,20	4,70	7,20	5,40	4,40	8,50	3,40	7,50	4,20	5,60
ME-MS61	Y	ppm	8,50	5,50	0,80	5,90	9,50	4,40	1,50	4,90	1,90	7,10	8,20	10,10
ME-ICP61	Zn	ppm	71,00	69,00	104,00	71,00	66,00	78,00	101,00	93,00	100,00	72,00	62,00	46,00
ME-MS61	Zr	ppm	26,00	11,90	4,60	15,30	27,20	8,60	3,80	15,70	3,60	15,20	16,90	18,60
PGM-ICP23	Au	ppm	0,0005	0,0020	0,0030	0,0080	0,0020	0,0020	0,0010	0,0010	0,0060	0,0050	0,0020	0,0005
PGM-ICP23	Pt	ppm	0,0040	0,0094	0,0079	0,0126	0,0042	0,0044	0,0042	0,0056	0,0156	0,0086	0,0045	0,0011
PGM-ICP23	Pd	ppm	0,0030	0,0080	0,0080	0,0170	0,0050	0,0050	0,0040	0,0060	0,0170	0,0110	0,0050	0,0010
PGM-MS25NS	Au	ppb	0,5	2	3	8	2	2	1	1	6	5	2	0,5